UNIVERSITÀ DEGLI STUDI DI TRIESTE

XXVII CICLO DEL DOTTORATO DI RICERCA IN NANOTECNOLOGIE

Coupling of experimental and computational approaches for the development of new dendrimeric nanocarriers for gene therapy

Settore scientifico-disciplinare: ING-IND/24

Dottorando
Domenico Marson

Coordinatore
prof.ssa Lucia Pasquato

Supervisore di tesi
prof.ssa Sabrina Pricl

ANNO ACCADEMICO 2013/2014

Abstract

Gene therapy is increasingly critical in the treatment of different types of maladies. The approach of gene therapy can be fundamental in dealing with many kinds of tumors, viral infections (e.g., HIV, HSV), and disturbs linked to genetic anomalies. However, the use of nucleic acids is limited by their ability to reach their action site—the target cell and, often, the inside of its nucleus.

Dendrimers, on the other hand, are an interesting kind of polymers, the general synthetic scheme of which is relatively of recent development (∼1980). Among the many possible uses of these polymers, they revealed themselves as great nanocarriers for drugs in general, and particularly for genetic material. Many of the properties of these molecules are directly linked to their structure, and this in turn is critically influenced by their molecular composition. Exploiting *in silico* techniques, we can reveal many informations about the atomistic structure of dendrimers, some of which are otherwise difficult to gather.

The interactions between the carrier and its cargo, and also with all the biological systems that are interposed between the administration and the reaching of the target (e.g., serum proteins, lipid membranes…) are of critical importance in the development of new dendrimers for gene therapy. These interactions can be described and studied at a detail once unthinkable, thanks to the *in silico* simulation of these systems.

In this thesis many different molecular simulation techniques will be employed to give a characterization as precise as possible of the structure and interactions of new families of dendrimers. In particular two new families of dendrimers (viologen and carbosilane) will be structurally characterized, and their interactions with albumin and two oligodeoxynucleotide, respectively, will be described. Then, the point of view of these interactions will be changed: the interactions between a fifth generation triethanolamine-core poly(amidoamine) dendrimer (G5 TEA-core PAMAM) and a sticky siRNA will be studied, varying the length and chemical compositions of the overhangs of the siRNA.

Studying dendrimers the use of new molecular simulations techniques were deepened, and such techniques will be employed in other parallel projects. We'll see the steered molecular dynamic method applied in the study of one mutation of the SMO receptor. The development

of biological membranes models (that will be used in future to study the interactions of dendrimers with such membranes) was also used to refine and better characterize the σ_1 receptor 3D model, previously developed by our research group. A detailed characterization of the putative binding site of this receptor will be given, employing this refined model.

SOMMARIO (ITALIAN ABSTRACT)

La terapia genica si sta rivelando sempre più importante nel trattamento di diversi tipi di malattie. Da diversi tipi di tumori alle infezioni virali, quale ad esempio da HIV, fino anche a malattie legate ad anomalie genetiche sono tutti disturbi in cui l'approccio della terapia genica può rivelarsi fondamentale. L'utilizzo di acidi nucleici quali agenti terapeutici è fortemente limitato dalla possibilità di portare queste molecole al loro sito d'azione—la cellula bersaglio e, spesso, l'interno del nucleo di quest'ultima.

I dendrimeri d'altro canto sono un interessante tipo di polimero, di cui lo schema generale di sintesi è relativamente recente (∼1980). Tra i diversi loro utilizzi, questi polimeri si sono rivelati anche ottimi agenti di trasporto per farmaci, ed in particolare per materiale genetico. Molte delle proprietà di queste molecole derivano direttamente dalla loro struttura, e questa è influenzata criticamente dalla loro composizione. Mediante tecniche *in silico* è possibile avere molte informazioni riguardo la struttura dei dendrimeri, alcune delle quali sono altrimenti difficilmente ottenibili.

L'interazione tra il trasportatore ed il suo "carico", come anche con tutti i diversi sistemi biologici che si frappongono tra la somministrazione ed il raggiungimento dell'obbiettivo (ad es. proteine seriche, membrane lipidiche...) è un parametro chiave nello sviluppo di nuovi dendrimeri per la terapia genica. Queste interazioni possono essere descritte e studiate con un dettaglio un tempo impossibile, mediante la simulazione *in silico* di tali sistemi.

In questo lavoro di tesi diverse tecniche di simulazione molecolare saranno utilizzate al fine di dare una caratterizzazione quanto più precisa possibile della struttura e delle interazioni di nuove classi di dendrimeri. In particolare sarà data una descrizione strutturale di due nuove famiglie di dendrimeri viologeni e carbosilani, e delle loro interazioni rispettivamente con albumina e due diversi oligodeossinucleotidi. Si alternerà poi il punto di vista da cui studiare tale interazione: sarà data una descrizione dell'interazione tra un dendrimero poliammidoamminico a nucleo trietanolamminico (TEA-core PAMAM) di generazione 5 e uno *sticky* siRNA, al variare della lunghezza e tipo di "braccia" del siRNA.

Nello studio di dendrimeri alcune nuove tecniche di simulazione molecolare sono state approfondite, e tali tecniche sono state utilizzate anche in altri progetti paralleli. Vedremo

la *steered molecular dynamic* applicata allo studio di una mutazione del recettore SMO. Lo sviluppo di modelli di membrane biologiche (utile in futuro per lo studio dell'interazione di dendrimeri con tali membrane) è stato utilizzato per perfezionare e meglio caratterizzare il modello tridimensionale del recettore σ_1, precedentemente sviluppato dal nostro gruppo di ricerca. Una caratterizzazione dettagliata del sito di binding putativo di questo recettore sarà descritta, usando tale perfezionato modello.

"Music has no effect on research work,

but both are born of the same source

and complement each other

through the satisfaction they bestow."

Albert Einstein

ACKNOWLEDGMENTS

I would like to express my gratitude to my supervisor, Prof. Sabrina Pricl, and collaborators Dr. Erik Laurini and Dr. Paola Posocco, whose expertise, understanding, and patience, were fundamental to my graduate experience. I would like to thank all the people at the MOSE lab that helped me during these three years, in particular: Prof. Maurizio Fermeglia, Dr. Valentina Dal Col, Dr. Francesca Santese, Andrea Mezgez.

I would also like to thank Prof. Bernhard Wünsch and all his collaborators, in particular Dr. Stefanie Brune, to our joint efforts in the enigmatic field of sigma receptors.

Contents

List of Figures

LIST OF TABLES

PART I

INTRODUCTION

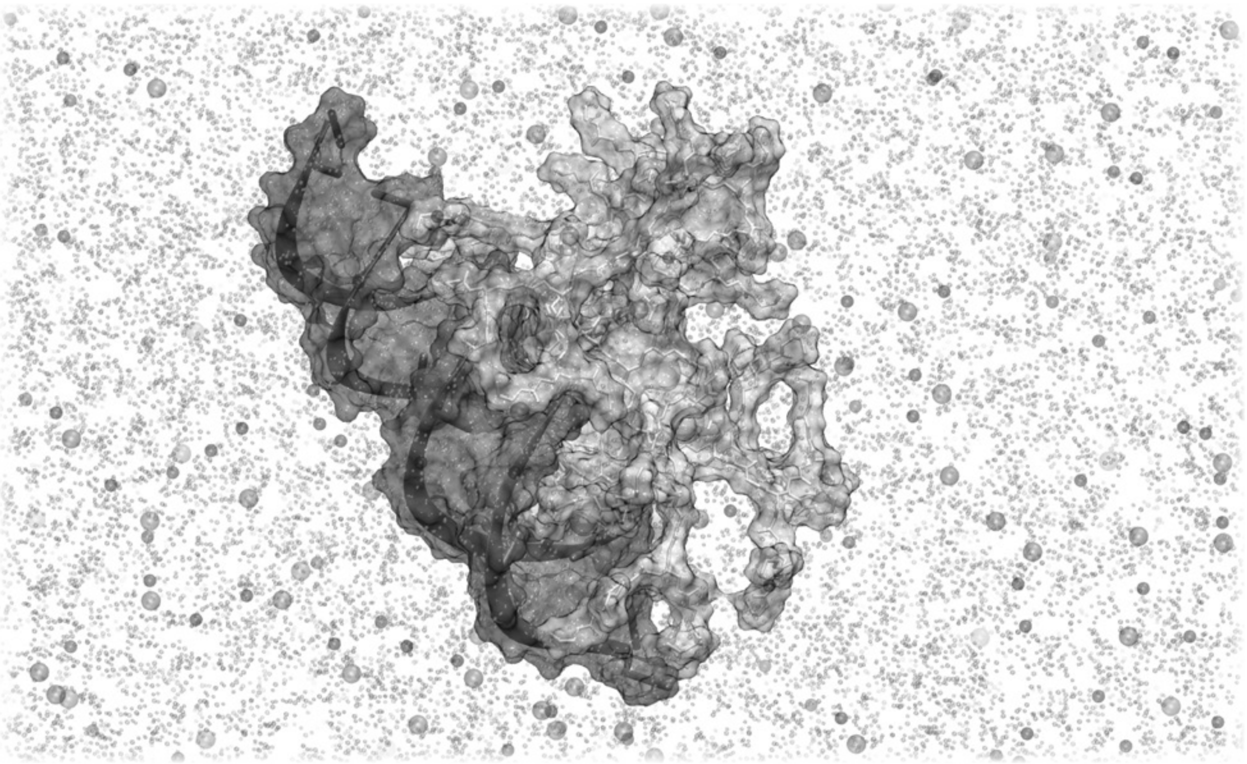

G4 PAMAM dendrimer in complex with a siRNA molecule.

1

Gene therapy

Cancer and genetic disorders are only the main serious diseases that can be addressed by gene therapy. To succeed with this strategy, it's of vital importance the creation of safe and efficient delivery vehicles. This is necessary because the main limitation of these therapy *in vivo* is the difficulty of transporting large and negatively charged molecules like nucleic acids (NAs) inside the nucleus of a cell, obviously without degradation. Most NAs as such not only experience transport problems across the cell membranes but also are subjected to rapid recognition and enzymatic digestion by nucleases. Therefore, appropriate nanovectors able to efficiently and safety allow genetic material to reach the desired population of cells, cross their membranes, discharge the exogenous nucleic acid bringing out maximum therapeutic effects are highly needed.

To ensure the delivering to the right target, the vehicle-NA complex must be able to remain in the bloodstream for the needed time, avoiding the uptake by the mononuclear phagocyte system. The complex must be able to enter the cell and, once inside the cytoplasm, avoid lysosomal degradation.

Taking inspiration from nature, the most commonly used carriers for delivering NA nowadays are of viral origin. As expected these molecules can trigger immunological responses, so it's needed the development of safer and cheaper alternatives.

Dendrimers currently play the leading role as premiere nanocarriers in general, and especially in gene delivery. These macromolecules provide great gene loading capacity, well-defined physicochemical properties, and a high degree of molecular diversity that allows extensive modification to help overcome extracellular and intracellular barriers.

1.1 Protein therapy and gene therapy

Proteins have been used for treating various kinds of diseases, an approach named protein therapy.[1, 2] The bioavailability of therapeutic proteins in the body is not surprisingly low, the rate of hepatic and renal clearance is high, and they are unstable *in vivo.* The simpler answer of increasing the doses is non available, as this operation increases also their toxic effects, and this molecules are expensive to produce industrially.[3] A simple in concept, but hard to realize, idea is that we can efficiently insert the gene which encodes the protein, that will be efficiently produced directly by the cells of the patient. The production of the therapeutic protein, once the gene has correctly reached his target, is long lasting and stable in quantity. Moreover unwanted effects produced by the systematic presence of a introduced protein are avoided.

1.2 Classification of gene therapy

The broad name of "gene therapy" collects many different methods of using NA to treat diseases. The common goal is to insert a NA that repair a dysfunction or interfere in the production of malign proteins. The first use of the term is referred to the insertion of a gene into the patient's cells, that can alter the number and kind of proteins produced. Targeting germ (reproductive) cells as sperm or zygotes, the gene inserted will be integrated into the genome and can be inherited.[4] This type of gene therapy can raise ethical resistance; however, the US Food and Drug Administration (FDA) has allowed the research in the field of germ line gene therapy in the United States of America, but does not allow federal funds to be used for this research in people. If the targeted cells are somatic (non-reproductive), the effect will be restricted to the individual and thus will not be inherited.

In a broader sense, is possible to transfer genetic material to cells infected by a virus, like Human Immunodeficiency Virus (HIV), to block the transcription of genes of the virus itself, but not interfering with the patient's genome. Another possibility is the insertion in a cell of small interfering RNA (siRNA), specific nucleic acid-targeting reagents for gene expression modulation. In this methodology, the goal is not to insert a gene into the target cell genome, but to block the production of proteins interfering with the messenger ribonucleic acid (RNA) produced by the cell.

1.3 HIV fight

Drug resistance and toxicity are the main obstacles for the development of new anti-viral drugs against HIV infection.[5] Moreover is a fundamental property of new drugs to be able to reach the latently infected cells. Short oligodeoxynucleotides (ODNs) are a class of antisense therapy drugs, promising in HIV control and also in the treatment of cancer, metabolic disfunction and other infections.[6] Two ODNs are promising in the fight against HIV: GEM91, and SREV.

GEM91 is a 25-base long ODN that binds to the translation initiation site of the *gag* gene of the HIV-1 pathogen of acquired immunodeficiency, inhibiting virus entry/reverse transcription and reducing steady state viral RNA levels.

SREV is of sufficient length to inhibit the expression of the *rev* gene and halt viral replication. The *rev* gene regulates the expression of HIV structural genes; *rev* mutants are incapable of synthesize structural proteins *gag*, *pol*, and *env.*

1.3.1 Cationic carbosilane dendrimers

Cationic carbosilane dendrimers containing ammonium (or amine) groups in their molecular architecture (and particularly at their surface) could be used as internalizing agents for gene therapy. Muñoz-Fernandez et al. have recently shown that generation 2 (G2) cationic carbosilane dendrimers present low toxicity and also retain and internalize genetic material as ODNs or siRNAs. Particularly four dendrimers (Figure 14.1 on page 97) were characterized for their capacity of binding to different ODNs and serum proteins and, most importantly, for their ability to transfect blood cells and inhibit HIV-1 replication in the presence of serum.[7–11] An important property of this family of dendrimers is that they can form complexes with ODNs or even with plasmids at biocompatible doses, even at a low generation as G2. The presence of Si$-$O bonds in their structure is also another important feature of these dendrimers, by exploiting the corresponding hydrolytic process.

1.4 siRNA

RNA-based therapeutics can be classified by the mechanism of activity, and include inhibitors of messenger RNA (mRNA) translation (antisense), the agents of RNA interference (RNAi), catalytically active RNA molecules (ribozymes), and RNAs that bind proteins and other molecular ligands (aptamers). siRNAs target specifically NAs to modulate gene expression, and are developed from the discovery of the RNAi process (late 1990s).[12] The cellular process of RNAi uses small RNAs to silence gene expression through post-transcriptional or transcriptional gene silencing. Post-transcriptional gene silencing (PTGS) is regulated by translational repression and degradation of mRNAs with imperfect complementarity, and sequence specific cleavage of perfectly complementary mRNAs. An endogenous microRNA (miRNA) repress translation of a perfectly complementary mRNA, while if the complementarity is limited, it can induce its degradation.

Figure 1.1 gives a brief overview of the mechanisms involved in PTGS. In general, primary miRNAs (pri-miRNAs) are processed by a complex into the nucleus, and then incorporated into the pre-RNA-Induced Silencing Complex (RISC) complex.[13] Similarly, the same pre-RISC complex directs the processing of short hairpin RNA (shRNA) and double-stranded RNA (dsRNA) molecules into ~21–23 nucleotides siRNAs.[14] One strand of the siRNA is loaded into RISC and can direct sequence-specific cleavage of mRNA.[15] While protected inside RISC, the guide siRNA strand can be repeatedly used to target many complementary mRNAs, needing a low concentration of siRNA molecules to achieve therapeutic knockdown of endogenous and viral mRNA. This is a main advantage with respect to some antisense therapies, which act stoichiometrically on the mRNA target. Therapeutic siRNAs and shRNAs utilize many of the same endogenous factors of natural miRNAs, so artificial siRNA/shRNA therapeutics may compete with the endogenous miRNA mechanisms.

A common approach to induce PTGS is the delivery of siRNA molecules to cells in dsRNA form. This method transiently knock down gene expression after each successful drug treatment; also, siRNAs are fragile molecules, and enough concentration of siRNA needs to reach the target cells.

shRNA, on the contrary, are constitutively expressed from promoters and can induce long-term gene silencing for the duration of their transcription and biogenesis. It has to be kept in mind that an over-expression of shRNAs can saturate the natural miRNA machinery, resulting in severe toxicity.[16, 17]

Similar to other RNA-based therapeutics, the efficacy of siRNA/shRNA drugs relies on maximizing targeted delivery while minimizing off-target toxicity and degradation: functional and effective delivery methods are crucial for this highly promising approach to therapy.

1.4.1 STICKY siRNA

Conventional artificial siRNA molecules bear $(dT)_2/(dT)_2$ overhangs at the 3´-ends, which protect the fragments from RNase degradation and exert a beneficial effect on the RNAi machinery.[18]

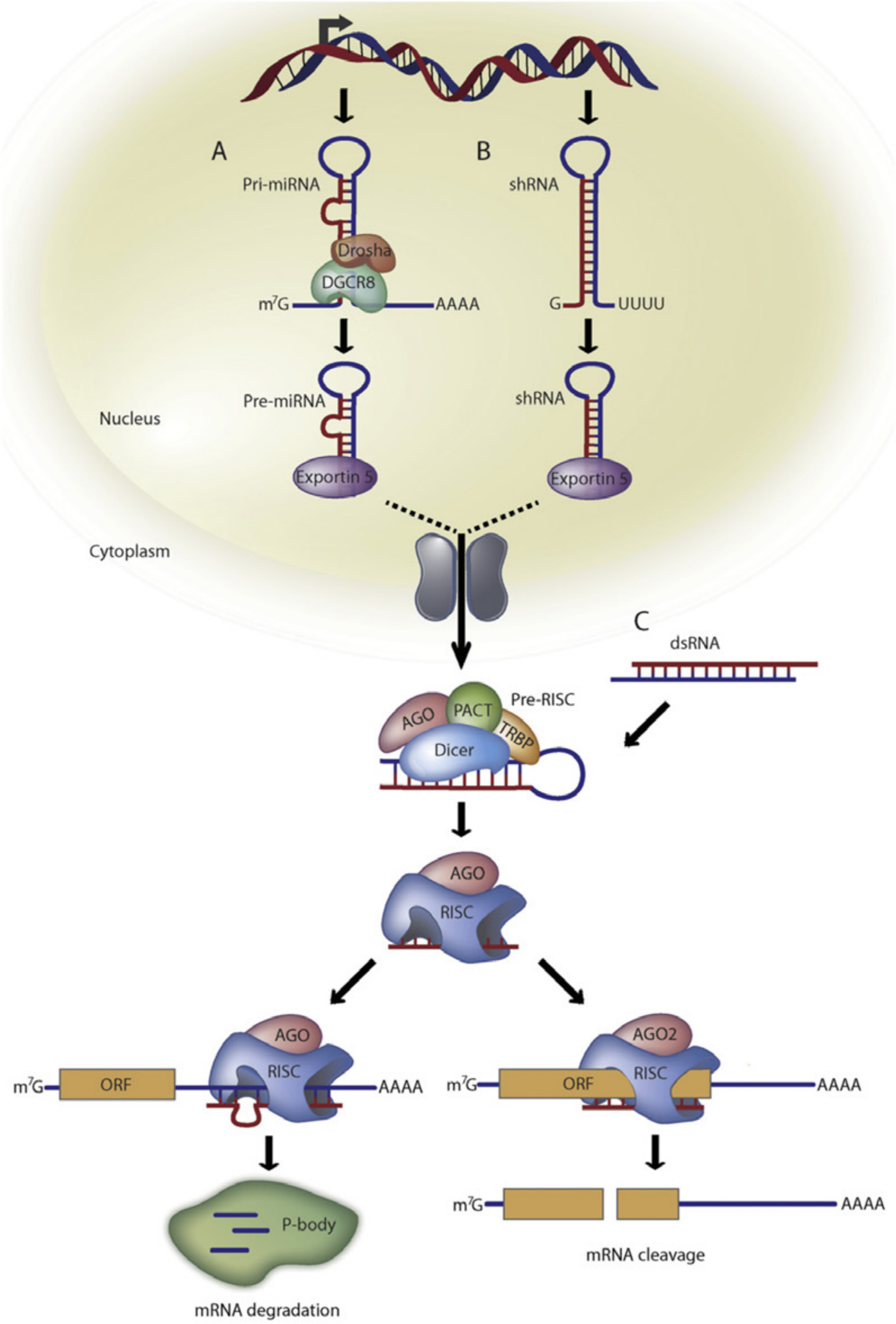

Figure 1.1: Mammalian PTGS pathway for miRNAs, shRNAs, and siRNAs.

A further improvement was performed by Behr and co-workers, which demonstrated that “sticky” siRNA, siRNA with complementary sequence overhangs such as $(\mathrm{dA})_\mathrm{n}/(\mathrm{dT})_\mathrm{n}$ (n $\geq$ 5) exhibit better gene silencing efficiency compared to their $(\mathrm{dT})_2/(\mathrm{dT})_2$ analogous.[19] This behavior was observed when polyethyleneimine (PEI) is used as the delivery agent, but has to be noted that PEI is not efficient in delivering conventional siRNA with standard overhangs—although is a good vector for gene delivery.[20]

A possible explanation of these observation could be the self-assembly of sticky siRNA into “gene-like” long double-stranded RNA (Figure 12.3 on page 74). This mechanism allows stronger cooperativity and multivalency in interactions with the PEI vector.

An additional contributing factor might also be the overhangs of the sticky siRNA. Thanks to the inherent flexibility of single strand nucleic acid fragment, the overhangs could behave as a sort of clamps to hold the nanovector just like protruding molecular arms.

2

DENDRIMERS

Dendrimers are polymeric macromolecules with a highly branched 3D structure, hence their name from the greek $\delta\varepsilon\nu\delta\rho o\nu$ (*dendron*, tree). The first conceptualization of such treelike structures is dated back to 1941, by Flory[21–23]. He proposed that highly branched molecules could be constructed by using a trifunctional monomer possessing two different functional groups, A and B, where A and B can react with one another. The first successful laboratory synthesis of something similar to this dendritic complexity did not occur until the late 1970s[24], developing the concept of repetitive growth with branching applied to the construction of low molecular weight amines. The first article using the term "dendrimer" and describing in great detail the preparation of poly(amidoamine) (PAMAM) dendrimers was presented in 1984 at the First International Polymer Conference, Society of Polymer Science, Japan (SPSJ).[25] In contrast to linear polymers, dendrimers have precisely controlled architecture with tailor-made surface groups, which could be finely tuned. These pioneering works demonstrated that polymers could be constructed possessing discrete sizes, shapes and molecular weights.

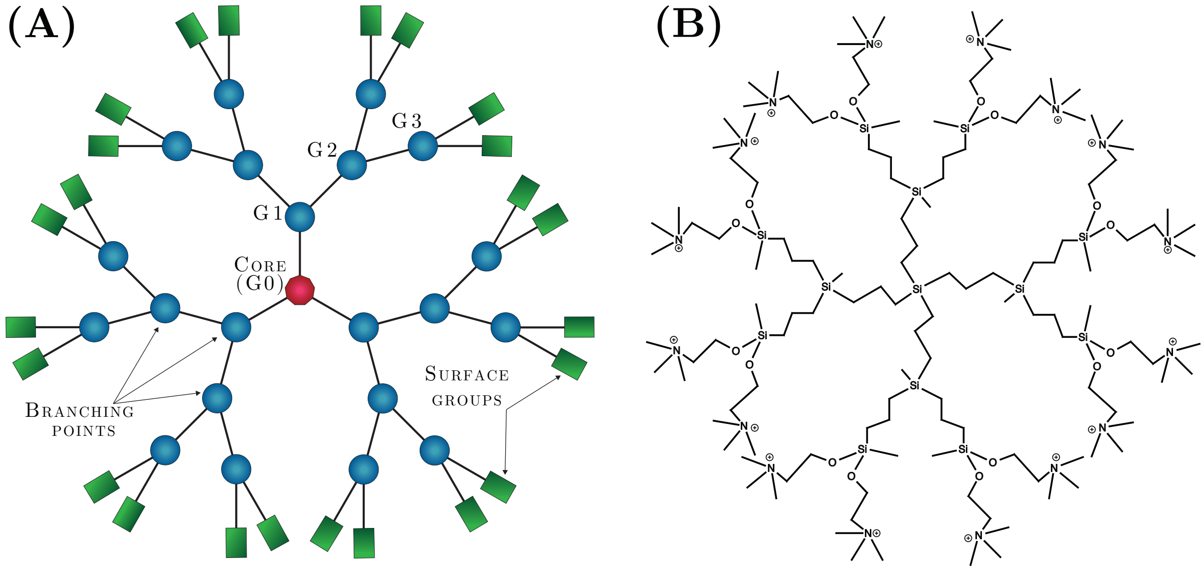

Figure 2.1: (A) 2D representation of a dendrimer, demonstrating its different component and (B) an example of the structure of a G2 carbosilane dendrimer; the Si atoms are the branching points, while the central Si atom is the core.

2.1 Of structure and generation

In the simpler scenario dendrimers are produced adding to a central core molecular groups. Repeating the process, successive layers are added and the structure can be expanded to the required size. To schematize, a dendrimer consists of (Figure 2.1):

- an initiative central core, that can be a single atom (e.g., Si) or a simple group (e.g., phenyl, triethanolamine (TEA)) with at least two identical chemical functions;
- many branches, emanating from the core, constituted of repeat units, organized in a geometrical progression that results in a series of radially concentric layers;
  - the branching (or focal) units, where the dendrimer branch is divided into two or more branches, that can also be a single atom or a simple group;
  - the homostructural spatial segments between the focal points (dendrimer shell), or between the last outer branching point and the surface (dendrimer outer shell);
- the terminal (or end, surface) groups, in other words the outer chemical moiety.

The number of focal points going from the core towards the dendrimer surface is often referred as the generation number of that dendrimer. This is useful to discriminate between different dendrimers of the same family (with the same core, branching, spatial and terminal groups).

So a dendrimer having four focal points is a 5th generation dendrimer, or G5 (letter G plus the number of generation). The smaller member of a family is the G0 dendrimer, that is the functionalized central core.

The branched topology confers dendrimers their important properties. For example a molecular architecture with chemically distinct interior and surface can be used to encapsulate and release molecules chemically incompatible with the environment external to the dendrimer (e.g., catalysts, drugs, or chromophores).[26] Another property that stems from the chemical structure of these objects is their multivalency. The number of surface groups increase with dendrimer generation and it's possible to have a dense presentation of multiple terminal groups on the dendrimer surface. Multivalency can be exploited as a means to achieve concentrated payloads of drugs or imaging labels chemically grafted to the dendrimer surface.

Similar to dendrimers are dendrons, monodisperse wedge-shaped dendrimer sections with multiple terminal groups and a single, different, reactive function at the core. In addition to the properties of dendrimers, this function gives an option of orthogonal reactions utilizing the distinct reactive point at the core and surface groups. For example, one can graft dendrons to a surface, to another dendron[27] or another macromolecule.[28]

2.2 Of synthesis

From the first successful laboratory synthesis of a dendrimer in 1978, many attempted were made to simplify and speed up the process. Different methods can have different advantages in creating a dendrimer with multifunctional terminal groups for example, or in reaching an higher generation number.

2.2.1 Divergent approach

In this approach, the core is reacted with at least twice of reagent containing at least two protected branching sties.[29] The reactions is followed by removal of the protecting groups, leading to the formation of first generation dendrimer, and this process can be repeated several times, until the dendrimer of the desired size is formed. This is the simplest scheme of synthesis, and PAMAM dendrimers are often prepared by this method. One advantage of this approach is that the end groups can be different from the inside groups, modifying the surface of the molecule.

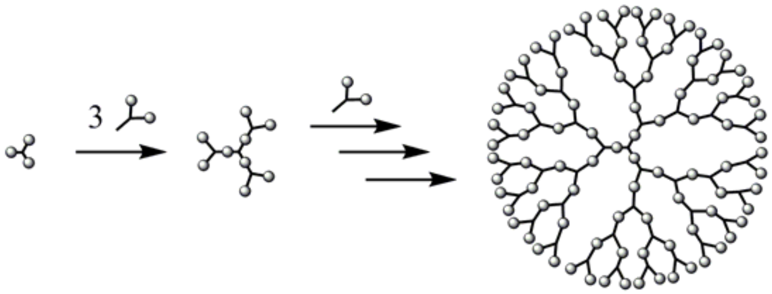

Figure 2.2: Scheme of the divergent growth approach for the synthesis of dendrimers.

2.2.2 Convergent approach

One of the main limitations of the divergent approach is that the terminal group is the same in all dendrimer's branches. To overcome this limit, the convergent method was proposed in 1990 by Hawker and Fréchet.[30] Firstly is synthesized a focal point functionalized dendron, that secondly will be anchored to a chore with other dendrons, to produce a hetero-dendron dendrimer.

However a common limitation to both these methods is the difficulty to synthesize the dendrimer in large quantities: repeated reactions are occurring while the active site needs to be protected.

2.2.3 Other approaches

The simplest methods previously described are both boring and time-consuming, while producing lots of waste products. Many other methods were developed in the last years, like the "double-stage",[31] "double-exponential growth",[32] "orthogonal coupling"[33] methods. The first methods that drastically reduces the number of passages needed, and also produces less waste products, uses the "lego" chemistry and was introduced by the group of J.P. Majoral.[34]

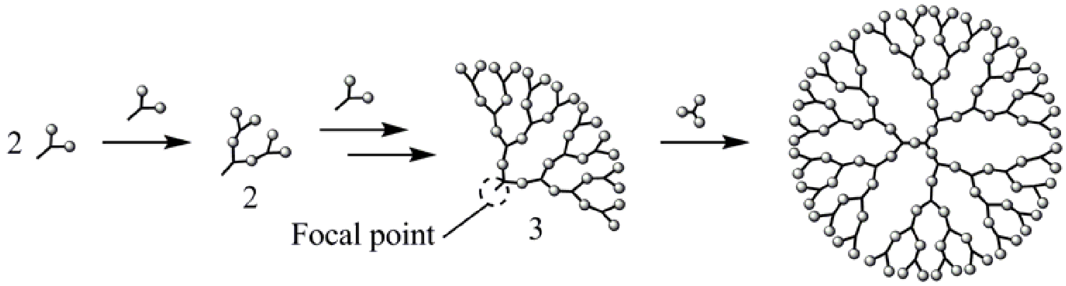

Figure 2.3: Scheme of the convergent growth approach for the synthesis of dendrimers.

2.3 Of properties

Dendritic architecture holds great potential over other carrier systems, particularly in the field of drug delivery, because of the unique properties compared to linear polymers.

2.3.1 Shape and size

The high level of control over dendrimers' architecture makes them an ideal carrier. The size of dendrimers increases proportionally to the generation number, ranging from several to tens of nanometers in diameter. The size of common dendrimers is similar to many biological structures (as example, a G5 PAMAM dendrimer is approximately the size of human serum albumin (HSA)—5.5 nM diameter).[35]

The size of a dendrimer influences also its shape; lower generation dendrimers tend to be open and amorphous whereas higher generations can adopt a spherical conformation. This parameter is obviously highly influenced by the internal chemical structure of the branches and the core.

2.3.2 Monodispersity

Dendrimers are monodisperse, unlike linear polymers. This property offers the advantage of working with a tool of well-defined and reproducible scalable size.[36] The convergent method generally produces the most isomolecular dendrimers, thanks to the purification at each step of synthesis. Dendrimer bridging and incomplete removal of protection blocks at each of the generation sequences may effect the degree of monodispersivity.[37]

2.3.3 Peripheral charge

An important property of the terminal units of a dendrimer is their charge. End groups may possess positive, negative or neutral charges, which are vital for the resulting properties of the final dendrimer. Cationic dendrimers (e.g., PAMAM) can form complexes with negatively charged NAs. The positive charges facilitates also the interaction with negatively charged biological membranes.

The polyvalency of dendrimers can also lead to their toxicities, mainly cytotoxicity and hemolysis.[38–46] One of the main effort in the development of new dendrimers is the engineering of their surface to overcome these toxicities.

2.3.4 End groups and toxicity

The interaction of dendrimers with many cells and cellular compartments is highly important, possibly leading to toxic effects for the patient. The main parameter that influences the toxicity of dendrimers is the number of terminal groups and surface charges. It has been reported an higher, dose-dependent, toxicity with positively charged dendrimers than neutral or negatively charged molecules. In light of these reports, modification of surface groups of cationic dendrimers with neutral molecules is preferred to possibly prevent toxicity.[47–50] The positive charge improve the permeability of biological membranes, facilitating the intracellular delivery of bioactive molecules. At higher generation, however, the disruption of the membrane integrity may be an outcome of the dendrimer-membrane interaction. This lead to the leakage of important intracellular components, which finally can cause cell death, hence the toxicity. This kind of toxicity is attached to higher generations of positively charged dendrimers, attributed to the high charge density of these molecules.

2.3.5 Dendrimer-membrane interactions

As seen, the interaction of higher generation dendrimers having positively charged surface groups with negatively charged biological membrane results in alteration in the membrane and cell lysis. In a study was observed the interaction between cationic phosphorus-containing dendrimers (CPDs, G3 and G4) and a bilayer consisting of 1,2-dimyristoyl-sn-glycero-3-phosphocholine (DMPC) as a model lipid membrane. Presence of dendrimers was observed to lead significant changes in the main transition enthalpy and phase transition temperature values. Rate of alteration of thermotropic behavior was found to be concentration-dependent. The fluidity rate of the lipid-dendrimer complexes was proportional to the dendrimer/lipid molar ratios.[49]

In another study were employed G1 and G4 PAMAM dendrimers with model lipid membranes. It was inferred that at this low generation PAMAM dendrimers interact electrostatically with membrane by inducing aggregation of lipid vesicles without affecting integrity of membrane significantly. This interaction was affected by two parameters; membrane fluidity and surface pressure with preferential interaction at subphysiologic surface pressure in liquid crystalline state, particularly evident in case of rapidly dividing cells.[50]

2.3.6 Biocompatibility

As stated before, the main drawback of dendrimers with cationic terminal ends is a pronounced cytotoxicity at high generations. This phenomena is less observed for neutral or negatively charged dendrimers. Fortunately the toxicity of cationic dendrimers can be overcame by partial or complete modification of their periphery with negatively charged or neutral groups.[38, 39, 42] While for PAMAM this toxicity increase with generation number, the pattern is different for poly (propylene imine) (PPI) dendrimers, although both the families have terminal positively charged amino groups. Development in the filed have resulted in dendrimers with decreased toxicity or even non-toxic dendrimers in both *in vitro* and *in vivo* studies as observed in case of neutral dendrimers like polyester, polyether and surface engineered dendrimers (for example glycosylated, PEGylated dendrimers).[40, 46]

Thiagarajan et al. evaluated the in vivo toxicity of PAMAM dendrimers including effect of surface charge and size of dendrimers on the permeability through epithelial barrier and acute toxicity, on oral administration in CD-1 mice. The scientists investigated the positively charged as well as anionic dendrimers for toxicity and determined the maximum tolerated dose (MTD). The MTD for anionic dendrimers was found to be 10 folds higher than for cationic dendrimers. For cationic dendrimers MTD was found to be in the range of 10–200 mg/kg, while anionic dendrimers were found to be tolerable at doses as high 500 mg/kg.[51] Also, they assessed oral drug delivery aptitude of G6.5 PAMAM dendrimers via *in vivo* oral translocation in CD-1 mice with evaluation of acute oral toxicity and physicochemical disposition, and concluded that dendrimers have the potential to permeate gut epithelial barrier.[52]

2.3.7 Pharmacokinetics

In case of intravenous administration, macromolecules are instantly introduced into the blood stream with restricted diffusion to the extravascular space. Subsequent elimination of these circulating macromolecules occurs followed by distribution to particular organs for disposition. Capillary permeability, organ blood flow and nature of the macromolecules are factors that play a major role in the specific tissue-macromolecules uptake. In case of dendrimers, effect of surface charge on excretion profile of non-biodegradable G5 PAMAM dendrimers was studied. As compared to cationic dendrimer, about twice as much of the uncharged dendrimer was excreted via the urine and feces over seven days, suggesting enhanced cellular uptake of the cationic dendrimers.[53]

Although enough reports are available on the pharmacokinetics of dendrimers yet systematic investigation on the in vivo fate of dendrimers is needed to certify their clinical utility.

2.4 Of the characterization

An important result of a controlled—per step—synthesis of these molecules is a well defined nanomeric architecture. Characterization of dendrimers is therefore a vital step in the designing and engineering of these versatile carriers. Various methods are used to differentiate generations of dendrimers having different surface groups, like high performance liquid chromatography (HPLC), ultra performance liquid chromatography (UPLC), NMR, UV-visible spectroscopy, and X-ray diffraction. The presence of tailor-made surface groups facilitates surface modification of dendrimers, which could be further confirmed by reliable analytical methods including infrared spectroscopy (IR), NMR, AFM, X-ray photoelectron spectroscopy, scanning electron microscopy (SEM), transmission electron microscopy (TEM), matrix-associated laser desorption ionization-time of flight (MALDI-TOF) mass spectrometry, size exclusion chromatography, electrospray ionization-mass spectrometry (ESI-MS), vapor phase osmometry (VPO), laser light scattering (LLS) and sodium dodecyl sulfate-poly acrylamide gel electrophoresis (SDS-PAGE).[54–59]

Various methods of characterization of dendrimers along with description of respective parameters are summarized in Table 2.1.

2.5 Of the applications

Dendrimers have many possible interaction sites, both on their surface and in their internal layers. The potential of dendrimers as vessels or hosts for other molecules was strikingly demonstrated by Jansen et al.[60] All the three architectural components of a dendrimer (core, internal branching units and surface groups) can be tailored to fulfill different goals.

Their multivalency structure might allow researchers to attach both targeting and drug molecules to the same dendrimer, reducing negative side effects of medications on healthy cells. Conjugation of poor-bioavailable drugs with dendrimer may also increase their bioavailability, decrease the dose frequency, and so increase the patient compliance.

2.5.1 Therapeutic activity of dendrimers per se

Poly-lysine dendrimers against Herpes Simplex Virus (HSV) are currently under Phase II clinical trials for their efficacy against vaginal infection. SPL7013 Gel (VivaGel®) developed by Starpharma Pty Ltd (Melbourne, Australia) is a vaginal microbicide for the prevention of HIV and HSV infections.[61] The active ingredient of this carbopol-based aqueous gel is a dendrimer with a divalent benzhydrylamine (BHA) core, four generations of lysine branches with the outermost branches capped with a total of 32 naphthalene disulfonic acid groups that impart hydrophobicity, and a high anionic charge to the dendrimer surface.[62]

PAMAM dendrimers were studied for antimicrobial activity against *Escherichia coli*, their activity being attributed mainly to the interaction with polyanionic lipopolysaccharide.[63]

Analytical method	Characterized parameter
Nuclear magnetic resonance (NMR)	Helps in determining chemical transformation undergone by end groups; applicable to structural analysis and step-by-step characterization of synthesis
Infrared and Raman spectroscopy	Ascertains the chemical transformation taking place during the synthesis or surface engineering
UV-visible spectroscopy	Helps in determining the change in chemical structure and synthesis method by detecting chromophores and auxochromes. Also used to test the purity
Fluorescence	Used to characterize the structure and synthesis of dendrimers having photochemical groups and to quantify defects occurred during the synthesis
Circular dichroism	Characterization of structure of dendrimers having optical activity
Atomic force microscopy	Characterization of size, shape and structure
Transmission electron microscopy (TEM), electron paramagnetic resonance	Characterization of surface structure
X-ray diffraction	Gives information about chemical composition, size and shape
X-ray photoelectron spectroscopy	Gives information about chemical composition and size
Electrochemistry	Gives information about the structure
Electrophoresis	Assess purity and homogeneity of water-soluble dendrimers
Small-angle X-ray scattering (SAXS)	Gives average radius of gyration (R_g) in solution; used for determination of average particle size, shape, distribution, and surface-to-volume ratio
Small-angle neutron scattering (SANS)	Gives average radius of gyration (R_g) in solution as well as detailed information about the internal structure
Laser light scattering (LLS)	Gives the hydrodynamic radius
Mass spectrometry (FAB-MS, ESI-MS, FT-ICR MS, MALDI-TOF MS)	For the determination of molecular mass and some structure information
Size exclusion (or Gel permeation) chromatography (SEC, GPC)	Gives molecular weight and size
Intrinsic viscosity	Gives physical characterization and morphological structure
Differential scanning calorimetry (DSC)	Gives the glass transition temperature (T_g), which is affected by the molecular weight, entanglement and chain-end composition of polymers
Dielectric spectroscopy	For studies of molecular dynamics

Table 2.1: Methods of characterization of dendrimers.

2.5.2 Solubilization and improvement in delivery

Many drug molecules are limited in their applications by their hydrophobicity, and so poor water solubility. Dendrimers are a promising candidate for solubilization of bioactive molecules. The main mechanisms that are involved in this regard are micellar solubilization, ionic interactions, hydrophobic interactions as well as hydrogen bonding. All of these properties are affected by various tunable factors as dendrimer size, generation, surface groups, internal branching, and also pH and temperature. A study performed with nonsteroidal anti-inflammatory drugs (NSAIDs) including ketoprofen, ibuprofen and diflunisal concluded that PAMAM dendrimers are effective solubility enhancer for these drugs.[64]

PAMAM dendrimers with amino and hydroxyl terminal were also tested for transdermal delivery of a model drug, indomethacin. In the in vivo pharmacokinetic and pharmacodynamic studies with Wistar rats, a significant increase in concentration of indomethacin in blood was observed in case of PAMAM dendrimers-mediated delivery of the molecule, in comparison to that observed with pure drug suspension.[65]

Dendrimers can also increase the retention of pilocarpine within the eyes, showing a possible application of dendrimers in ocular delivery of bioactives.[66]

PAMAM dendrimers of generation 2, 2.5 and 3 were assessed for pulmonary absorption of enoxaparin, a low molecular weight heparin. The increase of the relative bioavailability of enoxaparin was of about 40 % without any adverse effect on mucocilliary transport rate, and without producing severe damage to lung tissues for G2 and G3 dendrimers. Negatively charged dendrimers with carboxyl end groups (2.5G) did not influence the bioavailability, so dendrimer with surface cationic charge can serve as promising vehicle for pulmonary delivery of bioactives.[67]

2.5.3 Targeted delivery and reduction of toxicity

Fatal disorders like cancer and diseases caused by parasitic infections have a well-defined target site, and hence is possible to design a site-specific carrier to treat these disorders. One of the most explored examples in this context is folate conjugated dendrimer for targeting anti-cancer bioactives to tumor. Since the folate receptors are over-expressed on the surface of different types of cancer cells, hence folate conjugated dendrimers can efficiently target anticancer bioactives to the altered cells.[68, 69] In a study with the anticancer drug methotrexate coupled with PAMAM dendrimers and folic-conjugated PAMAM dendrimers, biodistribution of folic acid conjugated dendrimers showed three times higher accumulation in the tumor cells after 24 h compared to those conjugated without folic acid.[70]

The degree of functionalization of a dendrimer can be deeper, and was obtained a PA-

MAM dendrimer functionalized both with folic acid and fluorescein isothiocyanate (FITC), for tumor targeting and imaging, respectively. The obtained dendrimer was linked with complementary oligonucleotides for cell specific binding and internalization.[71] Is clear from this example that it is possible a multifunctional engineering of these macromolecules.

2.5.4 DIAGNOSTIC APPLICATIONS

Dendrimers have been used efficiently as imaging agent, in radiotherapy, as X-ray contrast agent as well as molecular probes. Dendrimers linked to various ligands have been used for molecular detection, separation, radiotherapy and as imaging agent. As an example, FITC tagged PAMAM dendrimers has been investigated for determining the cellular uptake.[72] The spectrum of the diagnostic applications of dendrimers is likely to broaden in near future, thanks to their multivalency and tunable surfaces.

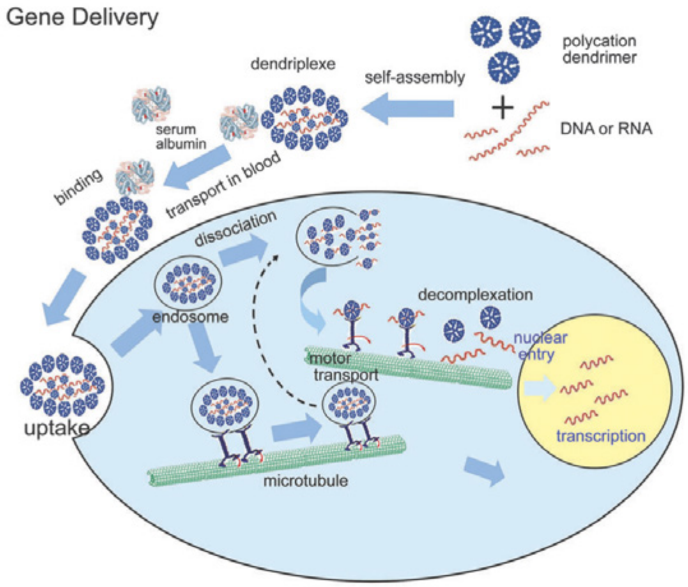

Figure 2.4: Model of gene transfection process with dendrimers.

2.5.5 GENE DELIVERY

Dendrimers with structural flexibility and hyperbranched architectures are suitable candidates for gene delivery operations owing to formation of compact complexes with DNA (dendriplexes), attributed to enhanced flexibility of dendrimers. Figure 2.4 shows a possible route for the use of dendrimers as delivery vectors. DNA is assembled with the dendrimers (forming a complex called dendriplex), and is transported to the specific target cell via the blood stream. Here the self-assembled complex encounter many types of proteins. Once reached its target, the dendriplex should bind to the cell membrane and wait for endosomial uptake, allowing internalization inside the cytoplasm. The endosome escape should happen once inside the cell, and the DNA should be released from the dendriplex. The last critical step is the transfer of the genetic material from the cytoplasm to the nucleus, that is still not completely clear.[73]

3

The broadened use of MD techniques

Molecular simulations are often an attempt to reproduce at the computer the evolution in time of a system of interest. Many detail levels are available to the researcher, and many tools can be used to derive different informations from the trajectories obtained. The, so to speak, simple and plain molecular dynamic can be enriched with different techniques and, once the method is validated, can be used, with due care, on different systems. In this thesis two main different simulations procedures were examined for the use on dendrimers and were applied also in other side projects on which our laboratory was involved. Primarily, I familiarized with the simulation of lipid membrane models, to study the interaction of dendrimers with biological membranes. These models were used to refine the σ_1 receptor 3D homology model developed by our group, and also in the study of two mutations of the smoothened receptor (SMO). In this second work I used also the steered molecular dynamic (SMD) technique to shed light on the mechanism of resistance to vismodegib in one of these two mutations.

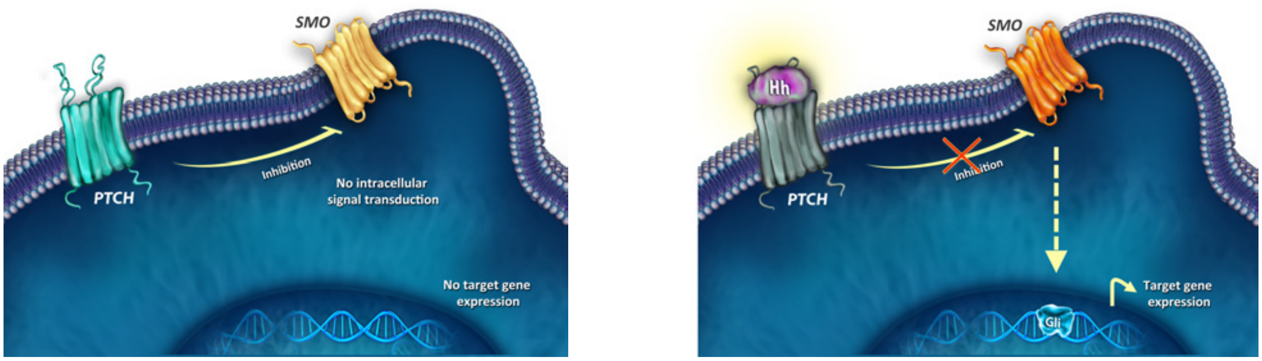

Figure 3.1: Hedgehog pathway scheme, in absence (left) and presence (right) of a PTCH ligand.

3.1 BASAL CELL CARCINOMA AND SMO RECEPTOR

Basal cell carcinoma (BCC) accounts for approximately 70% of all malignant diseases of the skin. The incidence of BCC is strongly associated with exposure to UV radiation, and has increased dramatically over the last 30 years.[74, 75]

Current treatments are mainly surgical approaches, which are the most effective strategy. Radiation therapy is employed to eliminate surgical residual not otherwise curable, or in patients that aren't surgical candidates.[76] There is although a significant rate of recurrence, often associated with increased aggressiveness, and also there is a poor prognosis upon metastatic spread.

3.1.1 THE HEDGEHOG PATHWAY

The pathogenesis of BCC involves the Hedgehog (Hh) pathway, that plays a critical role in embryonic development and is not active in most adult tissues. An exception are stem cells, hair follicles, and skin cells, for which the Hh pathway is important.[77] The "Hedgehog" terms comes from the description of *Drosophila melanogaster larvae*, which took the appearance of an hedgehog when the relevant gene was mutated.[78] The pathway activation starts with the Hh ligand binding to a 12-pass transmembrane receptor known as PTCH. This receptor acts as a tumor suppressor in the absence of its ligand, inhibiting the SMO protein, a G-protein-coupled receptor. So, it is the SMO receptor that is responsible for the propagation of the signal, once a ligand binds to PTCH and the inhibition on SMO is released. The subsequent mechanism is not completely clear, but certainly there is the release of the inhibition of glioma-associated (Gli) protein, a transcription factor linked to oncogenic effects on the cells. Gli transcriptional activation upregulate the expression of PTCH1 (negative feedback), Gli-1

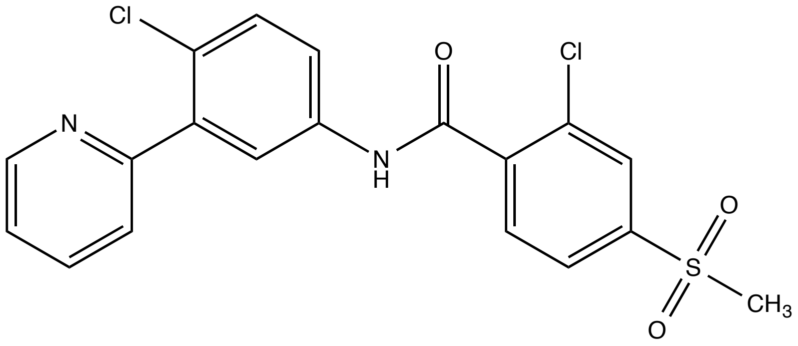

Figure 3.2: Chemical structure of vismodegib.

(positive feedback) and other factor important for the survival of the cell, involved in the cell cycle regulation and angiogenesis, as well as antiapoptosis mechanisms.

The Hh pathway interacts also with many other pathways, and a variety of diseases have been linked to abnormal Hh pathway signaling, including medulloblastoma, hematologic malignancies, and other solid tumors.

As was briefly described, there are many possible alterations in the Hh pathway that can alter it's functionalities. Mutations that inhibit the PTCH receptor, or that constitutively activate the SMO or Gli proteins can produce a ligand independent activation of the pathway.[79]

3.1.2 Drug-based therapeutic approach. . .

The ingestion of corn lilies (*Veratrum californicum*) during the gestation of sheep was observed to lead to cyclopia in the offspring. From the plant was isolated cyclopamine, a SMO antagonists. From this molecule more potent e selective SMO antagonists were developed and are used for a variety of cancer types, including advanced BCC cases.

A promising molecule is the orally administered SMO inhibitor GDC-0449 (vismodegib, Figure 3.2), currently in a trial of patients with locally advanced or metastatic BCC.[80, 81] At a dose of 150 mg once daily received FDA approval in 2012 for the treatment of adults with BCC that has recurred following surgery, or patients unsuitable for surgery or radiation.

3.1.3 . . . and drug resistance

The response to vismodegib treatment, and similar drugs, is usually dramatic. Unfortunately, as often is the case, resistance to SMO inhibition can occur: previously responding tumors restart their growth, or new tumors are developed by the patient. The mechanism of such resistance is complex, and only recently we are shedding light on it. An important observation was made comparing samples of before-treatment and vismodegib-resistant tumor of the same

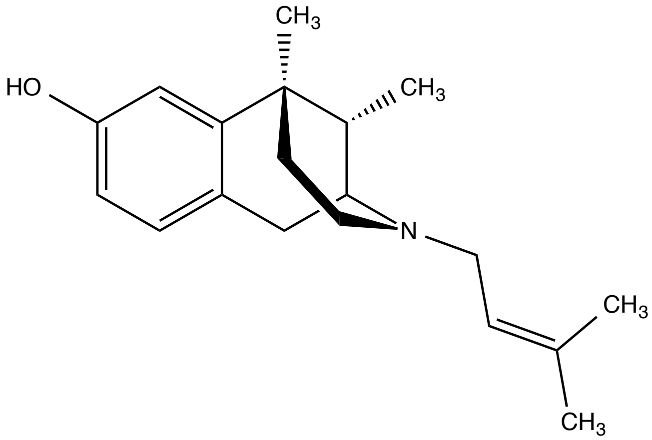

Figure 3.3: Chemical structure of (+)-pentazocine.

patient, in treatment with vismodegib. The pre-existing PTCH mutation found in the pre-treatment tumor was still present in the resistant tumor, but a new mutation in SMO was observed (D473). This mutation was found to affect vismodegib binding to SMO, conferring the drug-resistance.[82]

3.2 The σ_1 receptor

Discovered in 1976, the σ receptor was initially described as a subtype of opioid receptor. It was identified using the compound SKF 10,047 (N-allylnormetazocine), hence the name from the greek letter for *"s"*. Unfortunately, SKF 10,047 is now recognized as a non-selective ligand, and years later it was recognized that the σ are a distinct class of receptors, widely distributed in the central nervous system, as well as in the rest of the body.[83, 84]

To date, at least two subtype, σ_1 and σ_2, have been identified, with different pharmacology and molecular mass.[85, 86] Since their discovery, many studies have linked the σ receptors to different human disease; from cancer to central nervous system maladies and substance abuse. Unfortunately our knowledge on these elusive receptors is limited: we haven't identified an endogenous ligand (Fontanilla et al. identified as probable N,N,dimethyltryptamine[87]), and also their 3D structure is unknown.

Only the σ_1 receptor subtype has been cloned: a single polypeptide of 25 kDa, that shares no sequence homology with any known mammalian protein.[88] Another characteristic that makes harder the study of this receptor is that the σ_1 receptor is promiscuous in its binding; one of the most used radioligand is (+)-pentazocine (PTZ) (Figure 3.3), with an high affinity for the σ_1 subtype and low for the σ_2. A strong binder for σ_2 receptor that also can select between the two subtypes is currently missing.

The σ_1 receptor is localized in the plasma membrane and subcellular membranes; this is

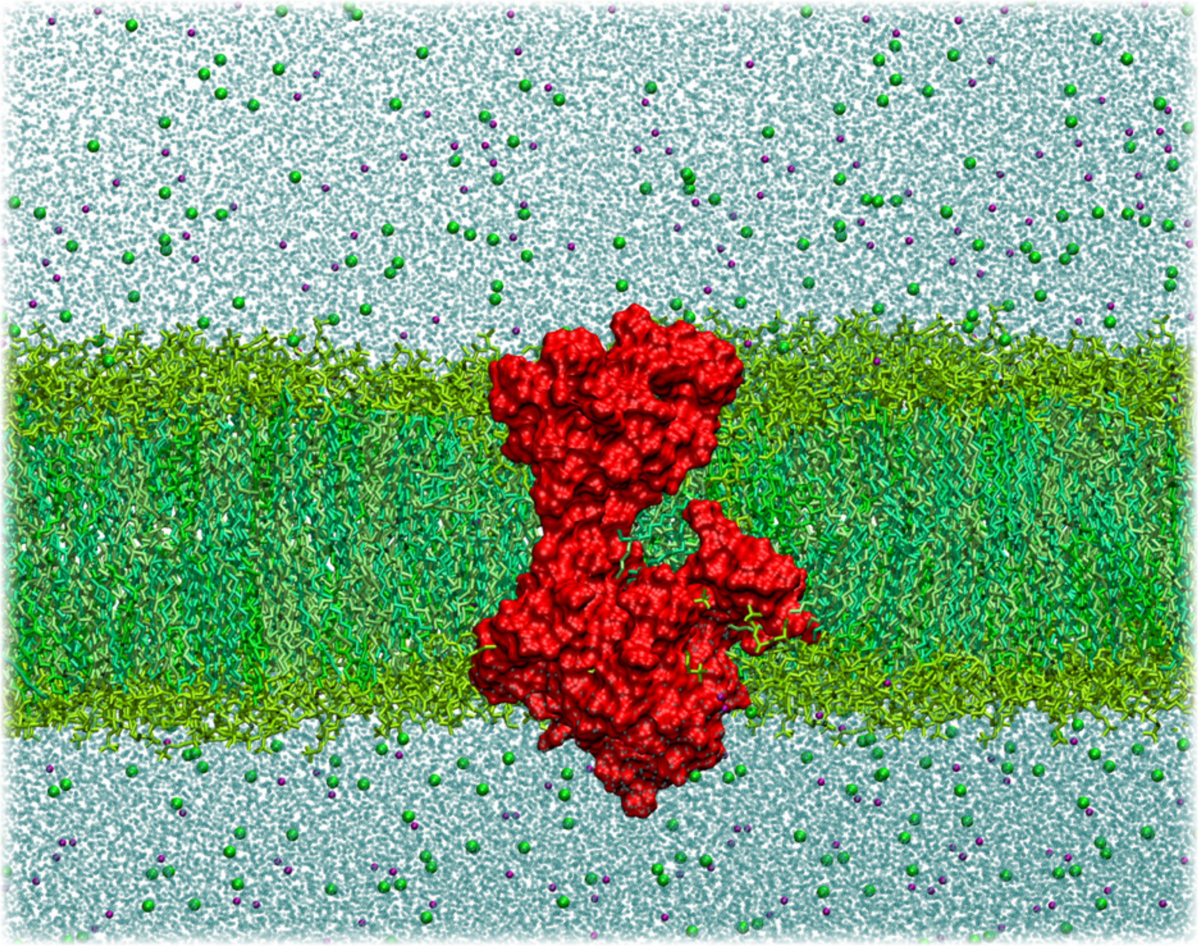

Figure 3.4: Cross section of the 3D structure of the σ_1 receptor embedded in a membrane model (POPC/POPE/CHL, 2:2:1). Water oxygens are shown in light cyan, while Na^+ and Cl^- ions are visible as green and purple spheres, respectively. Lipids are portrayed in different shades of green. The σ_1 receptor receptor protein is shown as red solvent accessible surface.

one of the reasons that makes it difficult to obtain a 3D crystal of this protein. Particularly, the σ_1 receptor is found in the endoplasmic reticulum, where it plays a modulatory role in intracellular ${Ca_2}^+$ signaling.[89] From the data available, our research group was able to built a 3D homology model of the σ_1 receptor, to date the only model of this protein (Figure 3.4).

PART II

MATERIAL & METHODS

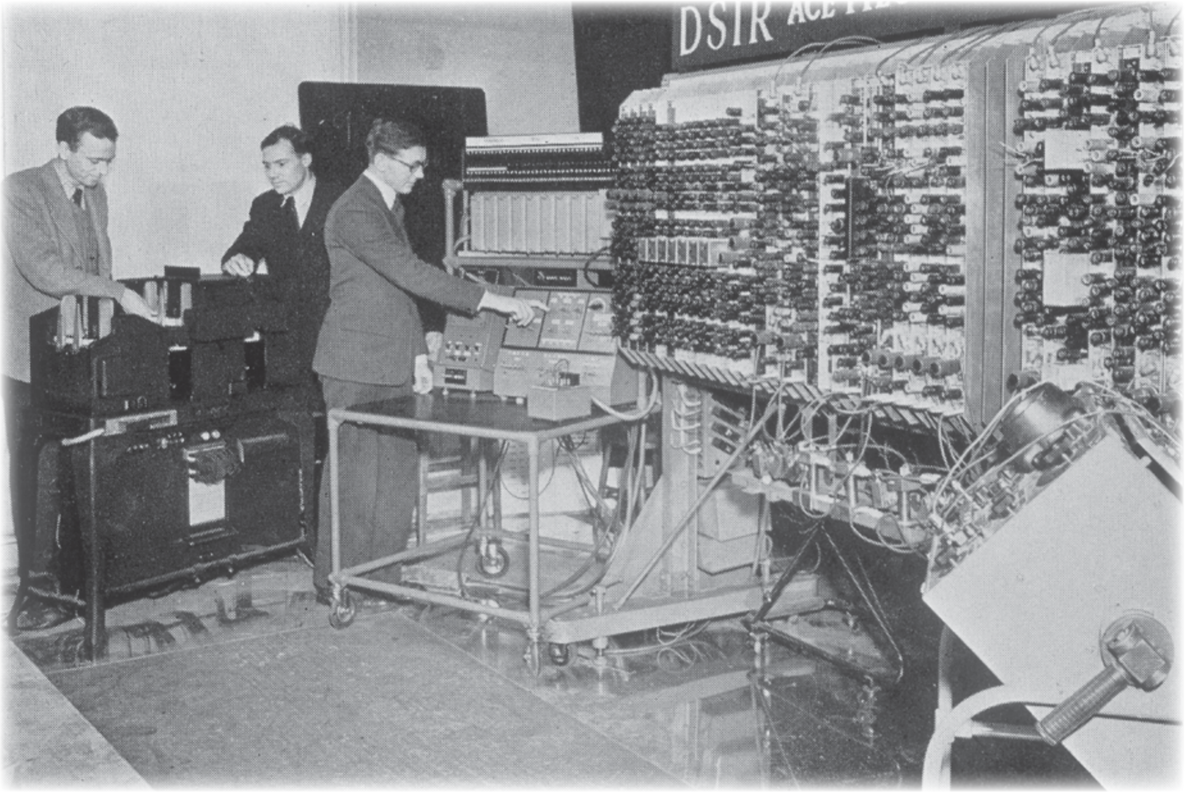

First demonstration of the Pilot ACE computer, 1950.

The gap between the nanoscale, referred as size and time, and the macroscopic world has been reduced exponentially in recent years, thanks to computer simulations. Using computational techniques increasingly "exact" prediction of molecular interactions and bulk properties can be obtained, the main limitation being the available computational power. Nowadays with affordable machines it's possible to have a precision at atomistic detail, with an accurate description of physical interactions. Molecular simulations are divided mainly in two branches: the study of equilibrium conditions (molecular mechanic (MM)) and the evolving of the system with time (molecular dynamics (MD)). In a typical MD simulation, the atomic trajectories of a system of N particles are generated by numerical integration of Newton's equation of motion, for a specific interatomic potential, with certain initial and boundary conditions. Post-processing the trajectory, it's possible to complement experimental data with energetic and structural informations. The precision obtained today in simulations on the order of hundreds of nanoseconds, thanks to modern and *ad-hoc* force fields, is incommensurable with what was achievable ten years ago; the main effort today is to extend the timescales of these simulations.

In this part, we will introduce and describe the molecular modeling techniques used in this thesis. Since the basis of the computational methods used are common for all the cases of interest, in this section we will present the common procedure, while the single exceptions will be described in the appropriate section of the results and discussion part. The presented procedures have been used for the publications related to this thesis.[90–96]

4

Molecular simulation in life sciences

The solution of the Schrödinger equation[97] should be carried out for a rigorous treatment of interatomic interactions, using quantum calculation methods. Unfortunately, nowadays it's impossible to apply these techniques to biological important systems like proteins or nucleic acids (NAs). Remembering the Born-Oppenheimer approximation[98] we can sacrifice the explicit description of electrons; every atom can be treated as a classical particle. The description of the system in this way is dependent only on nucleuses position and velocity, following Newton's second law in the form

$$-\frac{dE_{pot}(R)}{dR} = m\frac{d^2R}{dt^2}$$

. At the atomistic scale the atoms of a molecule are represented as a balls, centered on their nucleus, with a precise mass and charge. Every bonds is represented as a string with a certain force constant and resting length.

To precisely describe a system at the atomistic level, we need to be able to approximate its potential energy. The definition of *force field* by Otto Ermer is:

> *“the analytical expression that describes the potential energy of the studied molecular complex and all the parameters needed to describe it”*

so, as we’ll see in more detail in the next chapter, the term *force field* refers to both an interatomic potential functional form and its relative parameters. Once a system is correctly described with a *force field* the reaching of the equilibrium is described by

$$\frac{dE_{pot}}{dr_i} = 0$$

where the potential energy is function of the coordinates r_i of the atoms of the system. A simply MM is useful to reduce bad energetic configurations that typically occur in the early steps of the simulation, but is only a preliminary step for complex systems, since it does not take care of the temperature, and kinetic energy

$$E_{kin} = \frac{3}{2}k_b T$$

for which we have to consider the time evolution of the system.

4.1 Molecular dynamics

MD is simply an iteration in time of MM—at each time step of the simulation the system moves toward the equilibrium. The concept at the basis of this technique is rather simple: given a starting configuration for the molecular system of interest, corresponding to the position and connections of atoms, the forces that are acting on each atom are calculated, and thus trajectories can be computed as the evolution at each time step of the system toward the equilibrium. Differently form the MM, in MD an initial set of random velocities need to be calculated from the starting temperature: new positions and velocities for all the atom of the system are then calculated at each dynamic step. Obviously, the system fluctuates toward the equilibrium maintaining the total energy (E_{tot}) constant. If the new velocities are too low or too high to maintain the constancy, at each step they need to be rescaled in order to be consistent with the temperature of the system and with the E_{tot}. For this purpose thermostats and velocity scaling algorithms had been developed.

During a MD simulation we have to solve at each dynamic time step (across time) an equation like

$$F_i(t) = m_i a_i(t)$$

. It is thus necessary to calculate the force $F(t)$, dependent on the position of each atom in space, from the potential $V(R)$ defined by the *force field*. This will be done for all the atoms that constitute the system.

$$F_i = -\nabla V_i(R_1, \ldots, R_n)$$

Once the force is calculated—and thus the acceleration is known—by integration it is possible to calculate the new coordinates for all the atoms of the system with the so-called *Verlet algorithm*, represented by the equations

$$R_i(t + \Delta t) = R_i(t) + v_i(t)\Delta t + \frac{1}{2} a_i(t) d\Delta t^2$$

$$R_i(t - \Delta t) = R_i(t) - v_i(t)\Delta t + \frac{1}{2} a_i(t) d\Delta t^2$$

, that summed together give

$$R_i(t + \Delta t) = 2R_i(t) - R_i(t - \Delta t) + a_i(t) d\Delta t^2$$

. With this algorithm it is possible to compute the new positions of each atom of the system and thus to calculate the new potential energy ($E_{pot,i}$), as sum of the potential energetic contribution given by each atom, and the new velocities of all the atoms

$$v_i'(t) = \frac{R_i(t + \Delta t) - R_i(t - \Delta t)}{2\Delta t}$$

. From the velocities it's possible to calculate the new values of the kinetic energy as

$$E_{kin,i} = \frac{1}{2} m_i [v_i'(t)]^2$$

and the constancy of the total energy ($E_{tot,i}$) is checked.

$$E_{tot,i} = E_{pot,i} + E_{kin,i}$$

All this procedure is iteratively repeated at each time step for the whole length of MD simulation.

5

FORCE FIELD & SOFTWARE

As we highlighted in previous chapter, the choice and usage of the proper *force filed* is of primary importance for the reliability of the modeling. For instance, a *force field* that is dedicated to general material science could give completely wrong results for proteins simulations, or in most cases could be unable even to start the calculation. Transferability is an indispensable property to choose a *force field*, indeed it allows to use a set of parameters tested on a small number of cases and apply it in very different situations.

The studies presented in this work were all carried out exploiting AMBER (version 12 and 14)[99], that is both a set of molecular mechanics *force fields* for molecular dynamics of biomolecules—originally developed by the Peter Kollman's group at the University of California (San Francisco)—and a simulation package that implements these *force fields.* The form of the AMBER force field is

$$\begin{aligned} V(R^N) &= \sum_{bonds} \frac{1}{2} k_b (l - l_0)^2 + \sum_{angles} k_a (\theta - \theta_0)^2 + \sum_{torsions} \frac{1}{2} V_n [1 + cos(n\omega - \gamma)] + \\ & + \sum_{j=1}^{N-1} \sum_{i=j+1}^{N} \{\varepsilon_{i,j} [(\frac{\sigma_{ij}}{R_{ij}})^{12} - 2(\frac{\sigma_{ij}}{R_{ij}})^6] + \frac{q_i q_j}{4\pi\varepsilon_0 R_{ij}}\} \end{aligned} \tag{5.1}$$

where:

- the first term represents the harmonic force (ideal spring) linked to the energy between covalently bonded atoms. This is a good approximation near the equilibrium bond length, but becomes increasingly poor as atoms separate. K_b is a constant, and it's determined by the kind of atoms involved;
- the second term is associated to the variations in the angle term respect to the ideal value. It represents the energy due to the geometry of electron orbitals involved in covalent bonding. K_a is a constant, and it's determined by the kind of atoms involved;
- the third term is the potential function associated with the torsional angles. It represents the energy for twisting a bond, and depends on bond order (e.g., double bonds) and neighboring bonds or lone pairs of electrons;
- the last term involves the non-bonded energy between all atom pairs as decomposed by van der Waals (vdW) (first term) and electrostatic (second term of summation) energies.

All the constant (K_b , K_a, etc...) are unknown, a priori. In order to use the *force field*, it is necessary to have values for all the parameters (e.g., force constants, equilibrium bond lengths and angles, charges...). The AMBER software contains a fairly large number of these parameter sets. Each parameter set has a name, and provides parameters dedicated to certain types of molecules:

- "*ff*" followed by the year of creation (i.e. 95): peptide, protein and nucleic acid parameters;
- GAFF (Generalized AMBER *force field*)[100]: parameters for small organic molecules to facilitate simulations of drugs and small molecule ligands in complex with biomolecules (e.g., proteins);
- GLYCAM: parameters for simulating carbohydrates;
- LIPID: parameters for simulating lipid molecules (e.g., phospholipids, cholesterol...).

In all the calculations presented in this thesis, the *ff12* was used for proteins and NAs (and the updated *ff14*), being the most widely used in this studies. The lipid11[101] and lipid14SB[102] *force field* where used to parametrize lipid molecules, while GAFF was used for all unconventional organic molecules, as dendrimers and drugs.

5.1 THE AMBER PACKAGE

As said, AMBER refers also to the simulation package that implements these *force fields.* This is a list of the modules exploited in this work:

- **antechamber**[103] recognizes atom type and bond type, and also assigns partial charges to unconventional molecules using the GAFF *force field*;
- **parmchk** calculates the missing parameters for small organic molecules parametrized with GAFF;
- **leap** prepares files necessary to start the simulation, including adding ions and solvent and the parametrization of the system. It's also able to create initial structures of simple NA fragments;
- **parmed** is a program used to edit parameter-files;
- **sander** (Simulated Annealing with NMR-Derived Energy Restraints) is the central simulation program and provides facilities for energy minimization and molecular dynamics with a wide variety of options;
  - **pmemd** (Particle mesh Ewald molecular dynamics) is a newer version of sander by Bob Duke. It is optimized to improve the performance of the simulations in parallel;
  - **pmemd.cuda**[104, 105] is a recent porting of many **pmemd** functionalities on GPU architecture, considerably speeding up the calculations;
- **nmode** (Normal Mode analysis) calculates the entropy of the system;
- **MMPBSA.py**[106] performs free energy of binding calculations on snapshots from MD trajectories;
- **cpptraj**[107] is an analysis program for simulation results.

In all the studies described in this thesis, missing GAFF parameters for drugs molecules were calculated with semiempirical Austin model (AM1) calculation method with the *antechamber* module, corrected with an *ab initio* term for bonds (BCC bond term)[108–110]. This calculation method can guarantee results with precision comparable to the one of pure quantum-mechanic calculations allowing a consistent reduction in the computational time. For dendrimers, partial charges were derived using a more precise RESP methodology, using the R.E.D. server capabilities.[111–113]

The most used visualization tools were UCSF Chimera[114] and VMD (visual molecular dynamics)[115] programs. With these tools is possible to analyze trajectories, sequence alignments, docking results, conformational changes; also, both programs are able to export high quality images and movies.

6

Pharmacophore models

Pharmacophore mapping was one of the major elements of drug design in the past, and also today is really helpful, especially in the absence of structural data of the target receptor. A pharmacophore may be defined as the ensemble of steric and electronic features that is necessary to ensure the optimal supramolecular interactions with a specific biological target structure, and to trigger its biological response. The tool was initially applied to the discovery of lead molecules, and now is extended to lead optimization. Pharmacophores can be used for retrieving potential leads from structural databases (lead discovery), or for designing molecules with specific desired attributes (lead optimization), but also for assessing similarity and diversity of molecules using pharmacophore fingerprints.

The model structures of all compounds were built using the 2D-3D sketcher of Discovery Studio Catalyst (DS v. 2.5, Accelrys, San Diego, CA, USA); we employed an *ad hoc* procedure to derive molecular conformations, instead of using those automatically generated by DS Catalyst, for a better quality in covering the low-energy conformational space. Each molecular structure was subjected to energy minimization using the generalized CHARMM *force field* until the gradient dropped below 0.05. The minimized structures are used as the starting point for subsequent conformational searches. A 10000 step Monte Carlo torsional sampling conformational search was conducted for each compound. Unique low energy conformations within 20 kcal mol^{-1} of the corresponding global energy minimum were collected for each molecule. A conformation is considered unique only when the maximum displacement of at least one heavy atom is greater than 0.5 Å, and a maximum of 250 unique conformations were recovered for each compound. The classical conformational search was also carried out using the Poling algorithm and the CHARMM *force field* as implemented in DS Catalyst program for comparison. The "best quality" generation option was adopted to select representative conformers over a 0–20 kcal mol^{-1} interval above the computed global energy minimum in the conformational space, and again the number of conformers generated for each compound was limited to a maximum of 250.

Based on the conformations for each compound, the DS Catalyst Hypothesis module was used to generate three-dimensional pharmacophore models. During hypotheses generation, the software attempts to minimize a cost function containing two main terms: the first penalizes the deviation between the estimated affinities of the training set molecules and their experimental values, whilst the second penalizes the complexity of the hypothesis. The uncertainty factor for each compound represents the ratio range of uncertainty in the affinity value based on the expected statistical irregularity of biological data collection. Uncertainty influences the first step—also called the constructive phase—of the hypothesis generating process. An uncertainty value of 3.0 is the default factor, but sometimes if the experimental affinities of compounds barely span the required four orders of magnitude an uncertainty of 1.1 was preferred.

The overall costs of a model consist of three cost components, namely, the *weight cost*, the *error cost* and the *configuration cost*. The *weight cost* component is a value that increases in a Gaussian form as this function weights in a model deviate from the ideal value of 2. The *error cost* represents the difference between estimated and measured activities of the training set. The *configuration cost* quantifies the entropy of the hypothesis space.

In addition the following three cost values are calculated during the generation of pharmacophore models: the *fixed cost*, the *total cost* and the *null cost*. The *fixed cost* is the lowest possible cost representing an hypothetical simplest model that fits all data perfectly. The *null cost* represents the maximum cost of a pharmacophore with no features and estimates activity to be the average of activity data of training set molecules. The *null cost* value is equal to the maximum occurring error cost. For every pharmacophore generation 10 total cost values and each of *fixed cost* and *null cost* values are calculated by the pharmacophore generation protocol in the unit of bits. For a meaningful pharmacophore model, the *fixed cost* should be lower and the *null cost* should be higher and the *total cost* value should be closer to the *fixed cost* and away from the *null cost* value.

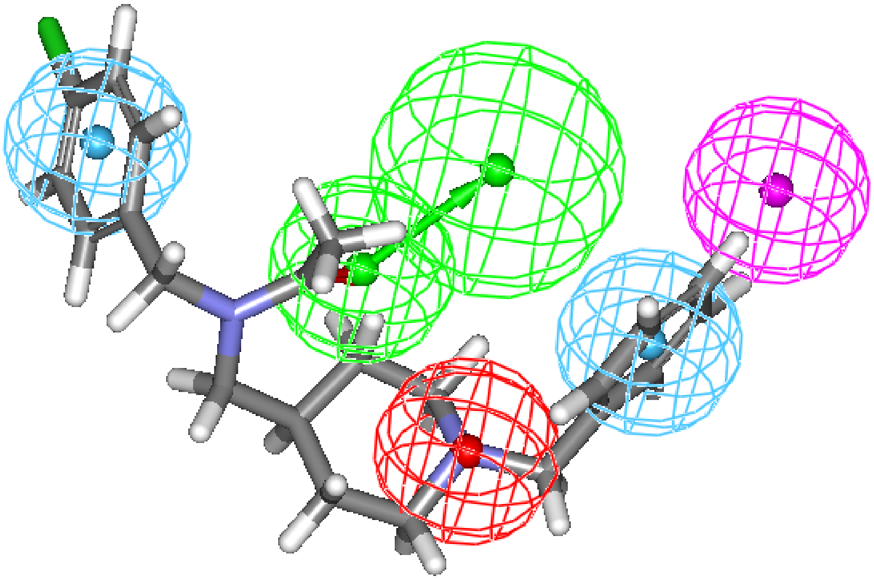

Figure 6.1: Example of a 3D pharmacophore hypothesis: the features are portrayed as meshed spheres, color-coded as follows: red, positive ionizable (PI); light blue, hydrophobic aromatic (HYAr); pink, hydrophobic (HY); light green, hydrogen bond acceptor (HBA).

6.1 Validation procedures

Three validation procedures are, usually, used to determine the statistical relevance and the validity of the proposed 3D pharmacophore models: the test set prediction method, the CatScramble method, and the leave-one-out procedure. A larger difference between the *fixed costs* and *null costs* than that between the *fixed costs* and *total costs* signifies the quality of a pharmacophore model. In this work, the first procedure consisted of the collection of further, different compounds into a test set, and in performing a regression analysis by mapping the test set molecules onto the best pharmacophore hypothesis. The high correlation coefficients obtained using the test set compounds revealed the good correlation between the actual and estimated affinities and, hence, the predictive validity of the corresponding 3D hypothesis. The CatScramble validation procedure is based on Fisher's randomization test. The goal of this type of validation is to check whether there is a strong correlation between the chemical structures and the biological activity. This is done by randomizing the affinity data associated with the training set compounds, generating pharmacophore hypotheses using the same features and parameters employed to develop the original pharmacophore model.

The statistical significance is calculated according to the following formula:

$$significance = 100 \times [1 - (1 + x/y)]$$

where x is the total number of hypotheses having a total cost lower than the original (best) hypothesis, and y is the total number of DS Catalyst Hypothesis runs (initial plus random runs). Thus, 49 random spreadsheets (i.e., 49 DS Catalyst Hypothesis) have to be generated to obtain a 98 % confidence level. Should any randomized data set result in the generation of a 3D pharmacophore with similar or even better cost values, root-mean-square deviations, and correlation coefficients, then it is likely that the original hypothesis does reflect a chance correlation.

Finally, the leave-one-out test checks if the correlation between experimental and computed affinities is heavily dependent on one particular molecule of the training set by recomputing the pharmacophore model with the exclusion of one molecule at a time. For each run, the hypothesis characterized by the lowest total cost was employed to predict the affinity of the excluded compound and to estimate the new correlation coefficient.

7

CREATION OF THE SYSTEMS

The procedure described in this section will be maintained as general as possible, since most of the steps that will follow are common for all the cases studied. Variations from this template will be eventually highlighted when needed.

It is worth noting that, since we want to simulate every system as close as possible to the real conditions, it is fundamental to mimic these conditions. In these studies, the main characters are molecules that are naturally inserted in physiological condition of the human body, so to obtain an accurate simulation we will recreate the correct salt concentration corresponding to the human ionic strength (NaCl 0.15 M) in a water environment (using TIP3P[116] water molecules).

As default starting files, AMBER is able to read a series of different formats (.pdb, .xyz, etc.). Typically, for protein and NA structures, the format that is most widely used is the .pdb file. The extension .pdb stats for, and is downloadable from, the Protein Data Bank (www.rcsb.org/pdb/home/home.do)—a free on line data base containing the *pdb* files for the most studied protein and organic structures. The file *pdb* is a simple coordinate file, often obtained by X-ray techniques—it contains only the atom numbers and names (Figure 7.1, columns 2 and 3), the name and number of the residues to whom these atoms belong (columns

```
ATOM      1  N   SER     1       0.839 -17.879  51.844  1.00  0.00
ATOM      2  HT1 SER     1       1.155 -17.060  52.402  1.00  0.00
ATOM      3  HT2 SER     1       1.622 -18.556  51.748  1.00  0.00
ATOM      4  HT3 SER     1       0.040 -18.339  52.325  1.00  0.00
ATOM      5  CA  SER     1       0.398 -17.412  50.459  1.00  0.00
ATOM      6  HA  SER     1       1.175 -16.786  50.045  1.00  0.00
ATOM      7  CB  SER     1       0.172 -18.628  49.604  1.00  0.00
ATOM      8  HB1 SER     1      -0.225 -18.330  48.610  1.00  0.00
ATOM      9  HB2 SER     1      -0.547 -19.316  50.098  1.00  0.00
ATOM     10  OG  SER     1       1.407 -19.287  49.434  1.00  0.00
ATOM     11  HG1 SER     1       1.260 -19.957  48.763  1.00  0.00
ATOM     12  C   SER     1      -0.942 -16.513  50.483  1.00  0.00
ATOM     13  O   SER     1      -1.751 -16.674  51.382  1.00  0.00
ATOM     14  N   GLY     2      -1.056 -15.639  49.479  1.00  0.00
ATOM     15  HN  GLY     2      -0.333 -15.640  48.801  1.00  0.00
ATOM     16  CA  GLY     2      -2.052 -14.652  49.161  1.00  0.00
ATOM     17  HA1 GLY     2      -1.801 -13.758  49.712  1.00  0.00
ATOM     18  HA2 GLY     2      -3.003 -15.041  49.494  1.00  0.00
ATOM     19  C   GLY     2      -2.178 -14.280  47.661  1.00  0.00
ATOM     20  O   GLY     2      -1.596 -15.036  46.877  1.00  0.00
ATOM     21  N   GLN     3      -2.980 -13.213  47.281  1.00  0.00
ATOM     22  HN  GLN     3      -3.378 -12.599  47.958  1.00  0.00
ATOM     23  CA  GLN     3      -3.309 -12.897  45.874  1.00  0.00
```

Figure 7.1: Extract from a *pdb* file.

4 and 5) and the coordinates of each atom within the structure (Figure 7.1, columns 6, 7 and 8).

7.1 System parametrization

To run a simulation both *sander* and *pmemd* need three starting files:

- a *mdin* file, that is a file containing all the instructions to run the calculations;
- a parameter file (usually called *.prmtop*), that is the parametrization file for the system. It contains all the values of the constants to put into Equation 5.1 on page 35, taken from the *force field* that was chosen for calculations;
- a coordinates file (usually called. *inpcrd*), that contains the coordinates of all the atoms of the system.

The parameter and coordinate files are separated, because the same parameter files will be used also in all the other programs in association with every MD trajectory file of the same system. The *leap* module of AMBER is able to create this files starting from simple coordinates files like *pdb*, for standard biological molecules like proteins and NAs. Also, it can create simple starting structures for NA fragments, needing only the sequence of nucleotides. Unconventional molecules, like drugs and dendrimers, are not automatically recognized by *leap*, so some preliminary steps are needed.

For small and simple molecules, like drugs, we used the *antechamber* module, that is able to assign GAFF atom types to simple molecules starting from their coordinates files. Partial charges were assigned with the semiempirical AM1-BCC method, and missing parameters were added successfully with the *parmchk* module. Once typed with GAFF atom types, *leap* is able to recognize the molecule.

7.2 Dendrimers parametrization

For dendrimers, that are quite big molecules, we used a quite different approach, conceptually similar to what is used for protein and aminoacids. Firstly every dendrimer was divided in smaller units: a central unit, a repeated branching unit and a terminal unit. Every unit was parametrized alone (with small fragments of adjacent units, to recreate it's molecular environment), creating a library file that was given to *leap* to parametrize the whole molecule.

To parametrize each units we employed a procedure similar to what was used for drugs, but we choose a more accurate RESP procedure for the partial charges assignment. Eventually missing *force field* terms (for Si atom) were derived from quantum mechanical calculations using the GAMESS software[117, 118] and the *paramfit* module of AMBER. For QM calculations, the MP2/HF/6-31G level of theory was used. vdW parameters for Si were taken from the MM3 force field.[119]

7.3 System finalization

All the simulations were performed in explicit solvent and under periodic boundary conditions (PBC)—the replication in the three dimension of the same box (Figure 7.2). This, from the calculation point of view, is carried out with the condition that all the atoms and molecules that get off the original box from one side, come in again from the opposite. In this way it is guaranteed that the content of the periodic box is always the same. With this model we avoid any boundary effect, during the simulation only one of the particles is represented but the effects are reproduced over all the image particles. Each particle not only interacts with the other particles but also with their images in neighboring boxes. Upon initial inspection such a method would appear to be very computationally intensive requiring the evaluation of an infinite number of interacting pairs. However, by employing a technique known as the Ewald

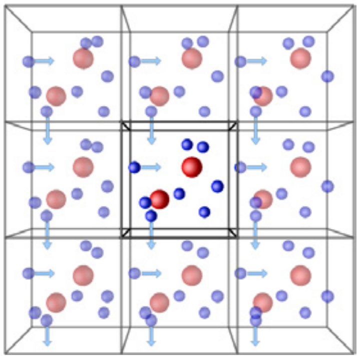

Figure 7.2: Representation of PBC. The central box is replicated in the three dimensions.

sum, or its more modern equivalent the Particle Mesh Ewald (PME)[120] method it is possible to obtain the infinite electrostatics. This involves dividing the calculation up between a real space component and a reciprocal space component. The PBC interactions still need to be computed though, which means we have to use a cut-off. For production calculations the ideal range is between 8 and 10 Å.

Leap can parametrize *pdb* files already containing water and ions, as the case of *pdb* files for lipid membranes built with the CHARMM-GUI interface[121–123], or can create a solvated box starting from a “dry” solute.

7.3.1 Box geometry

Basically, there are two geometries for the water box that are used for PBC in AMBER: the tetrahedric and octahedric. The geometry of the water box is chosen dependently on the geometry of the solute, in order to reduce as much as possible the presence of water molecules in the system. In fact, if the solute presents a spherical symmetry, to choose an octahedric water box allows a consistent saving of “useless” atoms in the system. On the other hand, if the solute is strongly un-spherical and present a geometry that is not isotropic (e.g., deoxyribonucleic acid (DNA) strands), the tetrahedric geometry is more indicated and guarantees more flexibility.

Leap is able to create a box of water molecules of a given dimension and shape, with the solute on its center. One important rule in MD is that solute molecules shouldn’t directly interact with their self images: box dimensions so are dependent on the cut-off used for vdW interactions and on the mobility of the solute. In all the works done we choose a box with a radius at least of 10–15 Å from the solute.

7.3.2 Water model

The most abundant molecule in an explicit solvent simulation is water. There are many different models of water that can be used, some more precise in recreating dipole effects—adding more than three interaction sites—and other that sacrifice a little of precision—fixing some parameter—speeding up calculations. In all our simulations we used the TIP3P water model. This model uses a total of three sites for the electrostatic interactions; the partial positive charges on the hydrogen atoms are exactly balanced by an appropriate negative charge located on the oxygen atom. The vdW interaction between two water molecules is computed using a Lennard-Jones (LJ) function, and no vdW interactions involving the hydrogen atoms are calculated. The angle between the two hydrogen atoms is constant, so this water model has a rigid geometry; this simplification decreases notably the CPU time required to simulate the systems.

This water model needs the use of the SHAKE[124] algorithm to constrain all the bonds involving hydrogen atoms on subsequent MD simulations. This is a further approximation that allow to speed up the calculations. Since the time step of MD should be faster than the highest frequency motion in the system, a standard MD simulation can't use a time step higher than 1 fs. Constraining the highest frequency motion given by the hydrogen atoms, we are able to enlarge the time step to 2 fs, and so sample more conformational space in the same simulation time.

7.3.3 Ions

Once we "immersed" the complex into the water, it is necessary to add the counterions in the system. In fact, ions can affect consistently the ability to move of the solute, influencing the final dynamic trajectories. The correct amount of ions to add to the system depends on the charges present in the solute and on the volume of the water box, in order to reproduce the physiological 0.15 M [NaCl] condition. The Na^+ and Cl^- ions can be added by *leap*, and are inserted in the system following the electrostatic potential surface of the solute. If during the addition of counterions positional conflict (superposition) with water molecules constituting the box are verified, the entire water molecule is substitute with the ion that is placed in the water molecule centre of mass. Since the number of water molecules in the box is rather high, usually almost all the counterions substitute a water molecule. This create a non-uniformity in the box, since one single atom (Na^+ or Cl^-) is replacing three atoms. That is one of the motivations why, for instance, during the first period of constant pressure and temperature (NPT) dynamic (which allows the volume of the water box to change) the box reduces its dimensions in order to adjust the density.

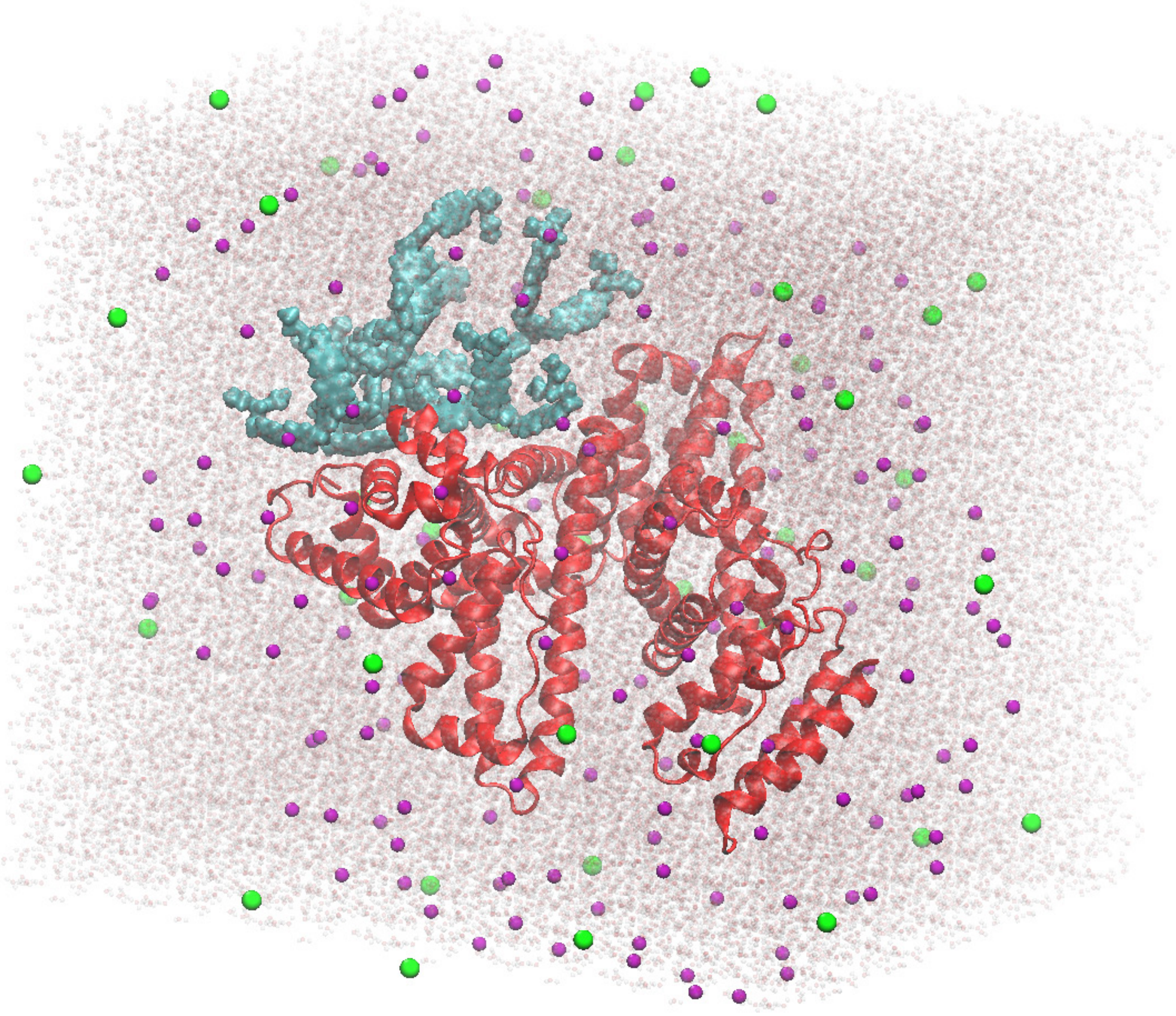

Figure 7.3: Example of a box prepared with *leap*. Water is represented as transparent balls, while Na^+ and Cl^- ions are portrayed in purple and green, respectively. In cyan is represented a viologen dendrimer SASA, while human serum albumin is portrayed in red ribbon.

7.4 CREATION OF MUTATED COMPLEXES

During the carcinogenesis process, it is very frequent to find mutations in important proteins. That could lead to drug resistance, if the protein was a drug-target, but could also be a new objective for the therapy. Changes in the DNA sequence can occur at the level of the chromosome, in which large segments of chromosomes are altered (deleted, duplicated, inverted, translocated to different chromosomes, or otherwise rearranged). This results in changes such as modification of gene dosage, the complete absence of genes, or the alteration of gene sequence. The type of variation that occurs when entire areas of chromosomes are duplicated or lost, called copy number variation (CNV), has especially important implications for human disease and evolution.

While a mutation is defined as any alteration in the DNA sequence, biologists use the term single nucleotide polymorphism (SNP) to refer to a single base pair alteration that is common in the population. Specifically, a polymorphism is any genetic location at which at least two different sequences are found, with each sequence present in at least 1 % of the population. Note that the term "polymorphism" is generally used to refer to a normal variation, one that does not directly cause disease. Moreover, the cutoff of at least 1 % prevalence for a variation to be classified as a polymorphism is somewhat arbitrary; if the frequency is lower than this, the allele is typically regarded as a mutation.

SNPs are important as markers, for scientists to use in an attempt to find genetic changes that predispose individuals to certain traits, including disease. On average, SNPs are found every 1000–2000 nucleotides in the human genome, and scientists participating in the International HapMap Consortium have mapped millions of these alterations (International Human Genome Sequencing Consortium, 2001).

- Point mutations:
  - substitution: one base is incorrectly added during replication and replaces the pair in the corresponding position on the complementary strand;
  - insertion: one or more extra nucleotides are inserted into replicating DNA, often resulting in a frameshift;
  - deletion: one or more nucleotides is "skipped" during replication or otherwise excised, often resulting in a frameshift.
- Chromosomal mutation:
  - inversion: one region of a chromosome is flipped and reinserted;

- deletion: a region of a chromosome is lost, resulting in the absence of all the genes in that area;
- duplication: a region of a chromosome is repeated, resulting in an increase in dosage from the genes in that region;
- translocation: a region from one chromosome is aberrantly attached to another chromosome.

So, it is important to be able to build the "mutated" complex in order to compare the results obtained between wild type (*wt*) and mutates complex. Particularly is important to analyze the effects in the protein/protein or protein/drug interaction occurred following the mutation. We will briefly describe how we introduced point mutations or amino acid deletions inside the protein chain.

All the computational mutagenesis procedure has been carried out exploiting the *Rotamers* module of UCSF Chimera[114]. Each mutated complex was then subjected to the same procedure as the *wt* protein, and a particularly long time was spent on the equilibration phase.

For the aminoacids that have several possible rotamers (for instance aspartic and glutamic acids), each rotamer structure is generated and minimize separately. We proceed with a systematic conformational search for 100 different conformations for the mutated residue. For each conformation obtained, a check of the steric bump is planned to avoid sterical clash between all the residue in the protein and the mutant. In particular, the conformation of the mutated residue is not taken in account if the new residue is closer than 1 Å to any aminoacid in the protein.

Looking at the final structure, while a point mutation provokes only adjustments in the secondary structure of the protein, a consistent deletion can provoke drastic distortions and final configurations that are considerably distant from the *wt* protein. Thus, it is perfectly clear that the huger the deletion, the more consistent the simplification and the risk that the final mutated protein conformation in the model could be completely different from the real one.

8

SIMULATION PROCEDURE

Pmemd is the module of AMBER that best scale up in parallel calculations, and nowadays has almost all the capabilities of the older *sander* module. For all the simulations performed we used *pmemd* and particularly, for calculations that are ported to the GPU version of the software, we used the GPU implementation *pmemd.cuda* every time it was possible. A standard procedure it's described in the following sections. It is worth noting that besides all kind of parameters that have to be monitored, a human eye on the trajectory obtained and on the minimized structure is mandatory to quickly catch many problems and anomalies that can arise during molecular simulations.

8.1 MINIMIZATION

It is always a good idea to minimize the structure before starting molecular dynamics, since the default geometry that was obtained building our system could result in conflict and small overlap with atom in different residues. A preliminary minimization is always performed, to eliminate bad contact and to relax the system to the *force field* used.

We performed 500 steps of Steepest Descent, followed by 500 steps of Conjugated Gradient minimization with 5.0 kcal mol^{-1} Å^{-2} restraint on the solute (solvent relaxation). Another round of 1000 steps of Conjugated Gradient minimization without restraints was done in order to eliminate all bad contacts.

8.2 HEATING AND DENSITY RELAXATION

From the minimized structures we started the proper MD simulations. For this first phases the time step used was 1.0 fs in order to avoid too large deviations due to the rising of temperature and to the high fluctuations of the molecules belonging to the solvent. The resulting structures were consequentially heated to the target temperature (usually 300 K). In this process was applied a restraint of 5.0 kcal mol^{-1} Å^{-2} on the solute. The heating phase took 50 ps and was performed in the canonical ensemble (constant volume and temperature (NVT)). Langevin thermostat[125] was used for temperature regulation (collision frequency = 2.0 ps^{-1}). In the next 50 ps we maintained the restraint on the solute and switched to the isothermal-isobaric ensemble (NPT), to equilibrate the density of the water box. Pressure control was exerted by coupling the system to a Berendsen barostat[126] (with a pressure relaxation time 1.0 ps).

8.3 EQUILIBRATION

All the restraint were then removed (gradually in subsequent steps if needed) and the systems were equilibrated in the NPT ensemble with a time step of 2.0 fs. This phase can take from few to tens of nanoseconds, depending on the conformation of the solute. Some values could be checked to verify the status of the equilibrium of the system. The quantities that usually are checked to monitor the status of the system are temperature (T), pressure (P), volume (V), potential energy (E_{pot}) and the root-mean-square deviation (RMSD) of structural atoms (for an explanation see Figure 8.1).

The first parameters monitor the energetic equilibrium, while we can say that the RMSD represent the vibrational one. Usually our systems attained the energetic equilibrium in correspondence of the reaching of the target temperature, in the first tens of picoseconds, while there are strong vibrations to maintain the constancy of the energy. The vibrational equilibrium takes much longer, from two to tens of nanoseconds for a drug-protein complex that is quite stable. In the case of NA and dendrimer complexes we performed at least 50 ns of equilibration, being these molecules fairly flexible. After the RMSD plot had reached a plateaux, as seen in Figure 8.1, we started the so called production phase, from which the data collection can be considered as reliable.

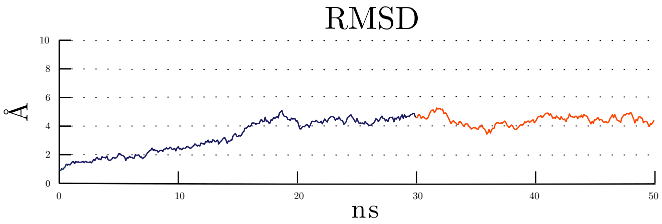

Figure 8.1: RMSD plot example. In blue is plotted the RMSD during the equilibration phase, while in red for the production phase.

8.3.1 Equilibrium for lipid membrane systems

Lipid membrane systems have a particular parameter that is very important to monitor their equilibrium: the area per lipid (APL). This is the average area that a single phospholipid occupies in an interface and is usually reported in Angstroms. Since this systems are built assembling together hundreds of equilibrated lipid molecules, in the first 50–100 ns they have to equilibrate their position in the membrane. As can be seen in Figure 8.2 the value of APL decrease highly in the first 50 ns of simulation, and can take up to 100 ns to reach an equilibrium.

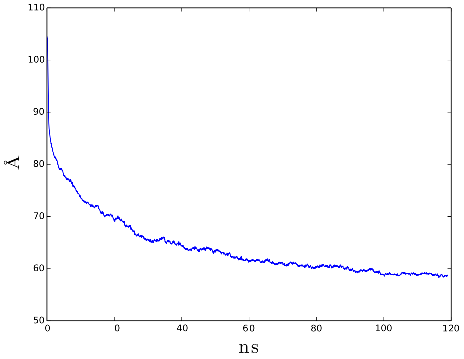

Figure 8.2: APL plot example.

8.4 Production

The production phase is where data for further analysis is collected. If high fluctuations in the density are not expected, it is possible to switch to the NVT ensemble to speed up the calculations. In this case the first 2 ns of simulations were discarded, to account for possible minimal perturbations due to the change of ensemble. Also this phase hadn't a fixed duration; we continued the simulation until we reached the convergence of the property on which we were interested. Usually that translates in 10–100 ns of simulation.

9

Binding energy analysis

The Molecular Mechanics/Poisson Boltzmann Surface Area (MM/PBSA) and the Molecular Mechanics/Generalized Born Surface Area (MM/GBSA) approaches can be used to estimate the binding free energies of a complex from snapshots obtained from an equilibrated MD trajectory (usually 200 snapshots were used). Both methods are scripted in the *MMPBSA.py* module of AMBER, and allow to calculate the affinity energy for the association of two molecules, represented in Figure 9.1 (e.g., dendrimer/NA and drug/protein) or to compare the free energy of two different solvated conformations of the same molecule.

By calculating the absolute free energy directly between the two “end points” instead of calculating the relative free energy along a mapping coordinate, we are avoiding computations on less interesting intermediate states. Nonetheless, it is clear that applications of this methodology will have intrinsically much larger errors than free energy perturbation/thermodynamic integration calculations. However, despite the larger uncertainties, we can most of the times, calculate ΔG_{bind} in respectable agreement with experiment. Especially, relative free energies of macromolecules and ligand-receptor interactions, $\Delta\Delta G$, are in very good agreement with experiment and can be computed relatively quickly.

In the simulation of these solvated states, the majority of the energy contributions would

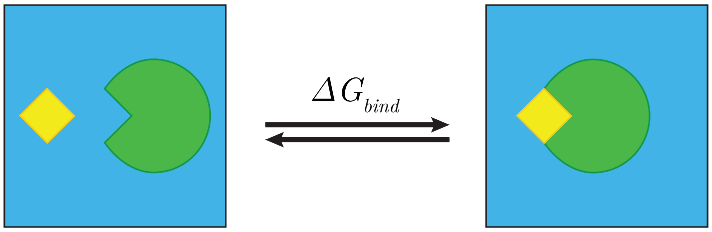

Figure 9.1: The two states, “bound” and “unbound”, of ligand (yellow) and receptor (green) in solution (blue).

come from solvent-solvent interactions and the fluctuations in total energy would be an order of magnitude larger than binding energy of the two molecules of interest. Thus the calculation would take an enormous amount of CPU time to converge. So explicit solvent and ions are stripped from the trajectory file to hasten convergence by preventing solvent-solvent interactions from dominating the energy terms.

9.1 THE MM/PB(GB)SA THERMODYNAMIC CYCLE

In order to simplify, the MM/PBSA methodology[127] is based on the thermodynamic cycle reported in Figure 9.2.

From the scheme in Figure 9.2, we derive

$$\Delta G_{bind,solv} = \Delta G_{bind,vacuum} + \Delta G_{solv,comp} - (\Delta G_{solv,lig} + \Delta G_{solv,rec}) \tag{9.1}$$

that could be simplified in the addition of a corrective factor to the free energy of binding computed in vacuum

$$\Delta G_{bind,solv} = \Delta G_{bind,vacuum} + \Delta G_{solv} \tag{9.2}$$

and ΔG_{solv} is computed as

$$\Delta G_{solv} = \Delta G_{POLAR} + \Delta G_{NP} \tag{9.3}$$

. The electrostatic contribution ΔG_{POLAR} is calculated with a numerical solver for the Poisson-Boltzmann method as implemented in the *pbsa* program in AMBER (ΔG_{PB}, MM/PBSA) or with generalized Born methods implemented in *sander* (ΔG_{GB}, MM/GBSA). The hydrophobic contribution, ΔG_{NP}, instead is determined using the relationship

$$\Delta G_{NP} = \gamma(SASA) + \beta \tag{9.4}$$

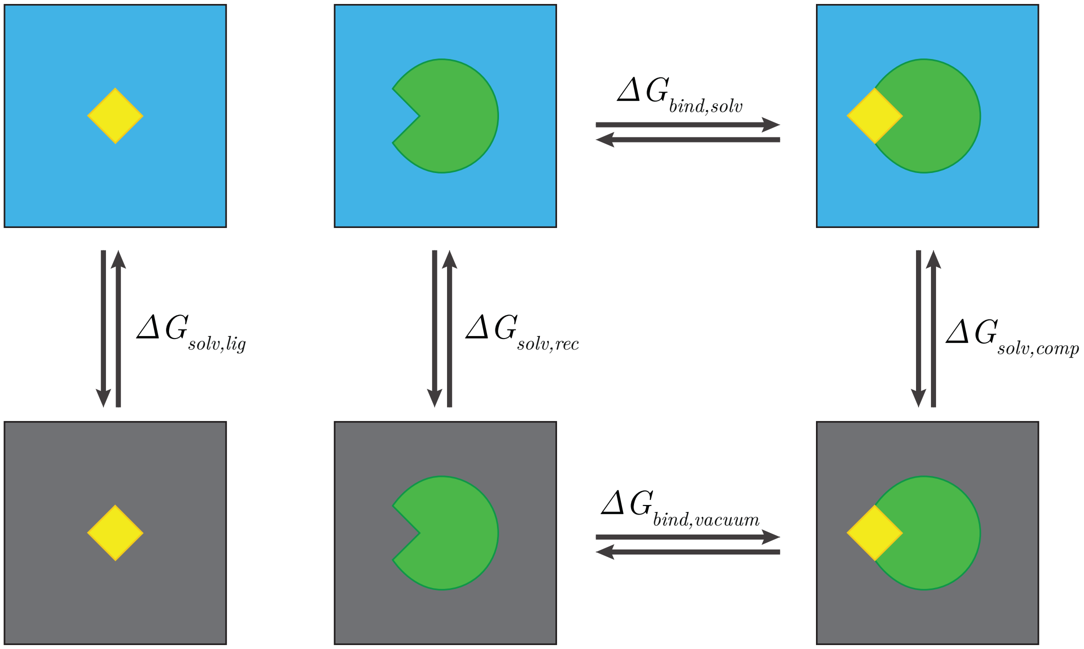

Figure 9.2: Thermodynamic cycle used to exploit $\Delta G_{bind,vacuum}$, vacuum to solve $\Delta G_{bind,solv}$.

where the surface tension parameter $\gamma = 0.005\,42\,\mathrm{kcal\,mol^{-1}\,\mathring{A}^{-2}}$, $\beta = 0.92\,\mathrm{kcal\,mol^{-1}}$, and solvent accessible surface area (SASA) is obtained with the LCPO method[128] implemented within *sander* or the *molsurf* method as implemented in *cpptraj*.

The gas phase free energy contributions, E_{MM}, are calculated by *sander* or *mmpbsa_py_energy* in AMBER, according to the *force field* with which the topology files were created.

$$E_{MM} = E_{int} + E_{vdW} + E_{ele} \tag{9.5}$$

$$E_{int} = E_{bond} + E_{angle} + E_{tors} \tag{9.6}$$

$$\Delta E_{MM} = E_{MM,complex} - (E_{MM,receptor} + E_{MM,ligand}) \tag{9.7}$$

$$\Delta G_{bind,vacuum} = \Delta E_{MM} - T\Delta S \tag{9.8}$$

Entropy contributions to the total free energy were added as a further refinement, and were computed performing a normal mode analysis in the gas phase using the *nmode* program called by *MMBPSA.py*. The normal mode analysis calculations are computationally expensive, so were performed on a subset made of 15 of the snapshots used in the calculation of ΔG_{bind}.

The final result from *MMBPSA.py* is the value of ΔG_{bind} expressed as

$$\Delta G_{bind,solv} = \Delta E_{MM} + \Delta G_{solv} - T\Delta S_{bind} = \Delta H_{bind} - T\Delta S_{bind} \tag{9.9}$$

. The more negative the value of ΔH_{bind}—meaning the complex has a lower energy than the two molecules taken separately—the more stable is the complex, and thus its formation is favored.

9.2 Single(multi) trajectory technique

MM/PB(GB)SA typically employs the approximation that the configurational space explored by the systems is very similar between the bound and unbound states, so every snapshot for each species is usually extracted from the same trajectory file, avoiding the need of producing three different MD trajectories. This is the so called "single trajectory" technique, and is a fairly good approximation for standard rigid systems like drug-protein complexes. When flexible molecules were involved, as the case for dendrimers and NAs, we used the "multi trajectory" techniques; one separated MD trajectory was generated for each macromolecule involved. This choice was dictated by the necessity for effectively sampling the unbound state of the dendrimer and the NAs, that reasonably is quite different from their bond state.

9.3 A link with experimental datas

The effectiveness of a certain inhibitor drug is defined by the half maximal inhibitory concentration (IC_{50}) that is defined as the amount of drug to put into the solution in order to inhibit the activity of the specific biological target of the 50. The correspondence between IC_{50} and the free energy of binding is defined as

$$\Delta G_{bind} = -RTln(IC_{50}) \tag{9.10}$$

. Thus, it is possible to compare the ΔG_{bind} obtained from our MD simulations with experimental values. If the values coming from our simulations are consistent with experimental measurement, the procedures and the molecular models used for the cases faced in this thesis can be considered reliable.

9.4 Per residue decomposition analysis

While the MM/PBSA approach usually gives results in better agreement with the experiments, and thus was used for all the calculations of ΔG_{bind} in this thesis, the MM/GBSA have the capability to make a *per residue* binding free energy decomposition.

$$\Delta H = \sum_{i=1}^{i=N} \Delta H_i \tag{9.11}$$

where N is the total number of residues of the complex. This can be used to evaluate the role of each residue in the stabilization of a receptor-ligand complex.

9.4.1 Protein-ligand complexes

The more negative is the value of ΔH_i, the stronger is the favorable action of the i^{th} residue in stabilizing the complex. This could help to identify a particular residue important for the binding site, or to understand a “domino effect” that rearrange all the structure of the complex.

Also, is important to evaluate the $\Delta\Delta H_i$, the difference in ΔH_i between a mutated and a wild type protein. This value can help understand if a residue tends to stabilize more the binding in the native conformation of the protein than in the presence of a given mutation along the amino acid chain.

This energetic analysis can be rather useful because it is able to provide unique details in the binding between protein and inhibitor drugs. Such details are impossible to obtain with other experimental techniques, and evidence this approach and the modeling in general as an extremely powerful instrument for the exploration and the analysis of the potentiality of different small inhibitor molecules.

9.4.2 Dendrimer-target complexes

One of the consequences of subdividing each dendrimer in smaller residues is that we can apply the *per residue* energy decomposition to identify the branches of the dendrimer that are effectively contributing to the binding. This was done summing together the values of ΔH_i for residues that are in the same branch, yielding the effective free energy of binding $\Delta G_{bind,eff}$, the contribution to binding yielded by the dendrimer branches in constant and productive contact with the nucleic acid fragment. The number of branches effectively contributing to the binding (N_{eff}) was important to normalize the values of $\Delta G_{bind,eff}$ obtained with different dendrimers of the same family. With this technique we were able to identify a critical molecular design parameter for carbosilane dendrimers: the normalized effective binding energy $\Delta G_{bind,eff}/N_{eff}$, i.e., the performance of each active individual dendrimer branch directly involved in a binding interaction.

10

STEERED MOLECULAR DYNAMICS

In steered molecular dynamic (SMD) simulations we increment or decrement the distance between the center of mass (COM) of one molecule (the ligand) and the COM of another molecule (or a part of another molecule, i.e., the binding site); all the atoms can adjust to the forced change in the structure so that conformations may be sampled along a particular pathway. In theory the unbinding/binding should happen spontaneously during the simulation, but its kinetic is often well beyond the maximum length of a simulation. Thus, we accelerate the process in order to understand how the systems energy changes.

10.1 SMD FOR BINDING STUDIES

In the discovery and study of safe and effective drugs and nanocarriers, it is important to determine the binding affinity of the studied molecule with its targets. A good affinity allow the use of a drug at low doses, limiting it's side effects and reaching only the target, and is important for a nanocarrier to take around the body its cargo.

As explained in the previous chapter, the most used technique employs the MM/PBSA approach. This methods take into consideration only the end-points of the binding process.

However a direct calculation of the change in free energy in some complexes is difficult for the intrinsic flexibility and natural change in conformation upon binding. An alternative approach is to use SMD to compute the force that is required to separate the two molecules in a complex.[129, 130]

By integrating the force used over time, a generalized work (W) can be computed and used to calculate ΔG using the so called Jarzynski relationship[131–133]

$$exp(-\Delta G/k_B T) = \langle exp(-W/k_B T)\rangle_A \tag{10.1}$$

where k_B is the Boltzmann constant, T is the temperature of the system at the equilibrium state A (bound complex). The bracket means that a configurational average is to be carried out. In practice we will run 10 simulations and average them to obtain the effect of the bracket.

10.2 SMD for unbinding studies

Another use of SMD is for the study of the kinetic of binding. Two different complexes can have a similar, low, ΔG_{bind}, thus the bound state is preferred than the unbound state from the energetical point of view. But sometimes a drug can have some difficulties in reaching its binding site in a mutated protein, although once inside the binding pocket the complex is stable.

Using SMD to force the entrance of the drug in its binding pocket we were able to observe this process, and this is another tool in the study of drug resistance.

10.3 SMD as a "docking" substitute

One of the problem in the creation of complexes with dendrimers is the laking of *ad-hoc* docking methods. The same is true if we want to put together two different proteins to form a dimer. Also in this situation SMD can be really helpful.

In our works with dendrimers and NAs we started with an equilibrated structure of the two macromolecules about 50 Å away from each others. Next, the dendrimer was pulled close to its target using a force of $50\,\mathrm{kcal\,mol^{-1}\,\AA^{-2}}$ and a velocity of $5\,\mathrm{\AA\,ns^{-1}}$. The phosphorous atoms of the NA were forced in their position by applying a weak restraint of $0.5\,\mathrm{kcal\,mol^{-1}\,\AA^{-2}}$. This allowed avoiding substantial deformation of the NA during the dendrimer pulling process. Once the dendrimer reached the proximity of the NA (i.e., a distance between the dendrimer and the NA COMs of approximately 12 Å), this restraint was released and both molecules were allowed to move to reach the final complex configuration. With this procedure the dendrimer was able to adapt its conformation approaching the NA, and that was impossible with other methods.

11

Structural analysis

The structural analysis of all the MD trajectories obtained was performed using the *cpptraj* program of AMBER. All the automatizations and further calculations were carried out using in-house developed *python* scripts.

11.1 Root-mean-square deviation

The root-mean-square deviation (RMSD) is defined as

$$RMSD = \sqrt{\frac{1}{N}\sum_{i=1}^{i=N} \delta_i^2} \tag{11.1}$$

where δ is the distance between N pairs of equivalent heavy atoms from a reference starting position.

11.2 Radius of gyration

A parameter that provides a quantitative characterization of the size of a molecule is the radius of gyration R_g. For a given molecule of N atoms, the mean-square radius of gyration is defined as

$$\left\langle R_g^2 \right\rangle = \left(\frac{1}{M}\right)\left\langle \left[\sum_{i=1}^{N} m_i [r_i - R]^2\right]\right\rangle \tag{11.2}$$

where R is the center of mass of the molecule, r_i and m_i are the position and mass of the i^{th} atom, and M is the total mass of the molecule.

11.3 Shape tensor

The shape tensor $\boldsymbol{S}$ describe the molecular mass distribution as

$$S = \sum_{i=1}^{N} m_i [(r_j r_i)\mathbf{1}_3 - (r_j r_i^{\mathrm{T}})] \tag{11.3}$$

where r_i is the position of the i^{th}atom with respect to the center of mass of the molecule and $\mathbf{1}_3$ is the unitary matrix of dimension 3. Transformation to the principal axis system diagonalizes $\boldsymbol{S}$ ($S = diag(I_x, I_y, I_z)$), and the three eigenvalues of $\boldsymbol{S}$ (I_z, I_y, and I_x, sorted in the descending order) are the principal moments of inertia of the equivalent ellipsoid.

The first invariant of $\boldsymbol{S}$ gives the squared radius of gyration ($\mathrm{Tr}\, S = I_x + I_y + I_z = R_g^2$) while the second invariant shape descriptor, or the asphericity δ, reflects the deviation from a spherical shape of a molecular conformation:[134]

$$\delta = 1 - 3\frac{\langle I_2 \rangle}{\langle I_1^2 \rangle} \tag{11.4}$$

where I_1 and I_2 refer to the first and second invariants of the shape tensor:

$$I_1 = I_x + I_y + I_z \tag{11.5}$$

$$I_2 = I_x I_y + I_y I_z + I_x I_z \tag{11.6}$$

11.4 Monomer density distribution

The average radial monomer density $\rho(r)$ can provide information about the internal structure of the simulated molecule. $\rho(r)$ can be defined as the number of atoms whose center of mass is located within a spherical shell of radius r and thickness Δr. Accordingly, integration over r yields the total number of atoms $N(r)$ as

$$N(r) = 4\pi \int_{0}^{R} r^2 \rho(r) \mathrm{d}r \tag{11.7}$$

. For dendrimers we used the center of mass of the whole molecule as the reference point.

PART III

RESULTS & DISCUSSION

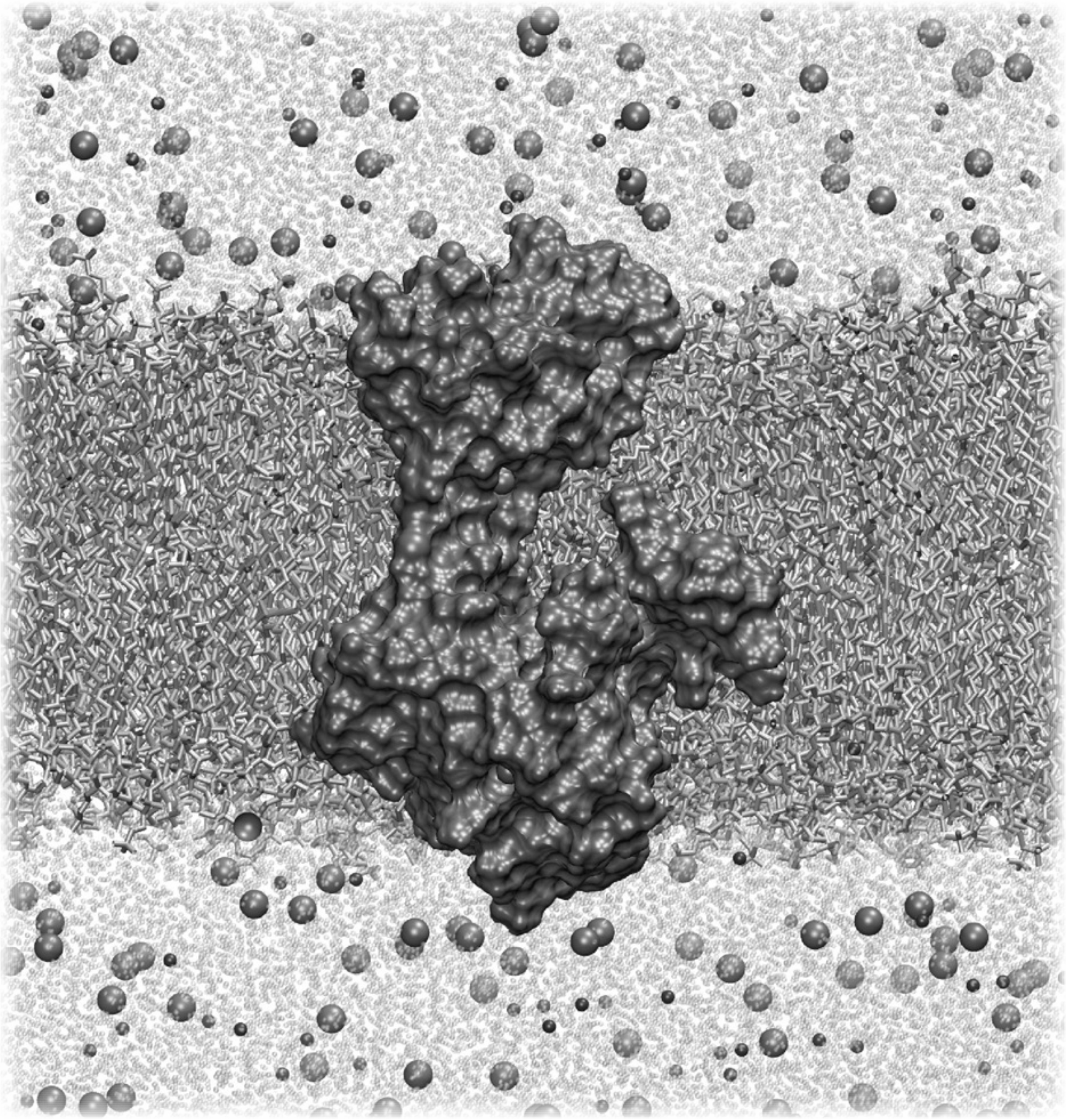

σ_1 receptor in a lipid membrane model.

12

Impact of siRNA overhangs for dendrimer-mediated siRNA delivery and gene silencing[1]

Small interfering RNA (siRNA) are increasingly interesting therapeutics, but as all the nucleic acids (NAs) they need an efficient nanocarrier to reach their target. Dendrimers are among the most promising nanovectors developed in the last years, and Ling Peng et al. recently proposed a structurally flexible fifth-generation triethanolamine (TEA)-core poly(amidoamine) (PAMAM) dendrimer (G5) as an effective nanocarrier for delivery of sticky siRNA bearing long complementary sequence overhangs $(dA)_n/(dT)_n$ (n = 5 or 7).[135, 136] The impact of different siRNA overhangs on the delivery potency and the underlying mechanism of interaction between the G5 dendrimer and siRNA molecules bearing either complementary or noncomplementary sequence overhangs (of different length and composition) were the main objectives of the work presented in this chapter. With a computational approach, combined with experimental datas, we showed that complementary overhangs offer the best gene silencing profile, through the formation of concatemers—supramolecular structures resulting from synergistic and cooperative binding via $(dA)_n/(dT)_n$ (n = 5 or 7) bridges.

---

[1] The matherial presented in this chapter was published at: Posocco, P., Liu, X., Laurini, E., Marson, D., Chen, C., Liu, C., et al. (2013). Molecular Pharmaceutics, 10(8), 3262−3273. doi:10.1021/mp400329g

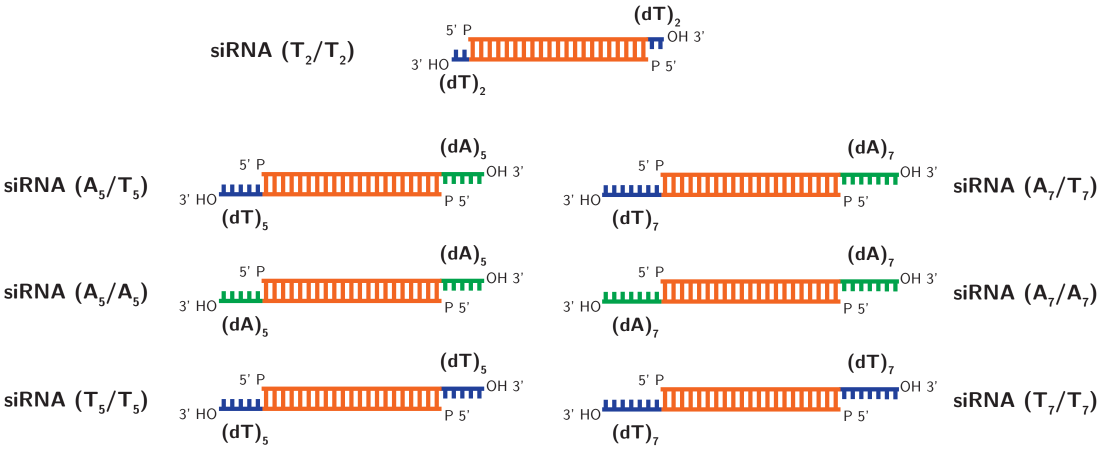

Figure 12.1: siRNA molecules studied, bearing overhangs of different lengths and sequences.

An interesting observation is that also siRNA with longer but noncomplementary overhangs [$(dX)_n/(dX)_n$, with X = T or A and n = 5 or 7] have a considerably higher gene silencing potency than normal siRNA with only 2-thymine long overhangs, although they are less effective than their complementary counterparts. Flexibility of the overhangs is a fundamental property of these systems, highly impacting siRNA delivery performance, and than gene silencing. The overhangs behave as a sort of clamps that hold the nanovectors.

12.1 DESIGN OF SIRNA MOLECULES WITH DIFFERENT OVERHANGS

To test whether the interaction of the siRNA overhangs with dendrimeric vectors effectively contributes toward improving siRNA delivery (in addition to self-assembly of sticky siRNA), we designed siRNA molecules carrying noncomplementary sequence overhangs, complementary sequence overhangs, and conventional $(dT)_2$ overhangs (Figure 12.1). All siRNA molecules share common sequences that target the heat shock protein 27 (Hsp27) and the translationally controlled tumor protein (TCTP), respectively. Hsp27 is a molecular chaperone, which plays an important role in resistance to anticancer drugs and has been recently considered as a novel target for treating drug-resistant prostate tumors and other cancer forms.[137, 138] TCTP, a highly conserved protein present in all eukaryotic organisms, has been lately reported to regulate cell survival in many human cancers; accordingly, it constitutes an interesting target in cancer therapy, especially in breast and prostate malignancies.[139, 140] While the classical siRNA bear $(dT)_2$ overhangs, our sticky siRNA feature complementary sequence overhangs of two different lengths: $(dA)_5/(dT)_5$ and $(dA)_7/(dT)_7$. The corresponding siRNA with noncomplementary sequence overhangs were decorated with $(dT)_5/(dT)_5$, $(dA)_5/(dA)_5$, $(dT)_7/(dT)_7$, and $(dA)_7/(dA)_7$, respectively (Figure 12.1). Accordingly, in what

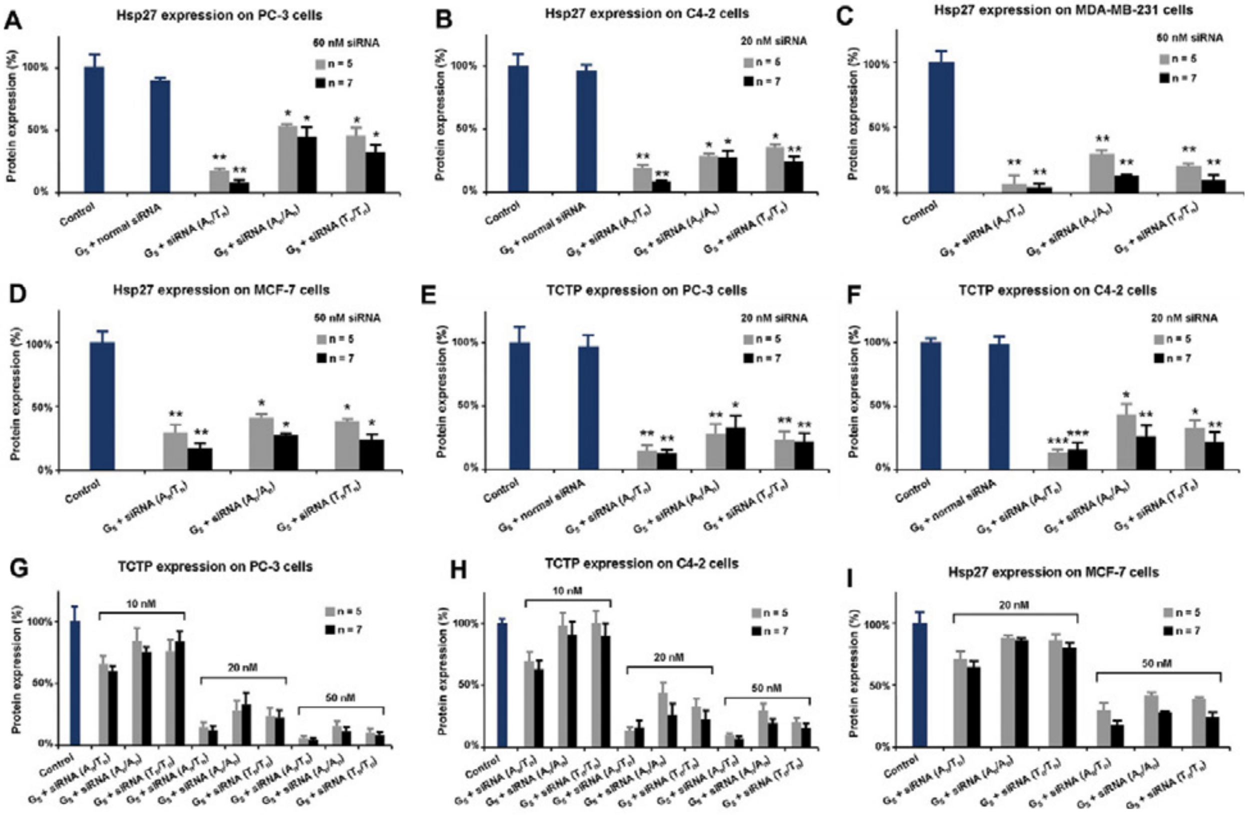

Figure 12.2: Dendrimer G5-mediated siRNA delivery and gene silencing of Hsp27 and TCTP in human prostate cancer PC-3 cells (A and E) and C4-2 cells (B and F) as well as in human breast cancer MDA-MB-231 cells (C) and MCF-7 cells (D) with siRNA carrying various overhangs at a N/P ratio of 10, respectively. The siRNA dose-dependent silencing of TCTP in PC-3 cells (G) and C4-2 cells (H) and of Hsp27 in MCF-7 cells (I). The vinculin protein was used as a reference protein. All of the transfections were done in triplicate. *, **, and *** differ from control ($p \leq 0.05$, $p \leq 0.01$, and $p \leq 0.001$, respectively) by Student's t test.

follows all of these siRNA molecules are denoted as siRNA(T_2/T_2) and, with n = 5 or 7, siRNA(A_n/T_n), siRNA(T_n/T_n), siRNA(A_n/A_n), for the sake of simplicity and convenience. It is to note here that we chose not to work with siRNA molecules bearing even longer overhangs for fear of such long oligonucleotides inducing undesired immune responses.[141]

12.2 Gene silencing using siRNA with different overhangs

The ability of our designed siRNA molecules to down-regulate Hsp27 and TCTP was assessed in human prostate cancer PC-3 and C4-2 cells, and in human breast cancer MDA-MB-231 and MCF-7 cells, respectively.[142, 143] The fifth generation TEA-core PAMAM dendrimer (G5) was chosen as nanovector for these siRNA molecules given its proven capacity to effectively deliver sticky siRNA in lieu of normal siRNA.[136] As expected, no gene silencing was observed

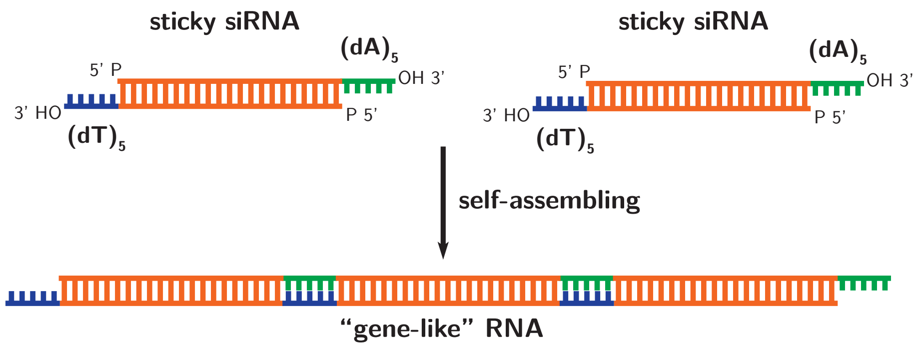

Figure 12.3: Self-assembly of sticky siRNA into "gene-like" longer double-stranded RNA.

with normal siRNA delivered by G5, while gene silencing up to 90 % was attained with siRNA molecules bearing complementary sequence overhangs of both lengths [$(dA)_5/(dT)_5$ and $(dA)_7/(dT)_7$, Figure 12.2]. This result is in agreement with our previous observations[136] and can be mainly ascribed to the sticky overhangs $(dA)_n/(dT)_n$ ($n = 5$ or 7): these complementary single-strand sequences induce siRNA self-assembly into "gene-like" longer double-stranded RNA (Figure 12.3), providing significantly enhanced cooperativity and multivalency when binding toward the nanovectors. This, in turn, endows a low generation dendrimer such as G5 with greater delivery capacity.

What was surprising was the considerably potent gene silencing (up to 70 %) observed with siRNA bearing noncomplementary overhangs $(dT)_5/(dT)_5$, $(dA)_5/(dA)_5$, $(dT)_7/(dT)_7$, and $(dA)_7/(dA)_7$. Namely, siRNA with noncomplementary overhangs could also substantially enhance gene silencing compared to normal siRNA, although they remained less effective than their complementary sticky counterparts (Figure 12.2), whereas no activity was observed with any scramble siRNA molecules. The observed gene silencing potency depended on the length and sequence of the overhangs as well as the concentration of siRNA. Compared with conventional siRNA bearing only the two nucleotide-long overhangs $(dT)_2/(dT)_2$, siRNA molecules with longer overhangs ($n > 2$) were much more effective in inducing gene silencing. In addition, siRNA with $(dT)_n/(dT)_n$ overhangs were slightly more efficient than those bearing $(dA)_n/(dA)_n$ overhangs of equal length ($n = 5$ or 7).

12.3 Nanoscale and stable siRNA/dendrimer complexes

Spurred on by these results, we next endeavored to investigate the reasons why siRNA molecules with longer overhangs of both complementary and noncomplementary sequences were more efficient in inducing gene silencing than the standard siRNA with $(dT)_2/(dT)_2$ overhangs. As the formation of stable complexes between siRNA and delivery nanovectors is

	size [nm]	polydispersity [PDI]	zeta potential [mV]
siRNA(A_5/T_5)/G5	108	0.18	+35
siRNA(T_5/T_5)/G5	124	0.12	+42
siRNA(A_5/A_5)/G5	118	0.14	+43
siRNA(A_7/T_7)/G5	117	0.19	+44
siRNA(T_7/T_7)/G5	114	0.18	+43
siRNA(A_7/A_7)/G5	124	0.12	+33

Table 12.1: DLS Measurement of size and zeta potential of the dendrimer G5 complexes with various siRNA molecules bearing different overhangs

one of the most important prerequisites for effective cell uptake and delivery of siRNA, we first examined the size and size distribution of various siRNA/G5 dendrimer complexes by dynamic light scattering (DLS). Also, the surface zeta potential of complexes was assessed by laser Doppler microelectrophoresis, a technique that derives the value of a surface zeta potential based on electro-osmosis measurements close to the sample surface. For the classical siRNA with $(dT)_2/(dT)_2$ overhangs, its complexes with G5 generated nanoparticles of various sizes ranging from 7 to 400 nm with large polydispersity, implying that G5 could not form stable neither uniform nanoparticles with these siRNA. With siRNA harboring both complementary and noncomplementary long overhangs, however, G5 readily formed stable and uniform nanoparticles with an average size of 100 nm in diameter at N/P = 10 and a polydispersity index around 0.15 (Table 12.1). Moreover, zeta-potential measurements gave positive values for the dendrimer complexes with siRNA bearing longer overhangs (n = 5 or 7) (Table 12.1), implying that these siRNA/G5 nanoparticles are stable colloids. A size around 100 nm and a positive surface potential are two requisites for successful delivery of nanoparticles into cells. Hence, these data for siRNA/dendrimer complexes further corroborate our experimental observation that G5 permits effective gene silencing with siRNA bearing longer overhangs, whether complementary or not, whereas no significant gene silencing is achieved with conventional siRNA/G5 complexes.

12.4 Insight into siRNA binding to G5 by molecular simulations

To understand if and how different siRNA overhangs could impact dendrimer-mediated delivery, we next performed molecular dynamics (MD) simulations to assess the binding of the tested siRNA molecules to the G5 dendrimer. We commenced our in silico study by considering a situation in which monomeric siRNA form a complex with their dendrimeric

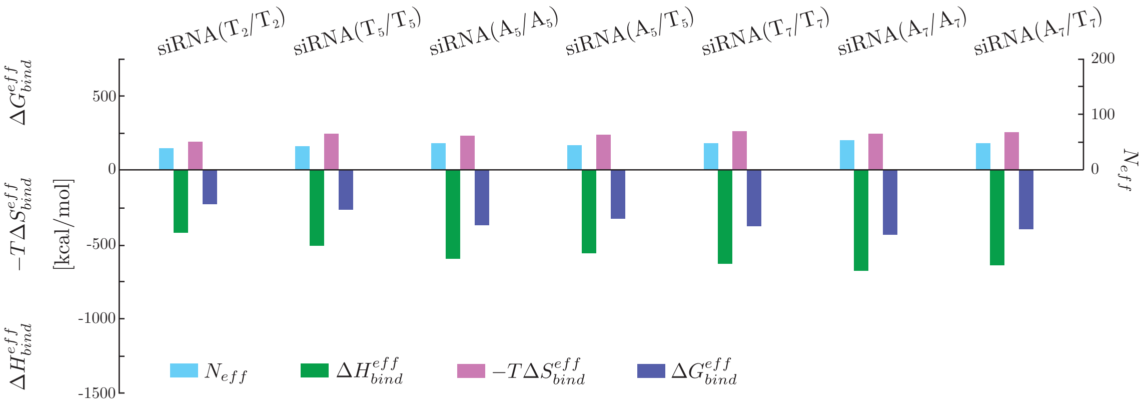

Figure 12.4: Total effective free energy ($\Delta G_{bind}^{eff} = \Delta H_{bind}^{eff} - T\Delta S_{bind}^{eff}$), enthalpic ($\Delta H_{bind}^{eff}$), and entropic ($T\Delta S_{bind}^{eff}$) components of binding of the siRNA molecules with different overhangs toward the G5 dendrimer as well as effective positive charges (N_{eff}) with G5 involved in siRNA binding.

nanocarrier. The relevant results are shown in Figure 12.4. According to our calculations, binding of siRNA toward the G5 dendrimer is affected both by the nature and length of the siRNA overhangs in the following interesting manner:

- for the two homologous siRNA series, the siRNA with (dA)$_n$/(dA)$_n$ overhangs are characterized by the most favorable ΔG_{bind} values, followed by the complementary overhangs (dA)$_n$/(dT)$_n$ and, last, by the siRNA bearing (dT)$_n$/(dT)$_n$ overhangs which show the lowest affinity for the G5 dendrimer;
- longer overhangs (n = 7) are more beneficial to dendrimer binding;
- the lowest affinity value for the G5 dendrimer pertains to the siRNA carrying the shortest overhangs (dT)$_2$/(dT)$_2$.

For a more rigorous and thorough understanding of the interaction between the different siRNAs and G5, we then assessed the effective free energy of binding (ΔG_{bind}^{eff}), that is, the contribution to binding yielded by the dendrimer branches in constant and productive interaction with the NA fragment. To estimate ΔG_{bind}^{eff} for each siRNA/G5 complex, all G5 branches involved in nucleic acid binding (N_{eff}) were precisely identified, and their individual contribution toward the overall binding energy estimated by a per-residue free energy decomposition technique.

The cumulative results of this analysis are reported in Figure 12.4, showing the values of N_{eff}, the effective total free energy of binding ΔG_{bind}^{eff}, and its enthalpic ΔH_{bind}^{eff} and entropic $T\Delta S_{bind}^{eff}$ components for all complexes. The first important finding from this study

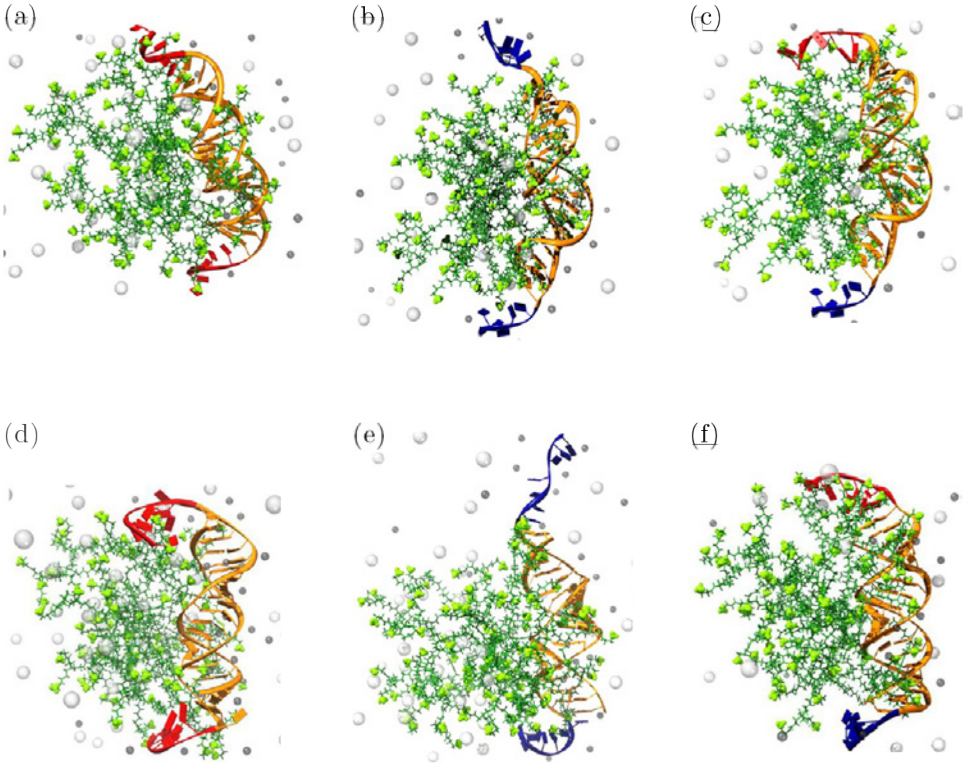

Figure 12.5: Selected equilibrated MD snapshots of the complexes between the G5 dendrimer and the siRNA molecules with 5-nucleotide long (upper panel) and 7-nucleotide long (lower panel) overhangs. These overhangs are respectively, (a) $(\mathrm{dA})_5/(\mathrm{dA})_5$; (b) $(\mathrm{dT})_5/(\mathrm{dT})_5$; (c) $(\mathrm{dA})_5/(\mathrm{dT})_5$; (d) $(\mathrm{dA})_7/(\mathrm{dA})_7$; (e) $(\mathrm{dT})_7/(\mathrm{dT})_7$, and (f) $(\mathrm{dA})_7/(\mathrm{dT})_7$. In the panels, the dendrimer is depicted as forest green sticks, the terminal charged amine groups as light green sticks-and-balls, the siRNA as an orange ribbon, and the two overhangs $(\mathrm{dA})_\mathrm{n}$ and $(\mathrm{dT})_\mathrm{n}$ are highlighted in red and navy blue, respectively. Some Cl^- and Na^+ and counterions are shown as big light gray and small dark gray spheres, respectively. Water molecules have been omitted for clarity.

concerns the number of dendrimer branches efficiently involved in siRNA binding, N_{eff}. As expected, N_{eff} is the smallest (38) for the siRNA with the shortest overhangs $[(\mathrm{dT})_2/(\mathrm{dT})_2]$, while a net trend is observed with N_{eff} increasing from siRNA($\mathrm{T_n/T_n}$) to siRNA($\mathrm{A_n/T_n}$) to siRNA($\mathrm{A_n/A_n}$) for the two homologous siRNA series (Figure 12.4). Contextually, the ΔG_{bind}^{eff} increases (i.e., became more negative and hence more favorable) in the same order.

Further examination of the main components of ΔG_{bind}^{eff} for all monomeric siRNA systems revealed that, although the binding process is essentially enthalpy-driven, entropy also plays a substantial role in modulating the ultimate, individual affinity of each siRNA toward the dendrimer nanovector G5. For example, the system with siRNA bearing $(\mathrm{dA})_5/(\mathrm{dA})_5$ overhangs has the most favorable effective enthalpic component ($\Delta H_{bind}^{eff} = -592.0\,\mathrm{kcal\,mol^{-1}}$) among the three homologous assemblies with $(\mathrm{dA})_5/(\mathrm{dA})_5$, $(\mathrm{dA})_5/(\mathrm{dT})_5$, and $(\mathrm{dT})_5/(\mathrm{dT})_5$

overhangs (Figure 12.4). This can be ascribed to the high number of favorable electrostatic interactions, characterized by the value of N_{eff} (46), alongside other nonbonded interactions between the charged G5 residues and this specific siRNA molecule, including its overhangs. At the same time, the siRNA (A_5/A_5) complex with G5 presents the lowest unfavorable entropic contribution ($T\Delta S^{eff}_{bind} = +227.2\,\mathrm{kcal\,mol^{-1}}$), by virtue of the rigid nature and aggregation propensity of the $(dA)_5$ overhangs; this allows for more permanent contacts between the entire siRNA (including its overhangs) and the G5 peripheral positively charged terminal groups (Figure 12.5a). The cumulative effect of these two contributing factors results in the most favorable value of the effective free energy of binding $\Delta G^{eff}_{bind} = -364.8\,\mathrm{kcal\,mol^{-1}}$. By contrast, the siRNA (T_5/T_5) in complex with G5 is characterized by the smallest N_{eff} value (41) in the series. Accordingly, this system presents the least favorable enthalpic contribution ($\Delta H^{eff}_{bind} = -503.1\,\mathrm{kcal\,mol^{-1}}$) and the highest entropic loss ($T\Delta S^{eff}_{bind} = +241.1\,\mathrm{kcal\,mol^{-1}}$) which, when combined, give the lowest ΔG^{eff}_{bind} value ($-262.0\,\mathrm{kcal\,mol^{-1}}$). The analysis of the entire MD trajectory reveals that the $(dT)_5$ overhangs are endowed with higher flexibility with respect to their $(dA)_5$ counterparts, and the flexibility of the T_n-overhangs is quantified by the highest loss of entropy upon their binding with siRNA and well-qualified by the higher fluctuations (higher degree of freedom) of these overhangs in the solvent, hence leading to a less optimized siRNA /dendrimer opposite-charge contacts (Figure 12.5b). Lastly, the siRNA with the complementary over-hangs $(dA)_5/(dT)_5$ displays a somewhat intermediate behavior (Figure 12.5c), both in terms of N_{eff} and ΔG^{eff}_{bind} values, suggesting a possible compensatory effect between a more rigid and hence more efficient $(dA)_5$ overhang on one side and a more flexible and less efficient $(dT)_5$ overhang on the other.

Analogous situation is found for the 27-mer siRNA/G5 complexes for which, in line with the 25-mer siRNA series, the affinity of the siRNA for the G5 dendritic vector (ΔG^{eff}_{bind}) increases according to the nature of the overhangs in the following order: $(dT)_7/(dT)_7 <$ $(dA)_7/(dT)_7 < (dA)_7/(dA)_7$. Once again, the relevant simulations highlights the higher flexibility of the $(dT)_7$ overhang and its role in dendrimer binding. Thus, in the case of the siRNA (T_7/T_7)/G5 complex, this property ultimately results in the smallest value of N_{eff} (45), the least favorable enthalpic contribution ($\Delta H^{eff}_{bind} = =626.7\,\mathrm{kcal\,mol^{-1}}$), the most unfavorable entropic term ($T\Delta S^{eff}_{bind} = +258.9\,\mathrm{kcal\,mol^{-1}}$) and, correspondingly, the lowest value of ΔG^{eff}_{bind} ($= -\ 367.8\,\mathrm{kcal\,mol^{-1}}$) (Figure 12.5e). On the contrary, the siRNA featuring the $(dA)_7/(dA)_7$ overhangs show the highest affinity for G5, the binding being driven by the most favorable enthalpic term ($\Delta H^{eff}_{bind} = -669.1\,\mathrm{kcal\,mol^{-1}}$) and the lowest unfavorable entropic loss ($T\Delta S^{eff}_{bind} = +243.1\,\mathrm{kcal\,mol^{-1}}$), in agreement with the highest value of N_{eff} (53) and the higher rigidity (and hence, binding efficiency) of the $(dA)_7$ overhangs (Figure 12.5d), respectively. Also in this case, the siRNA(A_7/T_7) shows an intermediate behavior between the two other members of the series (Figure 12.5f), confirming an overall balance between two opposing effects exerted by the two different $(dA)_n$ and $(dT)_n$ overhangs.

While these results should be considered with due care given all approximations assumed in the formulations of the molecular systems involved, they do allow for the following general considerations:

- the presence of longer overhangs on a siRNA duplex appears more advantageous for dendrimer binding when compared to shorter ones, due to the higher number of effective dendrimer charges in active and permanent contact with the nucleic acid;
- for siRNA with noncomplementary overhangs of a given length, the presence of less flexible [i.e., $(dA)_n$] overhangs affords a more favorable enthalpic contribution, a less unfavorable entropic penalty, and ultimately, a higher affinity of the siRNA for binding to its dendrimeric nano-carrier;
- in the case of very long overhangs (e.g., $n = 7$), the presence of more flexible nucleotides (e.g., $(dT)_7/(dT)_7$) might be of little benefit in dendrimer complexation with respect to shorter overhangs populated by more rigid counterparts (e.g., $(dA)_5/(dA)_5$) by virtue of an enthalpy/entropy compensation effect.

12.5 Concatemerization of sticky siRNA favors binding with dendrimer vector G5

Sticky siRNA can self-assemble into “gene-like” longer double-stranded RNA via hybrid bridges formed by the complementary sequence overhangs (Figure 12.3). This “oligomerization” or “concatemerization” may, in turn, permit stronger cooperativity and multivalency which would assist their interaction with the vectors and, eventually, lead to better delivery efficiency. So far, the stoichiometry and structure of these “gene-like” siRNA are unknown. Nevertheless, Behr et al.[19] clearly demonstrated that:

- sticky siRNA capable of forming noncovalent concatemers via $(dA)_8/(dT)_8$ bridges increased siRNA/vector complex stability and hence protected them from RNase degradation;
- since concatemers were not detected in the absence of vectors (e.g., polyethyleneimine (PEI)) mainly because of the low stability of the overhang duplex, the presence of polycationic vectors may favor encounters of siRNA/nanovector intercomplexes by shielding their repulsive forces, thus favoring sticky siRNA concatemerization.

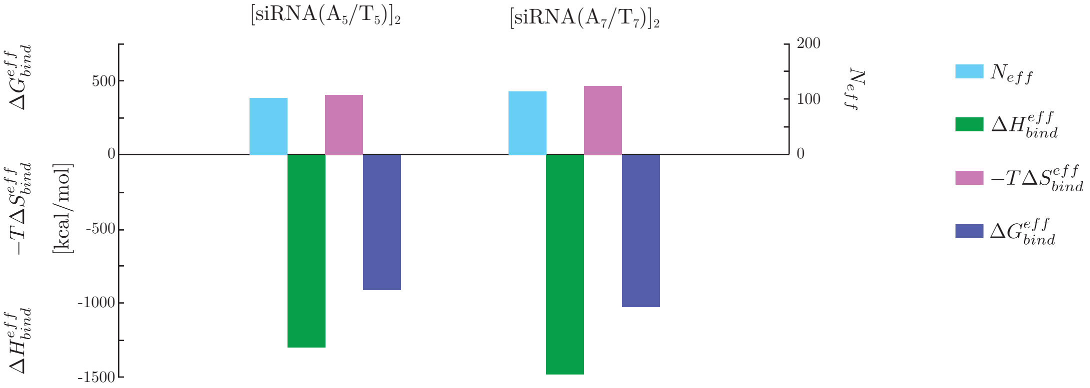

Figure 12.6: Total effective free energy ($\Delta G^{eff}_{bind} = \Delta H^{eff}_{bind} - T\Delta S^{eff}_{bind}$), enthalpic ($\Delta H^{eff}_{bind}$), and entropic ($T\Delta S^{eff}_{bind}$) components of binding of dimeric sticky siRNA toward the G5 dendrimer as well as effective positive charges (N_{eff}) with G5 involved in dimeric sticky siRNA binding.

To investigate these concepts, we carried out MD simulations and the appropriate ΔG_{bind} calculations for dendrimer G5 in complex with two dimeric sticky siRNAs, hereafter referred to as [siRNA (A$_5$/T$_5$)]$_2$ and [siRNA (A$_7$/T$_7$)]$_2$, respectively. The results obtained are shown in Figure 12.6. When the values of the dimeric complexes are compared with those of the corresponding monomeric assemblies multiplied by two (see Figure 12.4), we see that the ΔG_{bind} for the dimeric cases are substantially more favorable than those obtained for two monomeric systems (i.e., $-975.4\,\mathrm{kcal\,mol^{-1}}$ for [siRNA (A$_5$/T$_5$)]$_2$ vs $2 \times (-387.4) = -774.8\,\mathrm{kcal\,mol^{-1}}$ for two siRNAs (A$_5$/T$_5$) and $-1024.5\,\mathrm{kcal\,mol^{-1}}$ for [siRNA (A$_7$/T$_7$)]$_2$ vs $2 \times (-422.9) = -845.8\,\mathrm{kcal\,mol^{-1}}$ for two siRNAs (A$_7$/T$_7$), respectively). Although the models considered here likely represent a much simplified vision of the real systems, the results obtained not only support the hypothesis proposed by Behr et al.—namely, preformed sticky siRNA /vector complexes favor the subsequent concatemerization of the siRNA complementary sticky ends—but also indicate a synergistic and cooperative binding mechanism between sticky siRNA and dendrimer.

Further supportive evidence comes from the analysis of the effective free energy of binding (ΔG^{eff}_{bind}) of the dimeric complexes of the sticky siRNA , [siRNA (A$_5$/T$_5$)]$_2$, and [siRNA (A$_7$/T$_7$)]$_2$ (Figure 12.6). Indeed, in the systems containing dimeric complexes of siRNA , the number N_{eff} of effective G5 positive charges constantly in contact with the longer siRNA strand is more than two times that estimated for each corresponding monomeric complex {96 for the [siRNA (A$_5$/T$_5$)]$_2$/G5 vs 44 for the siRNA (A$_5$/T$_5$)/G5 complex, and 105 for the [siRNA -(A$_7$/T$_7$)]$_2$/G5 vs 47 for the siRNA (A$_7$/T$_7$)/G5 complex, respectively; Figure 12.6}. An inspection of the MD trajectories for these two systems reveals that the presence of the "hybridized" (dA)$_5$/(dT)$_5$ and (dA)$_7$/(dT)$_7$ double-stranded portions of these siRNAs,

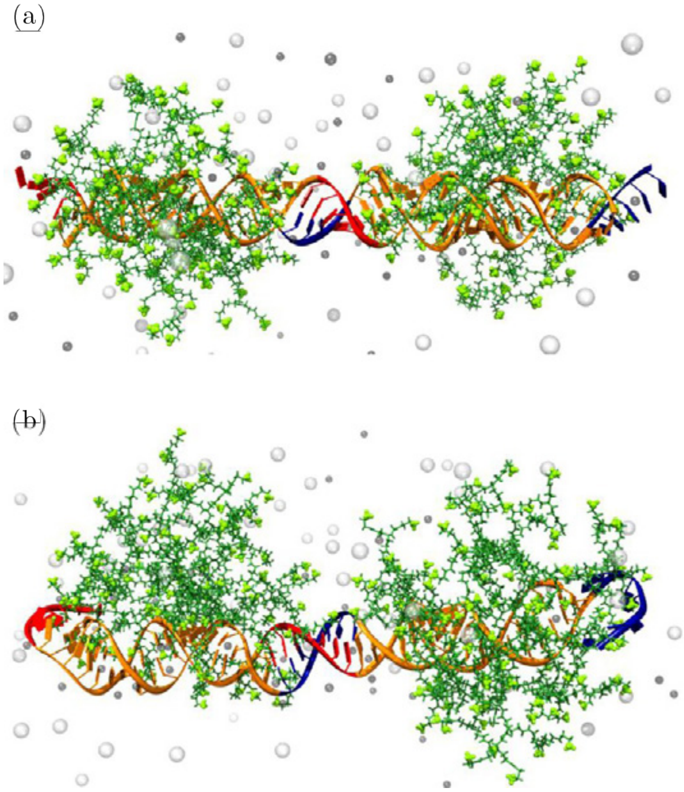

Figure 12.7: Selected equilibrated MD snapshots of the complexes between dendrimer G5 and the sticky siRNA dimers [siRNA(A_5/T_5)]$_2$ (a) and [siRNA(A_7/T_7)]$_2$ (b). The dendrimer is depicted as forest green sticks, the terminal charged amine groups as light green sticks-and-balls, the siRNA as an orange ribbon, and the two overhangs $(dA)_n$ and $(dT)_n$ are highlighted in red and navy blue, respectively. Some Cl^- and Na^+ are shown as big light gray and small dark gray spheres, respectively. Water has been omitted for clarity.

which are more rigid and globally more charged compared to each of their corresponding single-stranded overhangs, allows for a small but significant conformational rearrangement of the dendrimer outer branches which, in turn, leads to the augmented number of favorable, stabilizing electrostatic interactions (Figure 12.7). In addition to the total ΔG_{bind}, evidence of the beneficial action of the "concatemerization" of two siRNAs with complementary overhangs can also be found in the corresponding values of the effective quantities ΔG_{bind}^{eff}, ΔH_{bind}^{eff}, and $T\Delta S_{bind}^{eff}$ (Figure 12.6). In particular, it is interesting to note the concomitant synergistic enhancement in the enthalpic driving force toward binding $\{-1260.3\,\mathrm{kcal\,mol^{-1}}$ for [siRNA (A_5/T_5)]$_2$ vs $2 \times (-554.9) = -1109.8\,\mathrm{kcal\,mol^{-1}}$ for two siRNAs (A_5/T_5) and $-1441.2\,\mathrm{kcal\,mol^{-1}}$ for [siRNA (A_7/T_7)]$_2$ vs $2 \times (-637.3) = -1274.6\,\mathrm{kcal\,mol^{-1}}$ for two siRNAs (A_7/T_7)$\}$ and the decrease in the entropic contribution disfavoring siRNA/G5 complexation $\{+372.2\,\mathrm{kcal\,mol^{-1}}$ for [siRNA (A_5/T_5)]$_2$ vs $2 \times (+233.4) = +446.8\,\mathrm{kcal\,mol^{-1}}$ for two siRNAs (A_5/T_5) and $+437.2\,\mathrm{kcal\,mol^{-1}}$ for [siRNA (A_7/T_7)]$_2$ vs $2 \times (+248.2) = +496.4\,\mathrm{kcal\,mol^{-1}}$ for two siRNAs (A_7/T_7)$\}$.

These results demonstrate that the presence of a dimeric sticky siRNA constituted by two complementary overhangs and a central "$(dA)_n/(dT)_n$ hybridized double-stranded" tract synergistically enhances dendrimer binding, ultimately underlying the cooperative and multivalent nature of the dendrimeric nanovector/nucleic acid interactions. These in silico predictions

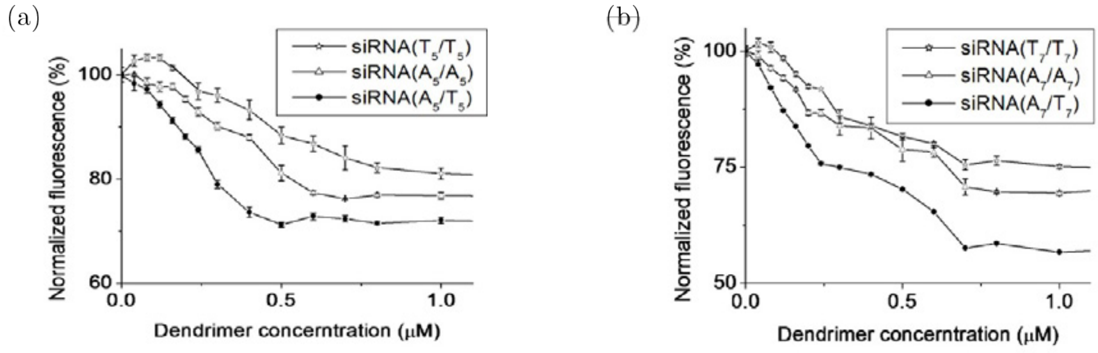

Figure 12.8: Binding of the dendrimer G5 toward siRNA bearing 5-nucleotide long (a) and 7-nucleotide long (b) overhangs was assessed by an ethidium bromide displacement assay.

are further confirmed by experimental results aimed at assessing the binding between siRNA and the G5 dendrimer using ethidium bromide (EB) displacement fluorescence spectroscopy (Figure 12.8). According to these tests, the siRNA carrying the complementary overhangs $(\mathrm{dA})_\mathrm{n}/(\mathrm{dT})_\mathrm{n}$ exhibited the strongest binding toward the G5 dendrimer, the affinity of the siRNA for G5 decreasing in the order $(\mathrm{dA})_\mathrm{n}/(\mathrm{dT})_\mathrm{n} > (\mathrm{dA})_\mathrm{n}/(\mathrm{dA})_\mathrm{n} > (\mathrm{dT})_\mathrm{n}/(\mathrm{dT})_\mathrm{n}$ (n = 5 or 7).

12.6 Dissociation process of siRNA/G5 complexes

Importantly, once siRNA/dendrimer complexes are internalized into cells, siRNA molecules need to be released from their corresponding supramolecular ensembles to reach the RNA interference (RNAi) machinery to start the gene silencing process. Therefore, siRNA release from its nanovector is also a crucial step for effective siRNA delivery and gene silencing. With the purpose of investigating in more detail the process of siRNA release from its dendrimer complex, we decided to explore the siRNA/dendrimer unbinding process using steered molecular dynamic (SMD). Accordingly, during our SMD simulation, the siRNA duplex was forcedly pulled away from its vector using a pulling force given by $F(t) = k[vt - (r - r_0)n]$ where k is the force constant, v is the pulling velocity, n is the pulling direction normal, and r_0 and r are the position of the siRNA at the beginning and at time t of the pulling experiment, respectively. We note here that SMD simulations were not attempted on the siRNA bearing complementary overhangs $(\mathrm{dA})_\mathrm{n}/(\mathrm{dT})_\mathrm{n}$ (n = 5 or 7) as even the simplest siRNA “dimeric concatemer” currently poses considerable technical computational problems.

Figure 12.9a presents the time profiles of the pulling forces during the SMD simulations of the dissociation of the standard siRNA (siRNA(T_2/T_2)) and four siRNA bearing noncomplementary overhangs—siRNA(T_5/T_5), siRNA(A_5/A_5), siRNA(T_7/T_7), and siRNA(A_7/A_7)—

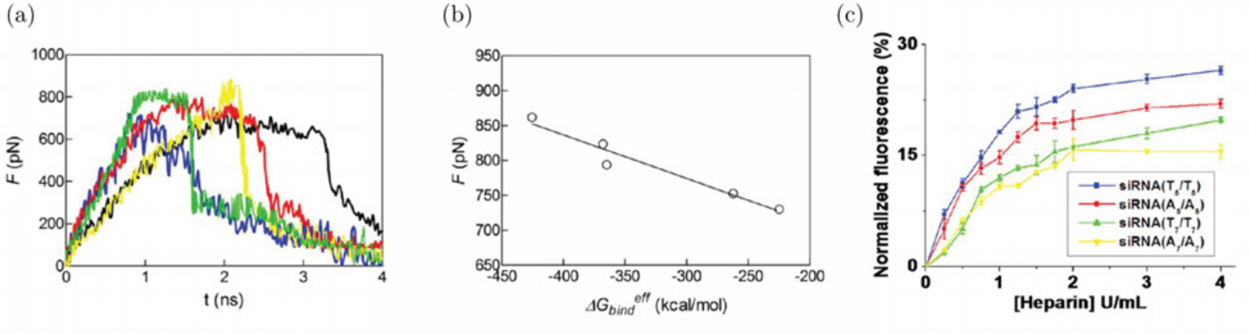

Figure 12.9: (a) Average force profile of siRNA unbinding from their G5 dendrimer complexes. Color legend: blue, siRNA(T_5/T_5); green, siRNA(T_7/T_7); yellow, siRNA(A_7/A_7); red, siRNA(A_5/A_5); black, siRNA(T_2/T_2). (b) Correlation between the SMD peak force and the effective binding free energy ΔG_{bind}^{eff} for the corresponding siRNA and the G5 dendrimer. The linear fit has a correlation level of $R^2 = 0.95$. (c) Dissociation of siRNA from the dendrimer complexes as revealed by heparin-coupled ethidium bromide assay.

from their respective G5 complexes. Clearly, an increased level of force is required to initiate movement of the siRNA double-strand away from the dendrimer, which implies that the nucleic acid encounters energy barriers to dissociation. The maximum pulling forces F are 730 pN for the siRNA(T_2/T_2), 753 pN for the siRNA(T_5/T_5), 794 pN for the siRNA(A_5/A_5), 842 pN for the siRNA(T_7/T_7), and 862 pN for the siRNA(A_7/A_7). After passing this peak, the force drops rapidly. In Figure 12.9b, these rupture forces are plotted as a function of the effective binding energies ΔG_{bind}^{eff} obtained from the classical MD simulations (Figure 12.4). As can be seen, a very strong correlation is found between these two quantities ($R^2 = 0.95$): the larger the rupture force, the more favorable (i.e., more negative) the effective binding free energy, and hence the more reluctant the release of siRNA from their corresponding dendrimer ensembles.

More interestingly, however, is the finding that, for the two siRNA with the most flexible overhangs, $(dT)_5/(dT)_5$ and $(dT)_7/(dT)_7$, the force reaches a maximum almost at the same, shortest time (≈150 ps), while the force peaks for siRNA(A_7/A_7) and siRNA(A_5/A_5) follow at ≈2.1 ns and ≈2.4 ns, respectively (Figure 12.9a). For the siRNA with the shortest overhangs $(dT)_2/(dT)_2$, the rupture force maximum occurs after a considerably longer time, ≈3.2 ns (Figure 12.9a). Notwithstanding the fact that longer overhangs enhance the binding of the siRNA carrying noncomplementary overhangs with the dendrimer vector, they also possess increased flexibility which, in turn, facilitates their detachment from the dendrimer. Thus, the siRNA with the most flexible overhangs, $(dT)_7/(dT)_7$ and $(dT)_5/(dT)_5$, are able to unbind at earlier time points, while those featuring more rigid and/or shorter overhangs such as $(dA)_5/(dA)_5$ require longer times to dissociate from their complex.

We further experimentally assessed siRNA release from their corresponding dendrimer complexes using the heparin-coupled EB assay. In this method heparin (a highly negatively charged polysaccharide) is employed in competing with siRNA for dendrimer binding. Upon addition of heparin, siRNA is gradually displaced from the dendrimer complexes by heparin, and the released siRNA is ready to intercalate the fluorescent EB probe, which hence emits a strong fluorescence. From the intensity of the emitted EB fluorescence, the corresponding siRNA release from its nanocarrier can be estimated. As revealed in Figure 12.9c, in agreement with our computational predictions, the siRNA with short and flexible overhangs $(dT)_5/(dT)_5$ are most easily displaced by heparin from their dendrimer complexes, followed in order by $(dA)_5/(dA)_5$, $(dT)_7/(dT)_7$, and $(dA)_7/(dA)_7$.

Altogether, the above results show that, among the siRNA molecules with noncomplementary overhangs, those characterized by $(dT)_n/(dT)_n$ overhangs appear to offer the best compromise in terms of dendrimer affinity and release. These conclusions greatly correlate with the experimental evidence, according to which siRNA(T_7/T_7) molecules are endowed with the best G5-mediated siRNA delivery and gene silencing among all investigated siRNA molecules carrying noncomplementary overhangs.

12.7 Conclusions

In our quest for safe and efficient vectors for the delivery of siRNA therapeutics, we discovered that the structurally flexible, fifth generation TEA-core PAMAM dendrimer G5 is an effective nanovector for delivering sticky siRNAs.[136] With the help of combined experimental and computational approaches, we have successfully identified the underlying mechanisms of interaction between the overhangs of the sticky siRNA with this dendrimeric nanovector and the contribution of siRNA overhangs to the observed improved delivery potency. siRNA molecules with complementary overhangs offer the best action in term of gene silencing. On the other hand, while siRNAs bearing noncomplementary long overhangs show considerably higher gene silencing potency than normal siRNAs, they are nevertheless still less effective than sticky siRNAs bearing complementary overhangs. The observed gene silencing potency, however, depends on the length and nature of the overhangs.

Overall, our results allowed us to formulate a sensible molecular rationale explaining the importance of the different siRNA overhangs in dendrimer-mediated siRNA delivery and gene silencing. Long and complementary overhangs on siRNA duplexes offer the best action in terms of dendrimer binding via concatemerization of the complementary overhang nucleotides. The formation of such concatemers via $(dA)_n/(dT)_n$ bridges is fostered by preformed siRNA/dendrimer complexes, and the effective free energy of binding of the "gene-like" RNA/dendrimer complex is the result of a synergistic and cooperative mechanism. Once decomplexed in the cytoplasm, the sticky siRNA concatemers fall apart to deliver siRNA molecules for effective gene silencing.**[19]** For siRNAs bearing noncomplementary overhangs, the sum of effects of overhang length, nature, and flexibility plays a major role in determining their ultimate performance in siRNA delivery and the resulting gene silencing. Thus, although higher overhang rigidity increases the siRNA binding capacity toward the G5 dendrimer, a higher overhang length—and hence higher flexibility—is more beneficial for the subsequent nucleic acid release process. Results from computer modeling show that, among the siRNAs with noncomplementary overhangs considered in the present work, those characterized by $(\mathrm{dT})_\mathrm{n}/(\mathrm{dT})_\mathrm{n}$ overhangs appear to offer the best compromise in terms of dendrimer binding and unbinding characteristics. These conclusions greatly correlate with experimental findings according to which siRNAs with $(\mathrm{dT})_\mathrm{n}/(\mathrm{dT})_\mathrm{n}$ overhangs are endowed with the best G5-mediated siRNA delivery and gene silencing, as discussed above. Collectively the results presented here demonstrate that the adoption of this kind of multi-disciplinary approach can yield fundamental insight into the importance of siRNA overhangs for dendrimer-mediated siRNA delivery. This will offer a new perspective on siRNA therapeutics and be of instrumental use in the future translational implementation of siRNAs in the treatment of various diseases.

13

VIOLOGEN-PHOSPHORUS DENDRIMERS[1]

Viologen phosphorus-containing dendrimers are relatively new compounds which have been seldom investigated in terms of their biological and structural properties.[144, 145] These types of compounds exhibit antimicrobial properties and their behavior depends on their size, the number of viologen units and the nature of the surface groups.[144] Quite recently, Erik De Clercq and collaborators[146] proved the antiviral activity of dendrimers containing a viologen against the Human Immunodeficiency Virus (HIV) and, to a lesser extent, against other viruses such as the Herpes Simplex Virus (HSV), the Reovirus (RV), and the Respiratory Syncytial Virus (RSV).

Accordingly, I embarked in a computational study to determine the main structural characteristics of some representative members of the viologen-based dendrimers, and their binding to albumin. In particular, I focused on two different families of new viologen dendrimers bearing phosphorus groups as additional units incorporated either at the focal point or at the periphery, or both of these key structural positions of the dendritic backbone.[144, 145] This choice of strategy was aimed by the fact that we already demonstrated the key role

---

[1] The matherial presented in this chapter was published at: Posocco, P., Laurini, E., Marson, D., Peng, L., Smith, D. K., Klajnert, B., et al. (2013), In B. Klajnert, L. Peng, V. Cena, Dendrimers in Biomedical Applications. Cambridge: Royal Society of Chemistry.

	charge	G	R_g [Å]	asphericity
D1	+6	0	9.25	0.078
D2	+6	0	10.76	0.063
D3	+12	0	12.32	0.020
D4	+6	0	12.19	0.081
D5	+12	0	13.07	0.023
D6	+18	1	16.59	0.069
D7	+36	1	18.82	0.026

Table 13.1: Main structural parameters for viologen dendrimers **D1**–**D7**

played by phosphorus dendrimers in biology and for biomedical applications due to several specificities.[147]

Accordingly, the two viologen-phosphorus dendrimers were built from a trifunctionalized $P(S)(NCH_3NH_2)_3$ (**D2**, **D4**, and **D6**) or hexafunctionalized core $(P_3N_3)(NCH_3NH_2)_6$ (**D3**, **D5**, and **D7**), and decorated on their surface either with aldehyde groups or with phosphonate groups, the latter being well-known for their biological properties. A dendron structurally similar to **D2** but stemming from a phenyl core (**D1**) was also considered for comparison.

Figure 13.1 illustrates the chemical structures of the viologen dendrimers **D1**–**D7**, while Figure 13.2 shows the MD equilibrated snapshots of **D4** and **D7** at neutral pH and in the presence of a physiological ionic strength (0.15 M) in solution.

13.1 Dimensions and shape of viologen-phosphorus dendrimers

The R_g values, Equation 11.2 on page 66, estimated by molecular dynamics (MD) simulations for all viologen dendrimer generations at pH = 7.4 and 0.15 M NaCl are listed in the fourth column of Table 13.1. As shown in Figure 13.3a, the dimensions of the viologen dendrimers linearly increase with increasing generation.

While the value of R_g yields an indication of the overall dimension of the dendrimers, it does not inform about the real shape of the molecules, that is, if the dendrimer is adopting a true spherical or, e.g., an oblong shape. The fifth column of Table 13.1 and the graph in Figure 13.3b show that all viologen dendrimers studied tend to assume a spherical conformation; nonetheless, the dendrimers featuring the cyclotriphosphazene moiety as a core (**D3**, **D5**, and **D7**) and characterized by 6 branches all present a δ value close to 0.02 and, thus, assume a more spherical than their 3-branched trihydrazidophosphine-core or phenyl-core counterparts (**D1**, **D2**, **D4**, and **D6**). Such a behavior can be ascribed to the presence of regularly spaced like-charges along the dendrimer branches, whose reciprocal repulsion

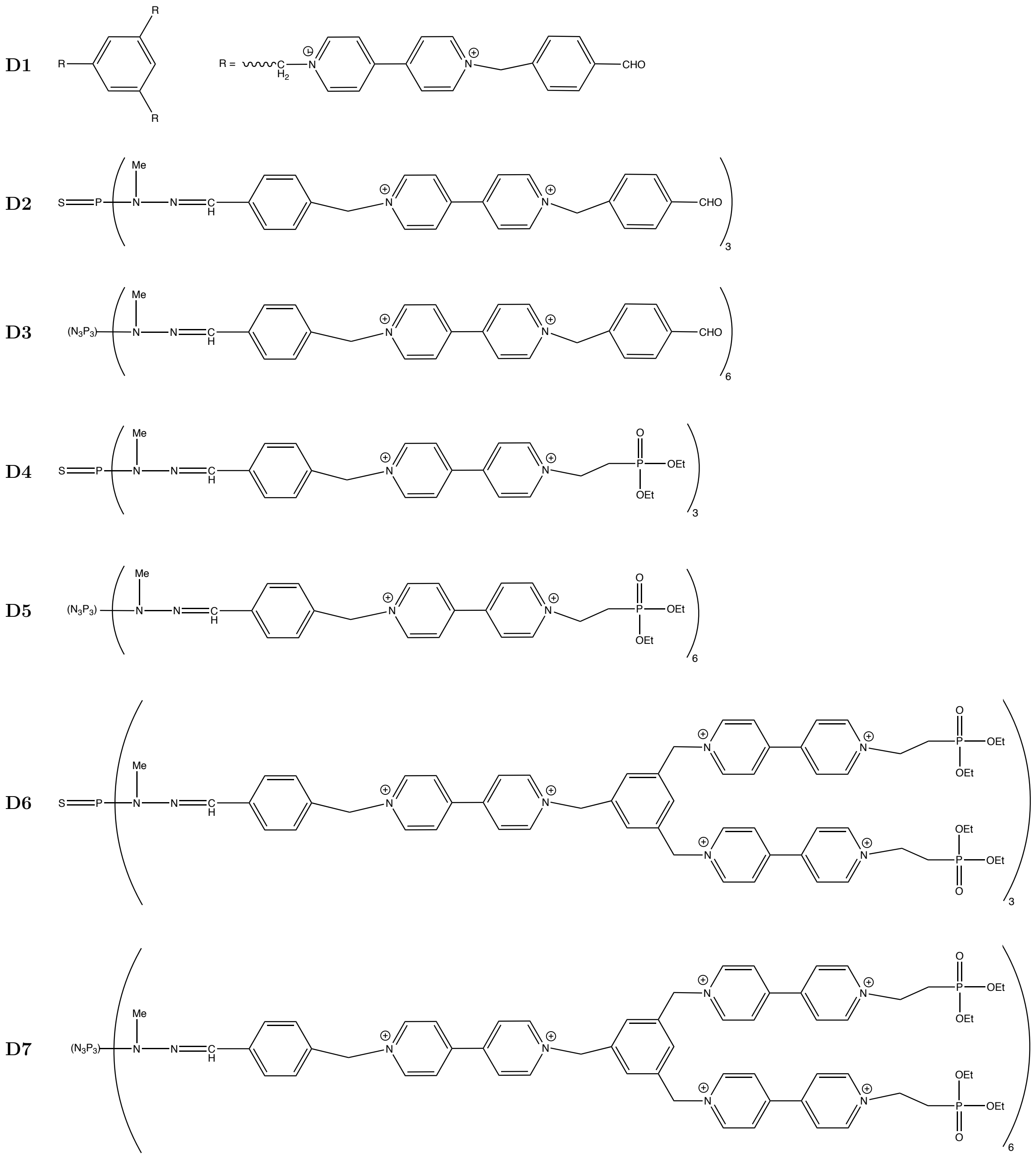

Figure 13.1: Chemical structures of the viologen dendrimers **D1**–**D7**.

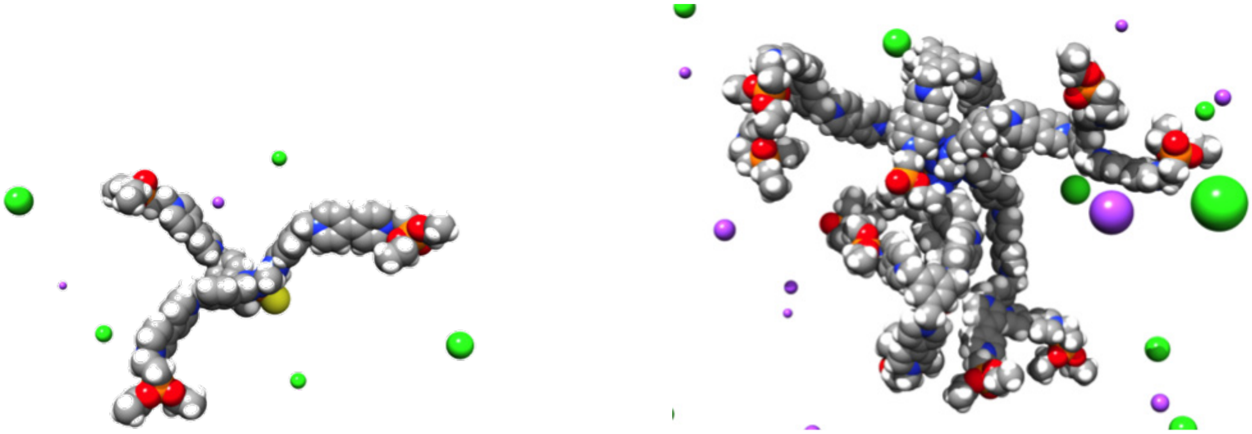

Figure 13.2: Equilibrated MD snapshots of viologen-phosphorus dendrimers **D4** (left) and **D7** (right) in solution at neutral pH and 0.15 M NaCl. The dendrimers are shown as atom-colored spheres (grey, C; red, O; yellow, S; blue, N, orange, P, white, H). Water molecules are omitted for clarity, while some counterions are shown as green (Cl^-) and purple (Na^+) spheres.

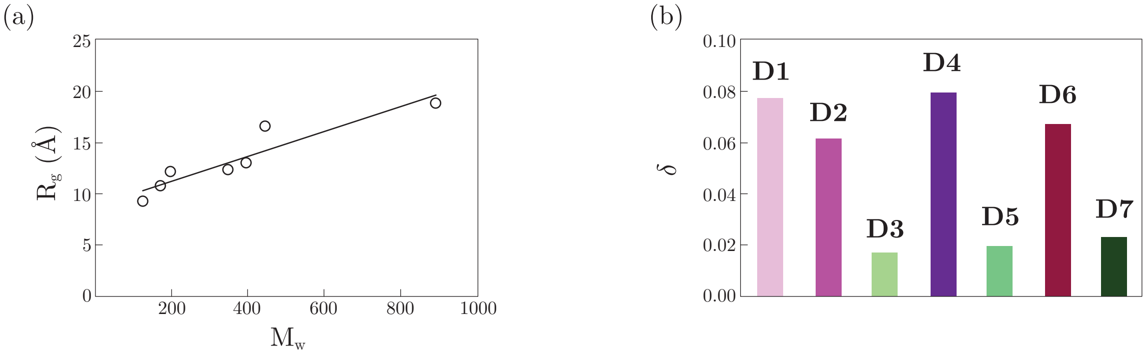

Figure 13.3: (a) Plot of R_g calculated from MD simulations as a function of the viologen dendrimers' molecular weight at pH = 7.4 and 0.15 M NaCl. (b) Plot of the asphericity parameter δ for viologen dendrimers **D1**–**D7**.

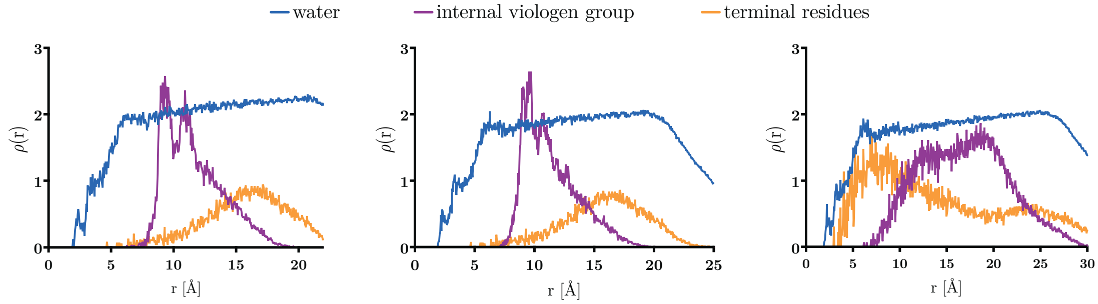

Figure 13.4: Average radial monomer density profiles for viologen-phosphorus dendrimers **D2** (first plot), **D4** (middle plot), **D6** (last plot).

(greater for those molecules with a higher number of ramifications) finds a global equilibrium condition in the adoption of a more regular and spherical shape.

13.2 FLEXIBILITY AND BACK-FOLDING OF VIOLOGEN-PHOSPHOROUS DENDRIMERS

From the average radial monomer density $\rho(r)$ (Equation 11.7 on page 67) plots reported in Figure 13.4 we can have an idea of the flexibility and space-filling of this family of dendrimers. In figure are reported the plots for the trihydrazidophosphine-core group of dendrimer, but the observations hold for the cyclotriphosphazene-core dendrimers. The first two plots are very similar, and represent the behavior of two generation 0 dendrimers. Here we see that the terminal residues are at an higher distance from the center of mass (COM) of the dendrimer than the external viologen groups, as is expected for an “all-open” conformation. The third plot is rather different, with the curve of the terminal residues more broad and with a peak much earlier than the previous plots. This explains an observation that we made analyzing the MD trajectories for this dendrimers. In higher generation viologen-phosphorus dendrimers, the end-groups can back-fold toward the dendrimer core. Obviously, the presence of a substantial back-folding can be detrimental to ligand binding, and can hinder the synthesis of higher generation dendrimers, as less terminal groups are available on the dendrimer surface.

13.3 DENDRIMER BINDING WITH HUMAN SERUM ALBUMIN

One of the most abundant proteins in the bloodstream is human serum albumin (HSA), so it’s important to study the interaction of a new molecule with this protein. Is is shown that viologen-phosphorus dendrimers can perturb biological membranes[144], and their interaction with HSA can have a protective role to this aspect. To describe the binding of the

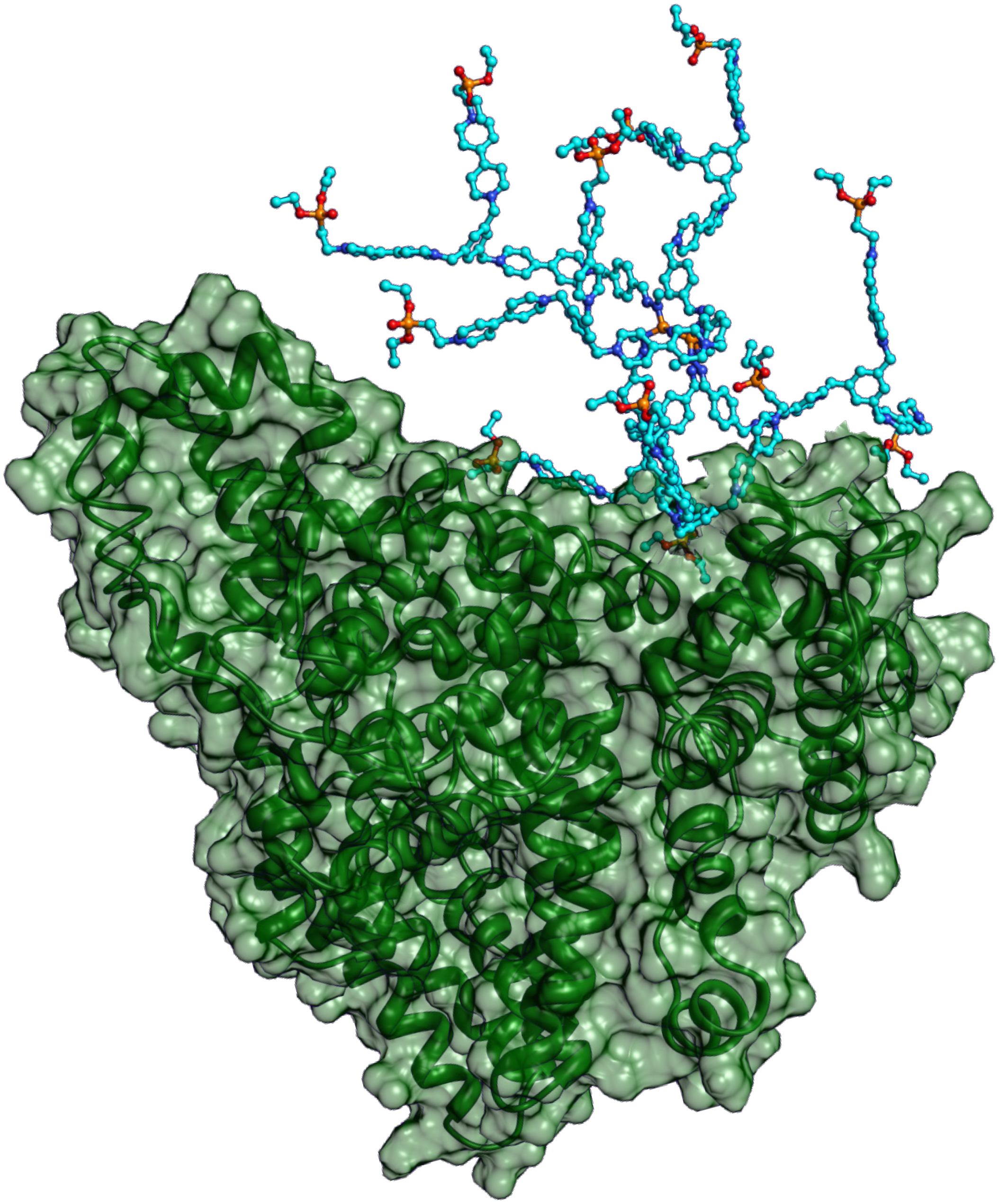

Figure 13.5: Equilibrated MD snapshot of **D6** in complex with HSA.

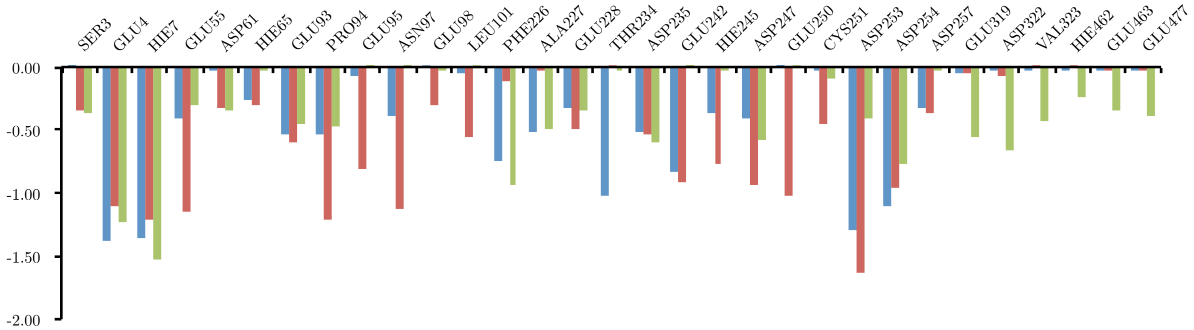

Figure 13.6: Per-residue decomposition of the ΔG_{bind} for viologen-phosphorus dendrimers **D3** (blue), **D5** (red) and **D7** (green).

viologen-phosphorus dendrimer studied with HSA, we used the effective free energy of binding $\Delta G_{bind,eff}$, that is the contribution to binding yielded by the dendrimer branches in constant and productive contact with the protein.

Observing the per-residue decomposition of the ΔG_{bind} (Figure 13.6) and the equilibrated MD snapshots in Figure 13.7, we see that at higher generation the number of interactions with HSA is only slightly increased, while the strength of the interactions is weaker than what's observed for generation 0 dendrimers.

13.4 Conclusions

With MD simulations we gave a morphological descriptions if this new family of viologen-phosphorus dendrimers. We observed that these dendrimers have a spherical shape, and we found that at higher generations the end-residues of these dendrimers tend to back-fold toward the dendrimer core, making them less available on the dendrimer surface for binding and further synthesis.

Studying the interactions between these dendrimers and HSA, that has an important role for lowering the side-effects of these molecules, we showed that increasing the generation of the dendrimer the interactions with HSA are weaker, lowering its protective effects.

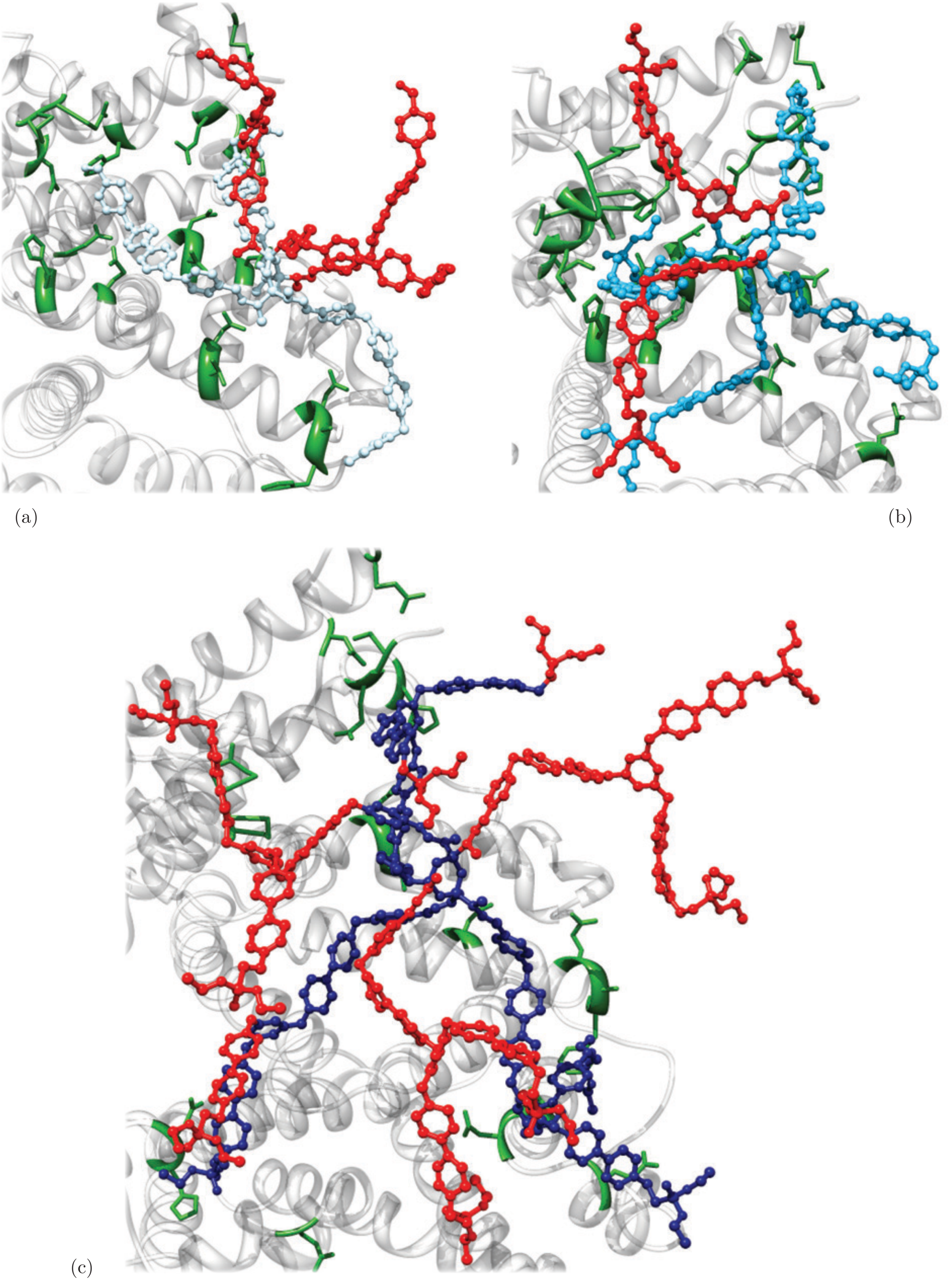
(a)

(b)

(c)

Figure 13.7: Equilibrated MD snapshots of **D3** (a), **D5** (b), **D7** (c) in complex with HSA. In red are depicted the dendrimer's residues not involved in the binding, while in green are depicted the protein's residues involved in the binding.

14

CATIONIC CARBOSILANE DENDRIMERS AND OLIGONUCLEOTIDE BINDING: AN ENERGETIC AFFAIR[1]

Cationic carbosilane dendrimers of generation 2 are shown to have low toxicity profiles and are able to internalize genetic material. In the work reported in this chapter, I performed a complete *in silico* structural characterization of a set of 2G carbosilane dendrimers (**1**–**4** in Figure 14.1), followed by a structural and energetical characterization of their interactions with two oligodeoxynucleotides (ODNs). In a dedicated study it was verified that while dendrimers **2**–**4** could effectively bind GEM91 and SREV (two short ODNs developed as antisense antivirals in HIV-1 treatment), dendrimer **1** showed a lower affinity for the nucleic acids (NAs) with respect to the other dendrimers studied (precisely, affinity was shown to decrease in the order $4 \geq 3 > 2 \gg 1$).[148] Moreover, it was shown that the affinity of these dendrimers is higher for the ODN GEM91 in respect to what was observed for the ODN SREV.

The simulations performed predict that all the four dendrimers and their corresponding complexes with the two ODNs are characterized by similar size and shape. The molecule-

---

[1] The matherial presented in this chapter was published at: Marson, D., Laurini, E., Posocco, P., Fermeglia, M., Pricl, S. (2014). Nanoscale. doi:10.1039/c4nr04510f

	N	R_g	δ	SASA
1	361	9.07 ± 0.21	0.0126	1910 ± 87
2	489	10.39 ± 0.13	0.0096	2699 ± 76
3	449	9.92 ± 0.28	0.0174	2288 ± 82
4	481	10.62 ± 0.25	0.0103	2555 ± 72

Table 14.1: Number of atoms N [–], radius of gyration R_g [Å], asphericity δ [–], and SASA [$Å^2$] of dendrimers **1**–**4**.

specific ODN binding ability can be rationalized considering a critical molecular design parameter: the normalized effective binding energy $\Delta G_{bind,eff}/N_{eff}$. This parameter assess performance of each active individual dendrimer branch, directly involved in a binding interaction.

14.1 STRUCTURAL ASPECTS OF G2 CARBOSILANE DENDRIMERS 1–4

To characterize the structure and properties of these dendrimers, we have selected the following quantities: (i) radius of gyration R_g, Equation 11.2 on page 66; (ii) solvent accessible surface area (SASA); (iii) shape tensor $\boldsymbol{S}$, Equation 11.3 on page 66; (iv) molecular asphericity δ, Equation 11.4 on page 66; and (v) monomer density distribution $\rho(r)$, Equation 11.7 on page 67.

Table 14.1 lists the values of R_g obtained from equilibrated molecular dynamics (MD) trajectories of **1**–**4** in water at 0.15 mM NaCl. As we see, dendrimers **1** and **3**, both characterized by 8 positive charges on their surface (Figure 14.1), have similar values of R_g (9.07 and 9.92 Å, Table 14.1). As somewhat expected, the two other dendrimers **2** and **4** bearing 16 positive charges on their scaffolds have larger dimensions with respect to their less charged counterparts (10.39 and 10.62 Å, Table 14.1). Interestingly, however, the different molecular architecture of **2** and **4** (containing eight groups of single and doubly methylated outer fragments, respectively, Figure 14.1) does not result in a significant difference in their R_g values.

Considering one of the most popular dendrimers family, the ethylenediamine-core (EDA) poly(amidoamine) (PAMAM) dendrimers, as a proof-of-concept for comparison it is interesting to observe that the literature R_g values for the G1-PAMAM, with 8 positively charged terminal groups at pH 7.4, fall in the interval 7.5–9.9 Å, while those for the G2-PAMAM, with 16 charged terminal groups at physiological pH range from 9.2 to 13.6 Å.[149, 150] Notwithstanding the well-known literature controversy about R_g values for PAMAM dendrimers, we are tempted to observe that, on average, the calculated R_g values of all G2 carbosilane den-

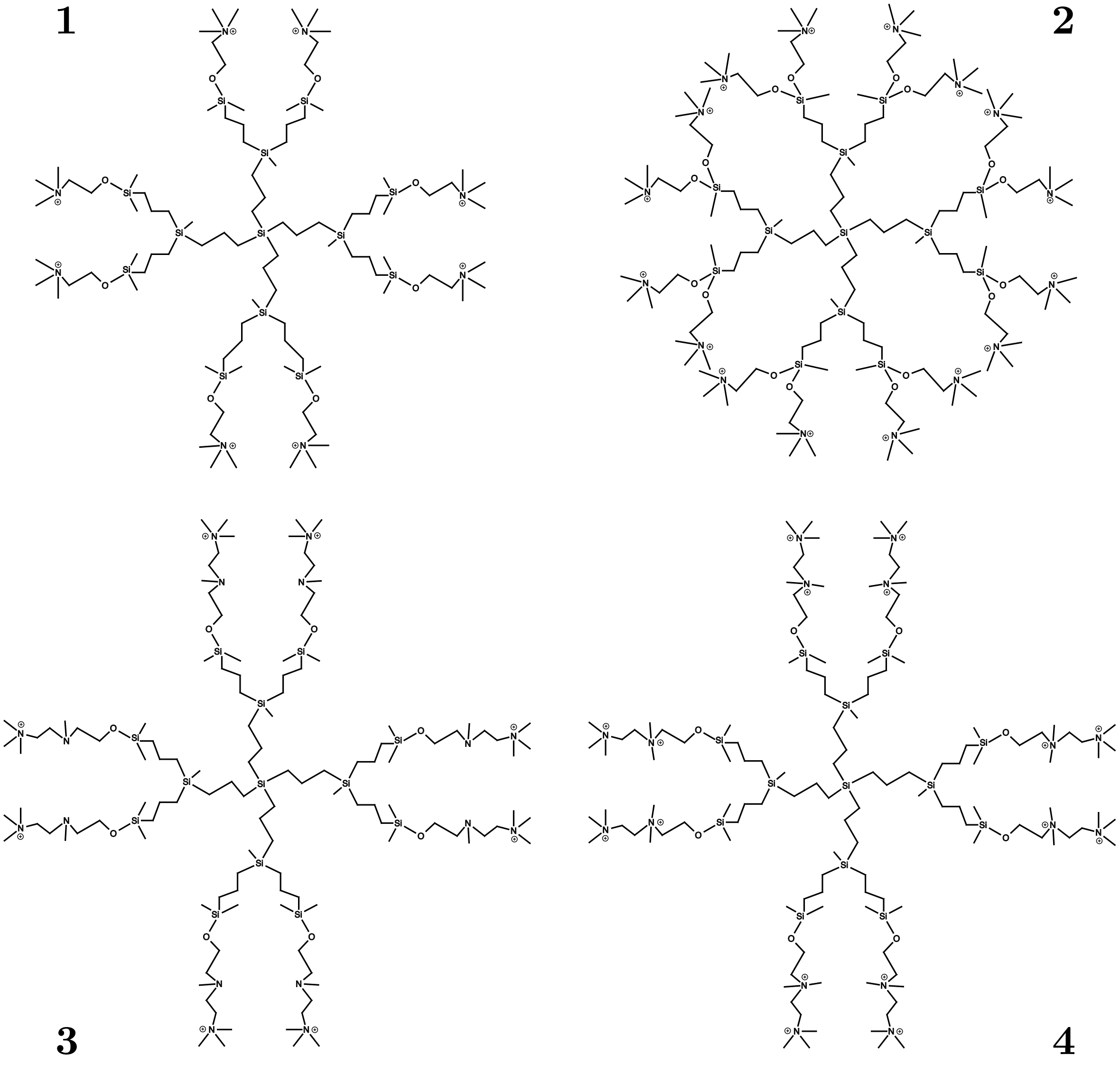

Figure 14.1: Structure of the G2 carbosilane dendrimers **1**–**4**.

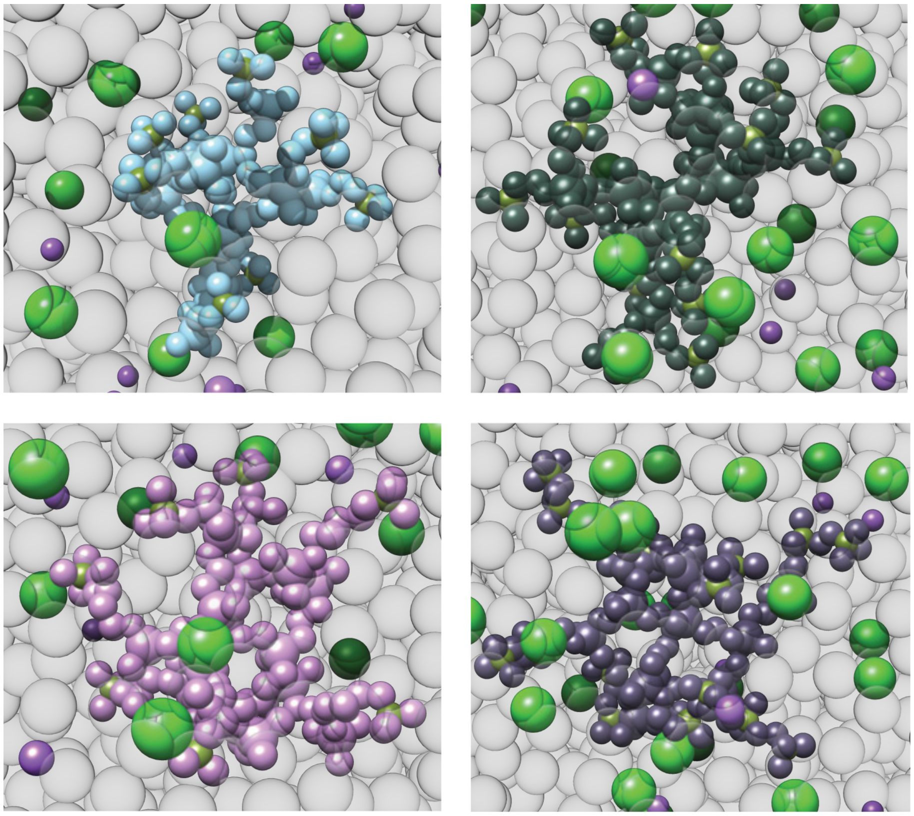

Figure 14.2: Zoomed view of equilibrated MD snapshots of G2 carbosilane dendrimers **1** (top left), **2** (top right), **3** (bottom left), and **4** (bottom right). In all panels, the dendrimers are shown as colored sticks (**1**, light blue; **2**, dark sea green, **3**, plum; **4**, dark lavender), water is portrayed as light gray transparent spheres, and some Na^+ and Cl^- ions are depicted as purple and green spheres, respectively. Hydrogen atoms are omitted for clarity.

drimers **1**–**4** fall in an intermediate range of dimensions between G1- and G2-PAMAMs. The comparison between G2 carbosilanes **2** and **4**, and the G2-PAMAM is straightforward: both G2 dendrimer families feature 16 positive charges in their outer shell and are characterized by similar values of atom numbers (N) and SASA. Indeed, N = 489, 481, and 532 and SASA = 2699, 2555, and 2333 Å^2 for **2**, **4**, and G2-PAMAM, respectively (Table 14.1 and ref. 149, 150). The results for the carbosilane dendrimers **1** and **3** can be rationalized by considering that these two molecules do bear the same charge of G1-PAMAM (+8) but, being a generation 2, they are also characterized by a number of atoms and, accordingly, a solvent accessible surface area quite larger than those pertaining to G1-PAMAM. In fact, while N = 361 and 489 for **1** and **3**, respectively (Table 14.1), the N value for a EDA-core G1 PAMAM is 236; in line with this, the calculated SASA for G1 PAMAM is quite smaller (1341 Å^2)[149, 150] than the corresponding SASA values obtained for **1** and **3** (1910 and 2288 Å^2, Table 14.1). This evidence supports the fact that the R_g values of **1** and **3** lie in the upper limit of the G1-PAMAM interval.

Figure 14.3: Moment of inertia-based aspect ratios (left) and asphericity parameter δ (right) for the G2 carbosilane dendrimers **1**–**4** generated from the corresponding equilibrated MD trajectories.

Concerning the shape of G2 carbosilane dendrimers **1**–**4**, the first, qualitative clue is provided by Figure 14.2, showing snapshots extracted from the corresponding equilibrated MD trajectories. From these images we see that, at variance with the reference G2 PAMAMs that are characterized by a highly asymmetrical conformation,[149, 150] all **1**–**4** molecules are characterized by a symmetrical, nearly spherical shape. A quantitative support to this qualitative assertion is afforded by the shape tensor $\boldsymbol{S}$.

Figure 14.3 shows the moment of inertia-based molecular aspect ratios and the asphericity parameter δ for the G2 carbosilane dendrimers **1**–**4** as obtained from the corresponding equilibrated MD trajectories. We see that for all dendrimers both aspect ratios I_z/I_x and I_z/I_y are in the range 1.0–1.7, indicating that these molecules are strongly compact spheroids independent of their charge (+8/+16). In keeping with this, the asphericity parameter δ values are all quite small and close to zero (Figure 14.3 and Table 14.1 for numerical values), confirming the spherical character of these dendrimer conformations.

At variance with EDA-core PAMAMs, for which lower generation molecules (G1–G3) tend to assume highly asymmetrical shapes whereas higher generations (G5–G7) become nearly spherical, G4 being a transition between the two forms,[149, 150] the carbosilane dendrimers **1**–**4** already attain a spherical distribution of mass at G2. Aside from eventual small differences in their branch flexibility and/or hydrophilicity, this difference can be essentially attributed to the geometry of the core. Indeed, we know that the size, shape, and initiator-core multiplicity N_c exert a dramatic influence on the ultimate critical molecular design parameters (CMDPs)[151] of a dendrimer. Thus, although for both dendrimer families $N_c = 4$, the initiator-core for the G2 carbosilane dendrimers consists of a single, Si atom from which the four branches emanate directly and radially in space. In contrast, in the case of the EDA-based PAMAMs the core consists of a small, flexible, four atom-long chain, to which the dendrons are tethered and extend from its extremes. As the initiator-core is a dendrimer

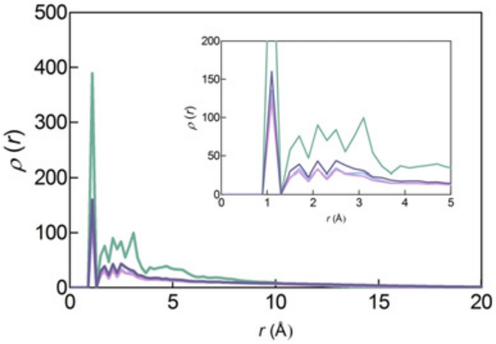

Figure 14.4: Monomer density distribution $\rho(r)$ for the G2 carbosilane dendrimers **1**–**4**. Color legend: **1**, light blue; **2**, dark sea green; **3**, plum; **4**, dark lavender.

primary template, these differences are transcribed and displayed through the dendrimer development; thus, the carbosilane dendrimers **1**–**4** are already spherical at lower generations while higher generation numbers are required for EDA-core PAMAMs to fold into a sphere.

Figure 14.4 shows the overall monomer density distribution ($\rho(r)$) for the G2 carbosilane dendrimers **1**–**4**, calculated taking the origin as the center of mass (COM) of the dendrimer. As we see, all dendrimers are characterized by almost superimposable profiles indicative of a rather uniform space filling: the curves spike at small R, and then almost monotonically decrease, the width of the tail zone being again very similar for all four dendrimers. This is a further confirmation of the fact that the same branching pattern and, above all, the presence of a tetravalent Si atom as the common initiator-core for these G2 carbosilane dendrimers dictate the overall, similar conformation of these molecules.

14.2 Complexation of G2 carbosilane dendrimers with ODNs

Given the similarities in size and shape shared by G2 carbosilanes **1**–**4**, in order to explain the difference in binding affinities of the four dendrimers for the two ODN sequences GEM91 and SREV we went on and performed MD simulations of the relevant complexes. At variance with other studies reported in the literature, in this work we adopted an alternative approach based on a combination of steered molecular dynamic (SMD) and classical MD experiments to determine the initial geometries of each dendrimer/ODN complex. Specifically, starting from a common initial configuration, each dendrimer was guided towards three different regions of the ODN (i.e., the two ends and the center of the ODN sequence) by SMD simulations and, once a distance of approximately 12 Å was achieved, each configuration was allowed to evolve to equilibrium by classical MD simulation runs. Figure 14.5 illustrated this procedure taking dendrimer **4** and the ODN GEM91 as examples. As can be seen from the images in Figure 14.5, independently of the initial binding region the ODN is completely wrapped around the dendrimer and the resulting complexes become virtually indistinguishable at the end of each combined MD process. Analogous results were obtained with all dendrimers and

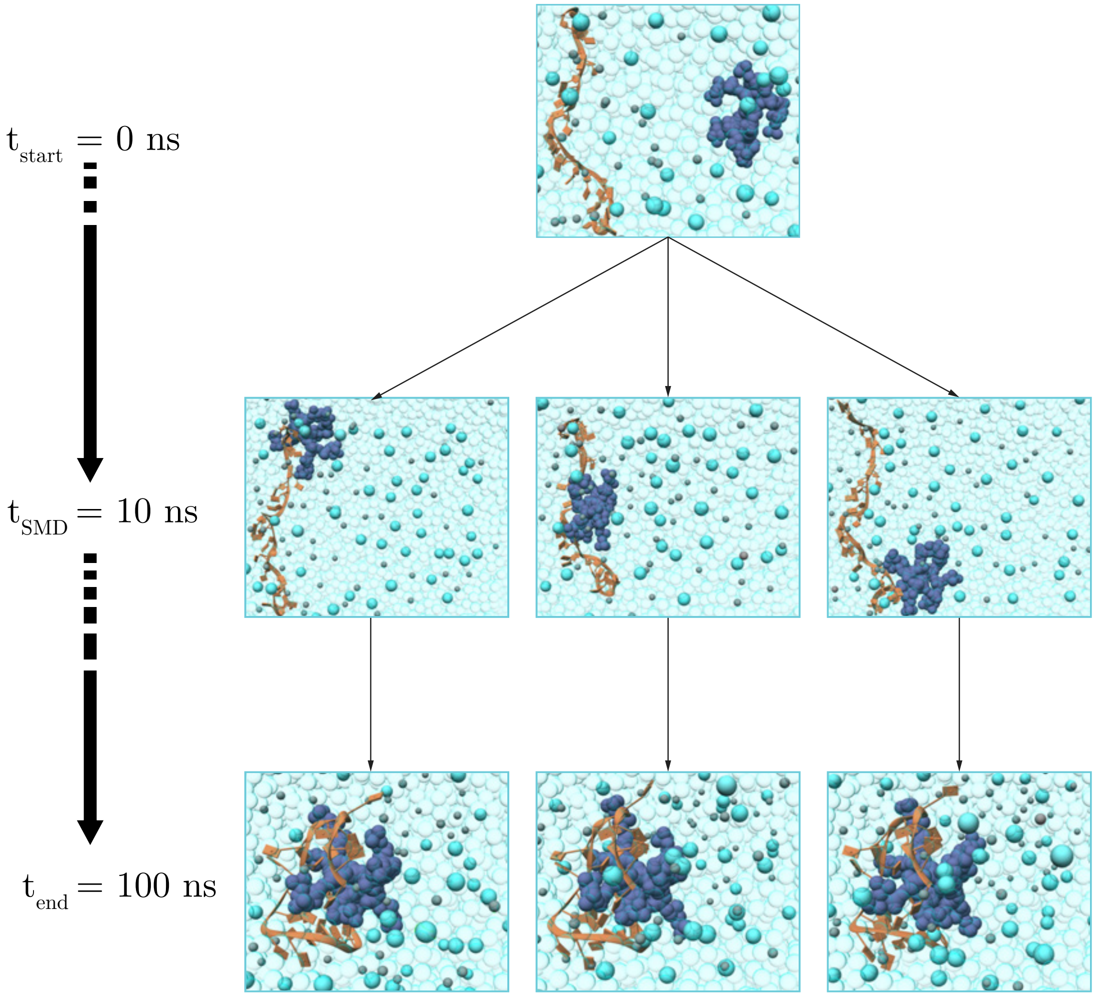

Figure 14.5: Coupling SMD and classical MD simulations to mimic the binding process of dendrimer **4** to the ODN GEM91. The dendrimer is portrayed as dark lavender spheres while the ODN strand is represented as an orange ribbon. Water and oxygen atoms are shown as transparent aqua spheres, whereas some Na^+ and Cl^- ions are portrayed as gray and cyan spheres, respectively.

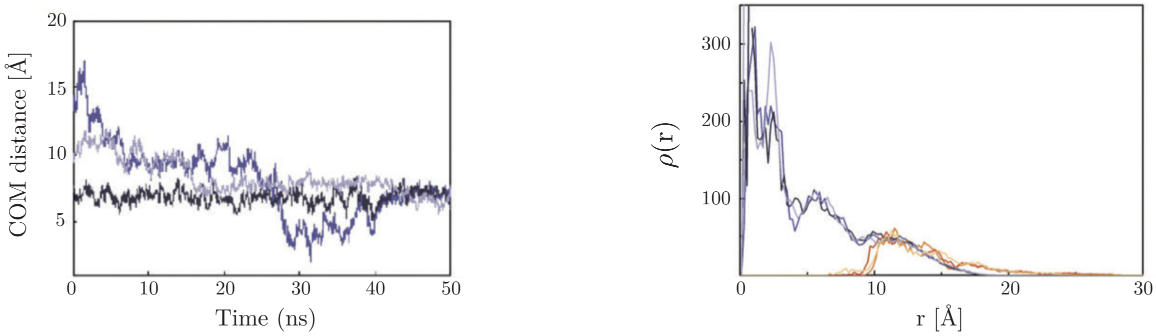

Figure 14.6: (left) COM distance between dendrimer **4** and the ODN GEM91 as a function of time for the three, different initial binding positions: light and medium lavender, dendrimer initially bound by SMD at the ends of the ODN strand; dark lavender, dendrimer initially bound by SMD in the middle of the ODN sequence. (right) Radial monomer distribution of dendrimer **4** and GEM91 of the three final, equilibrated complex structures. Color legend: light lavender (**4**)/light orange (ODN) and medium lavender (**4**)/medium orange (ODN): MD equilibrated configuration obtained from the dendrimer initially bound by SMD at the ends of the ODN strand; dark lavender (**4**)/dark orange (ODN): MD equilibrated configuration obtained from the dendrimer initially bound by SMD in the middle of the ODN strand.

with both ODN sequences.

To quantitatively substantiate the equivalence of the three final structures, we compared the distance between the dendrimer/ODN COM and the radial monomer distributions $\rho(r)$ of the corresponding complexes, as illustrated in Figure 14.6 taking again the complex between **4** and GEM91 as an example. The left panel in Figure 14.6 shows that, when the dendrimer/ODN binding process is started from a configuration where, at the end of the SMD part, the dendrimer docks into the center of the nucleic acid single strand, a very short time is required for the ODNs to wrap around the dendrimers; accordingly, the COM distance of the relevant complexes readily reach their equilibrium value (7 Å on average, Figure 14.6). When the dendrimers bind to either end of the ODN sequences, the nucleic acid needs to overcome larger energetic and entropic barriers in order to fold before it can find its wrapping around the dendrimer surface.

This more complex folding pathway clearly requires longer times, but in the end the COM distances between dendrimers and ODNs do converge to the same equilibrium value (Figure 14.6). Also, rather importantly, the degree of ODN strand/dendrimer compenetration, defined as the integral of the area shared by the dendrimer and ODN $\rho(r)$ curves (see the right panel of Figure 14.6), is very similar in the three cases of Figure 14.5, being equal to 72.1 %, 75.5 %, and 72.9 %, respectively.

Conclusive proof of the equivalence of the dendrimer/ODN final complex structures pro-

	GEM91					SREV			
	R_g	δ	INT	N_c		R_g	δ	INT	N_c
1	9.16 ± 0.11	0.0128	233 ± 32	6.1 ± 0.2	**1**	9.13 ± 0.12	0.0150	194 ± 29	5.7 ± 0.3
2	10.46 ± 0.12	0.0099	709 ± 46	9.7 ± 0.2	**2**	10.42 ± 0.10	0.0102	515 ± 38	7.9 ± 0.2
3	9.99 ± 0.10	0.0185	1723 ± 53	15.2 ± 0.3	**3**	9.87 ± 0.11	0.0188	1762 ± 51	15.5 ± 0.4
4	10.71 ± 0.11	0.0107	1953 ± 62	17.2 ± 0.3	**4**	10.70 ± 0.11	0.0108	1878 ± 66	15.5 ± 0.3

Table 14.2: Radius of gyration R_g [Å], asphericity δ [–], interface area between the dendrimer and ODN INT [Å^2], and the average number of contacts between the dendrimer positively charged nitrogen atoms and the ODN negatively charged oxygen atoms Nc [–] for dendrimers **1**–**4** in complex with GEM91 and SREV ODNs.

duced by the combined SMD/MD approach can be found in the corresponding values of the free energy of binding ΔG_{bind}, as calculated via the Molecular Mechanics/Poisson Boltzmann Surface Area (MM/PBSA) ansatz. Referring again to the GEM91/**4** assembly as an example , the ΔG_{bind} values calculated for the two equilibrated complex structures having the dendrimer initial position at one extreme of the ODN strand (e.g., the bottom panel in Figure 14.5, right and left images) are $(-53.4 \pm 4.6)\,\mathrm{kcal\,mol^{-1}}$ and $(-53.3 \pm 5.1)\,\mathrm{kcal\,mol^{-1}}$, respectively, while for the complex originating from the assembly featuring the dendrimer centrally with respect to the ODN strand (bottom panel, central in Figure 14.5 central image) ΔG_{bind} is $(-34.9 \pm 5.0)\,\mathrm{kcal\,mol^{-1}}$. It is evident that, also from an energetic standpoint, the three structures are indeed comparable, the difference in the affinity between the dendrimer and ODN being within the relevant ΔG_{bind} standard deviation intervals. Of note, utterly similar results are obtained for all other dendrimers, both in complex with GEM91 and SREV.

Given the structural equivalence of the three, final equilibrated structures of each dendrimer/ODN complex, all the remaining discussions will be focused on one single structure only, i.e. the one generated from SMD experiments placing the dendrimer central to the nucleic acid strand.

14.3 Structural aspects of the complexes

Figure 14.7 offers a zoomed view of the equilibrated structures of each SREV/dendrimer conformation.

From these images we can observe how, independently of the positive charge content of the dendrimers, the ODN not only wraps around them but we also see a significant compenetration of the two molecular entities. To quantify this pictorial evidence, Table 14.2 lists the values of some important structural parameters extracted from the analysis of the

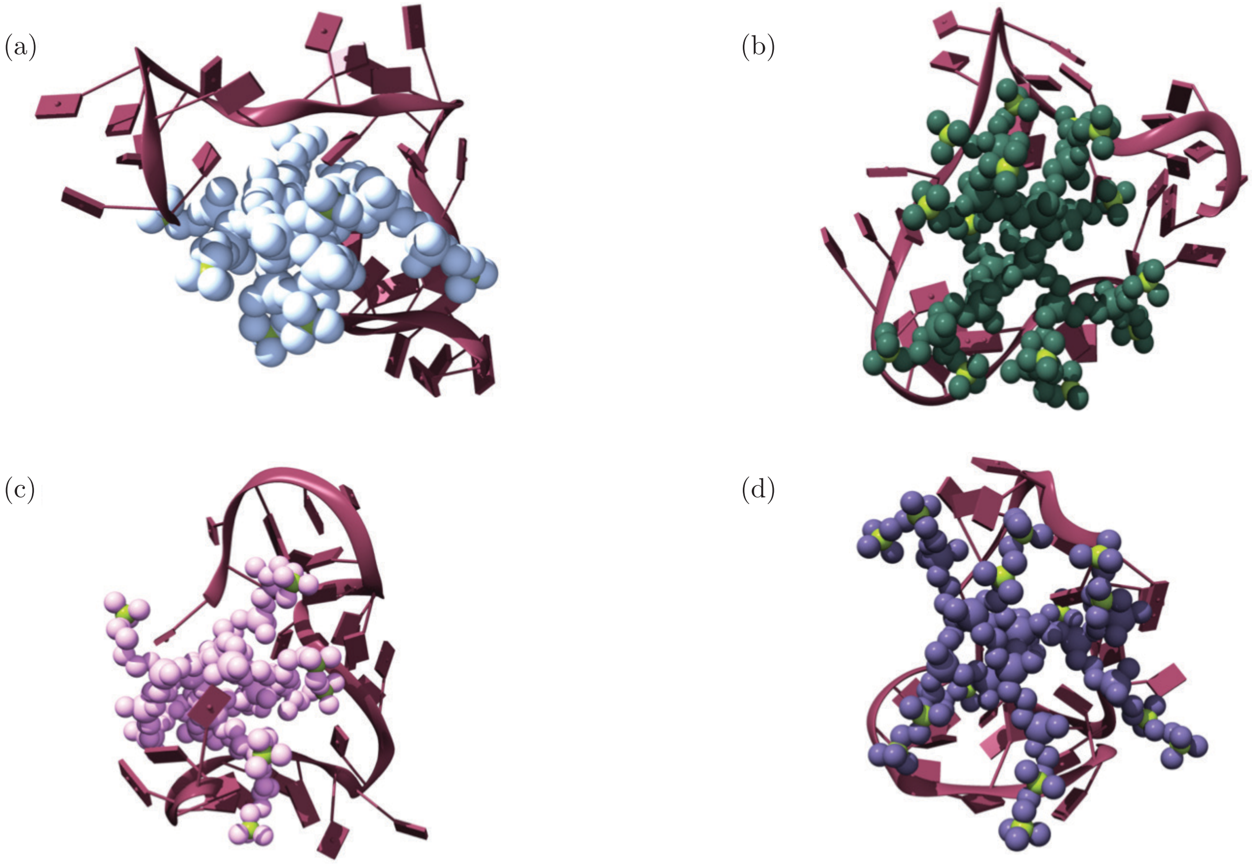

Figure 14.7: Equilibrated MD snapshots of dendrimers **1**–**4** in complex with the ODN SREV. Dendrimers **1** (a), **2** (b), **3** (c), and **4** (d) are depicted as light sky blue, dark sea green, plum, and dark lavender sticks and balls, respectively, with terminally charged amine groups highlighted in green. The SREV sequence is portrayed as an red grape ribbon. Water and ions are omitted for clarity.

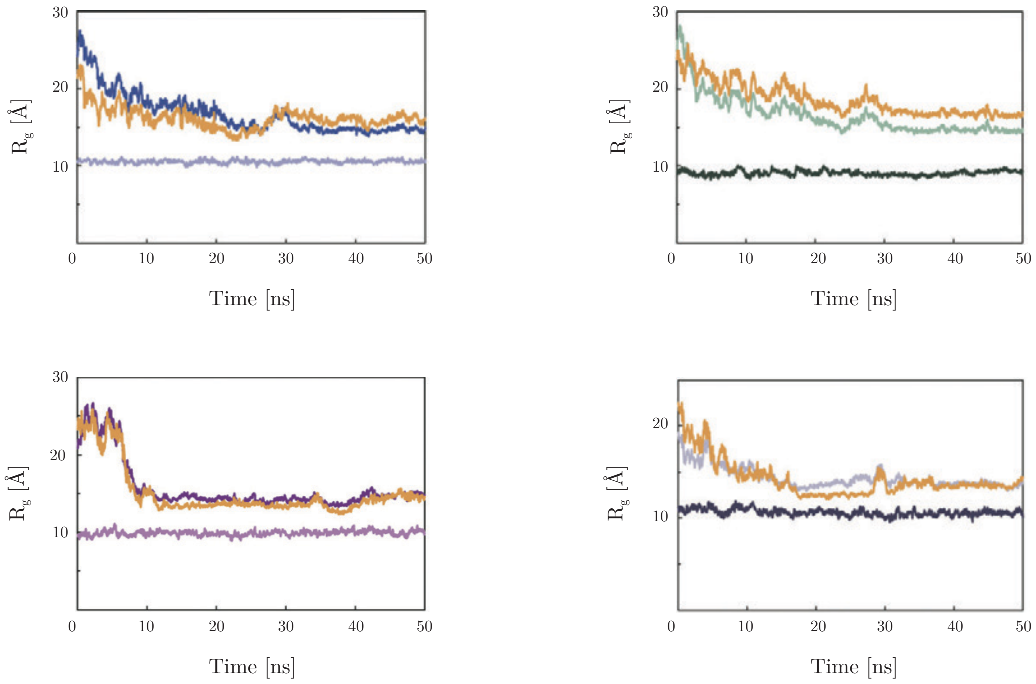

Figure 14.8: Evolution of the radius of gyration R_g of the ODN GEM91, the dendrimers **1**–**4**, and the relevant complexes showing the shape invariance of the dendrimers and the conformational adaptation of the ODN upon binding. (top left) **1**, light blue; ODN GEM91, orange, complex, dark blue; (top right) **2**, dark sea green, ODN GEM91, orange, complex, light sea green; (bottom left) **3**, plum; ODN GEM91, orange; complex, purple; (bottom right) **4**, dark lavender, ODN GEM91 orange, complex, light lavender.

equilibrated MD trajectory of all dendrimer/ODN complexes.

A swift survey of the values shown in Table 14.2 reveals that the G2 carbosilane dendrimers **1**–**4** do not change the size and shape upon binding to the ODNs. Indeed, both R_g and δ values for the dendrimers in the complexes are virtually indistinguishable from those of the dendrimers alone (Table 14.1 and Table 14.2). In line with this, Figure 14.8 shows the time evolution of the radius of gyration R_g of the ODN GEM91 in complex with dendrimers **1**–**4** as an example.

However, some differences between the dendrimer complexes with GEM91 and those involving SREV begin to appear. First, the values of the dendrimer/ODN interface areas (INTs) within the complexes (Table 14.2) are different between the 40 different dendrimers and, for a given dendrimer, between GEM91 and SREV. Specifically, for both ODNs INT monotonically increases in passing from **1** to **4**, although the difference in INTs values progressively levels off between dendrimers **3** and **4**. Also, the INTs values are lower for all dendrimers in complex with SREV with respect to the GEM91 complex counterparts (Table 14.2). In keeping with this, also the number of contacts between the positively charged nitrogen atoms on the den-

	GEM91			SREV	
	ODN	Complex		ODN	Complex
1	15.83 ± 0.55	15.44 ± 0.49	**1**	17.28 ± 0.28	15.69 ± 0.21
2	15.57 ± 0.36	15.00 ± 0.27	**2**	16.12 ± 0.23	15.50 ± 0.20
3	13.87 ± 0.25	14.34 ± 0.50	**3**	15.20 ± 0.19	14.44 ± 0.17
4	13.71 ± 0.50	13.98 ± 0.30	**4**	14.95 ± 0.25	14.20 ± 0.20

Table 14.3: Radius of gyration R_g [Å] of the two ODNs GEM91 and SREV wrapped around the dendrimers **1**–**4** and of the relevant complexes.

drimers and the negatively charged oxygen atoms of the ODN phosphate groups Nc follows the same trend: Nc increases from **1** to **4** and is larger (on average) for GEM91 with respect to SREV (Table 14.2). In keeping with these results, the values of R_g for the GEM91/dendrimer complexes are slightly lower than those of the SREV counterparts (Table 14.3), suggesting a smaller degree of penetration and, hence, somewhat weaker interactions between the G2 carbosilane dendrimers and the SREV strand.

Considering the monomer density distribution of the dendrimer/ODN complexes yields further information on the structural features of these supermolecular assemblies. For the purpose of discussion, Figure 14.9 shows these distributions for dendrimer **4** in complex with ODN GEM91.

Upon binding, the curve of the ODN single strand shows the maximum in the location of the dendrimer terminal groups, which roughly corresponds to the radius of gyration of the dendrimers. Also, we distinctly see a substantial penetration of the ODN within the dendrimer structure. However, considering again the degree of compenetration of the ODN strand and the dendrimer, differences among the diverse dendrimers and between the two strands can be detected. In fact, not only this parameter increases in going from dendrimer **1** to dendrimer **4** for a given ODN, but it also slightly decreases in passing from GEM91 to SREV (in the order: 37.6 % (**1**), 55.0 % (**2**), 72.0 % (**3**), and 75.7 % (**4**) for GEM91 and 32.1 % (**1**), 47.5 % (**2**), 65.2 % (**3**), and 73.7 % (**4**) for SREV, respectively). These pieces of evidence could be taken as the first, rough indication that the interactions of the dendrimers with a given ODN decrease in the order $\mathbf{4} \geq \mathbf{3} > \mathbf{2} > \mathbf{1}$ and that, for a given dendrimer, more favorable interactions characterize the complex with the ODN GEM91 than the assembly with ODN SREV.

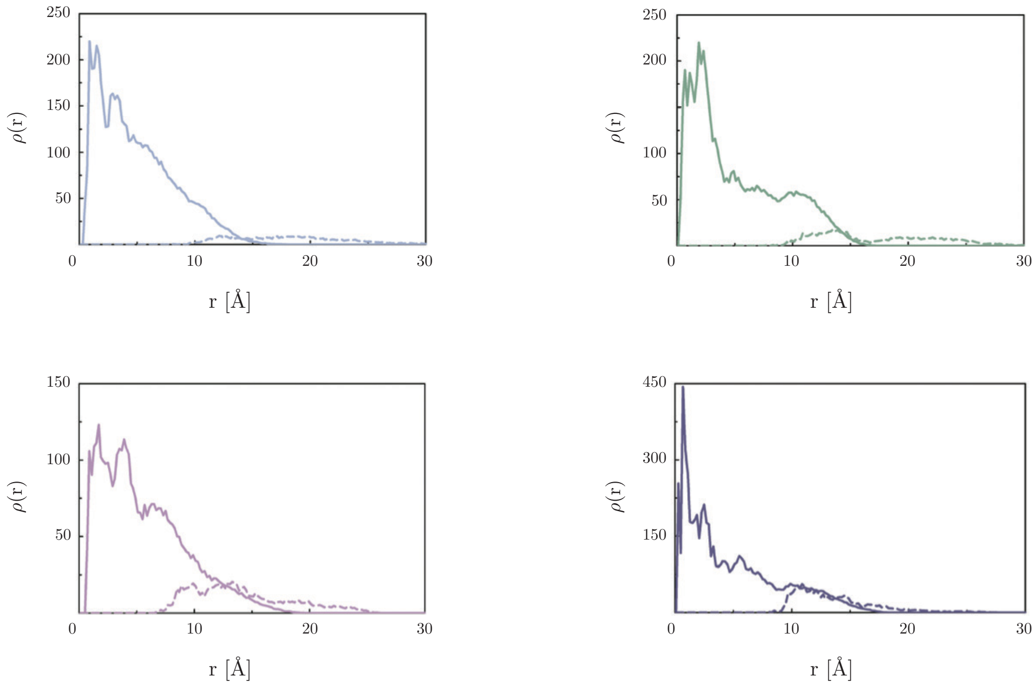

Figure 14.9: Density distribution $\rho(r)$ for the dendrimers **1**–**4** and the ODN GEM91 in the relevant complexes. Top left, **1**; top right, **2**; bottom left, **3**; bottom right **4**. Dendrimer and ODN curves are represented by continuous and broken lines, respectively.

14.4 Energetical aspects of ODN/dendrimer binding

To substantiate these seemingly different binding interactions among the G2 carbosilane dendrimers **1**–**4** and the two single strand nucleotide sequences GEM91 and SREV, we next processed the data collected during equilibrated MD simulations of the single molecular species and the relevant complexes in the framework of the MM/PBSA theory. Specifically, we assessed the effective free energy of binding $\Delta G_{bind,eff}$, that is the contribution to binding yielded by the dendrimer branches in constant and productive contact with the nucleic acid fragment, as shown in Table 14.4. To estimate $\Delta G_{bind,eff}$ for each dendrimer/ODN complex, all branches of dendrimers **1**–**4** involved in ODN binding (N_{eff}, Table 14.4) were precisely identified (see Figure 14.1) and their individual contribution towards the overall binding energy estimated via a per residue deconvolution of the binding free energy. The first, interesting finding of this analysis concerns a number of dendrimer branches efficiently involved in binding the two ODNs. Indeed, in both ODN complexes the G2 carbosilane dendrimer **1** has the smallest number of branches in contact with the nucleic acid ($N_{eff} = 6$), while the remaining three dendrimers have more branches (8/9, Table 14.4) effectively involved in ODN binding. Contextually, $\Delta G_{bind,eff}$ is larger (i.e., more negative and, hence, more favorable)

	GEM91				SREV		
	N_{eff}	$\Delta G_{bind,eff}$	$\Delta G_{bind,eff}/N_{eff}$		N_{eff}	$\Delta G_{bind,eff}$	$\Delta G_{bind,eff}/N_{eff}$
1	6	-11.9 ± 1.4	-2.0 ± 0.2	**1**	6	-11.3 ± 0.8	-1.9 ± 0.1
2	9	-23.9 ± 2.1	-2.7 ± 0.2	**2**	9	-22.0 ± 2.0	-2.4 ± 0.2
3	8	-34.6 ± 2.9	-4.3 ± 0.4	**3**	8	-32.2 ± 4.2	-4.0 ± 0.5
4	8	-45.9 ± 3.6	-5.7 ± 0.5	**4**	8	-43.1 ± 4.3	-5.4 ± 0.5

Table 14.4: Predicted number of effective dendrimer branches N_{eff} (–), effective free energy of binding $\Delta G_{bind,eff}$ ($\mathrm{kcal\,mol^{-1}}$), and normalized effective free energy of binding $\Delta G_{bind,eff}/N_{eff}$ ($\mathrm{kcal\,mol^{-1}}$) for dendrimers **1**–**4** in complex with the two ODN sequences GEM91 and SREV.

	GEM91				SREV		
	Salt bridge	H-bond	π-cation		Salt bridge	H-bond	π-cation
1	6	-	-	**1**	6	-	-
2	9	-	-	**2**	9	-	-
3	8	8	-	**3**	8	8	-
4	8	3	5	**4**	8	4	4

Table 14.5: The type and number of intermolecular interactions between dendrimers **1**–**4** and the two ODN sequences GEM91 and SREV as detected in the corresponding equilibrated MD trajectories

for dendrimers **2**–**4** with respect to dendrimer **1**, in both series of complexes (Table 14.4). Normalizing $\Delta G_{bind,eff}$ by N_{eff} yields the performance of the different dendrimers in using each active individual branch directly involved in a binding interaction ($\Delta G_{bind,eff}/N_{eff}$, Table 14.4). As we see, $\Delta G_{bind,eff}/N_{eff}$ increases substantially in passing from dendrimer **1** to dendrimer **4** for both ODN complexes, the difference between dendrimers leveling off between dendrimers **3** and **4**. Also, from data in Table 14.1 a small efficiency in binding GEM91 with respect to SREV can be envisaged.

The differential efficacy in binding the ODNs shown by the four G2 carbosilane dendrimers finds its molecular roots in the diverse number and type of interaction each dendrimer branch is able to establish with the nucleic acid. As shown in Table 14.5, independently of their structural details and their charge, all dendrimers exploit a conspicuous number of salt bridges between the terminal, positively charged nitrogen of the dendrimer atoms and the negatively charged oxygens of the ODN phosphate groups (see, for instance, Figure 14.10(a, b)).

However, the presence of a second N atom in the dendrimer branches as in dendrimers **3** and **4** allows for further intermolecular interactions, the nature and number of which depend

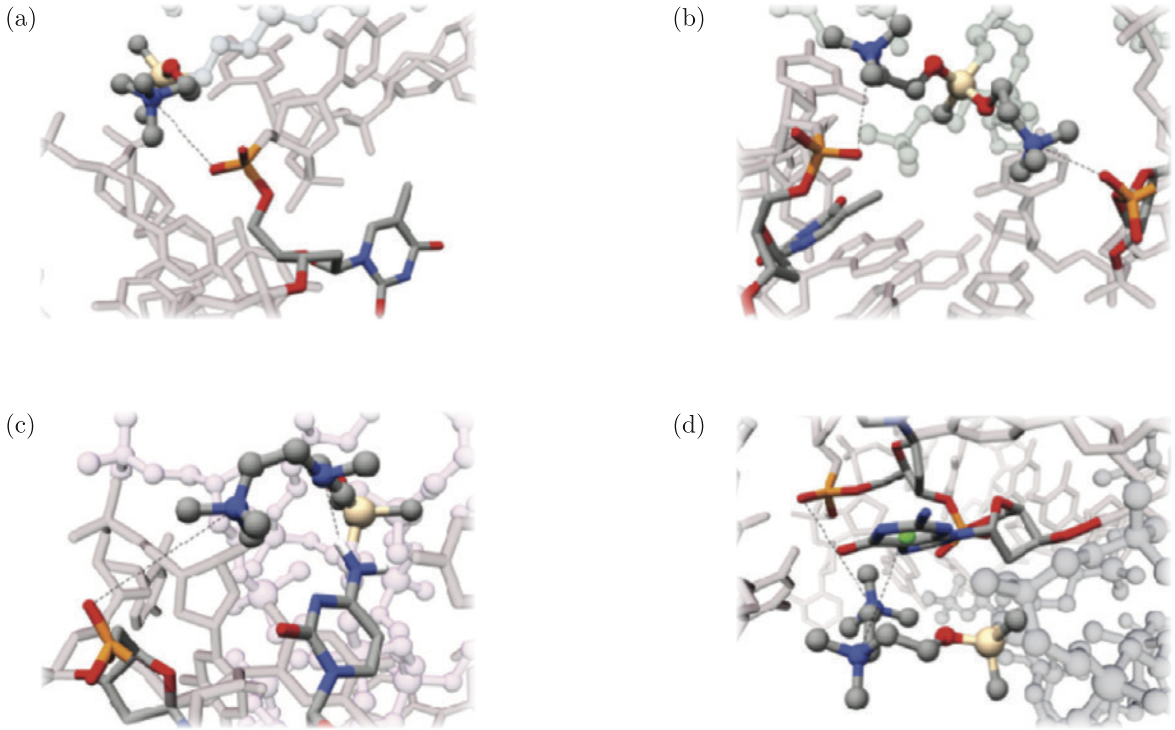

Figure 14.10: Zoomed view of the different intermolecular interactions between the G2 carbosilane dendrimers **1**–**4** and the ODN GEM91, as detected in the equilibrate portion of the corresponding MD trajectories. Dendrimers **1** (a), **2** (b), **3** (c), and **4** (d) are depicted as transparent sticks and balls, the terminal residues involved in ODN binding colored by the element. The GEM91 strand is portrayed as transparent sticks. Each non-covalent interaction (salt-bridges, H-bonds, and π-cation interactions) is highlighted by a dotted black line. Water and ions are omitted for clarity.

on that atom being electrically neutral (**3**) or positively charged (**4**). Indeed, a number of H-bonds are generated within each ODN/dendrimer complex in the case of **3** (Table 14.5 and Figure 14.10c), which justifies the higher efficacy of these dendrimer branches in ODN binding and, consequently, the greater stabilization of the relevant complex with respect to those made from **1** and **2** (Table 14.4). When this N atom bears a neat, positive charge as in **4**, beside the salt-bridges and some H-bonds, we detect the establishment of a number of permanent π-cation interactions involving this quaternary nitrogen and the aromatic rings of the nucleic bases, as shown in Figure 14.10d. These interactions are quite strong and, hence, contribute to the higher efficiency of per residue (as well as overall) ODN affinity of G2 carbosilane dendrimer **4**.

The free energy analysis described above allows for several, further comments. First, the different lengths of the dendrimer branches between molecules **1** and **3** reflect in a considerably higher efficiency of the latter dendrimer to bind both ODNs: thus, $\Delta G_{bind,eff}/N_{eff} = -2.0$ and $-1.9\,\mathrm{kcal\,mol^{-1}}$ for **1** in complex with GEM91 and SREV while $\Delta G_{bind,eff}/N_{eff} = -4.3$ and $-4.0\,\mathrm{kcal\,mol^{-1}}$ for **3** bound to the same two nucleotide sequences, respectively (Table 14.4). At the same time, doubling the number of branching, and hence the number of positive charges, in passing from **1** to **2** reflects only in a modest, although not negligible, increase in ODN affinity. That is to say, the architecture of the dendrimer branches rather than the dendrimer overall charge seems to be a fundamental parameter for effective ODN binding in this series of G2 carbosilane dendrimers. Comparing now the performance of dendrimers **2** and **4**, both with the overall charge +16, highlights the importance of another molecular architecture parameter, that is the location of the charges within the molecular structure. In fact, according to the present calculations, having two positive charges on the same branch as in **4** (Figure 14.1) is far more efficient as concerns ODN binding than having two positive charges on two vicinal branches, as in **2** (Figure 14.1). Indeed, the architecture of dendrimer **4** allows, aside from the ever-present salt bridges, the realization of other intermolecular dendrimer/ODN contacts such as H-bonds and π-cation interactions (Table 14.5) within the supermolecular complex. These, in turn, make dendrimer **4** not only dramatically more effective in binding the ODNs with respect to dendrimer **2** ($\Delta G_{bind,eff}/N_{eff} = -2.7$ and $-2.4\,\mathrm{kcal\,mol^{-1}}$ for **2** in complex with GEM91 and SREV while $\Delta G_{bind,eff}/N_{eff} = -5.7$ and $-5.4\,\mathrm{kcal\,mol^{-1}}$ for **4** in complex with the same ODNs, Table 14.4), but also make this molecule the best binder of the entire series. Lastly, it is instructive to compare dendrimers **3** and **4**. Indeed, these two molecules present the same molecular architecture but they differ by the number of positive charges (+8 and +16, respectively). Thus, while the tertiary nitrogen atoms characterizing the branches of **3** are involved in a plethora of permanent, stabilizing H-bonds with the nucleic acid bases, making this dendrimer a good ODN binder, the inner quaternary nitrogens of **4** are engaged in several π-cation interactions (Table 14.5), which decidedly enhance the affinity of these dendrimer branches toward the nucleic acid strand ($\Delta G_{bind,eff}/N_{eff} = -4.3$ and $-4.0\,\mathrm{kcal\,mol^{-1}}$ for **3** bound to GEM91 and SREV and $\Delta G_{bind,eff}/N_{eff} = -5.7$ and $-5.4\,\mathrm{kcal\,mol^{-1}}$ for **4** in complex with the same ODNs).

14.5 Conclusions

Insufficient concentrations and very short residence time of the anti-retroviral agents at the cellular and anatomical sites are among the major factors that contribute to the failure of eradicating HIV from reservoirs and the development of multi-drug resistance against antiretroviral agents. Gene therapy offers the promise of preventing progressive HIV infection by sustained interference with viral replication in the absence of chronic chemotherapy. Accordingly, gene-targeting strategies are being developed with RNA-based agents, such as ribozymes, antisense oligonucleotides, and small interfering RNA, just to name a few. Yet, to date, gene therapy targeting HIV-1 has not fulfilled its promises and hopes. Nonetheless, there is considerable motivation to be optimistic about its future for HIV-1 therapeutics as analysis of unsuccessful anti-HIV-1 gene therapy studies is providing fundamental insights for improvements. One of the major reasons of such failure resides in the fact that, to reach the therapeutic goal of gene delivery, the use of nanocarriers able to reach the desired population of cells avoiding all biological barriers is ineluctably required.

It is estimated that several hundreds of different nanovectors are in various stages of pre-clinical and clinical development toward regulatory approval in the USA and worldwide. These nano-sized molecular entities have the primary function of transporting the active agent to the target site, performing the multiple biobarrier-avoidance tasks required along the way. To perform these ambitious tasks, however, nanovectors must be carefully designed and engineered to employ several, concurrent strategies to localize preferentially at the target cells, and release its therapeutic payload.

G2 cationic carbosilane dendrimers **1**–**4** have been shown to hold great potential as gene carriers for HIV-1 treatment both in vitro and in vivo. In particular, the characterization of ODN binding properties of these dendrimers has highlighted a differential affinity for nucleic acid strands notwithstanding a remarkable similarity in structure and overall charge content of the members of this molecular series. Since the detailed knowledge of structure/activity relationships governing the performance of these nano-objects is the ultimate tool for:

- understanding the reasons of their success/failure;
- designing new, more efficient, second generation nanovectors, in this work we aimed

at unraveling a molecular rationale for the different ODN binding capacity of four G2 carbosilane dendrimers.

To the purpose, we performed a thorough *in silico* characterization of the structural and energetical features of G2 carbosilane dendrimers **1**–**4**, and their complexes with the two single strands ODN GEM91 and SREV. Our results show that these four dendrimers are all characterized by utterly similar shape and size, independently of their molecular architecture or overall molecular charge, and so are the relevant complexes with the nucleic acids. On the other hand, depending on the molecular architecture and/or the disposition of the positive charges within the molecular scaffold, these molecules display a remarkably different capacity of exploiting their charged groups for binding the negative ODNs in an efficient and productive way. Accordingly, the different ODN binding affinity of dendrimers **1**–**4** has been rationalized considering the normalized effective binding energy $\Delta G_{bind,eff}/N_{eff}$, i.e., the performance of each active individual dendrimer branch directly involved in a binding interaction. We have thus shown that different combinations of charge localization/molecular architecture reflect, upon dendrimer/ODN complex formation, in the intermolecular interaction of different nature and strength; this, in turn, makes some molecules more efficient ODN binders than others. Furthermore, this study conclusively shows that normalized effective binding energy plays a dominant role among the plethora of critical molecular parameters requiring optimization in the design of efficient nanovectors for gene therapy.

15

ANOTHER BRICK IN THE WALL. VALIDATION OF THE σ_1 RECEPTOR 3D MODEL BY COMPUTER-ASSISTED DESIGN, SYNTHESIS AND ACTIVITY OF NEW σ_1 LIGANDS[1]

Because of the broad contributions of σ_1 in maintaining cellular homeostasis, the receptor has been identified as a therapeutic target for the treatment of cancer[152] and neurodegenerative diseases, including amyotrophic lateral sclerosis[153], Alzheimer and Parkinson diseases[154], and for retinal neurodegeneration[155]. Several studies have also connected σ_1 to the possible treatment of drug addiction and toxicity related to derivatives of cocaine and amphetamine.[156–159]

Unfortunately, almost no information about the 3D structure of the receptor and a clear description of the possible modes of interaction of the σ_1 protein with its ligands have been unveiled so far. With the work presented in this chapter, we validated the σ_1 3D homology model developed by our group; we assessed its reliability as a platform for σ_1 ligand structure-based drug design.

Firstly we designed 33 new σ_1 ligands, exploiting the 3D σ_1 homology model in our possess;

---

[1] The matherial presented in this chapter was published at: Laurini, E., Marson, D., Dal Col, V., Fermeglia, M., Mamolo, M. G., Zampieri, D., et al. (2012). Molecular Pharmaceutics, 9(11), 3107–3126. doi:10.1021/mp300233y

cpd.	Ary	R^1	$K_i(\sigma_1)_{\mathrm{3DPh}}$ [nM]	cpd.	Ary	R^1	R^2	$K_i(\sigma_1)_{\mathrm{3DPh}}$ [nM]
1a	Ph	H	228	**1p**	pyridin-2-yl	Bz	-	810
1b	4-chlorophenyl	H	32.5	**1q**	pyridin-3-yl	Bz	-	1961
1c	4-methylphenyl	H	116	**1r**	pyridin-4-yl	Bz	-	785
1d	Ph	CH_3	27.0	**2a**	Ph	H	CH_3	24.1
1e	4-chlorophenyl	CH_3	66.7	**2b**	Ph	H	Ph	75.2
1f	4-methylphenyl	CH_3	43.7	**2c**	Ph	Cl	CH_3	1.04
1g	Ph	Bz	32	**2d**	Ph	Cl	Ph	9.7
1h	4-chlorophenyl	Bz	83	**2e**	4-chlorophenyl	H	CH_3	0.26
1i	4-methylphenyl	Bz	462	**2f**	4-chlorophenyl	H	Ph	37.1
1j	pyridin-2-yl	H	520	**2g**	4-chlorophenyl	Cl	CH_3	20.4
1k	pyridin-3-yl	H	4433	**2h**	4-chlorophenyl	Cl	Ph	25.7
1l	pyridin-4-yl	H	1148	**2i**	4-methylphenyl	H	CH_3	6.8
1m	pyridin-2-yl	CH_3	1186	**2j**	4-methylphenyl	H	Ph	319
1n	pyridin-3-yl	CH_3	2683	**2k**	4-methylphenyl	Cl	CH_3	86.5
1o	pyridin-4-yl	CH_3	3731	**2l**	4-methylphenyl	Cl	Ph	86.6

Table 15.1: 3D pharmacophore predicted σ_1 Receptor Affinities $K_i(\sigma_1)_{\mathrm{3DPh}}$ of compounds **1a**–**r** and **2a**–**l**

using extensive molecular dynamics simulation-based free energy calculations I ranked the molecules for σ_1 receptor affinity. All compounds were then synthesized in our laboratory and tested for σ_1 binding activity *in vitro*; the agreement between *in silico* and *in vitro* results confirms the reliability of the proposed σ_1 3D model, at least in the *a priori* prediction of the affinity of new σ_1 ligands.

Applying a per residue free energy deconvolution and in silico alanine scanning mutagenesis calculations, I analyzed the main interactions involved in receptor/ligand binding, producing the fist description of the possible modes of interaction of the σ_1 protein with these ligands. The data obtained support the currently available biochemical data concerning the σ_1 receptor residues considered essential for σ_1 ligand binding and activity.

15.1 3D PHARMACOPHORE-BASED DESIGN OF NEW σ_1 LIGANDS

The initial step of the present work consisted of exploiting our 3D pharmacophore model for the in silico design of new σ_1 ligands.[160] Accordingly, starting from compounds **1e** and **2c**[161] (see Figure 15.1, top panels), we designed two new molecular series **1a**–**r** and **2a**–**l** (Figure 15.1, bottom panels) with a wide range of σ_1 receptor affinity values $K_i(\sigma_1)$, as shown in Table 15.1.

Quite interestingly, compounds belonging to series **1** are generally endowed with a lower affinity toward the σ_1 receptor than those of series **2**. This aspect can be explained by

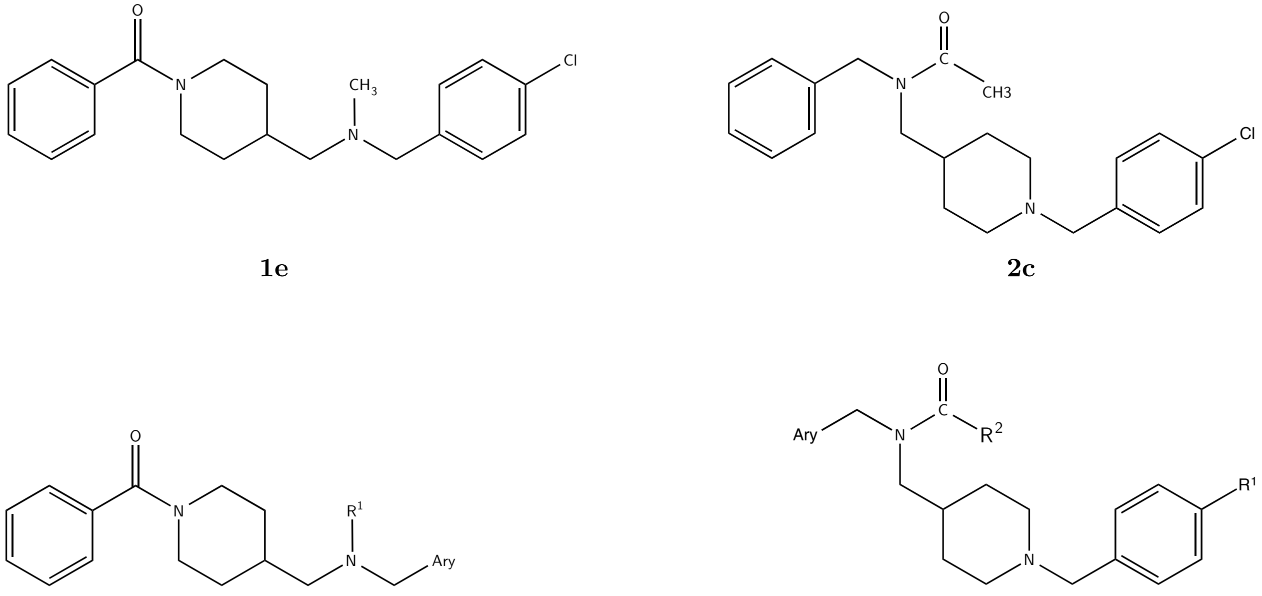

1e

2c

1(a–r)

2(a–l)

Figure 15.1: (Top) Chemical structure of compounds **1e** and **2c**. (Bottom) Molecular structures of compounds of series **1** and **2**.

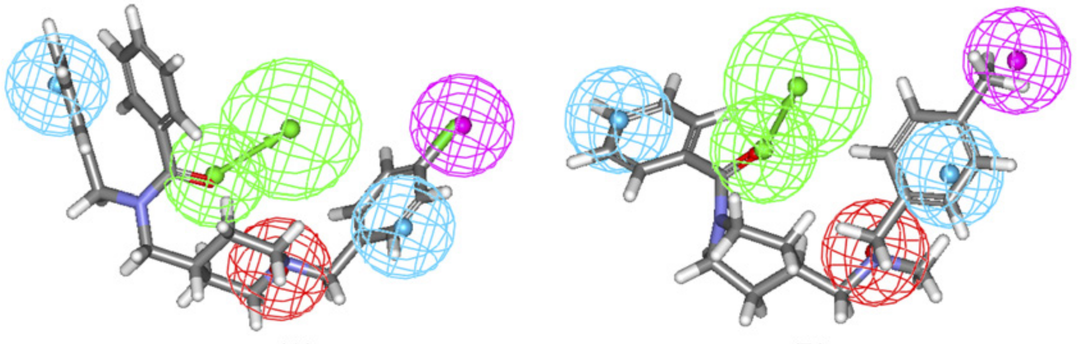

(A)

(B)

Figure 15.2: Pharmacophore mapping of **2d** (A) and **1f** (B). The 3D pharmacophore hypothesis features are portrayed as meshed spheres, color-coded as follows: red, PI; light blue, HYAr; pink, HY; light green, HBA.

comparing, for instance, the mapping of two of the most active compounds of both series (i.e., **1f** $K_i(\sigma_1)_{\text{3DPh}} = 43.7\,\text{nM}$) and 2d ($K_i(\sigma_1)_{\text{3DPh}} = 9.7\,\text{nM}$) on the corresponding 3D pharmacophore features, as shown in Figure 15.2.

The 3D pharmacophore model for σ_1 ligands shown in Figure 15.1 is characterized by five chemical features: one positive ionizable (PI) site, one hydrogen bond acceptor (HBA) group, two hydrophobic aromatic (HYAr) moieties, and one further hydrophobic (HY) site. Thus, when superposed on this pharmacophore model, compound **2d** maps all the chemical features with perfect overlap (Figure 15.2A): the phenyl ring matches the aromatic hydrophobic function, the chlorine atom fills the hydrophobic group of the model, and the basic nitrogen atom has the function of proton acceptor, while the carbonyl group matches the hydrogen bond feature. On the other hand, the chemical groups on compound **1f**, although suitable to fulfill all chemical requirements of the 3D pharmacophore, cannot be perfectly superposed to the corresponding pharmacophoric features due to a different molecular conformation and steric rigidity characterizing this molecule (Figure 15.2B).

15.2 Assisted-ligand docking into the σ_1 receptor 3D homology model

The putative binding site and binding modes of all compounds **1a**–**r** and **2a**–**l** in the σ_1 receptor 3D homology model structure were retrieved taking advantage of:

- the currently available preliminary information on sequence-structure relationships and mutagenesis studies;
- the ligand-binding pharmacophore requirements;
- the docking poses and receptor affinity ranking of compounds **1e** and **2c**.[161]

To summarize briefly, a protein isoform missing residues 119–149 was found devoid of ligand binding capacity, and the conversion of residues Asp126 and Glu172 to glycine led to a several-fold reduction in ligand-binding function for the σ_1 receptor.[162] Moreover, our hydrophobicity analysis identified, aside from the transmembrane (TM) domains, a third hydrophobic region matching the steroid binding domain-like II (SBDLII) region and centered on Asp188, a residue specifically photolabeled by [^{125}I]IACoc (3-iodo-4-azidoco-caine).[163] This protein region having been localized as a possible zone for ligand binding, a thorough search for a sequence satisfying the 3D pharmacophoric requirements[160] was performed and successfully retrieved. Thus, all compounds **1a**–**r** and **2a**–**l** were docked into the putative binding site

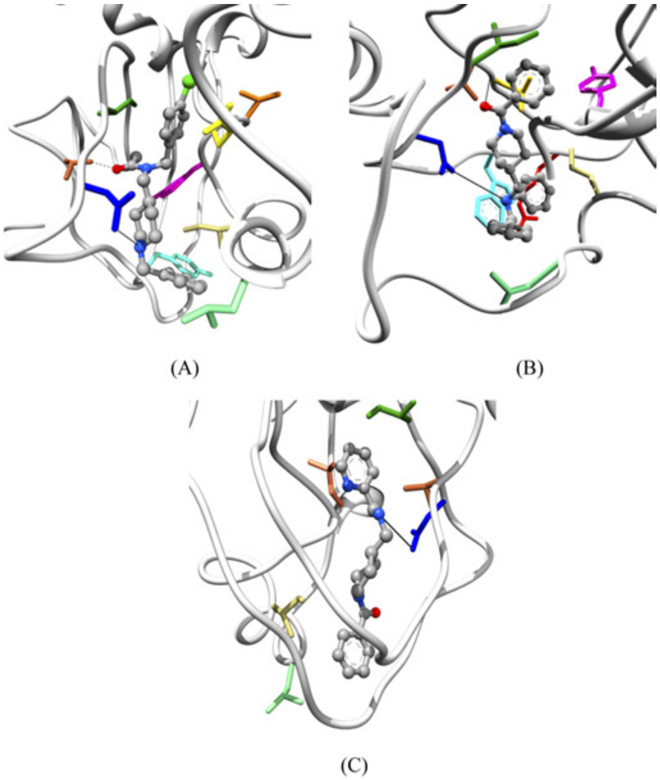

Figure 15.3: Details of the key interactions detected in the equilibrated MD snapshots of **2e** (A), **1g** (B), and **1j** (C) in complex with the σ_1 receptor 3D homology model. The main protein residues involved in ligand/receptor interactions are Arg119 (red), Tyr120 (aquamarine), Trp121 (cyan), Asp126 (blue), Ile128 (forest green), Thr151 (sienna), Val152 (gold), Val 171 (orange), Glu172 (yellow), Tyr173 (magenta), Ile178 (khaki), Leu182 (light green), and Leu186 (coral). Compounds **2e**, **1g**, and **1j** are shown in atom-colored sticks and balls: C, gray; O, red; N, blue; and Cl, green. H atoms are not shown, but H-bonds and salt bridges are indicated as black dotted and continuous lines, respectively. In all images, water molecules, ions, and counterions are not shown for clarity.

of the σ_1 receptor 3D model. For each compound, in the corresponding set of docked ligand conformations a solution was found that best reproduced the key 3D pharmacophore requirements (see Figure 15.3). Each resulting receptor/ligand complex was then relaxed by energy minimization and molecular dynamics (MD) simulations. Finally, the relevant values of the free energy of binding ΔG_{bind} between all compounds and the σ_1 receptor were evaluated by applying the well-known Molecular Mechanics/Poisson Boltzmann Surface Area (MM/PBSA) computational ansatz, as listed in Table 15.2.

Figure 15.3 shows three MD snapshots extracted from the corresponding equilibrated trajectories of **2e**, **1g**, and **1j** in complex with the σ_1 receptor, as an example. Among both series of compounds, **2e** is the molecule characterized by the highest MM/PBSA predicted affinity toward the σ_1 receptor, $K_i(\sigma_1)_{\Delta G_{bind}} = 0.01$ nM (see Table 15.2), in agreement with the corresponding estimation from the 3D pharmacophore model ($K_i(\sigma_1)_{\text{3DPh}} = 0.26\,\text{nM}$, Table 15.1). From Figure 15.3A it is instructive to observe how, for **2e**, an hydrogen bond (HB) is established between the carbonyl oxygen of the ligand and the side-chain $-$OH group of Thr151 on the receptor. This HB, which persists throughout the entire MD simulation period, is characterized by an average dynamic length (ADL) of (1.82 ± 0.21) Å and yields a substantial contribution to binding (vide infra for a quantitative discussion of these data). A permanent salt bridge (SB), (ADL $= (3.81 \pm 0.10)$ Å) is detected between the $-\text{COO}^-$ group of Asp126 on the receptor side and the piperidine $-\text{NH}^+$ moiety of **2e**. The 4-Cl-phenyl

compd.	ΔH [kcal mol^{-1}]	$T\Delta S$ [kcal mol^{-1} K^{-1}]	ΔG_{bind} [kcal mol^{-1}]	$K_i(\sigma_1)_{\Delta G_{bind}}$ [nM]
1a	-36.29 ± 0.19	-26.36 ± 0.34	-9.93 ± 0.39	53.0
1b	-34.39 ± 0.21	-23.87 ± 0.32	-10.52 ± 0.38	19.6
1c	-36.18 ± 0.17	-25.75 ± 0.31	-10.43 ± 0.35	22.8
1d	-35.02 ± 0.18	-24.62 ± 0.35	-10.40 ± 0.39	24.0
1e	-37.90 ± 0.18	-26.71 ± 0.30	-10.02 ± 0.35	6.32
1f	-36.21 ± 0.20	-25.09 ± 0.31	-11.12 ± 0.37	7.12
1g	-33.19 ± 0.16	-23.24 ± 0.35	-9.95 ± 0.38	51.2
1h	-32.60 ± 0.20	-23.39 ± 0.36	-9.21 ± 0.41	178
1i	-33.38 ± 0.19	-24.37 ± 0.33	-9.01 ± 0.38	250
1j	-30.33 ± 0.18	-24.49 ± 0.35	-5.84 ± 0.39	52 600
1k	-29.89 ± 0.21	-23.02 ± 0.31	-6.87 ± 0.37	9250
1l	-30.69 ± 0.17	-22.43 ± 0.36	-8.26 ± 0.40	880
1m	-29.88 ± 0.21	-23.35 ± 0.31	-6.53 ± 0.37	16 400
1n	-29.24 ± 0.18	-22.65 ± 0.32	-7.75 ± 0.37	14 800
1o	-28.87 ± 0.22	-22.27 ± 0.32	-6.60 ± 0.39	14 600
1p	-31.89 ± 0.89	-23.03 ± 0.37	-8.86 ± 0.40	322
1q	-30.92 ± 0.18	-23.67 ± 0.34	-7.25 ± 0.38	4870
1r	-29.97 ± 0.20	-22.11 ± 0.33	-7.86 ± 0.39	1740
2a	-38.31 ± 0.20	-25.81 ± 0.35	-12.50 ± 0.40	0.69
2b	-39.01 ± 0.15	-26.19 ± 0.36	-12.82 ± 0.39	0.40
2c	-38.81 ± 0.19	-25.54 ± 0.33	-11.31 ± 0.38	0.19
2d	-38.39 ± 0.19	-24.91 ± 0.33	-13.48 ± 0.38	0.13
2e	-48.83 ± 0.21	-25.71 ± 0.30	-15.12 ± 0.37	0.01
2f	-37.76 ± 0.17	-25.97 ± 0.35	-11.79 ± 0.39	2.30
2g	-38.33 ± 0.19	-26.38 ± 0.34	-11.95 ± 0.39	1.75
2h	-37.04 ± 0.18	-25.11 ± 0.36	-11.93 ± 0.40	1.81
2i	-38.61 ± 0.19	-26.09 ± 0.35	-12.52 ± 0.40	0.67
2j	-33.95 ± 0.18	-24.35 ± 0.32	-9.60 ± 0.37	92.5
2k	-34.61 ± 0.19	-25.03 ± 0.31	-9.58 ± 0.36	95.6
2l	-34.49 ± 0.21	-24.62 ± 0.35	-9.87 ± 0.41	58.6
HAL	-35.17 ± 0.19	-24.56 ± 0.38	-10.61 ± 0.42	16.8
PTZ	-27.56 ± 0.22	-17.54 ± 0.39	-10.02 ± 0.45	45.5

Table 15.2: Enthalpy (ΔH), entropy ($T\Delta S$), free energy of binding (ΔG_{bind}), and corresponding $K_i(\sigma_1)_{\Delta G_{bind}}$ values for compounds **1a**–**r** and **2a**–**l** and the σ_1 receptor homology model, as estimated using the MM/PBSA approach. The $K_i(\sigma_1)$ values were obtained from the corresponding ΔG_{bind} values. The values of two σ_1 ligand reference compounds, (+)-pentazocine (PTZ) and haloperidol (HAL), are also reported for comparison.

group of the compound is encased in a hydrophobic pocket, mainly lined by the side chains of Val171 and Ile128. An outer hydrophobic region accommodates the second phenyl ring of **2e**, with the contribution of residues Leu182, Ile178, and Tyr120. Also, this phenyl ring is further engaged in a parallel π-π stacking interaction with Tyr120. The synergistic effect of all these stabilizing interactions is reflected in the highly negative (i.e., favorable) value of ΔG_{bind} between **2e** and the σ_1 protein ($-15.12\,\mathrm{kcal\,mol^{-1}}$, Table 15.2) and, hence, of the predicted subnanomolar value of the corresponding $K_i(\sigma_1)_{\Delta G_{bind}}$.

For compound **1g**, MM/PBSA calculations yield an intermediate affinity for the σ_1 receptor—$K_i(\sigma_1)_{\Delta G_{bind}} = 51.2\,\mathrm{nM}$ (see Table 15.2)—a value quite close to that predicted by the 3D pharmacophore model ($K_i(\sigma_1)_{\mathrm{3DPh}} = 32\,\mathrm{nM}$, Table 15.1). Figure 15.3B illustrates how the stable HB and the SB outlined for **2e** are still present, although the hydrogen donor on the receptor side in this case is the $-$NH group of the backbone peptide bond between Thr151 and Val152. Both these interactions, however, are somewhat weaker than for **2e**, as the corresponding ADL are (2.09 ± 0.12) Å and (4.53 ± 0.18) Å, respectively. The hydrophobic pockets again enwrap two of the aromatic rings, residue Trp121 playing a role in determining a T-stacked π-π interaction with one of the two aryl groups. However, the conformation of the molecule is such that the last phenyl ring is not mapped by any suitable pharmacophore feature of **1g**; correspondingly, this interaction is lost within the receptor binding site (Figure 15.3B). In line with this analysis, the presence of these less effective, albeit still favorable, interactions is reflected in the higher (less negative) value of the estimated free energy of binding ($\Delta G_{bind} = -9.95\,\mathrm{kcal\,mol^{-1}}$, Table 15.2).

According to both 3D pharmacophore modeling and MM/PBSA simulations, compound **1j** is endowed with the lowest affinity toward the σ_1 receptor, with values of $K_i(\sigma_1)_{\mathrm{3DPh}} = 520\,\mathrm{nM}$ and $K_i(\sigma_1)_{\Delta G_{bind}} = 52\,600\,\mathrm{nM}$, respectively. In this case, the role exerted by Tyr120 and Thr151 in binding **1j** is negligible, while the two hydrophobic pockets described above are still able to accommodate the two aromatic moieties of this compound (Figure 15.3C). More importantly, the carbonyl group is positioned far too distant from any possible proton donor group on the receptor to set up any stabilizing HB bond. In agreement with these considerations, a very low activity is predicted for this compound, with a corresponding ΔG_{bind} value of $-5.84\,\mathrm{kcal\,mol^{-1}}$.

According to the present MM/PBSA analysis, the binding affinity of the two series of compounds **1** and **2** toward the σ_1 receptor is an enthalpy-driven process: indeed, panel A in Figure 15.4 shows that for both molecular sets the unfavorable entropic contribution $T\Delta S$ to ligand binding is overwhelmed by the favorable enthalpic component ΔH, resulting in an overall negative value of the free energy of binding ΔG_{bind}. It is also interesting to note that the higher MM/PBSA average σ_1 affinity value predicted for all compounds of series **2**

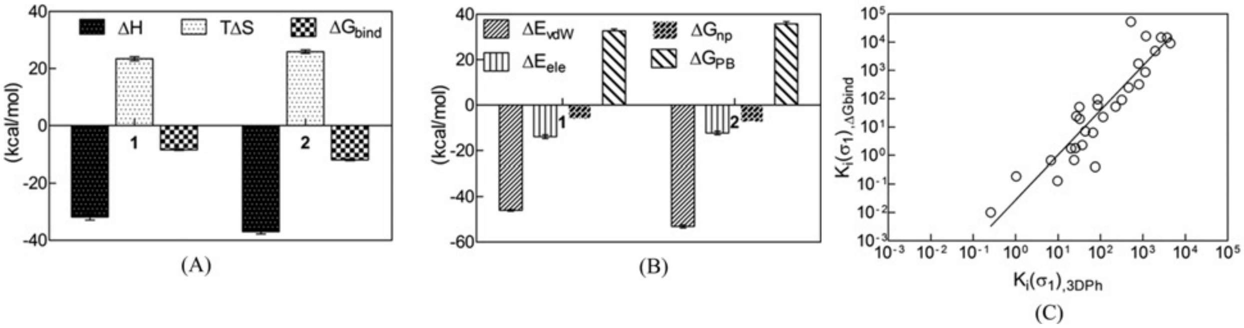

Figure 15.4: (A) Average MM/PBSA values of the enthalpy (ΔH), entropy ($T\Delta S$), and free energy of binding (ΔG_{bind}) for compound series **1** and **2** in complex with the σ_1 receptor. (B) Average values of the enthalpic components of ΔG_{bind} (van der Waals term ΔE_{vdW}, electrostatic term ΔE_{ELE}, polar solvation term ΔG_{PB}, and nonpolar solvation term ΔG_{NP}) for compound series **1** and **2** in complex with the σ_1 receptor. (C) Correlation between the σ_1 affinity constant K_i values for compounds **1a**–**r** and **2a**–**l** estimated using the 3D pharmacophore model ($K_i(\sigma_1)_{\mathrm{3DPh}}$) and the MM/PBSA methodology ($K_i(\sigma_1)_{\Delta G_{bind}}$).

originates solely from the difference in the enthalpic contributions between the two molecular sets ($\Delta\Delta H = \Delta H_{(\mathbf{2})}$ - $\Delta H_{(\mathbf{1})} = -4.91\,\mathrm{kcal\,mol^{-1}}$), as the corresponding difference in the entropic terms is significantly smaller ($\Delta(T\Delta S) = T\Delta S_{(\mathbf{2})}$ - $T\Delta S_{(\mathbf{1})} = 1.56\,\mathrm{kcal\,mol^{-1}\,K^{-1}}$).

The calculated ΔG_{bind} values are encouraging also in the light of the balance among the energy terms contributing to them. As observed in many other drug/receptor complex simulations including our own studies,[135, 136, 164–166] the favorable contribution of the electrostatic interactions between the σ_1 protein and compounds **1a**–**r** and **2a**–**l** (ΔE_{ELE}) is more than compensated by the electrostatic desolvation free energy upon complexation (ΔG_{PB}), so that the total electrostatic term ($\Delta E_{ELE} + \Delta G_{PB}$) contributes unfavorably to the binding (see Figure 15.4B). Interestingly, several recent papers have demonstrated that (natural) receptor—ligand pairs often show suboptimal electrostatic interactions that may be optimized, leading to increased affinity.[167–171] On the contrary, van der Waals (vdW) interactions (ΔE_{vdW}) contribute favorably to the binding affinity of **1a**–**r** and **2a**–**l** toward the receptor, as does the nonpolar part of the solvation free energy (ΔG_{NP}), again in agreement with other studies mentioned above[166–171] (Figure 15.4B). Therefore, for both **1** and **2** molecular series, the favorable binding free energy for receptor/ligand complex formation stems predominantly from the nonpolar terms ($\Delta E + \Delta G\ $), while the polar vdW interactions provide most of all the directional constraint for the complexation, that is, the relative positions of the molecules.

The analysis of the entire MD simulation trajectories for all 33 compounds in complex with the σ_1 receptor 3D model further reveals that the overall conformation of the protein backbone undergoes only minimal global conformational changes upon complex formation

2e	**1g**	**1j**	**2e/1g**	**2e/1j**	**1g/1j**
0.9	1.6	2.1	2.5	4.2	3.5

Table 15.3: Average RMSDs of the binding site of the σ_1 protein in complex with **2e**, **1g**, and **1j** with respect to the unbound protein and to each alternative complex. All values are reported in Å.

with the different compounds, while a rearrangement of the side chains of several residues lining the receptor binding site is required for ligand binding. In its uncomplexed form, the σ_1 model structure remained stable for the entire 10 ns MD trajectory, as testified by the small root-mean-square deviation (RMSD) values of the backbone atom positions with respect to those of the initial structure. The same parameter showed very low fluctuations during both MD equilibration and data harvesting steps also for all receptor/ligand complexes, indicating that the presence of a bound ligand does not result in large protein structural deviations. The first part of Table 15.3 reports the average RMSDs of the binding site region of the σ_1 receptor (i.e., from residue 100 to residue 200) determined between average structures of the proteins in the unbound and bound states for **2e**, **1g**, and **1j** as an example: this region deviates by very small amounts, confirming that the σ_1 binding pocket does not experience a significantly larger-than-average conformational change upon complex formations with ligands **1** and **2**.

These aspects can be further inspected and quantified considering the superposition of equilibrated snapshots extracted from the MD trajectory of the receptor in complex with compounds **2e**, **1g**, and **1j** reported in Figure 15.5 and the relevant RMSD values listed in the rightmost three columns of Table 15.3. This evidence confirms that the putative binding site of the σ_1 receptor is able to accommodate all ligands of series **1** and **2** with no major conformational readjustments, the difference in affinity toward the different compounds being ascribable to a better/worse rearrangement of the binding pocket residue side chains.

In concluding this section it is interesting to note that the affinity values of all 33 compounds toward the σ_1 receptor predicted by the 3D pharmacophore model are in good agreement with the corresponding values obtained from the MM/PBSA scoring, with a correlation coefficient of $\mathrm{R}^2 = 0.84$, as shown in Figure 15.4C. The quality of the overall linear correlation between these two $K_i(\sigma_1)$ data sets constitutes a first step toward the validation of the σ_1 3D homology model and the location of its putative binding site.

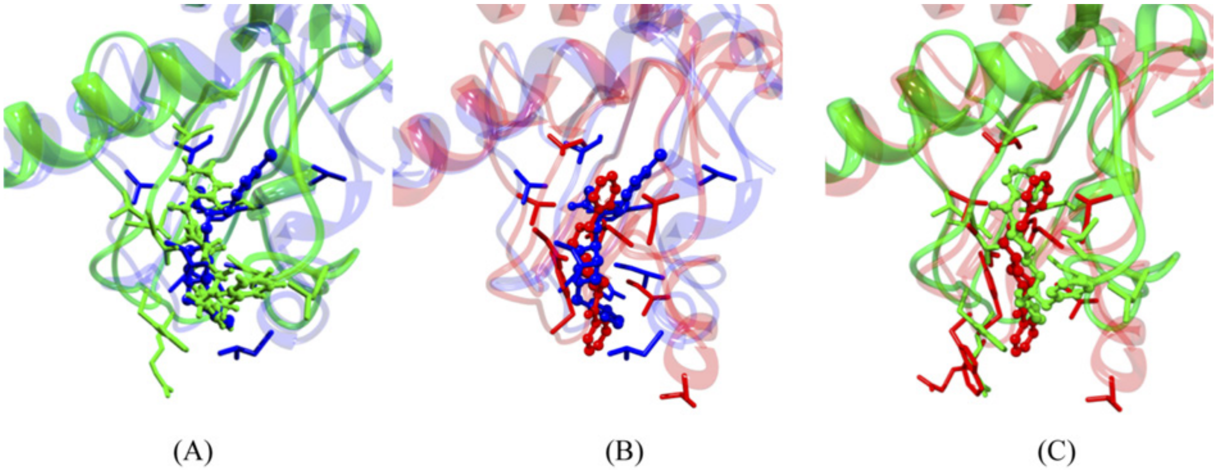

Figure 15.5: Superposition of equilibrated MD snapshots of the σ_1 receptor in complex with (A) **2e** (blue) and **1g** (green), (B) **2e** (blue) and **1j** (red), and (C) **1g** (green) and **1j** (red). The images are zoomed views of the receptor binding site. The ligands are portrayed in sticks and balls colored according to the protein in the corresponding complex. Water, ions, and counterions are not shown for clarity.

15.3 Residue-based description of ligand binding to σ_1: PRBFED and computational alanine scanning

15.3.1 Per residue binding free energy decomposition

Insight into the origin of binding of σ_1 to compounds **1** and **2** at an atomistic level may be obtained by decomposing the total free energy of binding ΔG_{bind} in terms of contributions from structural subunits of both binding partners. The molecular Molecular Mechanics/Generalized Born Surface Area (MM/GBSA), allows the decomposition of the electrostatic solvation free energy into atomic contributions in a straightforward manner. This, in turn, permits an easy and rapid per residue binding free energy decomposition (PRBFED), yielding the residue-based ΔH_{GB} values required for the detailed study of the ligand/protein interactions at each single amino acid level, including the backbone atoms. Therefore, we proceeded in our study of the binding modes of compounds **1a**–**r** and **2a**–**l** to the σ_1 receptor by applying PRBFED to the analysis of those residues that, as qualitatively discussed above (Figure 15.3), are predicted to be important for ligand binding to the protein.

Figure 15.6 illustrates the results of the PRBFED analysis obtained for compounds **2e**, **1g**, and **1j**, again taken as a proof of concept as they constitute examples of σ_1 high affinity (**2e**), intermediate affinity (**1g**), and very low affinity (**1j**) ligands. As can be seen from Figure 15.6, in all cases three clusters of residues (I, II, and III) are identified, centered around Glu123, Thr151, and Val177, respectively. In the case of **2e** (Figure 15.6A), according to analysis of

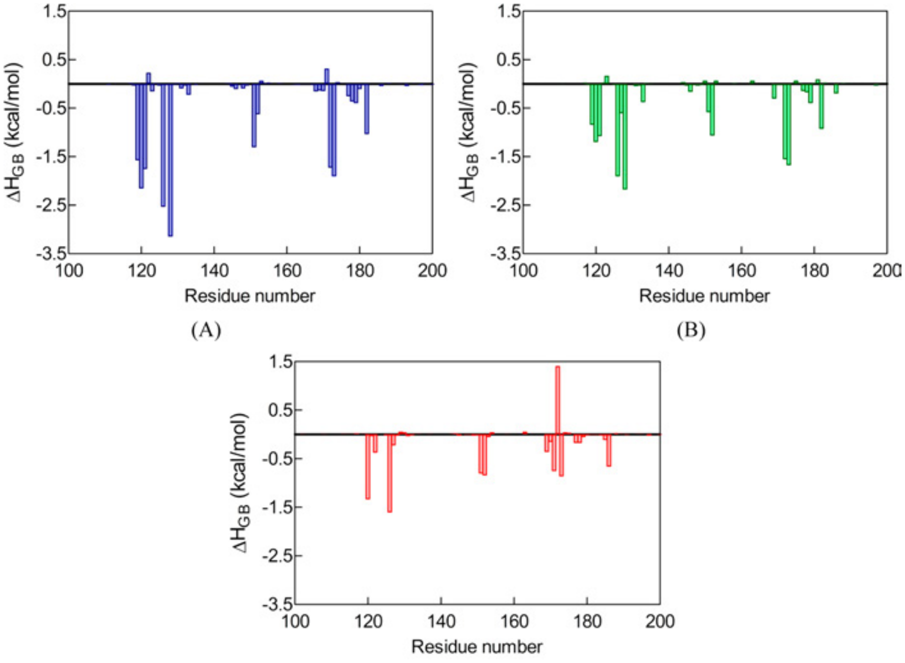

(A) (B)

(C)

Figure 15.6: Per residue binding free energy decomposition for σ_1 receptor in complex with **2e** (A), **1g** (B), and **1j** (C). Only σ_1 amino acids from position 100 to 200 are shown, as for all the remaining protein residues the contribution to ligand binding is irrelevant.

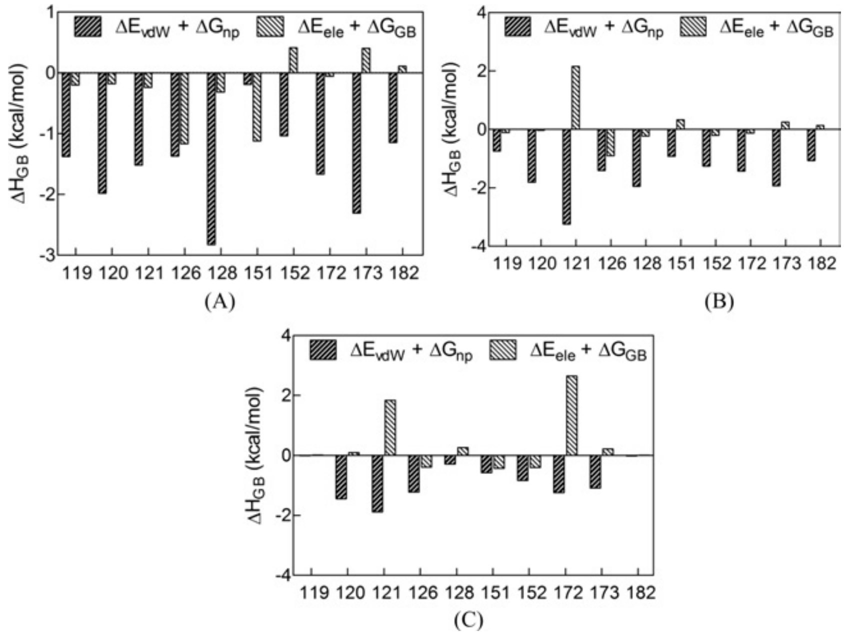

(A) (B)

(C)

Figure 15.7: Decomposition of ΔH_{GB} on a per residue basis into contribution of the nonpolar ($\Delta E_{vdW} + \Delta G_{NP}$) and polar ($\Delta E_{ELE} + \Delta G_{NP}$) terms for residues of the σ_1 receptor in complex with **2e** (A), **1g** (B), and **1j** (C). Only those residues for which $|\Delta H_{GB}| \geq 1\,\mathrm{kcal\,mol^{-1}}$ are shown in the respective panels.

the corresponding MD trajectory (Figure 15.3A,B) the side chain of Asp126 is engaged in a fundamental salt bridge with the piperidine $-NH^{+}$ moiety of the compound; indeed, this residue is responsible for the $-2.54\,\mathrm{kcal\,mol^{-1}}$ favorable contribution to binding, mostly provided by stabilizing electrostatic interactions. The stable hydrogen bond detected between the $-CO$ group of **2e** and the side chain $-OH$ group of Thr151 is responsible for the favorable $-1.31\,\mathrm{kcal\,mol^{-1}}$ contribution provided by the electrostatic interactions. The PRBFED approach then confirms that residues belonging to the two major clusters yield the required vdW and hydrophobic interactions to favorably encase the aromatic portions of the ligand: e.g., Arg119 ($-1.58\,\mathrm{kcal\,mol^{-1}}$), Tyr120 ($-2.16\,\mathrm{kcal\,mol^{-1}}$), Trp121 ($-1.76\,\mathrm{kcal\,mol^{-1}}$), and Ile128 ($-3.15\,\mathrm{kcal\,mol^{-1}}$) of cluster I, and Glu172 ($-1.73\,\mathrm{kcal\,mol^{-1}}$), Tyr 173 ($-1.91\,\mathrm{kcal\,mol^{-1}}$), and Leu182 ($-1.04\,\mathrm{kcal\,mol^{-1}}$) of cluster II, respectively.

Panel B in Figure 15.6 illustrates the PRBFED results for compound **1g**. The presence of weaker (i.e., longer) SB and HB interactions detected along the **1g**/σ_1 MD trajectory (Figure 15.3C,D) is confirmed by the lower ΔH_{GB} values of the residues involved: $-1.91\,\mathrm{kcal\,mol^{-1}}$ (SB) for Asp126 and $-1.07\,\mathrm{kcal\,mol^{-1}}$ (HB) for Val152, respectively. The minor entity of the contributions to binding from residues belonging to clusters I and II (120–128 and 171–182) supports the evidence that part of the hydrophobic and vdW interactions are lost in this ligand/protein complex. Of note, the proposed T-stacked π-π interaction of Trp121 with one of the two aryl groups of **1g** is captured by the PRBFED analysis, according to which the contribution afforded by this residue to binding is equal to $-1.08\,\mathrm{kcal\,mol^{-1}}$.

In our predictions, compound **1j** is the ligand characterized by the lowest affinity for the σ_1 receptor within both molecular series **1** and **2**. The PRBFED results shown in panel C of Figure 15.6 justify these calculations. While the presence of a salt bridge between the $-NH^{+}$ moiety of **1j** and the $-COO^{-}$ of Asp126 is preserved, providing a favorable contribution to binding of $-1.61\,\mathrm{kcal\,mol^{-1}}$, the absence of any H-bond between the $-CO$ group of **1j** and any possible acceptor group on the receptor is responsible for the small contributions to binding from residues of cluster II (e.g., Thr151, $-0.81\,\mathrm{kcal\,mol^{-1}}$). Some residues of clusters I and II are still able to provide some favorable contribution to complex formation, although the reorientation of Glu172 side chain upon binding **1j** is in part responsible for the $+1.41\,\mathrm{kcal\,mol^{-1}}$ unfavorable dispersion/electrostatic contribution to the binding made by this amino acid.

To gain additional insights into the different contributions to the binding free energy change, the per residue ΔH_{GB} values can be further decomposed into the nonpolar terms (i.e., the vdW energy ΔE_{vdW} and the nonpolar term of the solvation free energy ΔG_{NP}) and the sum of the Coulombic interaction and the polar solvation free energy ($\Delta E_{ELE} + \Delta G_{GB}$). Figure 15.7 depicts the ΔH_{GB} decomposition for the **2e**/, **1g**/, and **1j**/σ_1 complexes discussed above. The sum of electrostatic interactions in the gas phase and the change of the polar part of the solvation free energy is shown instead of the separate contributions, since, in most cases, the numbers are strongly anticorrelated.

Qualitatively, major differences are obvious among residues located in the binding site in the case of high, intermediate, and low affinity ligands, respectively. For compound **2e** ($K_i(\sigma_1)_{\Delta G_{bind}} = 0.01\,\mathrm{nM}$), stabilizing vdW and nonpolar interactions, reinforced by favorable overall electrostatic/desolvation terms, prevail for almost all residues lining the σ_1 binding pocket (Figure 15.7A). Interestingly, the overall stabilization of the salt bridge of **2e** with Asp126 ($\Delta G_{GB} = -2.54\,\mathrm{kcal\,mol^{-1}}$, see PRBFED analysis) is almost equivalently contributed by the dispersive ($\Delta E_{vdW} + \Delta G_{NP} = -1.37\,\mathrm{kcal\,mol^{-1}}$) and electrostatic ($\Delta E_{ELE} + \Delta G_{GB} = -1.17\,\mathrm{kcal\,mol^{-1}}$) components, while the pharmacophoric H-bond involving the side chain of Thr151 ($\Delta G_{GB} = -1.31\,\mathrm{kcal\,mol^{-1}}$) mainly gains from a favorable electrostatic interaction ($\Delta E_{ELE} + \Delta G_{GB} = -1.12\,\mathrm{kcal\,mol^{-1}}$ while $\Delta E_{vdW} + \Delta G_{NP} = -0.19\,\mathrm{kcal\,mol^{-1}}$). Figure 15.7A also confirms the dominant role played by the hydrophobic (i.e., overall nonpolar) interactions in binding of **2e** to σ_1, well exemplified by the values of $\Delta E_{vdW} + \Delta G_{NP}$ for residues Arg119 ($-1.38\,\mathrm{kcal\,mol^{-1}}$ and $\Delta H_{GB} = -1.58\,\mathrm{kcal\,mol^{-1}}$), Tyr120 ($-1.98\,\mathrm{kcal\,mol^{-1}}$ and $\Delta H_{GB} = -2.16\,\mathrm{kcal\,mol^{-1}}$), Trp121 ($-1.52\,\mathrm{kcal\,mol^{-1}}$ and $\Delta H_{GB} = -1.76\,\mathrm{kcal\,mol^{-1}}$), Ile128 ($-2.83\,\mathrm{kcal\,mol^{-1}}$ and $\Delta H_{GB} = -3.15\,\mathrm{kcal\,mol^{-1}}$), Glu172 ($-1.67\,\mathrm{kcal\,mol^{-1}}$ and $\Delta H_{GB} = -1.73\,\mathrm{kcal\,mol^{-1}}$), Tyr 173 ($-2.31\,\mathrm{kcal\,mol^{-1}}$ and $\Delta H_{GB} = -1.91\,\mathrm{kcal\,mol^{-1}}$), and Leu182 ($-1.15\,\mathrm{kcal\,mol^{-1}}$ and $\Delta H_{GB} = -1.04\,\mathrm{kcal\,mol^{-1}}$).

In the case of compound **1g** ($K_i(\sigma_1)_{\Delta G_{bind}} = 51.2\,\mathrm{nM}$), the dispersive forces benefit by a lower synergistic interaction with the polar terms of ΔH_{GB} with respect to the case of **2e** (Figure 15.7B). Notably, while the salt bridge between **1g** and Asp126, although decreased in strength ($\Delta H_{GB} = -1.91\,\mathrm{kcal\,mol^{-1}}$), shows a relative contribution from the different ΔH_{GB} components which parallels that discussed for **2e** (i.e., $\Delta E_{vdW} + \Delta G_{NP}$ amounts to approximately 74 % of the total ΔH_{GB}), the other, distinctive pharmacophoric element (i.e., H-bond with Val152) not only is weaker but features contributions from the two main ΔH_{GB} components in a reverse trend with respect to **2e** ($\Delta E_{vdW} + \Delta G_{NP} = -1.26\,\mathrm{kcal\,mol^{-1}}$ and $\Delta E_{ELE} + \Delta G_{GB} = -0.20\,\mathrm{kcal\,mol^{-1}}$, respectively). Of importance is the quantification of the π-π stacking interaction between one aromatic moiety of **1g** and the side chain of Trp121 ($\Delta H_{GB} = -1.08\,\mathrm{kcal\,mol^{-1}}$), for which the dispersive and the electrostatic terms show strong contributions of opposite sign ($\Delta E_{vdW} + \Delta G_{NP} = -3.24\,\mathrm{kcal\,mol^{-1}}$ and $\Delta E_{ELE} + \Delta G_{GB} = +2.16\,\mathrm{kcal\,mol^{-1}}$, respectively).

Lastly, for compound **1j** ($K_i(\sigma_1)_{\Delta G_{bind}} = 52\,600\,\mathrm{nM}$) both the number of useful contacts with the amino acids belonging to the putative σ_1 binding site and also the overall intensity of the interactions between these residues and the ligand are highly diminished with respect to those characterizing compounds **2e** and **1g** discussed above. Also, at some specific positions already identified during PRBFED analysis (e.g., Trp121 and Glu172), a gain in favorable vdW interactions and the nonpolar part of solvation free energy is overcompensated by unfavorable contributions from the $\Delta E_{ELE} + \Delta G_{GB}$ components of ΔH_{GB}.

15.3.2 COMPUTATIONAL ALANINE SCANNING MUTAGENESIS

The MD simulations performed in the MM/PBSA framework of theory can be further employed to perform the so-called computational alanine scanning (CAS) mutagenesis,[172] in which the absolute binding free energy is calculated for the wild type protein, as well as for several mutants in which one residue has been replaced by an alanine. Aside from yielding information complementary to that obtained from a PRBFED analysis, the difference in the binding free energy of the wild type and of the mutants estimated by CAS may be directly compared with the results of an experimental alanine scanning (ASM) mutagenesis. Undoubtedly, in the CAS approach it is questionable whether simply modifying a given side chain to alanine in the corresponding MD simulation trajectory of the wild type system can lead to a good representation of the conformational space of the mutant, since no eventual conformation induced by the mutation is investigated. However, it is also questionable how the binding free energy contribution of a given side chain in the wild type complexation may be always representative of the change in the binding free energy upon mutation, since the conformational modifications induced by the mutations are not included in the model either and since, for instance, the modification of the solvation free energy of close side chains upon mutation is not directly evaluated. Also, contrarily to the total free energy, the free energy components are not state functions, and the values of these contributions are thus dependent on the decomposition scheme adopted. Obviously, both CAS and the PRBFED methods cannot be expected to provide results exactly comparable to experimental values obtained from an experimental ASM; nonetheless, the application of both methodologies can give a good, preliminary indication of which protein residues play a key role in ligand binding, ultimately enabling the biochemist to avoid trial-and-error tests and perform targeted ASM experiments with the obvious advantages of cost and time saving.

The CAS was applied to all compounds **1a**–**r** and **2a**–**l**; for the sake of brevity and in keeping with the previous discussion, Table 15.4 gives the results of the CAS for compounds **2e**, **1g**, and **1j** only. Note that, according to the definition adopted in this work, a negative value of $\Delta\Delta G_{bind}$ corresponds to a residue for which the wild type (*wt*) side chain is more favorable to the binding than an alanine side chain. From the values listed in Table 15.4, the pivotal role exerted by Asp126 in ligand binding is clearly attested by the highly unfavorable free energy of binding of the Ala126 σ_1 mutant with respect to the *wt* protein. Also, Tyr173

		$\Delta\Delta G_{bind} = \Delta G_{bind,wt} - \Delta G_{bind,mut}$						
compd.	$\Delta G_{bind,wt}$	D126A	I128A	T151A	V152A	E172A	Y173A	L182A
2e	-15.12 ± 0.37	-3.69 ± 0.42	-2.27 ± 0.43	-0.67 ± 0.38	-0.56 ± 0.40	-2.04 ± 0.37	-1.79 ± 0.38	-1.11 ± 0.37
1g	-9.95 ± 0.38	-3.25 ± 0.39	-1.35 ± 0.40	-0.71 ± 0.39	-0.45 ± 0.39	-1.19 ± 0.40	-2.03 ± 0.41	-0.79 ± 0.43
1j	-5.84 ± 0.39	-2.82 ± 0.43	-0.12 ± 0.42	-0.57 ± 0.38	-0.39 ± 0.43	-0.21 ± 0.39	-1.27 ± 0.38	0.02 ± 0.44

Table 15.4: Computational alanine scanning mutagenesis results for the σ_1 receptor in complex with ligands **2e**, **1g**, and **1j**. All values are inkcal mol^{-1}.

is confirmed to play a substantial role in the complex stabilization for each compound. Interestingly, residues Ile128 and Leu182 afford a significant contribution to the stabilization of the protein/ligand complex for those ligands with high or intermediate affinity (**2e** and **1g**) but seem to be less critical for bind compounds endowed by a poor affinity for the receptor.

The importance of the hot spot residues detected by CAS can be verified by experimental binding assays of various σ_1 mutants. For instance, in their seminal work Seth et al. clearly demonstrated the obligatory nature of the fully conserved Asp126 and Glu172 for the ligand binding function of the σ_1 receptor via in vitro binding assays of the Asp126Gly and Glu172Gly σ_1 mutants to radiolabeled haloperidol.[162] Also, other mutational studies identified Tyr173 as a residue critical for the cholesterol binding activity of the protein.[173]

To summarize all the *in silico* work discussed above, we used MM/PBSA-based simulations and analysis to design and rank 33 compounds for their affinity toward our 3D homology model of the σ_1 receptor. The $K_i(\sigma_1)$ values derived from the MM/PBSA calculations are in agreement ($R^2 = 0.84$) with those obtained using a 3D pharmacophore model, previously shown to be reliable in reproducing and/or predicting the affinity of similar compounds to the same receptor. Lastly, the combined application of a per residue free energy deconvolution and computational alanine scanning mutagenesis allowed us to dissect the contribution of each single residue belonging to the putative σ_1 receptor binding pocket to ligand binding, yielding fundamental information for further design and development of σ_1 ligands. Furthermore, and perhaps most importantly in the perspective of the present manuscript, those σ_1 residues experimentally found to be involved in ligand binding activity of the receptor were also found critical in our 3D model, according to our PRBFED and CAS simulations.

15.4 Synthesis and activity of new σ_1 ligands, and comparison with *in silico* predictions

The two series of phenylmethanone (**1a**–**r**) and amide (**2a**–**l**) derivatives designed using the molecular modeling methodology described so far were then synthesized.

All molecules were subsequently subjected to in vitro binding assays, in order to assess their experimental affinity toward the σ_1 receptor. The $K_i(\sigma_1)$ values for all 33 compounds were determined using a protocol based on the competitive displacement of [^{3}H]-(+)-pentazocine in a rat liver homogenate preparation.[174, 175]

With respect to compounds **1a**–**r**, the results confirm the presence of a basic nitrogen atom substituted with a small group (H, $-CH_3$) as a fundamental factor to endow the compound with σ_1 affinity. Actually, the N-substitution with a benzyl group decreases the affinity of the derivatives **1g**–**i** toward the receptor with respect to the corresponding derivatives **1a**–**f**; contrarily, the presence of a $-CH_3$ group linked to the basic nitrogen atom in compounds **1e** ($K_i(\sigma_1) = 30.3\,\text{nM}$) and **1f** ($K_i(\sigma_1) = 36.4\,\text{nM}$) improves the σ_1 affinity of this compound. However, the simultaneous absence of a small substituent (e.g., chlorine or methyl group) on the para position of the benzyl moiety decreases the σ_1 receptor affinity of compound **1d** ($K_i(\sigma_1) = 75.5\,\text{nM}$) with respect to the corresponding para-substituted compounds **1e** and **1f**. Compound **1e**, characterized by the presence of a chlorine atom on the para position of the benzyl residue and of a methyl group linked to the basic nitrogen atom, explicates the highest σ_1 affinity. The para substitution with chlorine in compound **1b** ($K_i(\sigma_1) = 42.3\,\text{nM}$) maintains some level of σ_1 affinity, inferior to that of the corresponding N-methyl derivative **1e**, but superior to that of the analogues **1a** ($K_i(\sigma_1) = 114\,\text{nM}$) and **1c** ($K_i(\sigma_1) = 139\,\text{nM}$). The replacement of the phenyl or substituted phenyl residues in compounds **1j**–**r** with the pyridine-2-yl, pyridine-3-yl, or pyridine-4yl moieties abolishes the σ_1 affinity of the corresponding compounds. In the derivative series **2a**–**l**, the amide nitrogen atom is linked to variously substituted benzyl residues and to a 4-methylpiperidin-1-yl spacer, substituted on the benzene ring. The basic nitrogen atom that allows the ionic bond with a receptor acid site belongs to the piperidine cycle. The experimental σ_1 affinity of compound **2c** is rather high ($K_i(\sigma_1) = 1.87\,\text{nM}$). Compound **2c** is substituted with chlorine on the para position of the benzyl group linked to piperidine nitrogen atom. The most potent compound of the series, however, is the acetamide derivative **2e**, characterized by a $K_i(\sigma_1)$ value as low as $0.09\,\text{nM}$. Interestingly, the corresponding benzamide derivative **2f** shows a much lower σ_1 receptor affinity ($K_i(\sigma_1) = 23.2\,\text{nM}$). Actually, acetamide derivatives are endowed with σ_1 affinity higher than that of corresponding benzamide derivatives, except for compound **2g**. The superior affinity of acetamide derivatives may be attributed to the electron donating effect of the acetamide methyl group that may increase the electronegative character of the carbonyl oxygen and further contribute to the σ_1 binding affinity as hydrogen bond acceptor.

One of the main purposes of the entire work was a general validation of our originally proposed 3D model of the σ_1 receptor. Therefore, the direct comparison of the results stemming from the experimental ligand binding assays and the corresponding values predicted by

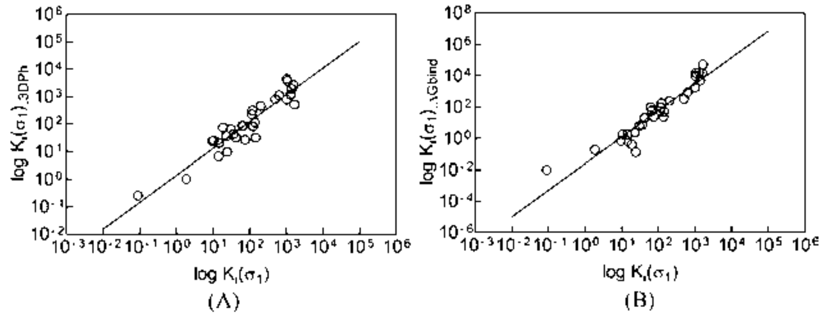

(A)

(B)

Figure 15.8: (A) Plot of the experimental vs 3D pharmacophore predicted $K_i(\sigma_1)$ values for the 33 compounds of series **1** and **2** ($R^2 = 0.89$). (B) Plot of the experimental vs MM/PBSA predicted $K_i(\sigma_1)$ values for the 33 compounds of series **1** and **2** ($R^2 = 0.89$).

the application of the entire computational ansatz constitutes a fundamental and important point of the entire discussion. Figure 15.8 illustrates the results of this direct comparison. In detail, Figure 15.8A shows the remarkable agreement between the affinities for the σ_1 receptor of compounds **1** and **2** predicted by the 3D pharmacophore model ($K_i(\sigma_1)_{\mathrm{3DPh}}$) and the corresponding experimental $K_i(\sigma_1)$ values, quantified by a correlation coefficient of 0.89. If this could be a somewhat expected result, the correlation between the experimental $K_i(\sigma_1)$ values and those derived from the application of the MM/PBSA ranking is even more gratifying: indeed, Figure 15.8B shows how well the calculated $K_i(\sigma_1)_{\Delta G_{bind}}$ values reproduce the experimental ones ($R^2 = 0.89$), with a correct ranking order. To further confirm the capability of the entire MM/PBSA computational procedure in ranking the affinities of all 33 compounds toward the σ_1 receptor, we compared the values of the ΔG_{bind} calculated by MM/PBSA (Table 15.2) with those derived from the biological assays: we observe that the average unsigned error between these two data sets is $0.93\,\mathrm{kcal\,mol^{-1}}$, and the corresponding root-mean-square deviation is $1.19\,\mathrm{kcal\,mol^{-1}}$. Thus, the remarkable quality of all these correlations, coupled with the correct ranking of the wide range of the σ_1 affinity values, constitutes a further, decisive validation of the putative σ_1 binding site and, overall, of the entire 3D homology model of this intriguingly enigmatic receptor.

15.5 Conclusions

σ receptors were first postulated by Martin et al.[83] based on the actions of SKF 10,047 (N-allylnormetazocine) and related benzomorphans. The name "σ" originated from the first letter "S" in SKF 10,047, which was thought to be the prototypic ligand for these binding sites. Unfortunately, SKF 10,047 is now recognized as a nonselective ligand, which contributed to the turbulent early history surrounding these enigmatic receptors. One distinguishing feature of the σ_1 receptor is its promiscuity in binding a wide range of different pharmacological agents, although how binding of these various compounds translates into function(s) through the σ_1 receptor is currently not clear.[175] Since the discovery of the σ_1 receptor, many preclinical studies have implicated the receptor in many important human diseases, from maladies of the central nervous system to cancer, just to name a few. Notwithstanding many pharmacologic responses have been linked to the σ receptors, the function of the σ_1 protein is still a subject of intense study and current debate. Importantly, until very recent times relatively little information regarding the structure of the σ_1 receptor or its ligand binding site was available to the scientific community. Cloning of the σ_1 receptor revealed that the rat brain receptor σ_1 protein consists of 223 amino acids, which results in a molecular weight of 23 kDa. Although human and animal σ_1 receptors show a similarity of more than 95 %, unfortunately there is no resemblance of this receptor to other known mammalian proteins.

Lately our group published for the first time a 3D model of the σ_1 receptor protein as obtained from a multistep computational recipe based on homology modeling techniques.[176] The reliability of the proposed σ_1 model and the validity of its putative ligand binding site were assessed by a docking/MM/PBSA-based small-scale virtual screening of a series of available σ_1 ligands, and by the receptor model-based design of three new σ_1 ligands, featuring a wide range of activity (from 1.87 to 1578 nM). To definitely confirm the validity of this σ_1 3D model and its reliability as a platform for σ_1-ligand structure-based drug design, in the present work we expanded our study by designing 33 new σ_1 ligands, with affinity for the receptor spanning five orders of magnitude. All these compounds were then ranked for receptor affinity by extensive molecular dynamics simulation-based free energy calculations, and the main interactions/receptor residues involved in ligand binding were thoroughly analyzed by applying per residue free energy deconvolution and in silico alanine scanning mutagenesis. All compounds were subsequently synthesized in our laboratory and then tested for σ_1 binding activity in vitro.

Remarkably, the experimental affinity ranking for all 33 compounds toward the σ_1 receptor was found to be fully consistent with the corresponding predictions obtained from our in silico procedure. Therefore, we are convinced that the computational methodology adopted here can be generally employed to estimate the affinity of new σ_1 ligands prior to their synthesis, with an obvious optimization of time and resources. Furthermore, if we reconsider all experimental affinity data, we can see that both sets of compounds **1** and **2** can be classified on the basis of their experimental activity as highly affine ($K_i(\sigma_1) \leq 40.0\,\mathrm{nM}$, +++), moderately affine ($40.0 < K_i(\sigma_1) < 600\,\mathrm{nM}$, ++), and poorly affine ($K_i(\sigma_1) \geq 600\,\mathrm{nM}$, +). According to this classification, and looking at the in silico ranking shown it Table 15.2, we can also conclude that all compounds classified as highly affine (+++) are characterized by ΔG_{bind} values $\leq -11.00\,\mathrm{kcal\,mol^{-1}}$, those with a moderate affinity (++) have $-11.00 <$

$\Delta G_{bind} < -8.50\,\mathrm{kcal\,mol^{-1}}$, and finally the less affine ones have $\Delta G_{bind} \geq -8.50\,\mathrm{kcal\,mol^{-1}}$. Taking into account that the entire computational methodology is based on a protein structure obtained via homology modeling techniques, these ranking capacities and the related results ultimately assess the reliability of the σ_1 receptor 3D model in structure-based ligand design.

16

THE SIGMA ENIGMA: IN VITRO/IN SILICO SITE-DIRECTED MUTAGENESIS STUDIES UNVEIL σ_1 RECEPTOR LIGAND BINDING[1]

The σ_1 receptor is an integral membrane protein that play critical roles in a wide variety of cell functions. Unfortunately it shares no homology with other receptor systems; moreover it has no unequivocally identified natural ligands. The only structural model of this receptor is the 3D homology model developed by our group. In this chapter I will describe the exhaustive *in vitro/in silico* investigation that we performed to analyze the molecular interactions of the σ_1 receptor with its prototypical agonist (+)-pentazocine (PTZ).

We developed 23 mutant σ_1 isoforms, and their interactions with (+)-pentazocine were determined experimentally. Once the effects of the mutations was correctly observed also *in silico,* proving the reliability of our model, the rationalization of all the effects exerted by all the mutant residues on the receptor-agonist interactions were performed. With this work, we further validated our 3D homology model of the σ_1 receptor as a trustworthy tool in the

---

[1] The matherial presented in this chapter was published at: Brune, S., Schepmann, D., Klempnauer, K. H., Marson, D., Dal Col, V., Laurini, E., et al. (2014). Biochemistry, doi:10.1021/bi401575g

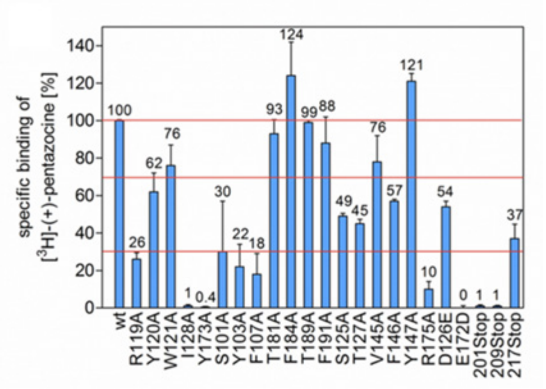

Figure 16.1: Specific [^{3}H]-(+)-pentazocine binding (SB) at a concentration of 40 nM to different alanine mutants of the human σ_1 receptor (n $\geq$ 2). SB refers to the PTZ binding of the wild-type (*wt*) receptor (100 %, first column). $**p \leq 0.001$; $*p \leq 0.01$. With respect to the red lines, SB $< 30\,\%$ indicates a strong influence of the particular amino acid on ligand binding, $30\,\% \leq$ SB $\leq 70\,\%$ indicates a moderate influence on ligand binding, and SB $> 70\,\%$ indicates no influence on ligand binding.

study of this enigmatic protein, and also we gave a deep description of its putative ligand binding site.

The model used in this work was an improvement of the previously developed model[176] in our possess. I further optimized its structure with a long molecular dynamic simulation in which the receptor was inserted in a lipid membrane (2:2:1 POPC:POPE:cholesterol), a very good approximation of its physiological environment.

16.1 MUTANTS SELECTION

On the basis of preliminary *in silico* information, 23 mutants of the σ_1 receptor were cloned and expressed and their interactions with PTZ were assessed experimentally (Figure 16.1). As described below, all direct and indirect effects exerted by the mutant residues on the receptor-agonist interactions could be reproduced in silico and rationalized at the molecular level.

At first, we considered those σ_1 residues to belong to the protein putative ligand binding site. For this purpose, the interaction of PTZ with the wild-type (*wt*) σ_1 receptor 3D model was simulated using molecular dynamics (MD): the corresponding estimated drug-receptor affinity (K_i^c) value of 45 nM compares well with the experimentally measured K_i^e value of 15 nM.[162] Specifically, the following interactions were found to be essential for PTZ binding (Figure 16.2):

- a permanent salt bridge between the $-\mathrm{NH}^+$ moiety of PTZ and the $-\mathrm{COO}^-$ group of D126 [average dynamic length (ADL) of (3.93 ± 0.09) Å];

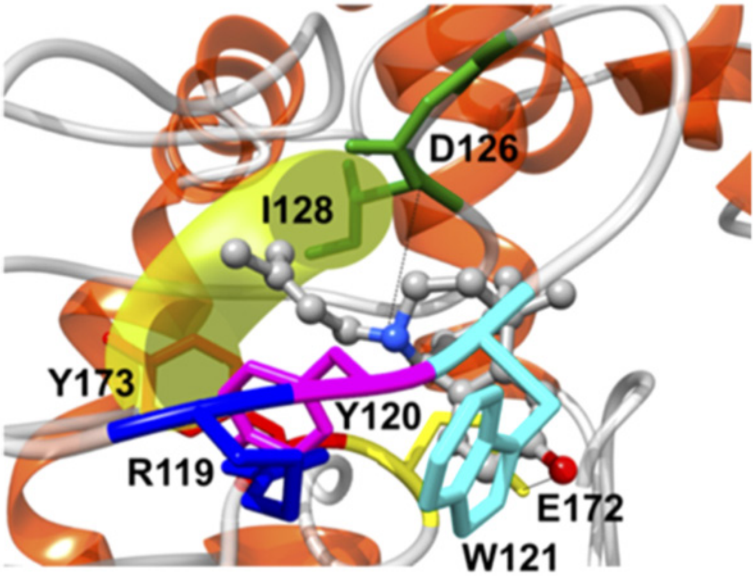

Figure 16.2: Equilibrated MD snapshot of the *wt* σ_1 receptor in complex with PTZ. The image is a close-up of the receptor binding site. The ligand is shown with colored balls and sticks (C, gray; N, blue; O, red). The protein residues mainly involved in the interaction with PTZ are highlighted as labeled colored sticks. Salt bridges and H-bond interactions are shown as solid and dotted black lines, respectively. The yellow shadow denotes the hydrophobic pocket generated by the side chains of I128 and Y173.

- a stable hydrogen bond between the carboxylate group of E172 and the hydroxyl substituent of PTZ (ADL of (1.98 ± 0.04) Å);
- a T-stacking π-π interaction between the side chains of Y120 and W121 and the heteroaromatic condensed rings of PTZ;
- highly stabilizing van der Waals (vdW) and electrostatic interactions between R119, I128, and Y173 and the aliphatic/aromatic portions of the ligand.

These receptor—ligand interactions were quantified via a per residue deconvolution of the free energy of binding (Figure 16.3). Accordingly, the salt bridge and the hydrogen bond involving D126 and E172 are responsible for stabilizing contributions of -2.89 and $-1.83\,\mathrm{kcal\,mol^{-1}}$, respectively. Substantial vdW and electrostatic interactions are further contributed by R119 ($-0.98\,\mathrm{kcal\,mol^{-1}}$), Y120 ($-1.49\,\mathrm{kcal\,mol^{-1}}$), W121 ($-1.37\,\mathrm{kcal\,mol^{-1}}$), I128 ($-2.04\,\mathrm{kcal\,mol^{-1}}$), and Y173 ($-1.95\,\mathrm{kcal\,mol^{-1}}$). T151 and V152 additionally contribute to the stabilization of PTZ-σ_1 binding with -0.36 and $-0.38\,\mathrm{kcal\,mol^{-1}}$, respectively.

Interestingly, in a recent work, Chu at al. discussed the possibility of σ_1 receptors existing in a homo- or heterodimeric form when bound to a single ligand.[177] Specifically, these authors suggested that the observed σ_1 binding and activity of the N-[3-(4-nitrophenyl)propyl]alkan-

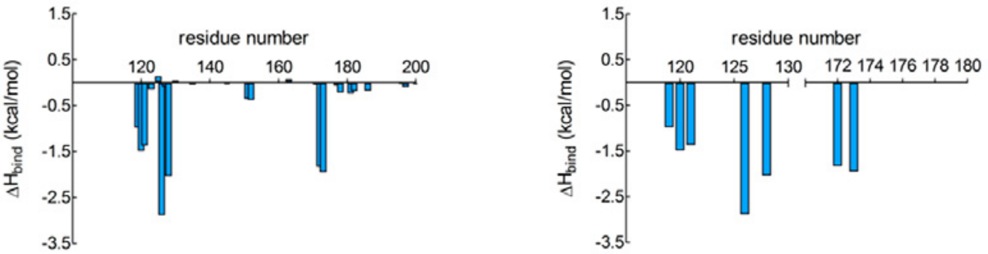

Figure 16.3: Per residue energy decomposition for the *wt* σ_1 receptor in complex with PTZ. Only σ_1 amino acids from position 100 to 200 are shown, as for all remaining residues the contribution to ligand binding is irrelevant. On the left, an expanded view of the first panel showing those σ_1 residues for which $|\Delta H_{bind}| \geq 0.5\,\mathrm{kcal\,mol^{-1}}$.

σ_1 residue	specific binding of PTZ [%]	ΔG_{bind} [$\mathrm{kcal\,mol^{-1}}$]	$\Delta\Delta G_{bind}$ [$\mathrm{kcal\,mol^{-1}}$]
wt	100	-10.02 ± 0.05	-
R119A	26 ± 3.5	-8.31 ± 0.05	-1.71
Y120A	62 ± 10	-9.34 ± 0.08	-0.68
W121A	76 ± 12	-8.48 ± 0.06	-1.54
I238A	1.1 ± 0.6	-7.55 ± 0.06	-2.47
Y173A	0.4 ± 0.4	-7.32 ± 0.11	-2.70
D126E	54 ± 3	-9.13 ± 0.07	-0.89
E172D	0 ± 0.1	-7.88 ± 0.06	-2.14

Table 16.1: *In vitro/in silico* site-directed mutagenesis of σ_1 residues directly involved in PTZ binding. $\Delta\Delta G_{bind} = \Delta G_{bind,wt} - \Delta G_{bind,mutant}$; by this definition, a negative value of $\Delta\Delta G_{bind}$ indicates a favorable contribution for the *wt* residue in that position and vice versa.

1-amine 4-NPPC12 might evoke a ligand binding model for the σ_1 receptor that likely involves a receptor dimer and/or oligomer. Undoubtedly, more conclusive studies are needed to conclusively ascertain this interesting hypothesis and to discard specific ligand-dependent oligomerization mechanisms. On the other hand, the monomeric 3D model of the σ_1 receptor discussed in this work has been comprehensively employed to predict and rationalize the binding modes and affinities of a broad series of structurally unrelated σ_1 ligands, including PTZ, and the results of these *in silico* predictions were successfully validated against relevant experimental data. Therefore, should a dimeric ligand-bound form of the σ_1 receptor be verified for different, known σ_1 ligands,[93, 161, 178, 179] the present monomeric σ_1-ligand binding model may eventually constitute a step along the dimerization pathway.

16.2 R119, I128, AND Y173 ARE ESSENTIAL RESIDUES FOR PTZ BINDING

The results of the site-directed mutations of those residues identified *in silico* as being crucial for PTZ binding are listed in Table 16.1. We see that mutating residues R119, I128, and Y173 within the σ_1 binding site to alanine leads to an almost complete loss of ligand binding, as predicted from simulation. Indeed, residues I128 and Y173 afford a significant contribution to the PTZ-σ_1 complex (Figure 16.3), as their side chains generate a hydrophobic pocket tailored to encase the methylbut-2-enyl moiety of PTZ. Accordingly, the favorable hydrophobic interactions exerted by these two residues in the binding of PTZ are lost upon alanine substitution [for I128, specific binding, SB = 1 % and $\Delta\Delta G_{bind} = -2.47\,\mathrm{kcal\,mol^{-1}}$; for Y173, SB = 0.4 % and $\Delta\Delta G_{bind} = -2.70\,\mathrm{kcal\,mol^{-1}}$ (Figure 16.1)]. On the other hand, the affinity of the Y120A and W121 σ_1 mutants for PTZ was only partly reduced (SB values of 62 and 76 %, respectively). Interestingly, the relevant modeling analysis reveals that, although each of these two aromatic residues concurs in stabilizing PTZ binding mainly via π-π interactions (Figure 16.3), the effect of mutating either of these two positions to alanine results in an apt rearrangement of the alternative residue side chain within the binding site and, hence, in a partial compensation of the receptor affinity loss [$\Delta\Delta G_{bind}$ values of $-0.68\,\mathrm{kcal\,mol^{-1}}$ for Y120A and bind $-1.54\,\mathrm{kcal\,mol^{-1}}$ for W121A (Table 16.1)].

16.3 D126 AND E172 ARE STRATEGICALLY LOCATED WITHIN THE σ_1 BINDING SITE

The anionic amino acids D126 and E172 are known to be essential for ligand (i.e., haloperidol) binding,[162] and our combined study indeed confirms their role in binding PTZ (Figure 16.1 and Figure 16.3). To substantiate this prediction, however, we decided to swap these two residues with each other instead of replacing them with alanine in the corresponding site-directed mutagenesis experiments. Interestingly, the E172D σ_1 mutant was totally devoid of PTZ binding, while the D126E isoform preserved 54 % of the *wt* affinity. These results clearly demonstrate the specific and strategic location of these two negative charges within the σ_1 binding site: while the elongation of the side chain from aspartate to glutamate at position 126 is somewhat tolerated [$\Delta\Delta G_{bind} = -0.89\,\mathrm{kcal\,mol^{-1}}$ (Table 16.1)], resulting in a mild rearrangement of the protein binding pocket that preserves the main network of interactions between the ligand and the protein, the corresponding reduction in chain length in the E172D mutant fully abrogates the ability of the protein to bind the radioligand [$\Delta\Delta G_{bind} = -2.14\,\mathrm{kcal\,mol^{-1}}$ (Table 16.1)]. In detail, the substitution of D/E at position

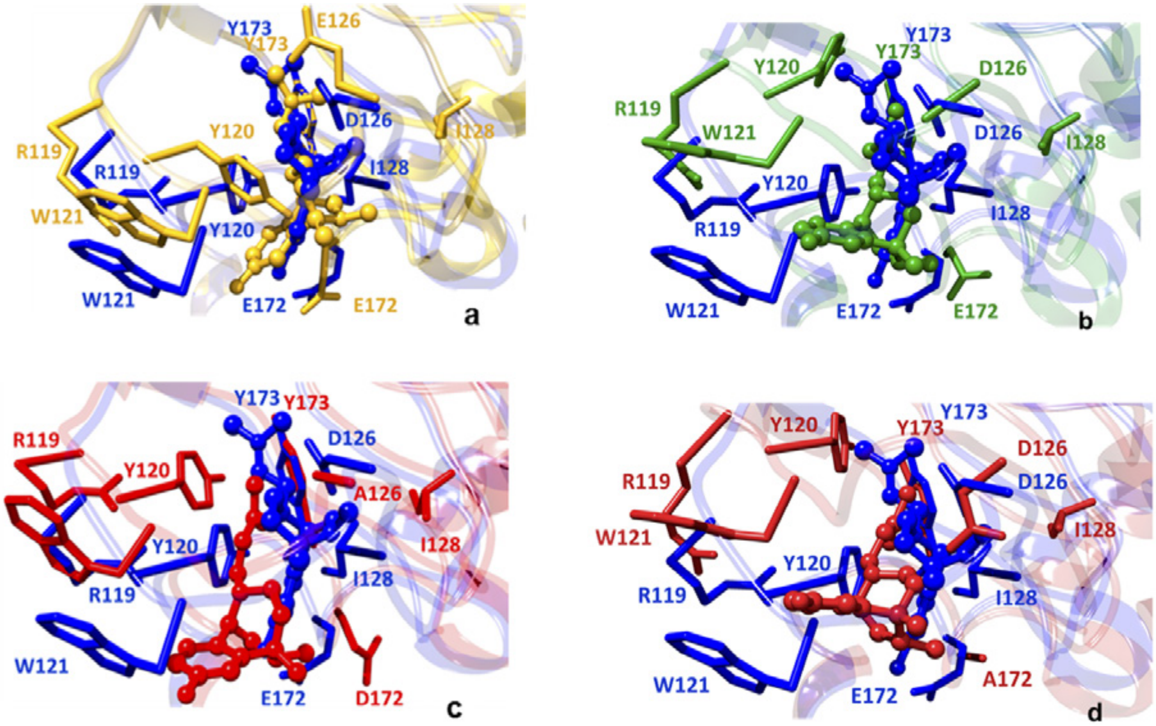

Figure 16.4: Comparison of the equilibrated MD snapshots of the *wt* σ_1 receptor (blue) with (a) D126E (goldenrod), (b) E172D (forest green), (c) D126A (red), and (d) E172A (firebrick) mutants in complex with PTZ. All images are close-ups of the receptor binding site. The ligand is shown as balls and sticks colored according to the respective protein complex. Hydrogen atoms, water molecules, ions, and counterions were omitted for the sake of clarity.

126 leads to a longer, and hence less stable, salt bridge between the $-NH^+$ group ion of PTZ and the $-COO^-$ group of the E126 side chain (ADL of (4.85 ± 0.08) Å), leaving all other ligand-receptor interactions almost unaltered (Figure 3a). Upon E172D substitution, however, the missing H-bond between position 172 and the $-OH$ group on PTZ leads to a global readjustment of the protein binding site (Figure 16.4b), which ultimately leads to an overall decrease in the favorable contributions to ligand binding.

To further corroborate this fundamental finding, we also performed *in silico* mutagenesis of D126 and E172 to alanine. As expected, the prominent role exerted by D126 and E172 in binding PTZ is reflected in the highly unfavorable affinity predicted for the D126A and E172A mutants [$\Delta\Delta G_{bind}$ values of -3.01 and $-2.02\,\mathrm{kcal\,mol^{-1}}$, respectively. The missing critical salt bridge and H-bond interactions in which these residues are engaged in the *wt* protein bound to PTZ result in a catastrophic loss of drug interaction when the residues are mutated to alanine (Figure 16.4c and Figure 16.5). These predictions match the results previously reported by Seth et al.[162] for in vitro PTZ binding assays of the D126G and E172G σ_1 mutants; taken together, these results ultimately confirm the obligatory nature of the highly conserved D126 and E172 residues for the ligand binding function of the σ_1

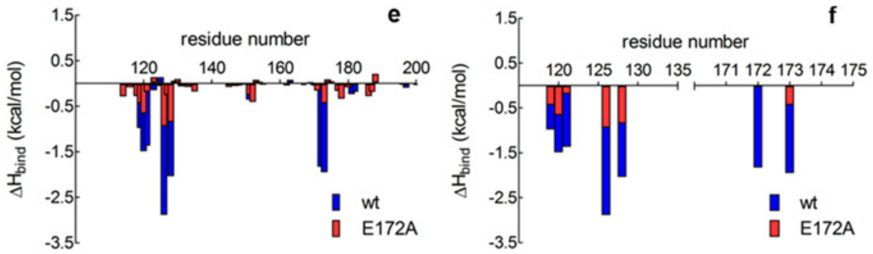

Figure 16.5: Comparison of σ_1 residue contributions to PTZ binding for the *wt* and the E172D mutant protein. On the right, the expanded view of the left panel, showing those σ_1 residues for which $|\Delta H_{bind}| \geq 0.5\,\mathrm{kcal\,mol^{-1}}$ in the *wt* receptor.

σ_1 residue	domain	specific binding of PTZ [%]	ΔG_{bind} [kcal mol^{-1}]	$\Delta\Delta G_{bind}$ [kcal mol^{-1}]
S101A	SBDLI	30 ± 27	-8.16 ± 0.08	-1.86
Y103A		22 ± 12	-7.89 ± 0.09	-2.13
F107A		18 ± 11	-8.05 ± 0.05	-1.97
T181A	SBDLII	93 ± 7.5	-9.99 ± 0.11	-0.03
F184A		124 ± 18	-10.55 ± 0.07	$+0.53$
T189A		99 ± 1.1	-9.87 ± 0.07	-0.15
F191A		88 ± 14	-9.13 ± 0.10	-0.89
201stop		1.0 ± 0.6	–	–
209stop		0.9 ± 0.5	–	–
217stop		37 ± 7.7	8.80 ± 0.06	-1.22

Table 16.2: *In vitro/in silico* site-directed mutagenesis of σ_1 residues belonging to the SBDLI and SBDLII motifs. $\Delta\Delta G_{bind} = \Delta G_{bind,wt} - \Delta G_{bind,mutant}$; by this definition, a negative value of $\Delta\Delta G_{bind}$ indicates a favorable contribution for the *wt* residue in that position and vice versa.

receptor.

16.4 POLAR RESIDUES ARE REQUIRED IN THE SBDLI DOMAIN TO MAINTAIN THE BINDING SITE GEOMETRY

Next, we explored the effect of mutations on residues belonging to the steroid binding domain-like I (SBDLI) and steroid binding domain-like II (SBDLII) σ_1 domains by performing a systematic substitution of the polar (S and T) and aromatic (F and Y) amino acids of these protein regions with alanine. The results are listed in Table 16.2. Mutating the polar and aromatic amino acids of SBDLI (S101, Y103, and F107) to alanine both *in silico* and *in vitro* led to a considerable decrease in the level of PTZ binding [SB = 18–30 %, and $\Delta\Delta G_{bind} = -2.13$ to $-1.86\,\mathrm{kcal\,mol^{-1}}$ (Table 16.2)]. A sensible explanation of these results is that all three alanine-mutated residues are in the proximity of the transmembrane domain of the σ_1 receptor

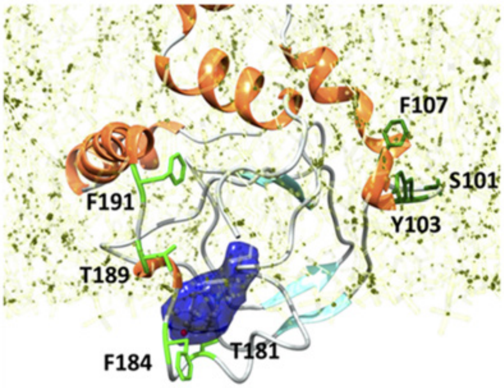

Figure 16.6: Close-up the residues belonging to the σ_1 SBDLI and -II domains, represented as forest and light green sticks, respectively. The ligand is shown as element-colored balls and sticks (C, gray; N, blue; O, red) with its vdW surface colored blue. The membrane phospholipids are portrayed as semitransparent light yellow balls and sticks.

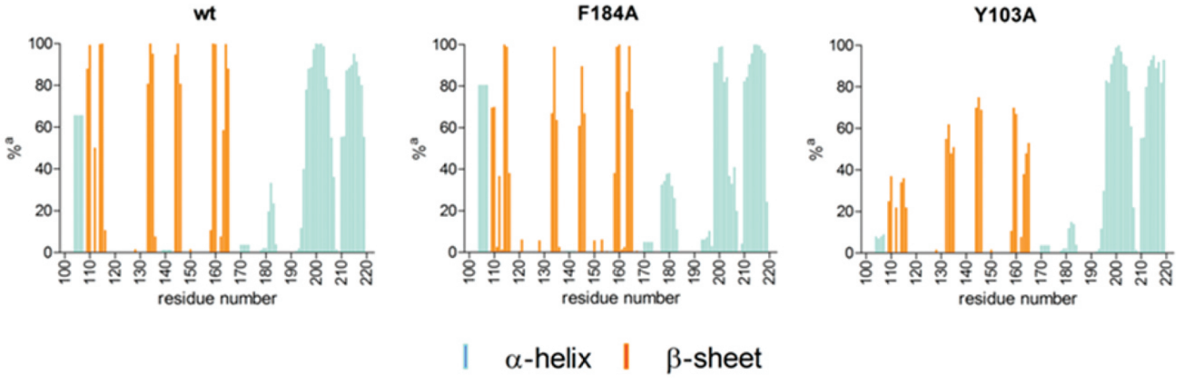

Figure 16.7: General secondary structure description of the σ_1 receptor (amino acids 100–223) during MD simulations of the wt-, Y103A-, and F184A-PTZ complexes. The y-axis gives the percentage of specific secondary structure for each σ_1 residue.

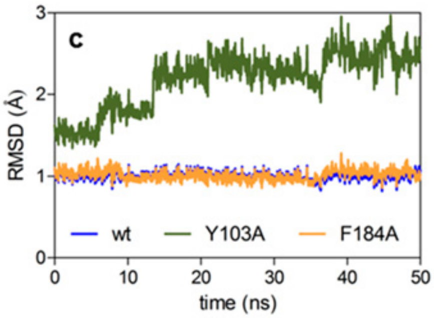

Figure 16.8: RMSD values of the coordinates of the heavy atoms of PTZ along the MD simulation compared with those of the initial structure.

(Figure 16.6) and, during the long MD simulation, they promote a substantial modification of both the entire binding site and the surrounding protein regions. Taking the PTZ-σ_1(Y103A) complex as a proof of concept, we observed a different rearrangement of the secondary structure of this protein portion with respect to the PTZ-*wt* assembly (Figure 16.7, top and central panels), ultimately resulting in an expansion of the receptor binding pocket from an average dynamic volume (ADV) of $(509 \pm 5)\,\text{Å}^3$ to an ADV of $(573 \pm 7)\,\text{Å}^3$. Accordingly, the ligand binds the receptor more loosely, as its interactions with the protein residues lining the binding site become weaker. This effect is clearly seen in the behavior of the root-mean-square deviation (RMSD) of the heavy atom of PTZ during the MD simulation (Figure 16.8): after equilibration, the ligand assumes a stable conformation in the *wt* binding pocket with an average RMSD of $(1.01 \pm 0.06)\,\text{Å}$, while a larger RMSD fluctuation ($(2.18 \pm 0.35)\,\text{Å}$) and a longer time to equilibrium are observed for the Y103A mutant σ_1-PTZ complex.

16.5 RESIDUES IN THE SBDLII DOMAIN SCARCELY CONTRIBUTE TO LIGAND BINDING

In stark contrast, analogous mutations in the SBDLII domain barely influenced PTZ binding, if they did at all [SB = 93–100 %, and $\Delta\Delta G_{bind} = -0.59$ to $-0.03\,\text{kcal}\,\text{mol}^{-1}$ (Table 16.2, rows 4–7)]. A comparison of the membrane-bound *wt* and SDBLII mutated σ_1 isoforms reveals that the presence of mutations at the SBDLII domain does not lead to substantial alteration of both the membrane and the protein binding site and/or overall structure. Indeed, in the representative example of the PTZ-σ_1(F184A) complex, the fingerprint of the protein secondary structure is conserved (Figure 16.7, top and bottom panels) and the ADV is essentially unchanged ($(507 \pm 7)\,\text{Å}^3$). Moreover, PTZ maintains a very stable conformation in the binding site during the entire MD simulation, as substantiated by the relevant RMSD [$(1.01 \pm 0.07)\,\text{Å}$ (Figure 16.8)]. Lastly, all ligand-receptor interactions detected for the *wt* complex are maintained in this as well as in all other SBDLII mutated complexes examined with no significant differences in binding mode or strength. Remarkably, in a previous study, SBDLII was postulated to be part of the σ_1 ligand binding site.[180] Our results clearly do not support this hypothesis. It has been further proposed that SBDLII is responsible for anchoring the σ_1 receptors to the membrane and, in so doing, stabilizing the 3D structure of the protein. Once again, our combined *in vitro/in silico* experiments point in the opposite direction. Taken together, our findings lead to the conclusion that, while the SBDLI domain is part of the binding site of the σ_1 receptor and, as such, mutations at this domain lead to a drastic decrease in receptor-ligand affinity, the SBDLII domain does not belong to the σ_1 ligand binding site. Accordingly, mutations in this protein domain exert only a marginal

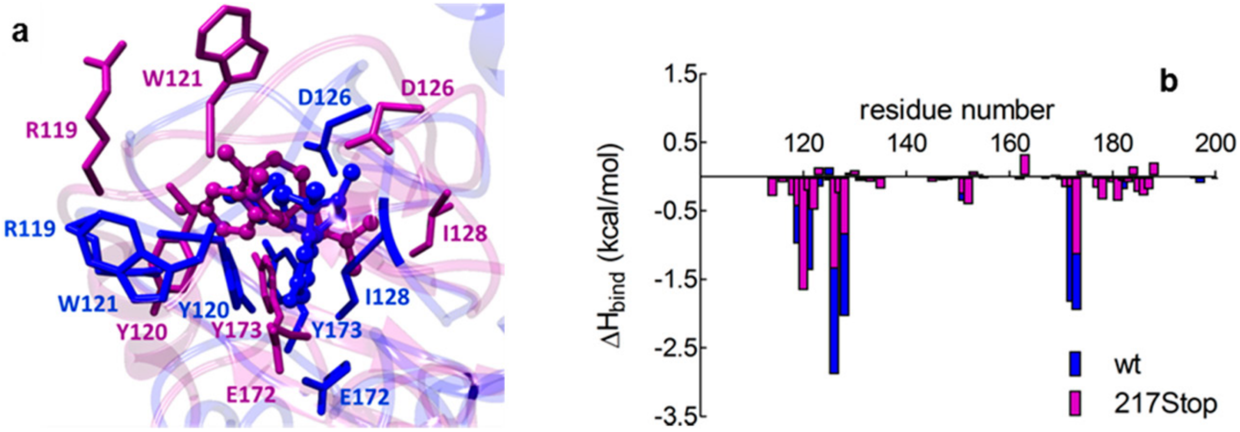

Figure 16.9: In silico mutagenesis of σ_1 receptor residues via deletion of the seven-residue YLFGQDP sequence from the protein C-terminal domain. (a) Comparison of the equilibrated MD snapshots of the *wt* (blue) and C-terminal seven-residue-truncated σ_1 receptor (magenta) in complex with PTZ. The image is a close-up of the receptor binding site. The ligand is shown as balls and sticks colored according to the respective protein complex. Hydrogen atoms, water molecules, ions, and counterions were omitted for the sake of clarity. (b) Comparison of contributions of σ_1 receptor residues to PTZ binding for the *wt* and C-terminal seven-residue-truncated protein.

effect on ligand binding, if any at all.

16.6 Even small deletions in the σ_1 C-terminal end abrogate ligand binding

As briefly mentioned above, σ_1 ligand binding is abrogated when more than 15 amino acids are removed from the C-terminal end of the protein.[181] Thus, we further investigated this aspect by deleting 7, 15, and 23 amino acids from the C-terminal end of the σ_1 receptor and determined the affinity of the truncated receptors for PTZ. As expected, elimination of 15 and 23 amino acids resulted in the loss of PTZ binding ability (Figure 16.1 and Table 16.2). More interestingly, also, the removal of only seven residues from the receptor C-terminal end led to a considerable decrease in the level of PTZ binding (SB = 37 %). Again, these experiments were rationalized by the corresponding *in silico* assays. While the major deletions resulted in a partially unfolded structure of the receptor missing a large portion of the ligand binding site, the affinity of the seven-residue-truncated protein for PTZ remained low (Figure 16.9a), as quantified by the ΔG_{bind} value of $-8.80\,\mathrm{kcal\,mol^{-1}}$. The corresponding $\Delta\Delta G_{bind}$ of $-1.22\,\mathrm{kcal\,mol^{-1}}$ nicely correlates with the 63 % decrease in affinity with respect to that of the *wt* protein reported by in vitro mutagenesis. The seven deleted amino acids are not directly involved in ligand binding; however, the missing YLFGQDP sequence results

σ_1 residue	specific binding of PTZ [%]	ΔG_{bind} [kcal mol^{-1}]	$\Delta\Delta G_{bind}$ [kcal mol^{-1}]
wt	100	-10.02 ± 0.05	-
S125A	49 ± 1.5	-8.57 ± 0.09	-1.45
T127A	45 ± 2.3	-8.78 ± 0.1	-1.24
V145A	78 ± 14	-9.89 ± 0.07	-0.13
F146A	57 ± 0.3	-9.42 ± 0.09	-0.60
Y147A	121 ± 4.1	-8.80 ± 0.06	-1.22
R175A	10 ± 4.1	-8.00 ± 0.10	-2.02

Table 16.3: *In vitro/in silico* site-directed mutagenesis of σ_1 residues belonging to the region between the protein SBDLI and SBDLII motifs. $\Delta\Delta G_{bind} = \Delta G_{bind,wt} - \Delta G_{bind,mutant}$; by this definition, a negative value of $\Delta\Delta G_{bind}$ indicates a favorable contribution for the *wt* residue in that position and vice versa.

in a structural modification of the receptor that, like a domino effect, propagates along the protein backbone to the binding site (Figure 16.9b). This overall configuration rearrangement directly affects three σ_1 residues most important for ligand binding: R119, D126, and E172. Specifically, the interaction of D126 with PTZ becomes less favorable by 1.54 kcal mol^{-1} with respect to the wt isoform, while E172 decreases its contribution by 1.68 kcal mol^{-1}.

16.7 DISTAL RESIDUES ALSO SHAPE THE σ_1 BINDING SITE

Lastly, to determine whether other σ_1 receptor residues could play a critical role in binding PTZ, several alternative positions between the SBDLI and -II protein domains were substituted with alanine. *In silico* mutagenesis results suggested that the hydrophobic V145 and the aromatic F146 and Y147 residues, when mutated to alanine, result in minor (if any) changes in the protein binding site conformation (Table 16.3). These results are confirmed by the corresponding in vitro experiments, showing that for these three residues the SB values range between 57 and 121 %. However, the alanine mutants of the basic amino acid R175 and of the two polar residues (S125 and T127) show a moderate (S125A and T127A) to strong (R175A) influence on PTZ binding, as revealed by the drastically less favorable $\Delta\Delta G_{bind}$ values of -1.45, -1.24, and -2.02 kcal mol^{-1}, respectively (Table 16.3), and supported by the corresponding SB values (49 %, 45 %, and 10 %, respectively). The S145A and T127A mutations transform the environment in the proximity of the negatively charged D126 from polar to hydrophobic that, in turn, decreases the strength of its salt bridge with PTZ (ADL values of (4.76 ± 0.07) Å and (4.69 ± 0.10) Å for S145A and T127A, respectively). The case of the R175A mutant is more complex, as experiments detect a drastically reduced affinity of this mutant σ_1 isoform for PTZ (SB = 10 %). The calculated free energy of binding differs

wt	Y120	Y173	R175	*wt*	Y120	Y173	A175
R114	$+0.02$	-0.91	-0.88	R114	-0.01	-0.73	$+0.02$
Y120	-	-0.26	-0.71	Y120	-	-0.03	-0.12
Y173	-	-	$+0.02$	Y173	-	-	-0.02
R175	-	-	-	A175	-	-	-
$\sum \Delta H_{bind}$	-	-	-2.72	$\sum \Delta H_{bind}$	-	-	-0.89

Table 16.4: Per residue free energy decomposition for *wt* and R175A mutant σ_1 receptors in complex with PTZ. All energy values are inkcal mol^{-1}. Standard deviations range from ±0.01 to ±0.10.

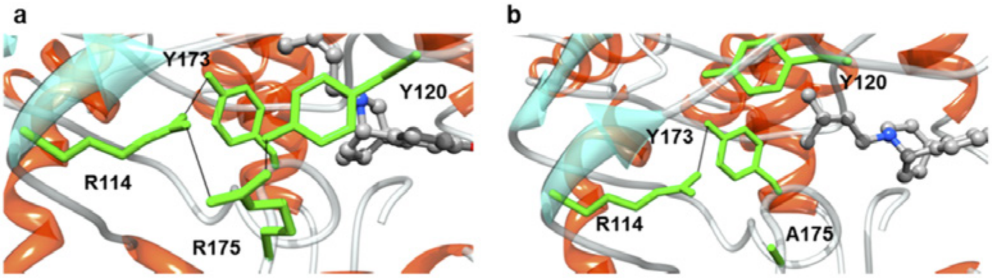

Figure 16.10: Details of the residues involved in a structurally stabilizing interaction of the (a) *wt* and (b) R175A mutant σ_1 receptor in complex with PTZ as obtained from equilibrated MD simulation snapshots. The protein backbone is shown as a transparent ribbon colored by secondary type (orange, α- helices; cyan, β-sheets; light gray, coils). The main residues involved in the interactions are shown as labeled green sticks. PTZ is shown as balls and sticks colored by element (C, gray; O, red; N, blue). In all panels, hydrogen atoms, water molecules, ions, and counterions were omitted for the sake of clarity.

considerably from that of the *wt* σ_1 complex ($\Delta\Delta G_{bind} = -2.02\,\text{kcal mol}^{-1}$), although this residue is not directly involved in PTZ binding. Importantly, however, along the entire MD course R175 forms a stable, bifurcated H-bond with Y120 and R114. These residues, in turn, stabilize the conformation of Y173 for productive binding via another direct H-bond (Figure 16.10). All these interactions translate into a $-2.72\,\text{kcal mol}^{-1}$ global favorable enthalpic contribution of these four amino acids to ligand binding, as detailed in Table 16.4. As discussed above, both Y120 and Y173 play a major role not only in direct PTZ binding but also in shaping the entire σ_1 binding site. Thus, replacing R175 with alanine results in an almost complete loss of the H-bond interaction network (Figure 16.10): the aromatic interaction between Y120 and PTZ is lost, the entire binding site is enlarged, and the corresponding complex stabilization energy decreases dramatically [$0.89\,\text{kcal mol}^{-1}$ (Table 16.4)].

16.8 CONCLUSIONS

The combined *in vitro/in silico* mutagenesis study reported here confirms some previous knowledge of the structural features of the σ_1 receptor and its binding site but also, and perhaps more importantly, qualifies and quantifies the role of several receptor residues that figure prominently in receptor-ligand binding.

Specifically, among those residues belonging to the putative receptor binding pocket, replacing I128 and Y173 with alanine almost abrogates PTZ binding, which is consistent with a drastic reduction of stabilizing, hydrophobic interactions. The specific nature of the anionic residue E172 is critical for PTZ binding in that not only its replacement with alanine but also an exchange with a residue of a similar nature but with a smaller side chain (E172D) results in the total failure of receptor ligand binding. The role of σ_1 amino acids belonging to the SBDLI and -II domains has been differentiated and rationalized: while a critical role in maintaining the protein secondary structure of this protein portion with respect to the cellular membrane has been verified for those residues belonging to the first domain, mutagenesis performed on residues in the SDBLII region did not affect the affinity of the receptor for PTZ. The removal of small sequences from the C-terminal part of the protein (e.g., seven residues) resulted in a substantial decrease in ligand binding activity, as these deletions result in a general reconfiguration of the receptor binding pocket, ultimately involving those residues that constitute the PTZ main anchor points. Finally, this combined approach unveiled the substantial role exerted by other σ_1 residues in ligand binding; for instance, the series of polar residues S125, T127, and R175 all serve to maintain the high affinity of the σ_1 receptor for PTZ, and their replacement with the small, apolar alanine results in a neat decrease in receptor ligand binding activity.

17

SMOOTHENED RECEPTOR MUTATIONS DICTATE RESISTANCE TO VISMODEGIB IN BASAL CELL CARCINOMA[1]

The smoothened receptor (SMO) regulates the Hedgehog (Hh) pathway, and the tumor suppressor gene PTCH1 normally functions by repressing the activity of this receptor. Inactivating PTCH1 mutations are frequent in basal cell carcinomas (BCCs) and in a subset of medulloblastomas, resulting in a constitutive Hh pathway activity. When defects in this pathway are detected, a treatment with vismodegib—a SMO inhibitor— results in impressive tumor regression. BCC is the most frequent skin cancer, with an incidence increasing in the last 30 years.[182] A secondary mutation that interfere with drug binding, but keeps the pathway active, has been reported in medulloblastoma patients, conferring drug resistance to the unlucky patients.

In the work described in this chapter, we reported the molecular mechanisms of resistance to vismodegib in two different BCC cases: a primary resistance with SMO$^{\mathrm{G497W}}$ mutation, and a secondary resistance with SMO$^{\mathrm{D473Y}}$ mutation. Two patients enrolled in a phase II trial with vismodegib for metastatic and locally advanced BCC (ClinicalTrials.gov Identifier:

---

[1] The matherial presented in this chapter was published at: Pricl, S., Cortelazzi, B., Dal Col, V., Marson, D., Laurini, E., Fermeglia, M., et al. (2014). Molecular Oncology. doi:10.1016/j.molonc.2014.09.003

NCT01367665) are reported and discussed, as examples of primary and acquired resistance to the vismodegib, respectively. The *in silico* analysis, on which I collaborated, demonstrated that:

- in SMO^{G497W} (primary resistance) there is a partial obstruction of the protein drug entry site, caused by a conformational rearrangement;
- in SMO^{D473Y} (secondary resistance) there is a direct effect on the binding site geometry, with a complete disruption of a binding-stabilizing hydrogen bond network.

Patient 1: a case of vismodegib primary resistance in BCCs

The first patient was an 82-years old woman presenting with a BCC metastatic to liver, lung and bones. After histological confirmation of liver metastasis, she received radiation therapy to lumbar (L2-L4) and cervical (C3) secondary lesions and she started vismodegib 150 mg/die. After two months of continuous treatment, CT scans showed disease progression at all sites (primary resistance).

Patient 2: a case of vismodegib acquired resistance in BCCs

The second patient was a 78-years old man presenting with a large (12 cm), ulcerated lesion of the supra-scapular skin on which a diagnosis of BCC was rendered. Because a surgical approach would have led to substantial morbidity, this patient was started on a 150 mg/die vismodegib regimen. The lesion dramatically reduced after the first month, and a complete clinical response was obtained five months later. However, after eleven months on vismodegib, two subcutaneous nodules appeared in the area of the previous lesion. Both lesions were surgically removed and the histology was consistent with recurrent BCC suggesting the development of an acquired resistance.

Personal contribution

In this work particularly I focused on the use of steered molecular dynamic (SMD) to study the entrance of vismodegib into the binding site of the mutated SMO^{G497W} receptor. With this approach, we were able to give a molecular explanation of the drug resistance conferred by this mutation, that occur away from the drug-binding site. Also, this work was one of the first in which I used the lipid membrane simulation protocol employing the *lipid11 force filed.* The receptor structure was optimized inserted in an explicit membrane, a better model of its physiological environment.

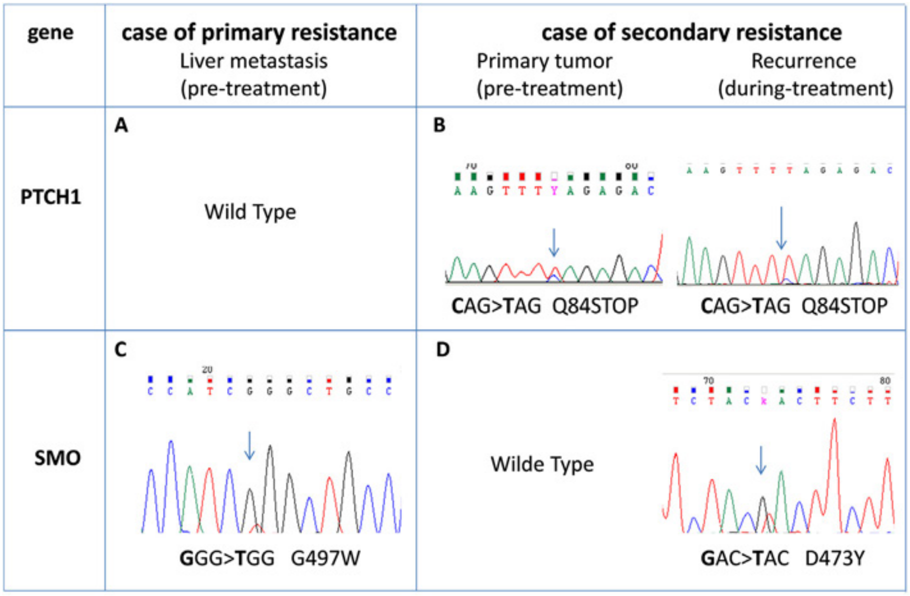

Figure 17.1: Pre-treatment BCC liver metastasis of the first case (patient 1, primary resistance) showed PTCH1 wild type gene (A) and the SMO G49W mutation (C). Pre-treatment primary tumor and BCC recurrence of the second case (patient 2, acquired resistance) carried the nonsense Q84Stop PTCH1 mutation (B) while the SMO D473Y mutation was observed only in the recurrence BCC sample (D).

17.1 PTCH1 is wild type in vismodegib primary resistance and mutated in acquired resistance to SMO in BCC

To explore possible mechanisms of Hh pathway activation in these two BCC cases considered, we first performed PTCH1 sequencing. In the pre-treatment BCC liver metastasis of the case showing primary resistance (patient 1), no PTCH1 mutation was observed (Figure 17.1A). By contrast, the pre-treatment primary biopsy of the case showing acquired resistance (patient 2) revealed the PTCH1 nonsense mutation CAG > TAG creating a premature STOP codon (pQ84) in the exon 2 (Figure 17.1B). This PTCH1 mutation predicts translation to a heavily truncated protein, causing loss of function of the protein and preventing inhibition of SMO. As expected, the same PTCH1 mutation was also observed in the recurrence sample taken during vismodegib (Figure 17.1B).

17.2 Two distinct missense SMO mutations characterize primary and secondary vismodegib resistance in BCCs

Next, we evaluated the SMO mutational status. In the case showing primary resistance (patient 1), the analysis of pretreatment liver metastasis revealed the SMO missense mutation

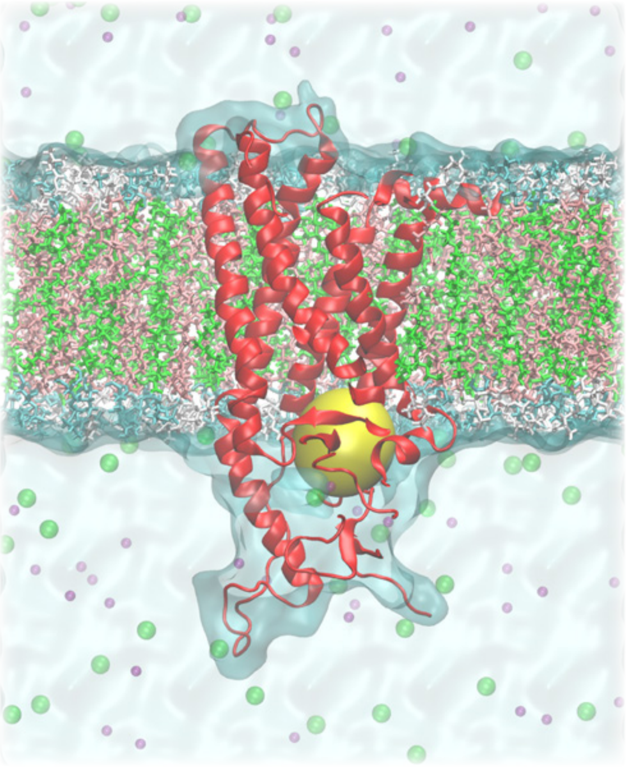

Figure 17.2: Cross section of the 3D structure of the SMO receptor embedded in a POPC/POPE (2:2) membrane model. Water is shown as a light cyan surface, while Na^+ and Cl^- ions are visible as green and purple spheres, respectively. Lipids are portrayed as ball-and-sticks, the polar heads of POPC and POPE depicted in white and cyan, respectively, while the corresponding hydrophobic tails are colored green and salmon, respectively. The membrane solvent accessible surface area is highlighted in transparent forest green. The SMO receptor protein is shown as a red ribbon, the inhibitor binding region being evidenced by a yellow sphere.

GGG > TGG at exon 9, leading to the amino acid substitution G497W in the corresponding protein (Figure 17.1C). Primary tumor and node metastasis also exhibited the same SMO missense mutation GGG > TGG at exon 9. By contrast, in the pre-treatment primary BCC of the second case (acquired resistance, patient 2), no SMO mutations were detected (Figure 17.1D, left panel); however the sample obtained from the recurrence on vismodegib showed the missense mutation GAC > TAC at exon 8, leading to the single amino acid substitution D473Y (Figure 17.1D, right panel) confirming the acquired resistance to the inhibitor.

17.3 SMO^{G497W}: A DISTAL MUTATION THAT OBSTRUCTS VISMODEGIB ENTRY TO SMO BINDING SITE LEADING TO PRIMARY BCC RESISTANCE

To gain mechanistic insight regarding the resistance posed by the mutant SMO proteins we performed a thorough in silico analysis of the wild type and both clinically relevant SMO mutant alleles (Figure 17.2).

As shown in Table 17.1, the MM/PBSA-derived IC_{50} for the SMO^{G497W}/vismodegib complex is 69 nM, a value slightly higher than the experimental/calculated IC_{50} derived for the wild-type (*wt*) receptor (3 and 2.5 nM, respectively). This result indicates only a moderate

SMO complex	ΔG_{bind} [kcal mol^{-1}]	$\Delta\Delta G_{bind}$ [kcal mol^{-1}]	$IC_{50,\mathrm{calc}}$ [nM]	$IC_{50,\mathrm{exp}}$ [nM]
wt	-11.75 ± 0.11	-	2.5	3
D473H	-9.27 ± 0.10	-2.48	159	-
G497W	-9.78 ± 0.10	-1.97	69	-

Table 17.1: *In silico* estimation of free energy of binding (ΔG_{bind}) for *wt*, SMO$^{\mathrm{D473H}}$ and SMO$^{\mathrm{G497W}}$ mutant receptors in complex with vismodegib.

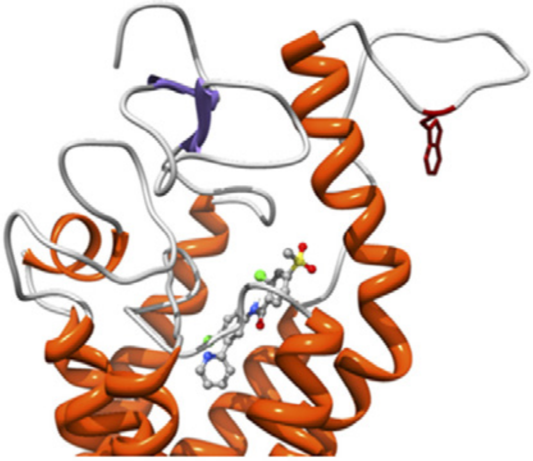

Figure 17.3: Zoomed view of the SMO$^{\mathrm{G497W}}$ binding site in complex with vismodegib. The receptor is shown as a secondary-structure colored ribbon (orange, α-helices; purple, β-sheets; gray, coils). Vismodegib is portrayed as atom-colored sticks-and-balls (red, O; blue, N; green, Cl; S, sulfur; gray, C). Residue W497 is evidenced as dark red sticks. Hydrogen atoms, water molecules, ions and counterions are omitted for clarity.

direct effect of the mutation G497W on the protein affinity for the inhibitor, in keeping with a distal position of G497W with respect to the protein drug binding site.

However, in the presence of the mutant residue the entire protein region undergoes a conformational rearrangement, ultimately resulting in a partially obstructed drug entry site. Our simulations of the binding process of vismodegib to SMO indeed shows that the vismodegib link with the protein binding pocket is substantially hindered in the presence of the G497W mutation (Figure 17.3 and Figure 17.4).

This fundamentally implies that, in time, the effective vismodegib concentration within the SMO$^{\mathrm{G497W}}$ binding site is significantly lower than in the case of the *wt* receptor. Accordingly to our simulation, other molecular mechanisms are likely contributing to the resistance of SMO$^{\mathrm{G497W}}$ to vismodegib. A direct comparison of the *wt*/mutated protein structures in the area surrounding position 497 revealed that, in the presence of the tryptophan mutant residue, the entire region undergoes a conformational rearrangement, thus resulting in a narrowing of the protein drug entry site (Figure 17.3). For this reason, in the presence of the G497W mutation vismodegib might be less able to reach the protein binding pocket and, hence, less effective in its inhibitory activity. Further, as we can see from Figure 17.4 and Figure 17.6, not only quite a higher force (and hence energy) is required to vismodegib to

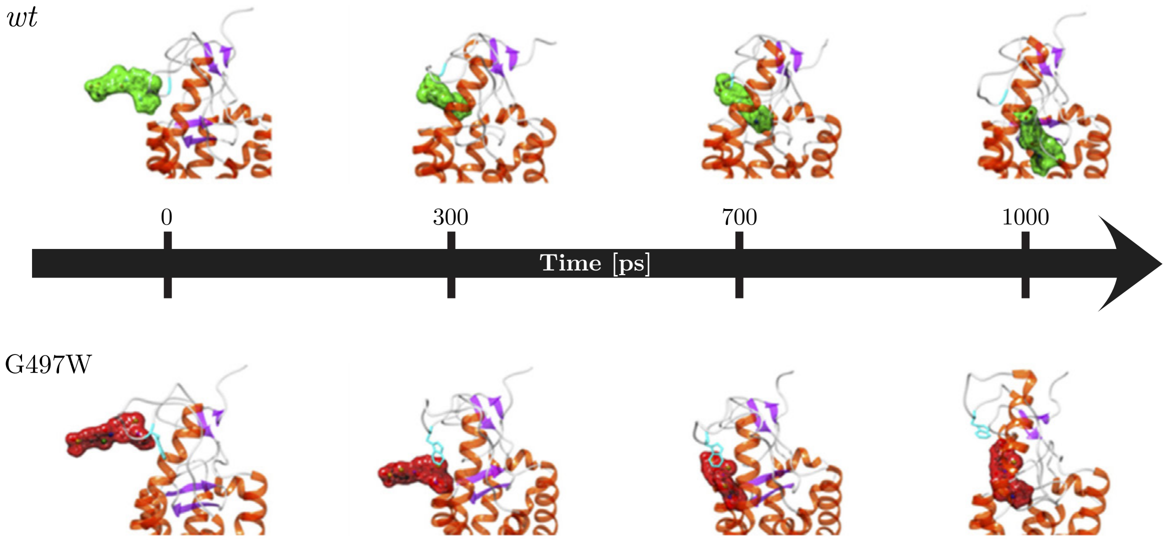

Figure 17.4: SMD snapshots of vismodegib entering the receptor binding pocket. The receptor is shown as a secondary-structure colored ribbon (orange, α-helices; purple, β-sheets; gray, coils), while vismodegib is highlighted by its green/red van der Waals surface. Hydrogen atoms, ions, counterions and water molecules are omitted for clarity.

reach its binding site in the presence of the mutant residue (Figure 17.6) but also, and perhaps even more interestingly, contrarily to the *wt* case, for SMO$^{\mathrm{G497W}}$ the drug has not yet reached its correct orientation within the protein binding pocket after the same time lag (Figure 17.4). In practical terms this fundamentally might imply that, in time, the effective vismodegib concentration within the SMO$^{\mathrm{G497W}}$ binding site is significantly lower than in the case of the *wt* receptor and this, is our opinion, constitutes a novel and effective mechanism of drug primary resistance.

17.4 SMO$^{\mathrm{D473Y}}$: a binding site mutation that directly interferes with vismodegib binding and leads to secondary BCC resistance

When considering vismodegib in complex with SMO$^{\mathrm{D473Y}}$, the alternative mutant isoform of SMO detected in the patient specimen with acquired BCC resistance, the calculated IC$_{50}$ value is 159 nM. This translates into an almost two orders of magnitude decrease in protein affinity to vismodegib with respect to the *wt* receptor (Table 17.1), clearly revealing a direct effect of the mutated residue on vismodegib binding. Notably, D473 is involved with other two residues (R400 and H470) in a pivotal network of hydrogen bonds that keeps the SMO binding pocket in the proper shape and stabilizes vismodegib binding (Figure 17.5). The

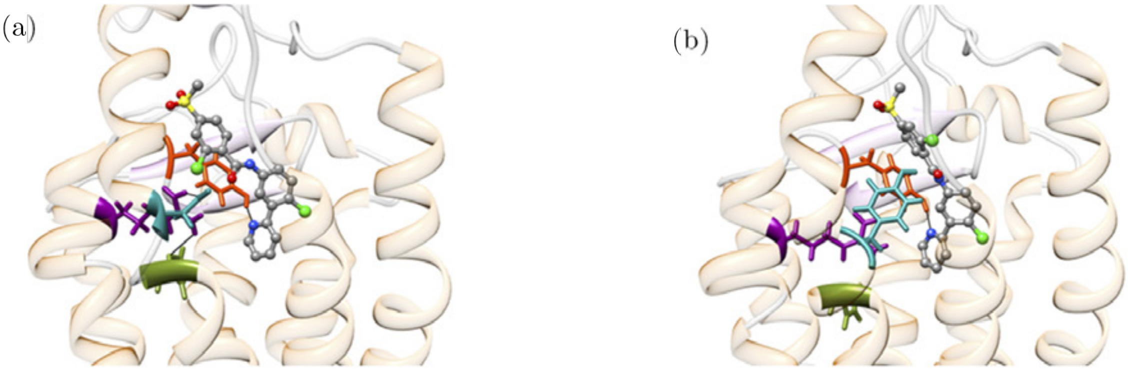

Figure 17.5: Zoomed views of the (a) *wt* and (b) SMO^{D473Y} mutant binding sites in complex with vismodegib. In both panels, the receptor secondary structure is outlined as a semi-transparent ribbon (orange, α-helices; purple, β-sheets; gray, coils). Vismodegib is portrayed as atom-colored sticks-and-balls (red, O; blue, N; green, Cl; S, sulfur; gray, C). The triad of residues involved in the hydrogen-bond network are highlighted colored sticks: R300, dark magenta; H470, olive drab; D/Y473, dark cyan. Y394 is also shown as dark red sticks. H-bonds are evidenced as black lines.

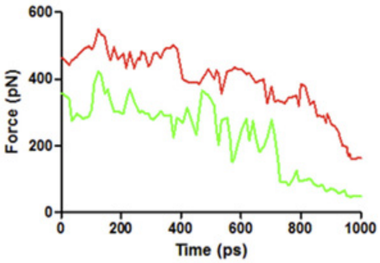

Figure 17.6: Rupture force vs. time during the entry process of vismodegib within the *wt* (green) and SMO^{G497W} (red) binding site.

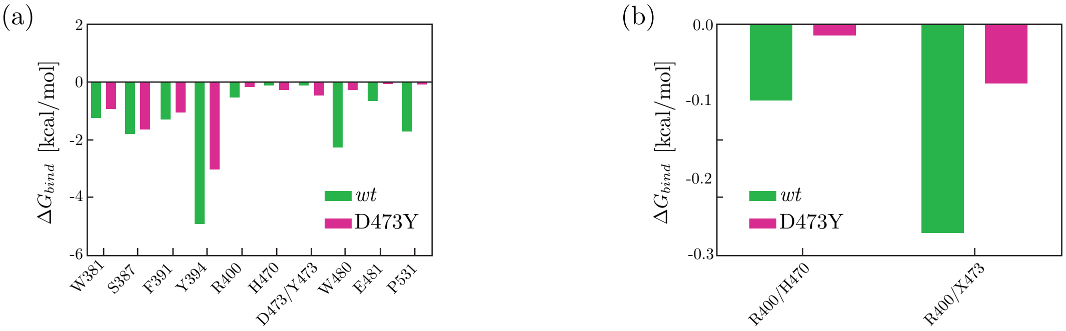

Figure 17.7: Comparison of vismodegib binding energy contributions from *wt* and D473Y SMO residues (a). Comparison between hydrogen bond network stabilization energies for SMO residues belonging to the *wt* and SMO^{D473Y} triad residues in the relevant vismodegib complexes (b). X denotes either D or Y residue at position 473.

aromatic side chain of the 473Y residue induces a considerable effect on the binding site geometry and leads to the total disruption of the stabilizing hydrogen bond network; hence, the inhibitor is shifted from its optimal position (Figure 17.5b). In details, in the presence of the D473Y mutation, a considerable effect on the binding site geometry is induced, required for the proper accommodation of the residue aromatic side chain, ultimately leading to the total disruption of the stabilizing hydrogen bond network. The inhibitor is hence shifted from its optimal position, the only surviving interaction with the receptor being an intermitted hydrogen bond with Y394.

These evidences are substantiated by the corresponding per residue energy deconvolution of the free energy of binding, as shown in Figure 17.7. As we see, all receptor residues mainly involved in vismodegib binding undergo a severe reduction in the stabilizing contribution to inhibitor binding in the presence of the mutation (Figure 17.7a). Analogously, upon disruption of the hydrogen bond network among the SMO triad residues, the relevant, favorable contribution to receptor/inhibitor binding plummets drastically (Figure 17.7b).

17.5 Further discussion and conclusions

This study presents for the first time clinical, molecular and in silico evidence of primary and acquired SMO mutation-mediated resistance to vismodegib in BCC. Indeed, the true-cut based assessment of the SMO G497W missense mutation in the liver pre-treatment metastasis of the first patient exhibiting a progression of disease after two months on vismodegib provides a good example of primary resistance to the drug. To our knowledge, this SMO mutation has never been previously described. However, its location in the most frequently mutated SMO region in BCC (exons 8–10) where other SMO mutations have already shown a constitutive ligand-independent signal transduction, argues in favor of its oncogenic role.[183] Furthermore, since the lack of a PTCH1 inactivating mutation reinforced this assumption, we sought to explore the effects exerted by this mutation on the inhibitor binding to the mutated SMO protein. By *in silico* experiments we demonstrated that in the presence of the W497 residue the entire protein region undergoes a conformational rearrangement, which ultimately results in a partial obstruction of the protein drug entry site. This obstruction, leading to a significant decreasing of the effective vismodegib concentration within the $\mathrm{SMO}^{\mathrm{G497W}}$ binding site (lower than that in the case of the *wt* receptor), gives a mechanistic explanation for a novel effective drug resistance. In this respect, the presence of such a SMO mutation in BCC candidate to vismodegib should definitely be assessed in a greater number of tumors with primary resistance to the inhibitor. This would eventually allow defining $\mathrm{SMO}^{\mathrm{G497W}}$ as a possible biomarker for drug resistance, ultimately resulting in the avoidance of unnecessary toxicity effects and costs limitation to non-responding patients.

Concerning the second patient, the presence of the PTCH1 inactivating mutation in the pre-treatment primary lesion along with absence of SMO mutation could explain the complete clinical response obtained after six months of continuous vismodegib treatment. Indeed, loss of PTCH1 function by inactivating mutations relieves normal SMO inhibition leading to the activation of Hh targets genes. By contrast, the secondary drug resistance observed after eleven months is likely to be ascribable to the appearance of the missense SMO D473Y substitution in the recurrence sample. Notably, another amino acid substitution of the same SMO aspartic acid (D473H) was designated as the mechanism of vismodegib resistance in medulloblastoma.[82] More recently, the detrimental role of D473 in SMO function has been found out by an elegant in vitro study where, by replacing this aspartic acid residue with every other amino acid, all mutants were resistant to vismodegib.[184] In keeping with these findings, our analysis of the structural effects of the SMO D473Y clearly revealed a direct and significant effect on the binding site geometry. The inhibitor is shifted from its optimal position because the aromatic side chain of the 473Y residue causes the total disruption of the stabilizing hydrogen bond network involving the D473 with other two residues (R400 and H470). As for G497W, this SMO point mutation should also be confirmed in a greater series of BCCs in order to definitely claim its role in secondary resistance to vismodegib. As a general remark, we acknowledge that the presented evidences could be considered only reasonably correlated to the resistance phenotype, and indeed our analysis requires further confirmation through functional analysis. Under this perspective, in vitro and in vivo experiments are under way in our laboratories to definitively assess the role of these two SMO mutations as possible biomarkers for vismodegib resistance.

Similarly to medulloblastoma, our data further raise the issue of overcoming the resistance due to mutation of the drug target. Under this perspective, efforts aimed at identifying second-generation drugs showing potent activity against SMO mutants are mandatory. To this goal, a panel of compounds has already been screened *in vitro*. Several promising antagonists able to inhibit tumor growth mediated by drug-resistant SMOs were selected in murine allograft model of medulloblastoma,[184] that could be tested also in BCC.

Another strategy worth pursuing is the inhibition of the Hh pathway through other mechanisms, the activity of itraconazole or arsenic oxide in blocking vismodegib-resistant BCC both in vitro and in vivo being prime examples.[185, 186]

A further alternative approach for facing vismodegib resistance could consist in exploring other pathways interacting with Hh signaling in BCC and leading to an SMO-independent stimulation of Gli1 such as EGFR,[187] the atypical protein kinase C ι/λ,[188] the protein kinase A[189] and, similarly to medulloblastoma, the PI3K pathway.[184, 190]

Finally, a clinical point to be stressed is that our two cases of vismodegib resistance occurred in patients who had not received previous radiation therapy. We cannot exclude that Hh inhibitor resistance outbreak could be higher in patients having received a radiation insult, as well as it is possible that alternative therapeutic schedules may alter resistance mechanism development.[190]

In this work we discussed two different SMO mutations representing examples of primary or secondary resistance respectively to vismodegib in two distinct BCC cases. The screening for the reported SMO mutations and the search for new therapeutic strategies to overcome related resistance mechanisms represent a priority in the treatment of patients with advanced BCCs.

18

CONCLUSIONS & FUTURE DIRECTIONS

Gene therapy holds great expectations for the treatment of maladies very different in nature. With the right medicament it's possible to tackle problems with a very precise and targeted approach, limiting considerably the effects on non-damaged compartments. Possibles targets are first and foremost different kind of cancers, many viral infections, such as HIV, and all human disease that are caused by a genetic disfunction.

One of the most limiting factors on the use of nucleic acids in this, although promising, approach is the difficulty of these molecules in reaching their site of action. To this regard, dendrimers are one of the most interesting vehicles proposed. In continuous development from 1978, this class of polymers has great potential as nanocarriers for different kind of drugs, nucleic acids among others. Many of the key properties of dendrimers are strictly linked to their particular structure, which in turn is affected by the chemical composition of the molecule. To better understand their morphology and their interactions with other key macromolecules (e.g., nucleic acids, proteins, lipid membranes) molecular simulations are a fundamental tool that can give uniques informations.

In this regard, we saw the morphological characterization of two new families of dendrimers, viologen and carbosilane. In particular a back-folding phenomena was observed for the viologen dendrimers of higher generations. To better understand the binding interactions of the dendrimers with their partner, we enlightened the importance of a parameter that can assess the performance of each active individual dendrimer branch directly involved and interacting. With respect to carbosilane dendrimers, this parameter was the normalized effective binding energy $\Delta G_{bind,eff}/N_{eff}$.

For the first time, steered molecular dynamics was used for the creation of the complexes between the oligodeoxynucleotide and the carbosilane dendrimer, overtaking the lacking of good docking procedures for this kind of molecules.

We changed then the point of view in the study of carrier-cargo binding and efficacy in siRNA delivery. We studied the effects of different—in length and structure—overhangs in the transfection capability of a G5-siRNA complex. A primary parameter was found to be the flexibility of the overhangs, to achieve a good binding but also an optimal siRNA release.

A lipid membranes simulation protocol was also developed, and will be used to shed light on dendrimer-membrane interactions, one of the most important property for dendrimers efficacy and toxicology.

Many of the techniques examined in these works were also used in some side projects in which our research group was involved. One of the main fields of work of our group is the σ_1 receptor, and the lipid membrane simulation protocol was used to refine our σ_1 receptor 3D homology model recently developed. Furthermore, we used this optimized model of the receptor to give a better description of its binding site. Also, in the study of two different mutations of the smothered (SMO) receptor, we simulated the protein in a lipid membrane to have a better representation of its physiological conditions. The steered molecular dynamics technique was fundamental in the study of the $\mathrm{SMO}^{\mathrm{G497W}}$ mutation, giving a possible explanation of the resistance to the drug vismodegib conferred by this mutation.

As we have seen, computer simulations today are an important tool in the hands of researchers in different fields. The applicability of these techniques to different objects of study also gives a big opportunity to the researcher to contribute in key aspects of different projects. Increase in computational power and refinement of algorithms are making feasible the study of different problems at an increasing precision level. In the near future our intention is to use the lipid membrane model developed as a tool to study the interactions of dendrimer with biological membranes.

Differentiate in the binding of similar dendrimers with their cargo is also a delicate task, for which often the MM/PBSA approach is used. This method has some limitation in the case of highly charged molecules like dendrimers and nucleic acids, and so it will be important to implement other estimation of the free energy of binding, like Free Energy Perturbation methods. Currently we are implementing these techniques in the “simpler” study of B-Raf ligands, with in mind the applicability of the methodology in the study of carrier-cargo complexes.

Acronyms

ADL average dynamic length. 117, 119, 134, 135, 138, 143
ADV average dynamic volume. 141
APL area per lipid. 53
ASM experimental alanine scanning. 126

BCC basal cell carcinoma. 22, 23, 147–150, 152, 154–156

CAS computational alanine scanning. 126, 127
CNV copy number variation. 49
COM center of mass. 61, 62, 91, 100, 102

DMPC 1,2-dimyristoyl-sn-glycero-3-phosphocholine. 14
DNA deoxyribonucleic acid. 46, 49
dsRNA double-stranded RNA. 6

EB ethidium bromide. 82, 84
EDA ethylenediamine-core. 96, 98–100

FDA US Food and Drug Administration. 4, 23

HB hydrogen bond. 117, 119, 124
HBA hydrogen bond acceptor. 116
Hh Hedgehog. 22, 23, 147, 149, 155, 156
HIV Human Immunodeficiency Virus. 4, 5, 16, 87

HSA human serum albumin. 13, 91, 93
Hsp27 heat shock protein 27. 72, 73
HSV Herpes Simplex Virus. 16, 87
HY hydrophobic. 116
HYAr hydrophobic aromatic. 116

INT interface area. 105

LJ Lennard-Jones. 47

MD molecular dynamics. 29, 32, 33, 37, 44, 46, 47, 52, 55, 58, 65, 75, 78, 80, 83, 88, 91, 93, 96, 99, 100, 103, 105, 107, 117, 120, 121, 124, 126, 134, 141, 144
miRNA microRNA. 6
MM molecular mechanic. 29, 32
MM/GBSA Molecular Mechanics/Generalized Born Surface Area. 55, 56, 58, 122
MM/PBSA Molecular Mechanics/Poisson Boltzmann Surface Area. 55, 56, 58, 61, 103, 107, 117, 119, 121, 126, 127, 129
mRNA messenger RNA. 5, 6

NA nucleic acid. 3, 4, 6, 13, 31, 36, 37, 43, 45, 52, 55, 58, 62, 63, 71, 76, 95
NPT constant pressure and temperature. 47, 52
NSAID nonsteroidal anti-inflammatory drug. 18
NVT constant volume and temperature. 52, 53

ODN oligodeoxynucleotide. 5, 95, 96, 100, 102, 103, 105–108, 110–112

PAMAM poly(amidoamine). 9, 11, 13–16, 18, 19, 71, 84, 96, 98–100
PBC periodic boundary conditions. 45, 46
PEI polyethyleneimine. 8, 79
PI positive ionizable. 116
PPI poly (propylene imine). 15
PRBFED per residue binding free energy decomposition. 122, 124–127
pri-miRNA primary miRNA. 6
PTGS post-transcriptional gene silencing. 6
PTZ (+)-pentazocine. 24, 133–139, 141–145

RISC RNA-Induced Silencing Complex. 6
RMSD root-mean-square deviation. 52, 121, 141
RNA ribonucleic acid. 5, 6
RNAi RNA interference. 5, 6, 82

SASA solvent accessible surface area. 57, 96, 98
SB salt bridge. 117, 119, 124
SBDLI steroid binding domain-like I. 139, 141, 143, 145
SBDLII steroid binding domain-like II. 116, 139, 141
shRNA short hairpin RNA. 6
siRNA small interfering RNA. 4–6, 8, 71–85
SMD steered molecular dynamic. 21, 61, 62, 82, 100, 102, 103, 148
SMO smoothened receptor. 21–24, 147, 149–152, 154–156
SNP single nucleotide polymorphism. 49

TCTP translationally controlled tumor protein. 72, 73
TEA triethanolamine. 10, 71, 84
TM transmembrane. 116

vdW van der Waals. 36, 45–47, 120, 124–126, 135

BIBLIOGRAPHY

[1] P. Goddard. Therapeutic proteins - A pharmaceutical perspective. *Advanced Drug Delivery Reviews*, 6(2):103–131, 1991. 4

[2] J. E. Talmadge. The pharmaceutics and delivery of therapeutic polypeptides and proteins. *Advanced Drug Delivery Reviews*, 10(2-3):247–299, 1993. 4

[3] S.-o. Han, R. I. Mahato, Y. K. Sung, and S. W. Kim. Development of biomaterials for gene therapy. *Molecular Therapy*, 2(4):302–317, 2000. 4

[4] J. M. Stribley, K. S. Rehman, H. Niu, and G. M. Christman. Gene therapy and reproductive medicine. *Fertility and sterility*, 77(4):645–657, April 2002. 4

[5] G. Maartens, C. Celum, and S. R. Lewin. HIV infection: epidemiology, pathogenesis, treatment, and prevention. *Lancet*, 384(9939):258–271, July 2014. 5

[6] J. P. Dassie and P. H. Giangrande. Current progress on aptamer-targeted oligonucleotide therapeutics. *Therapeutic delivery*, 4(12):1527–1546, December 2013. 5

[7] A. J. Perisé-Barrios, J. L. Jiménez, A. Domínguez-Soto, F. J. de la Mata, A. L. Corbí, R. Gómez, and M. A. Muñoz-Fernandez. Carbosilane dendrimers as gene delivery agents for the treatment of HIV infection. *Journal of controlled release : official journal of the Controlled Release Society*, 184:51–57, June 2014. 5

[8] E. Pędziwiatr-Werbicka, E. Fuentes, V. Dzmitruk, J. Sánchez-Nieves, M. Sudas, E. Drozd, A. Shakhbazau, D. Shcharbin, F. J. de la Mata, R. Gomez-Ramirez, M. A.

Muñoz-Fernandez, and M. Bryszewska. Novel 'Si-C' carbosilane dendrimers as carriers for anti-HIV nucleic acids: studies on complexation and interaction with blood cells. *Colloids and surfaces. B, Biointerfaces*, 109:183–189, September 2013.

[9] E. Pędziwiatr-Werbicka, D. Shcharbin, L. Chonco, P. Ortega, F. J. de la Mata, R. Gómez, B. Klajnert, M. Bryszewska, and M. A. Muñoz-Fernandez. Binding properties of water-soluble carbosilane dendrimers. *Journal of fluorescence*, 19(2):267–275, March 2009.

[10] L. Chonco, J. F. Bermejo-Martín, P. Ortega, D. Shcharbin, E. Pedziwiatr, B. Klajnert, A.-M. Caminade, F. J. de la Mata, R. Eritja, R. Gómez, M. Bryszewska, and M. A. Muñoz-Fernandez. Water-soluble carbosilane dendrimers protect phosphorothioate oligonucleotides from binding to serum proteins. *Organic and Biomolecular Chemistry*, 5(12):1886–1893, 2007.

[11] J. F. Bermejo, P. Ortega, L. Chonco, R. Eritja, R. Samaniego, M. Müllner, E. de Jesus, F. J. de la Mata, J. C. Flores, R. Gómez, and M. A. Muñoz-Fernandez. Water-soluble carbosilane dendrimers: synthesis biocompatibility and complexation with oligonucleotides; evaluation for medical applications. *Chemistry (Weinheim an der Bergstrasse, Germany)*, 13(2):483–495, 2007. 5

[12] B. L. Davidson and P. B. McCray. Current prospects for RNA interference-based therapies. *Nature Reviews Genetics*, 12(5):329–340, 2011. 6

[13] J. Han, Y. Lee, K.-H. Yeom, J.-W. Nam, I. Heo, J.-K. Rhee, S. Y. Sohn, Y. Cho, B.-T. Zhang, and V. N. Kim. Molecular basis for the recognition of primary microRNAs by the Drosha-DGCR8 complex. *Cell*, 125(5):887–901, June 2006. 6

[14] E. Bernstein, A. A. Caudy, S. M. Hammond, and G. J. Hannon. Role for a bidentate ribonuclease in the initiation step of RNA interference. *Nature*, 409(6818):363–366, January 2001. 6

[15] J. Martinez, A. Patkaniowska, H. Urlaub, R. Lührmann, and T. Tuschl. Single-stranded antisense siRNAs guide target RNA cleavage in RNAi. *Cell*, 110(5):563–574, 2002. 6

[16] D. Castanotto, K. Sakurai, R. Lingeman, H. Li, L. Shively, L. Aagaard, H. Soifer, A. Gatignol, A. Riggs, and J. J. Rossi. Combinatorial delivery of small interfering RNAs reduces RNAi efficacy by selective incorporation into RISC. *Nucleic Acids Research*, 35(15):5154–5164, 2007. 6

[17] D. Grimm, L. Wang, J. S. Lee, N. Schürmann, S. Gu, K. Börner, T. A. Storm, and M. A. Kay. Argonaute proteins are key determinants of RNAi efficacy, toxicity, and persistence in the adult mouse liver. *The Journal of Clinical Investigation*, 120(9): 3106–3119, September 2010. 6

[18] S. M. Elbashir, J. Martinez, A. Patkaniowska, W. Lendeckel, and T. Tuschl. Functional anatomy of siRNAs for mediating efficient RNAi in Drosophila melanogaster embryo lysate. *The EMBO journal*, 20(23):6877–6888, December 2001. 6

[19] A.-L. Bolcato-Bellemin, M.-E. Bonnet, G. Creusat, P. Erbacher, and J.-P. Behr. Sticky overhangs enhance siRNA-mediated gene silencing. In *Proceedings of the National Academy of Sciences of the United States of America*, pages 16050–16055. Polyplus-Transfection, Bioparc, Boulevard Sebastien Brant, 67400 Illkirch, France., National Acad Sciences, 2007. 8, 79, 85

[20] O. Boussif, F. Lezoualc'h, M. A. Zanta, M. D. Mergny, D. Scherman, B. Demeneix, and J.-P. Behr. A versatile vector for gene and oligonucleotide transfer into cells in culture and in vivo: Polyethylenimine. In *Proceedings of the National Academy of Sciences of the United States of America*, pages 7297–7301. Laboratoire de Chimie Génétique, Centre National de la Recherche Scientifique, Faculté de Pharmacie, Illkirch, France., 1995. 8

[21] P. J. Flory. Molecular Size Distribution in Three Dimensional Polymers. I. Gelation 1. 63(11):3083–3090, November 1941. 9

[22] P. J. Flory. Molecular Size Distribution in Three Dimensional Polymers. II. Trifunctional Branching Units. *Journal Of The American Chemical Society*, 63(11):3091–3096, November 1941.

[23] P. J. Flory. Molecular Size Distribution in Three Dimensional Polymers. III. Tetrafunctional Branching Units. 63(11):3096–3100, November 1941. 9

[24] E. Buhleir, W. Wehner, and F. Vogtle. "Cascade"- and "Nonskid-Chain-like" Syntheses of Molecular Cavity Topologies. *Synthesis*, 1978(02):155–158, January 1978. 9

[25] D. A. Tomalia, M. Hall, S. Martin, and P. Smith. Preprints of the 1st SPSJ International Polymer Conference, Society of Polymer Science Japan, Kyoto, 1984 . In *1st SPSJ International Polymer Conference*, Kyoto, 1984. Conf. Soc. Polym. Sci. Jpn. 9

[26] S. Svenson and A. S. Chauhan. Dendrimers for enhanced drug solubilization. *Nanomedicine (London, England)*, 3(5):679–702, October 2008. 11

[27] P. Wu, M. Malkoch, J. N. Hunt, R. Vestberg, E. Kaltgrad, M. G. Finn, V. V. Fokin, K. B. Sharpless, and C. J. Hawker. Multivalent, bifunctional dendrimers prepared by click chemistry. *Chemical communications (Cambridge, England)*, (46):5775–5777, December 2005. 11

[28] E. R. Gillies and J. M. J. Fréchet. Designing macromolecules for therapeutic applications: polyester dendrimer-poly(ethylene oxide) "bow-tie" hybrids with tunable molecular weight and architecture. *Journal Of The American Chemical Society*, 124(47): 14137–14146, November 2002. 11

[29] D. A. Tomalia, V. Berry, M. Hall, and D. M. Hedstrand. Starburst dendrimers. 4. Covalently fixed unimolecular assemblages reiminiscent of spheroidal micelles. *Macromolecules*, 20(5):1164–1167, 1987. 11

[30] C. J. Hawker and J. M. J. Fréchet. A new convergent approach to monodisperse dendritic macromolecules. *Journal of the Chemical Society, Chemical Communications*, (15):1010–1013, 1990. 12

[31] K. L. Wooley, C. J. Hawker, and J. M. J. Fréchet. Hyperbranched Macromolecules via a Novel Double-Stage Convergent Growth Approach. *Journal Of The American Chemical Society*, 113(11):4252–4261, 1991. 12

[32] T. Kawaguchi, K. L. Walker, C. L. Wilkins, and J. S. Moore. Double exponential dendrimer growth. *Journal Of The American Chemical Society*, 117(8):2159–2165, 1995. 12

[33] R. Spindler and J. M. J. Fréchet. Two-step approach towards the accelerated synthesis of dendritic macromolecules. *Journal of the Chemical Society, Perkin Transactions 1*, (8):913–918, 1993. 12

[34] V. Maraval, J. Pyzowski, A.-M. Caminade, and J.-P. Majoral. "Lego" chemistry for the straightforward synthesis of dendrimers. *The Journal of organic chemistry*, 68(15): 6043–6046, July 2003. 12

[35] R. Esfand and D. A. Tomalia. Poly(amidoamine) (PAMAM) dendrimers: from biomimicry to drug delivery and biomedical applications. *Drug Discovery Today*, 6 (8):427–436, April 2001. 13

[36] P. Kumar, K. P. Meena, C. Choudhary, P. Kumar, P. Bajpayee, and D. S. Thakur. *Dendrimer: a novel polymer for drug delivery.* JITPS, 2010. 13

[37] D. A. Tomalia, H. Baker, J. Dewald, M. Hall, G. Kallos, S. Martin, J. Roeck, J. Ryder, and P. Smith. A new class of polymers: Starburst-dendritic macromolecules. *Polymer Journal*, 34(5 2):132–147, 2002. 13

[38] J. C. Roberts, M. K. Bhalgat, and R. T. Zera. Preliminary biological evaluation of polyamidoamine (PAMAM) Starburst™ dendrimers. *Journal of Biomedical Materials Research*, 30(1):53–65, 1996. 13, 15

[39] N. Malik, R. Wiwattanapatapee, R. Klopsch, K. Lorenz, H. Frey, J.-W. Weener, E. W. Meijer, W. Paulus, and R. Duncan. Dendrimers: Relationship between structure and biocompatibility in vitro, and preliminary studies on the biodistribution of 125I-labelled polyamidoamine dendrimers in vivo. *Journal of controlled release : official journal of the Controlled Release Society*, 65(1-2):133–148, 2000. 15

[40] H. R. Ihre, O. L. Padilla De Jesús, F. C. Szoka Jr, and J. M. J. Fréchet. Polyester dendritic systems for drug delivery applications: Design, synthesis, and characterization. *Bioconjugate Chemistry*, 13(3):443–452, 2002. 15

[41] O. L. Padilla De Jesús, H. R. Ihre, L. Gagne, J. M. J. Fréchet, and F. C. Szoka Jr. Polyester dendritic systems for drug delivery applications: In vitro and in vivo evaluation. *Bioconjugate Chemistry*, 13(3):453–461, 2002.

[42] R. Jevprasesphant, J. Penny, R. I. Jalal, D. Attwood, N. B. McKeown, and A. D'Emanuele. The influence of surface modification on the cytotoxicity of PAMAM dendrimers. *International journal of pharmaceutics*, 252(1-2):263–266, 2003. 15

[43] M. T. Morgan, M. A. Carnahan, C. E. Immoos, A. A. Ribeiro, S. Finkelstein, S. J. Lee, and M. W. Grinstaff. Dendritic Molecular Capsules for Hydrophobic Compounds. *Journal Of The American Chemical Society*, 125(50):15485–15489, 2003.

[44] E. R. Gillies, E. Dy, J. M. J. Fréchet, and F. C. Szoka. Biological evaluation of polyester dendrimer: poly(ethylene oxide) "bow-tie" hybrids with tunable molecular weight and architecture. *Molecular Pharmaceutics*, 2(2):129–138, March 2005.

[45] K. Jain, P. Kesharwani, U. Gupta, and N. K. Jain. Dendrimer toxicity: Let's meet the challenge. *International journal of pharmaceutics*, 394(1-2):122–142, July 2010.

[46] P. Kesharwani, V. Gajbhiye, R. K. Tekade, and N. K. Jain. Evaluation of dendrimer safety and efficacy through cell line studies. *Current drug targets*, 12(10):1478–1497, September 2011. 13, 15

[47] M. El-Sayed, M. Ginski, C. Rhodes, and H. Ghandehari. Transepithelial transport of poly(amidoamine) dendrimers across Caco-2 cell monolayers. *Journal of controlled release : official journal of the Controlled Release Society*, 81(3):355–365, 2002. 14

[48] A. Mecke, D.-K. Lee, A. Ramamoorthy, B. G. Orr, and M. M. B. Holl. Synthetic and natural polycationic polymer nanoparticles interact selectively with fluid-phase domains of DMPC lipid bilayers. *Langmuir*, 21(19):8588–8590, September 2005.

[49] M. Ionov, K. Gardikis, D. Wróbel, S. Hatziantoniou, H. Mourelatou, J.-P. Majoral, B. Klajnert, M. Bryszewska, and C. Demetzos. Interaction of cationic phosphorus dendrimers (CPD) with charged and neutral lipid membranes. *Colloids and surfaces. B, Biointerfaces*, 82(1):8–12, January 2011. 14

[50] V. Tiriveedhi, K. M. Kitchens, K. J. Nevels, H. Ghandehari, and P. Butko. Kinetic analysis of the interaction between poly(amidoamine) dendrimers and model lipid membranes. *Biochimica et Biophysica Acta - Biomembranes*, 1808(1):209–218, 2011. 14

[51] G. Thiagarajan, K. Greish, and H. Ghandehari. Charge affects the oral toxicity of poly(amidoamine) dendrimers. *European Journal of Pharmaceutics and Biopharmaceutics*, 84(2):330–334, 2013. 15

[52] G. Thiagarajan, S. Sadekar, K. Greish, A. Ray, and H. Ghandehari. Evidence of oral translocation of anionic G6.5 dendrimers in mice. *Molecular Pharmaceutics*, 10(3): 988–998, March 2013. 15

[53] S. S. Nigavekar, L. Y. Sung, M. Llanes, A. El-Jawahri, T. S. Lawrence, C. W. Becker, M. K. Khan, and L. P. Balogh. 3H dendrimer nanoparticle organ/tumor distribution. *Pharmaceutical research*, 21(3):476–483, March 2004. 15

[54] J. D. Eichman, A. U. Bielinska, J. F. Kukowska-Latallo, and J. R. Baker Jr. The use of PAMAM dendrimers in the efficient transfer of genetic material into cells. *Pharmaceutical science & technology today*, 3(7):232–245, July 2000. 16

[55] A. Dirksen, E. Zuidema, R. M. Williams, L. De Cola, C. Kauffmann, F. Vogtle, A. Roque, and F. Pina. Photoactivity and pH sensitivity of methyl orange functionalized poly(propyleneamine) dendrimers. *Macromolecules*, 35(7):2743–2747, 2002.

[56] C. D. Simpson, G. Mattersteig, K. Martin, L. Gherghel, R. E. Bauer, H. J. Räder, and K. Müllen. Nanosized Molecular Propellers by Cyclodehydrogenation of Polyphenylene Dendrimers. *Journal Of The American Chemical Society*, 126(10):3139–3147, 2004.

[57] X. Shi, I. Bányai, W. G. Lesniak, M. T. Islam, I. Országh, L. P. Balogh, J. R. Baker Jr, and P. Balogh. Capillary electrophoresis of polycationic poly(amidoamine) dendrimers. *Electrophoresis*, 26(15):2949–2959, 2005.

[58] A. Agarwal, U. Gupta, A. Asthana, and N. K. Jain. Dextran conjugated dendritic nanoconstructs as potential vectors for anti-cancer agent. *Biomaterials*, 30(21):3588–3596, 2009.

[59] P. Kesharwani, R. K. Tekade, V. Gajbhiye, K. Jain, and N. K. Jain. Cancer targeting potential of some ligand-anchored poly(propylene imine) dendrimers: a comparison. *Nanomedicine : nanotechnology, biology, and medicine*, 7(3):295–304, June 2011. 16

[60] J. F. G. A. Jansen, E. W. Meijer, and E. M. M. De Brabander-van Den Berg. The dendritic box: Shape-selective liberation of encapsulated guests. *Journal Of The American Chemical Society*, 117(15):4417–4418, 1995. 16

[61] R. Rupp, S. L. Rosenthal, and L. R. Stanberry. VivaGel™ (SPL7013 Gel): A candidate dendrimer - Microbicide for the prevention of HIV and HSV infection. *International Journal of Nanomedicine*, 2(4):561–566, 2007. 16

[62] D. Tyssen, S. A. Henderson, A. Johnson, J. Sterjovski, K. Moore, J. La, M. Zanin, S. Sonza, P. Karellas, M. P. Giannis, G. Krippner, S. Wesselingh, T. McCarthy, P. R. Gorry, P. A. Ramsland, R. Cone, J. R. A. Paull, G. R. Lewis, and G. Tachedjian. Structure activity relationship of dendrimer microbicides with dual action antiviral activity. *PLoS ONE*, 5(8):e12309, 2010. 16

[63] B. Wang, R. S. Navath, A. R. Menjoge, B. Balakrishnan, R. Bellair, H. Dai, R. Romero, S. Kannan, and R. M. Kannan. Inhibition of bacterial growth and intramniotic infection in a guinea pig model of chorioamnionitis using PAMAM dendrimers. *International journal of pharmaceutics*, 395(1-2):298–308, August 2010. 16

[64] F. E. Koç and M. Şenel. Solubility enhancement of Non-Steroidal Anti-Inflammatory Drugs (NSAIDs) using polypolypropylene oxide core PAMAM dendrimers. *International journal of pharmaceutics*, 451(1-2):18–22, 2013. 18

[65] A. S. Chauhan, S. Sridevi, K. B. Chalasani, A. K. Jain, S. K. Jain, N. K. Jain, and P. V. Diwan. Dendrimer-mediated transdermal delivery: Enhanced bioavailability of indomethacin. *Journal of controlled release : official journal of the Controlled Release Society*, 90(3):335–343, 2003. 18

[66] T. F. Vandamme and L. Brobeck. Poly(amidoamine) dendrimers as ophthalmic vehicles for ocular delivery of pilocarpine nitrate and tropicamide. *Journal of controlled release : official journal of the Controlled Release Society*, 102(1):23–38, 2005. 18

[67] S. Bai, C. Thomas, and F. Ahsan. Dendrimers as a carrier for pulmonary delivery of enoxaparin, a low-molecular weight heparin. *Journal of Pharmaceutical Sciences*, 96 (8):2090–2106, 2007. 18

[68] A. Agarwal, A. Asthana, U. Gupta, and N. K. Jain. Tumour and dendrimers: a review on drug delivery aspects. *Journal of Pharmacy and Pharmacology*, 60(6):671–688, June 2008. 18

[69] A. Quintana, E. Raczka, L. Piehler, I. Lee, A. Myc, I. J. Majoros, A. K. Patri, T. P. Thomas, J. Mulé, and J. R. Baker Jr. Design and function of a dendrimer-based therapeutic nanodevice targeted to tumor cells through the folate receptor. *Pharmaceutical research*, 19(9):1310–1316, 2002. 18

[70] J. F. Kukowska-Latallo, K. A. Candido, Z. Cao, S. S. Nigavekar, I. J. Majoros, T. P. Thomas, M. K. Khan, J. R. Baker, and L. P. Balogh. Nanoparticle targeting of anticancer drug improves therapeutic response in animal model of human epithelial cancer. *Cancer Research*, 65(12):5317–5324, June 2005. 18

[71] Y. Choi, T. P. Thomas, A. Kotlyar, M. T. Islam, and J. R. Baker Jr. Synthesis and functional evaluation of DNA-assembled polyamidoamine dendrimer clusters for cancer cell-specific targeting. *Chemistry and Biology*, 12(1):35–43, 2005. 19

[72] P. Kolhe, J. Khandare, O. Pillai, S. Kannan, M. Lieh-Lai, and R. M. Kannan. Preparation, cellular transport, and activity of polyamidoamine-based dendritic nanodevices with a high drug payload. *Biomaterials*, 27(4):660–669, February 2006. 19

[73] A.-M. Caminade, C.-O. Turrin, and J.-P. Majoral. Dendrimers and DNA: combinations of two special topologies for nanomaterials and biology. *Chemistry (Weinheim an der Bergstrasse, Germany)*, 14(25):7422–7432, 2008. 20

[74] M. Kasper, V. Jaks, D. Hohl, and R. Toftgård. Basal cell carcinoma - molecular biology and potential new therapies. *The Journal of Clinical Investigation*, 122(2):455–463, February 2012. 22

[75] E. H. Epstein. Basal cell carcinomas: attack of the hedgehog. *Nature Reviews Cancer*, 8(10):743–754, October 2008. 22

[76] A. I. Rubin, E. H. Chen, and D. Ratner. Basal-cell carcinoma. *The New England journal of medicine*, 353(21):2262–2269, November 2005. 22

[77] S. Gupta, N. Takebe, and P. Lorusso. Targeting the Hedgehog pathway in cancer. *Therapeutic advances in medical oncology*, 2(4):237–250, July 2010. 22

[78] P. W. Ingham and A. P. McMahon. Hedgehog signaling in animal development: paradigms and principles. *Genes & development*, 15(23):3059–3087, December 2001. 22

[79] C. M. L. J. Tilli, M. A. M. Van Steensel, G. A. M. Krekels, H. A. M. Neumann, and F. C. S. Ramaekers. Molecular aetiology and pathogenesis of basal cell carcinoma. *The British journal of dermatology*, 152(6):1108–1124, June 2005. 23

[80] P. M. LoRusso, C. M. Rudin, J. C. Reddy, R. Tibes, G. J. Weiss, M. J. Borad, C. L. Hann, J. R. Brahmer, I. Chang, W. C. Darbonne, R. A. Graham, K. L. Zerivitz, J. A. Low, and D. D. Von Hoff. Phase I trial of hedgehog pathway inhibitor vismodegib (GDC-0449) in patients with refractory, locally advanced or metastatic solid tumors. *Clinical cancer research : an official journal of the American Association for Cancer Research*, 17(8):2502–2511, April 2011. 23

[81] D. D. Von Hoff, P. M. LoRusso, C. M. Rudin, J. C. Reddy, R. L. Yauch, R. Tibes, G. J. Weiss, M. J. Borad, C. L. Hann, J. R. Brahmer, H. M. Mackey, B. L. Lum, W. C. Darbonne, J. C. Marsters, F. J. de Sauvage, and J. A. Low. Inhibition of the hedgehog pathway in advanced basal-cell carcinoma. *The New England journal of medicine*, 361 (12):1164–1172, September 2009. 23

[82] R. L. Yauch, G. J. P. Dijkgraaf, B. Alicke, T. Januario, C. P. Ahn, T. Holcomb, K. Pujara, J. Stinson, C. A. Callahan, T. Tang, J. F. Bazan, Z. Kan, S. Seshagiri, C. L. Hann, S. E. Gould, J. A. Low, C. M. Rudin, and F. J. de Sauvage. Smoothened mutation confers resistance to a Hedgehog pathway inhibitor in medulloblastoma. *Science*, 326 (5952):572–574, October 2009. 24, 155

[83] W. R. Martin, C. G. Eades, J. A. Thompson, R. E. Huppler, and P. E. Gilbert. The effects of morphine- and nalorphine- like drugs in the nondependent and morphine-dependent chronic spinal dog. *The Journal of Pharmacology and Experimental Therapeutics*, 197(3):517–532, June 1976. 24, 129

[84] R. R. Matsumoto, Y. Liu, M. Lerner, E. W. Howard, and D. J. Brackett. Sigma receptors: potential medications development target for anti-cocaine agents. *European journal of pharmacology*, 469(1-3):1–12, May 2003. 24

[85] S. B. Hellewell and W. D. Bowen. A sigma-like binding site in rat pheochromocytoma (PC12) cells: decreased affinity for (+)-benzomorphans and lower molecular weight suggest a different sigma receptor form from that of guinea pig brain. *Brain research*, 527(2):244–253, September 1990. 24

[86] R. Quirion, W. D. Bowen, Y. Itzhak, J. L. Junien, J. M. Musacchio, R. B. Rothman, T.-P. Su, S. W. Tam, and D. P. Taylor. A proposal for the classification of sigma binding sites. In *Trends in pharmacological sciences*, pages 85–86, March 1992. 24

[87] D. Fontanilla, M. Johannessen, A. R. Hajipour, N. V. Cozzi, M. B. Jackson, and A. E. Ruoho. The hallucinogen N,N-dimethyltryptamine (DMT) is an endogenous sigma-1 receptor regulator. *Science*, 323(5916):934–937, February 2009. 24

[88] M. Hanner, F. F. Moebius, A. Flandorfer, H.-G. Knaus, J. Striessnig, E. Kempner, and H. Glossmann. Purification, molecular cloning, and expression of the mammalian sigma1-binding site. *Proceedings of the National Academy of Sciences of the United States of America*, 93(15):8072–8077, July 1996. 24

[89] T. Hayashi, T. Maurice, and T.-P. Su. Ca(2+) signaling via sigma(1)-receptors: novel regulatory mechanism affecting intracellular Ca(2+) concentration. *The Journal of Pharmacology and Experimental Therapeutics*, 293(3):788–798, June 2000. 25

[90] D. Marson, E. Laurini, P. Posocco, M. Fermeglia, and S. Pricl. Cationic carbosilane dendrimers and oligonucleotide binding: an energetic affair. *Nanoscale*, 7(9):3876–3887, February 2015. 29

[91] E. Laurini, D. Harel, D. Marson, D. Schepmann, T. J. Schmidt, S. Pricl, and B. Wünsch. Identification, pharmacological evaluation and binding mode analysis of novel chromene and chromane based $\sigma 1$ receptor ligands. *European Journal of Medicinal Chemistry*, 83:526–533, August 2014.

[92] S. Brune, D. Schepmann, K.-H. Klempnauer, D. Marson, V. Dal Col, E. Laurini, M. Fermeglia, B. Wünsch, and S. Pricl. The Sigma Enigma: In Vitro/ in SilicoSite-Directed Mutagenesis Studies Unveil σ 1Receptor Ligand Binding. *Biochemistry*, page 140428065447006, April 2014.

[93] E. Laurini, D. Marson, V. Dal Col, M. Fermeglia, M. G. Mamolo, D. Zampieri, L. Vio, and S. Pricl. Another brick in the wall. Validation of the σ 1 receptor 3d model by computer-assisted design, synthesis, and activity of new σ 1 ligands. *Molecular Pharmaceutics*, 9(11):3107–3126, 2012. 136

[94] S. Pricl, B. Cortelazzi, V. Dal Col, D. Marson, E. Laurini, M. Fermeglia, L. Licitra, S. Pilotti, P. Bossi, and F. Perrone. Smoothened (SMO) receptor mutations dictate resistance to vismodegib in basal cell carcinoma. *Molecular Oncology*, September 2014.

[95] P. Posocco, X. Liu, E. Laurini, D. Marson, C. Chen, C. Liu, M. Fermeglia, P. Rocchi, S. Pricl, and L. Peng. Impact of siRNA Overhangs for Dendrimer-Mediated siRNA Delivery and Gene Silencing. *Molecular Pharmaceutics*, 10(8):3262–3273, August 2013.

[96] P. Posocco, E. Laurini, D. Marson, D. K. Smith, B. Klajnert, M. Bryszewska, A.-M. Caminade, J.-P. Majoral, M. Fermeglia, K. Karatasos, S. Pricl, and L. Peng. Multiscale modeling of dendrimers and dendrons for drug and nucleic acid delivery. In B. Klajnert, L. Peng, and V. Cena, editors, *Dendrimers in Biomedical Applications*. Royal Society of Chemistry, Cambridge, 2013. 29

[97] E. Schrödinger. Abhandlungen zur Wellenmechanik. 1928. 31

[98] M. Born and R. Oppenheimer. On the quantum theory of molecules. *Annalen der Physik*, 84(20):457–484, 1927. 31

[99] P. A. Kollman, D. A. Case, V. Babin, J. T. Barryman, Q. Cai, R. M. Betz, D. S. Cerutti, T. E. Cheatham III, T. A. Darden, R. Duke, H. Gohlke, A. W. Goetz, S. Gusarov, N. Homeyer, J. Janowski, I. Kolossvary, J. Kaus, A. Kovalenko, T. S. Lee, S. LeGrand, T. Luchko, R. Luo, B. D. Madej, K. M. Merz Jr, F. Paesani, D. R. Roe, A. E. Roitberg, C. Sagui, R. Salomon-Ferrer, G. M. De Seabra, C. Simmerling, W. Smith, J. M. Swails, R. C. Walker, J. Wang, R. M. Wolf, X. Wu, and P. Kollman. AMBER. 35

[100] J. Wang, R. M. Wolf, J. W. Caldwell, P. A. Kollman, and D. A. Case. Development and testing of a general amber force field. *Journal of Computational Chemistry*, 25(9): 1157–1174, July 2004. 36

[101] R. C. Walker, B. D. Madej, I. R. Gould, and C. J. Dickson. Lipid 12: Accurate membrane simulations with a redesigned modular phospholipid force field for AMBER. *Abstracts of Papers of the American Chemical Society*, 245, 2013. 36

[102] C. J. Dickson, B. D. Madej, Å. A. Skjevik, R. M. Betz, K. Teigen, I. R. Gould, and R. C. Walker. Lipid14: The Amber Lipid Force Field. *Journal of chemical theory and computation*, page 140130133233003, January 2014. 36

[103] J. Wang, W. Wang, P. A. Kollman, and D. A. Case. Automatic atom type and bond type perception in molecular mechanical calculations. *Journal of molecular graphics & modelling*, 25(2):247–260, October 2006. 37

[104] A. W. Götz, M. J. Williamson, D. Xu, D. Poole, S. Le Grand, and R. C. Walker. Routine Microsecond Molecular Dynamics Simulations with AMBER on GPUs. 1. Generalized Born. *Journal of chemical theory and computation*, 8(5):1542–1555, May 2012. 37

[105] R. Salomon-Ferrer, A. W. Götz, D. Poole, S. Le Grand, and R. C. Walker. Routine microsecond molecular dynamics simulations with AMBER on GPUs. 2. Explicit solvent particle mesh ewald. *Journal of chemical theory and computation*, 9(9):3878–3888, 2013. 37

[106] B. R. Miller III, T. D. McGee, Jr., J. M. Swails, N. Homeyer, H. Gohlke, and A. E. Roitberg. MMPBSA.py: An Efficient Program for End-State Free Energy Calculations. *Journal of chemical theory and computation*, 8(9):3314–3321, September 2012. 37

[107] D. R. Roe and T. E. Cheatham III. PTRAJ and CPPTRAJ: Software for Processing and Analysis of Molecular Dynamics Trajectory Data. *Journal of chemical theory and computation*, page 130610164835005, June 2013. 37

[108] M. J. S. Dewar, E. G. Zoebisch, E. F. Healy, and J. P. Stewart. AM1: A new general purpose quantum mechanical molecular model. *Journal Of The American Chemical Society*, 107(13):3902–3909, 1985. 37

[109] A. Jakalian, B. L. Bush, D. B. Jack, and C. I. Bayly. Fast, Efficient Generation of High-Quality Atomic Charges. AM1-BCC Model: I. Method. *Journal of Computational Chemistry*, 21(2):132–146, 2000.

[110] A. Jakalian, D. B. Jack, and C. I. Bayly. Fast, efficient generation of high-quality atomic charges. AM1-BCC model: II. Parameterization and validation. *Journal of Computational Chemistry*, 23(16):1623–1641, December 2002. 37

[111] C. I. Bayly, P. Cieplak, W. D. Cornell, and P. A. Kollman. A well-behaved electrostatic potential based method using charge restraints for deriving atomic charges: The RESP model. *Journal of Physical Chemistry*, 97(40):10269–10280, 1993. 37

[112] F.-Y. Dupradeau, A. Pigache, T. Zaffran, C. Savineau, R. Lelong, N. Grivel, D. Lelong, W. Rosanski, and P. Cieplak. The R.E.D. tools: advances in RESP and ESP charge derivation and force field library building. *Physical chemistry chemical physics : PCCP*, 12(28):7821–7839, July 2010.

[113] E. Vanquelef, S. Simon, G. Marquant, E. Garcia, G. Klimerak, J. C. Delepine, P. Cieplak, and F.-Y. Dupradeau. R.E.D. Server: a web service for deriving RESP

and ESP charges and building force field libraries for new molecules and molecular fragments. *Nucleic Acids Research*, 39(Web Server issue):W511–7, July 2011. 37

[114] E. F. Pettersen, T. D. Goddard, C. C. Huang, G. S. Couch, D. M. Greenblatt, E. C. Meng, and T. E. Ferrin. UCSF Chimera–a visualization system for exploratory research and analysis. *Journal of Computational Chemistry*, 25(13):1605–1612, October 2004. 38, 50

[115] W. Humphrey, A. Dalke, and K. Schulten. VMD: Visual molecular dynamics. *Journal of Molecular Graphics*, 14(1):33–38, 1996. 38

[116] W. L. Jorgensen, J. Chandrasekhar, J. D. Madura, R. W. Impey, and M. L. Klein. Comparison of simple potential functions for simulating liquid water. *The Journal of Chemical Physics*, 79(2):926–935, 1983. 43

[117] Iowa State University. Department of Chemical Engineering and Nuclear Engineering. General Atomic and Molecular Electronic Structure System, 1993. 45

[118] M. S. Gordon and M. W. Schmidt. Advances in electronic structure theory: GAMESS a decade later. In C. E. Dykstra, G. Frenking, K. S. Kim, and G. E. Scuseria, editors, *Theory and Applications of Computational Chemistry the first forty years*, pages 1167–1189. Amsterdam, May 2007. 45

[119] J. H. Lii and N. L. Allinger. The MM3 force field for amides, polypeptides and proteins. *Journal of Computational Chemistry*, 12(2):186–199, March 1991. 45

[120] T. Darden, D. York, and L. G. Pedersen. Particle mesh Ewald: An NâŃĚlog(N) method for Ewald sums in large systems. *The Journal of Chemical Physics*, 98(12):10089–10092, June 1993. 46

[121] S. Jo, T. Kim, V. G. Iyer, and W. Im. CHARMM-GUI: a web-based graphical user interface for CHARMM. *Journal of Computational Chemistry*, 29(11):1859–1865, August 2008. 46

[122] S. Jo, J. B. Lim, J. B. Klauda, and W. Im. CHARMM-GUI Membrane Builder for Mixed Bilayers and Its Application to Yeast Membranes. *Biophysj*, 97(1):50–58, July 2009.

[123] Y. Qi, X. Cheng, W. Han, S. Jo, K. Schulten, and W. Im. CHARMM-GUI PACE CG Builder for Solution, Micelle, and Bilayer Coarse-Grained Simulations. *Journal of chemical information and modeling*, page 140304043638008, March 2014. 46

[124] J.-P. Ryckaert, G. Ciccotti, and H. J. Berendsen. Numerical integration of the cartesian equations of motion of a system with constraints: molecular dynamics of n-alkanes. *Journal of Computational Physics*, 23(3):327–341, 1977. 47

[125] X. Wu and B. R. Brooks. Self-guided Langevin dynamics simulation method. *Chemical Physics Letters*, 381(3-4):512–518, 2003. 52

[126] H. J. Berendsen, J. P. M. Postma, W. F. Van Gunsteren, A. Dinola, and J. R. Haak. Molecular dynamics with coupling to an external bath. *The Journal of Chemical Physics*, 81(8):3684–3690, 1984. 52

[127] J. Srinivasan, T. E. Cheatham III, P. Cieplak, P. A. Kollman, and D. A. Case. Continuum solvent studies of the stability of DNA, RNA, and phosphoramidate-DNA helices. *Journal Of The American Chemical Society*, 120(37):9401–9409, 1998. 56

[128] J. Weiser, P. S. Shenkin, and W. C. Still. Approximate solvent-accessible surface areas from tetrahedrally directed neighbor densities. *Biopolymers*, 50(4):373–380, October 1999. 57

[129] W. L. Jorgensen. Drug discovery: Pulled from a protein's embrace. *Nature*, 466(7302): 42–43, July 2010. 62

[130] F. Colizzi, R. Perozzo, L. Scapozza, M. Recanatini, and A. Cavalli. Single-Molecule Pulling Simulations Can Discern Active from Inactive Enzyme Inhibitors. *Journal Of The American Chemical Society*, 132(21):7361–7371, June 2010. 62

[131] C. Jarzynski. Nonequilibrium equality for free energy differences. *Physical Review Letters*, 78(14):2690–2693, 1997. 62

[132] G. Hummer and A. Szabo. Free energy reconstruction from nonequilibrium single-molecule pulling experiments. *Proceedings of the National Academy of Sciences of the United States of America*, 98(7):3658–3661, March 2001.

[133] G. Hummer and A. Szabo. Kinetics from nonequilibrium single-molecule pulling experiments. *Biophysj*, 85(1):5–15, July 2003. 62

[134] G. Gaspari and J. Rudnick. n-vector model in the limit n–>0 and the statistics of linear polymer systems: A Ginzburg-Landau theory. *Physical review. B, Condensed matter*, 33(5):3295–3305, March 1986. 66

[135] X. Liu, J. Wu, M. Yammine, J. Zhou, P. Posocco, S. Viel, C. Liu, F. Ziarelli, M. Fermeglia, S. Pricl, G. Victorero, C. Nguyen, P. Erbacher, J.-P. Behr, and L. Peng. Structurally flexible triethanolamine core pamam dendrimers are effective nanovectors for DNA transfection in vitro and in vivo to the mouse thymus. *Bioconjugate Chemistry*, 22(12):2461–2473, 2011. 71, 120

[136] X. Liu, C. Liu, E. Laurini, P. Posocco, S. Pricl, F. Qu, P. Rocchi, and L. Peng. Efficient delivery of sticky siRNA and potent gene silencing in a prostate cancer model using a generation 5 triethanolamine-core PAMAM dendrimer. *Molecular Pharmaceutics*, 9 (3):470–481, 2012. 71, 73, 74, 84, 120

[137] P. Rocchi, E. Beraldi, S. Ettinger, L. Fazli, R. L. Vessella, C. Nelson, and M. Gleave. Increased Hsp27 after androgen ablation facilitates androgen-independent progression in prostate cancer via signal transducers and activators of transcription 3-mediated suppression of apoptosis. *Cancer Research*, 65(23):11083–11093, 2005. 72

[138] A. Zoubeidi and M. Gleave. Small heat shock proteins in cancer therapy and prognosis. *International Journal of Biochemistry and Cell Biology*, 44(10):1646–1656, 2012. 72

[139] A. Telerman and R. Amson. The molecular programme of tumour reversion: The steps beyond malignant transformation. *Nature Reviews Cancer*, 9(3):206–216, 2009. 72

[140] V. Baylot, M. Katsogiannou, C. Andrieu, D. Taieb, J. Acunzo, S. Giusiano, L. Fazli, M. Gleave, C. Garrido, and P. Rocchi. Targeting TCTP as a new therapeutic strategy in castration-resistant prostate cancer. *Molecular Therapy*, 20(12):2244–2256, 2012. 72

[141] O. Bagasra and K. R. Prilliman. RNA interference: The molecular immune system. *Journal of Molecular Histology*, 35(6):545–553, 2004. 73

[142] P. Rocchi, P. Jugpal, A. So, S. Sinneman, S. Ettinger, L. Fazli, C. Nelson, and M. Gleave. Small interference RNA targeting heat-shock protein 27 inhibits the growth of prostatic cell lines and induces apoptosis via caspase-3 activation in vitro. *BJU International*, 98(5):1082–1089, 2006. 73

[143] S. K. Calderwood and J. Gong. Molecular chaperones in mammary cancer growth and breast tumor therapy. *Journal of Cellular Biochemistry*, 113(4):1096–1103, 2012. 73

[144] K. Ciepluch, N. Katir, A. El Kadib, A. Felczak, K. Zawadzka, M. Weber, B. Klajnert, K. Lisowska, A.-M. Caminade, M. Bousmina, M. Bryszewska, and J.-P. Majoral. Biological properties of new viologen-phosphorus dendrimers. *Molecular Pharmaceutics*, 9 (3):448–457, March 2012. 87, 91

[145] K. Milowska, J. Grochowina, N. Katir, A. El Kadib, J.-P. Majoral, M. Bryszewska, and T. Gabryelak. Interaction between viologen-phosphorus dendrimers and α-synuclein. *Journal of Luminescence*, pages 1–6, September 2012. 87

[146] S. Asaftei and E. De Clercq. "Viologen" dendrimers as antiviral agents: the effect of charge number and distance. *Journal of Medicinal Chemistry*, 53(9):3480–3488, May 2010. 87

[147] A.-M. Caminade, C.-O. Turrin, and J.-P. Majoral. Biological properties of phosphorus dendrimers. *New Journal of Chemistry*, 34(8):1512–1524, 2010. 88

[148] D. Shcharbin, E. Pedziwiatr, L. Chonco, J. F. Bermejo-Martín, P. Ortega, F. J. de la Mata, R. Eritja, R. Gómez, B. Klajnert, M. Bryszewska, and M. A. Muñoz-Fernandez. Analysis of interaction between dendriplexes and bovine serum albumin. *Biomacromolecules*, 8(7):2059–2062, July 2007. 95

[149] P. K. Maiti, T. Çağin, S.-T. Lin, and W. A. Goddard III. Effect of solvent and pH on the structure of PAMAM dendrimers. *Macromolecules*, 38(3):979–991, 2005. 96, 98, 99

[150] P. K. Maiti, T. Çağin, G. Wang, and W. A. Goddard III. Structure of PAMAM dendrimers: Generations 1 through 11. *Macromolecules*, 37(16):6236–6254, 2004. 96, 98, 99

[151] D. A. Tomalia, A. M. Naylor, and W. A. Goddard III. Starbust dendrimers: Molecular-level control of size, shape, surface chemistry, topology, and flexibility from atoms to macroscopic matter. *Angewandte Chemie - International Edition in English*, 29(2): 138–175, 1990. 99

[152] E. J. Cobos, J. M. Entrena, F. R. Nieto, C. M. Cendán, and E. Del Pozo. Pharmacology and therapeutic potential of sigma1 receptor ligands. *Current Neuropharmacology*, 6 (4):344–366, 2008. 113

[153] A. Al-Saif, F. Al-Mohanna, and S. Bohlega. A mutation in sigma-1 receptor causes juvenile amyotrophic lateral sclerosis. *Annals of neurology*, August 2011. 113

[154] M. Mishina, M. Ohyama, K. Ishii, S. Kitamura, Y. Kimura, K.-i. Oda, K. Kawamura, T. Sasaki, S. Kobayashi, Y. Katayama, and K. Ishiwata. Low density of sigma1 receptors in early Alzheimer's disease. *Annals of nuclear medicine*, 22(3):151–156, April 2008. 113

[155] S. B. Smith, J. Duplantier, Y. Dun, B. Mysona, P. Roon, P. M. Martin, and V. Ganapathy. In vivo protection against retinal neurodegeneration by sigma receptor 1 ligand (+)-pentazocine. *Investigative ophthalmology & visual science*, 49(9):4154–4161, September 2008. 113

[156] T. Hayashi, Z. Justinova, E. Hayashi, G. Cormaci, T. Mori, S.-Y. Tsai, C. Barnes, S. R. Goldberg, and T.-P. Su. Regulation of sigma-1 receptors and endoplasmic reticulum chaperones in the brain of methamphetamine self-administering rats. *The Journal of Pharmacology and Experimental Therapeutics*, 332(3):1054–1063, March 2010. 113

[157] G. Navarro, E. Moreno, M. Aymerich, D. Marcellino, P. J. McCormick, J. Mallol, A. Cortés, V. Casadó, E. I. Canela, J. Ortiz, K. Fuxe, C. Lluís, S. Ferré, and R. Franco. Direct involvement of sigma-1 receptors in the dopamine D1 receptor-mediated effects of cocaine. *Proceedings of the National Academy of Sciences*, 107(43):18676–18681, October 2010.

[158] T. Hiranita, P. L. Soto, G. Tanda, and J. L. Katz. Reinforcing effects of sigma-receptor agonists in rats trained to self-administer cocaine. *The Journal of Pharmacology and Experimental Therapeutics*, 332(2):515–524, February 2010.

[159] S. Ramachandran, H. Lu, U. Prabhu, and A. E. Ruoho. Purification and characterization of the guinea pig sigma-1 receptor functionally expressed in Escherichia coli. *Protein expression and purification*, 51(2):283–292, February 2007. 113

[160] D. Zampieri, M. G. Mamolo, E. Laurini, C. Florio, C. Zanette, M. Fermeglia, P. Posocco, M. S. Paneni, S. Pricl, and L. Vio. Synthesis, biological evaluation, and three-dimensional in silico pharmacophore model for sigma(1) receptor ligands based on a series of substituted benzo[d]oxazol-2(3H)-one derivatives. *Journal of Medicinal Chemistry*, 52(17):5380–5393, September 2009. 114, 116

[161] E. Laurini, V. Dal Col, M. G. Mamolo, D. Zampieri, P. Posocco, M. Fermeglia, L. Vio, and S. Pricl. Homology model and docking-based virtual screening for ligands of the sigma-1 receptor. pages 1–6, August 2011. 114, 116, 136

[162] P. Seth, M. E. Ganapathy, S. J. Conway, C. D. Bridges, S. B. Smith, P. Casellas, and V. Ganapathy. Expression pattern of the type 1 sigma receptor in the brain and identity of critical anionic amino acid residues in the ligand-binding domain of the receptor. *Biochimica et Biophysica Acta*, 1540(1):59–67, July 2001. 116, 127, 134, 137, 138

[163] A. Pal, A. R. Hajipour, D. Fontanilla, S. Ramachandran, U. B. Chu, T. A. Mavlyutov, and A. E. Ruoho. Identification of regions of the sigma-1 receptor ligand binding site using a novel photoprobe. *Molecular Pharmacology*, 72(4):921–933, October 2007. 116

[164] K. Karatasos, P. Posocco, E. Laurini, and S. Pricl. Poly(amidoamine)-based dendrimer/siRNA complexation studied by computer simulations: effects of pH and generation on dendrimer structure and siRNA binding. *Macromolecular Bioscience*, 12(2): 225–240, February 2012. 120

[165] M. Yarim, M. Koksal, D. Schepmann, and B. Wünsch. Synthesis and in vitro evaluation of novel indole based sigma receptors ligands. *Chemical biology & drug design*, August 2011.

[166] G. M. Pavan, A. Danani, S. Pricl, and D. K. Smith. Modeling the Multivalent Recognition between Dendritic Molecules and DNA: Understanding How Ligand “Sacrifice” and Screening Can Enhance Binding. *Journal Of The American Chemical Society*, 131 (28):9686–9694, July 2009. 120

[167] H. Gohlke, C. Kiel, and D. A. Case. Insights into protein-protein binding by binding free energy calculation and free energy decomposition for the Ras-Raf and Ras-RalGDS complexes. *Journal of molecular biology*, 330(4):891–913, July 2003. 120

[168] T. Sulea and E. O. Purisima. Optimizing Ligand Charges for Maximum Binding Affinity. A Solvated Interaction Energy Approach. *Journal of Physical Chemistry B*, 105 (4):889–899, 2001.

[169] L.-P. Lee and B. Tidor. Optimization of binding electrostatics: charge complementarity in the barnase-barstar protein complex. *Protein science : a publication of the Protein Society*, 10(2):362–377, February 2001.

[170] T. Selzer, S. Albeck, and G. Schreiber. Rational design of faster associating and tighter binding protein complexes. *Nature structural biology*, 7(7):537–541, July 2000.

[171] E. Kangas and B. Tidor. Optimizing electrostatic affinity in ligand-receptor binding: Theory, computation, and ligand properties. *The Journal of Chemical Physics*, 109 (17):7522–7545, 1998. 120

[172] S. Huo, I. Massova, and P. A. Kollman. Computational alanine scanning of the 1:1 human growth hormone-receptor complex. *Journal of Computational Chemistry*, 23 (1):15–27, January 2002. 126

[173] C. P. Palmer, R. Mahen, E. Schnell, M. B. A. Djamgoz, and E. Aydar. Sigma-1 receptors bind cholesterol and remodel lipid rafts in breast cancer cell lines. *Cancer Research*, 67 (23):11166–11175, December 2007. 127

[174] D. Zampieri, M. G. Mamolo, E. Laurini, C. Zanette, C. Florio, S. Collina, D. Rossi, O. Azzolina, and L. Vio. Substituted benzo[d]oxazol-2(3H)-one derivatives with preference for the σ1 binding site. *European Journal of Medicinal Chemistry*, 44(1):124–130, January 2009. 128

[175] S. B. Hellewell, A. Bruce, G. Feinstein, J. Orringer, W. Williams, and W. D. Bowen. Rat liver and kidney contain high densities of sigma 1 and sigma 2 receptors: characterization by ligand binding and photoaffinity labeling. *European journal of pharmacology*, 268(1):9–18, June 1994. 128, 130

[176] E. Laurini, V. Dal Col, M. G. Mamolo, D. Zampieri, P. Posocco, M. Fermeglia, L. Vio, and S. Pricl. Homology Model and Docking-Based Virtual Screening for Ligands of the σ 1Receptor. *ACS Medicinal Chemistry Letters*, 2(11):834–839, November 2011. 130, 134

[177] U. B. Chu, S. Ramachandran, A. R. Hajipour, and A. E. Ruoho. Photoaffinity Labeling of the Sigma-1 Receptor with N-[3-(4-Nitrophenyl)propyl]- N-dodecylamine: Evidence of Receptor Dimers. *Biochemistry*, 52(5):859–868, February 2013. 135

[178] C. Meyer, D. Schepmann, S. Yanagisawa, J. Yamaguchi, V. Dal Col, E. Laurini, K. Itami, S. Pricl, and B. Wünsch. Pd-catalyzed direct C-H bond functionalization of spirocyclic σ1 ligands: Generation of a pharmacophore model and analysis of the reverse binding mode by Docking into a 3D homology model of the σ1 receptor. *Journal of Medicinal Chemistry*, 55(18):8047–8065, 2012. 136

[179] D. Rossi, A. Pedrali, R. Gaggeri, A. Marra, L. Pignataro, E. Laurini, V. Dal Col, M. Fermeglia, S. Pricl, D. Schepmann, B. Wünsch, M. Peviani, D. Curti, and S. Collina. Chemical, pharmacological, and in vitro metabolic stability studies on enantiomerically pure RC-33 compounds: promising neuroprotective agents acting as σâĆĄ receptor agonists. *ChemMedChem*, 8(9):1514–1527, September 2013. 136

[180] A. Pal, U. B. Chu, S. Ramachandran, D. Grawoig, L.-W. Guo, A. R. Hajipour, and A. E. Ruoho. Juxtaposition of the steroid binding domain-like I and II regions constitutes a ligand binding site in the α-1 receptor. *Journal of Biological Chemistry*, 283(28): 19646–19656, 2008. 141

[181] J. R. Kahoun and A. E. Ruoho. (125I)iodoazidococaine, a photoaffinity label for the haloperidol-sensitive sigma receptor. In *Proceedings of the National Academy of Sciences of the United States of America*, pages 1393–1397, 1992. 142

[182] S. C. Flohil, I. Seubring, M. M. van Rossum, J.-W. W. Coebergh, E. de Vries, and T. Nijsten. Trends in Basal cell carcinoma incidence rates: a 37-year Dutch observational study. *The Journal of investigative dermatology*, 133(4):913–918, April 2013. 147

[183] J. Xie, M. Murone, S.-M. Luoh, A. Ryan, Q. Gu, C. Zhang, J. M. Bonifas, C.-W. Lam, M. Hynes, A. Goddard, A. Rosenthal, E. H. Epstein, and F. J. de Sauvage. Activating Smoothened mutations in sporadic basal-cell carcinoma. *Nature*, 391(6662): 90–92, January 1998. 154

[184] G. J. P. Dijkgraaf, B. Alicke, L. Weinmann, T. Januario, K. West, Z. Modrusan, D. Burdick, R. Goldsmith, K. Robarge, D. Sutherlin, S. J. Scales, S. E. Gould, R. L. Yauch, and F. J. de Sauvage. Small molecule inhibition of GDC-0449 refractory smoothened mutants and downstream mechanisms of drug resistance. *Cancer Research*, 71(2):435–444, January 2011. 155

[185] D. J. Kim, J. Kim, K. Spaunhurst, J. Montoya, R. Khodosh, K. Chandra, T. Fu, A. Gilliam, M. Molgo, P. A. Beachy, and J. Y. Tang. Open-label, exploratory phase II trial of oral itraconazole for the treatment of basal cell carcinoma. *Journal of clinical oncology : official journal of the American Society of Clinical Oncology*, 32(8):745–751, March 2014. 155

[186] J. Kim, B. T. Aftab, J. Y. Tang, D. J. Kim, A. H. Lee, M. Rezaee, J. Kim, B. Chen, E. M. King, A. Borodovsky, G. J. Riggins, E. H. Epstein, P. A. Beachy, and C. M. Rudin. Itraconazole and arsenic trioxide inhibit Hedgehog pathway activation and tumor growth associated with acquired resistance to smoothened antagonists. *Cancer cell*, 23(1):23–34, January 2013. 155

[187] M. Eberl, S. Klingler, D. Mangelberger, A. Loipetzberger, H. Damhofer, K. Zoidl, H. Schnidar, H. Hache, H.-C. Bauer, F. Solca, C. Hauser-Kronberger, A. N. Ermilov, M. E. Verhaegen, C. K. Bichakjian, A. A. Dlugosz, W. Nietfeld, M. Sibilia, H. Lehrach, C. Wierling, and F. Aberger. Hedgehog-EGFR cooperation response genes determine the oncogenic phenotype of basal cell carcinoma and tumour-initiating pancreatic cancer cells. *EMBO molecular medicine*, 4(3):218–233, March 2012. 155

[188] S. X. Atwood, M. Li, A. H. Lee, J. Y. Tang, and A. E. Oro. GLI activation by atypical protein kinase C ι/λ regulates the growth of basal cell carcinomas. *Nature*, 494(7438): 484–488, February 2013. 155

[189] E. Makinodan and A. G. Marneros. Protein kinase A activation inhibits oncogenic Sonic hedgehog signalling and suppresses basal cell carcinoma of the skin. *Experimental dermatology*, 21(11):847–852, November 2012. 155

[190] S. Buonamici, J. Williams, M. Morrissey, A. Wang, R. Guo, A. Vattay, K. Hsiao, J. Yuan, J. Green, B. Ospina, Q. Yu, L. Ostrom, P. Fordjour, D. L. Anderson, J. E. Monahan, J. F. Kelleher, S. Peukert, S. Pan, X. Wu, S.-M. Maira, C. García-Echeverría, K. J. Briggs, D. N. Watkins, Y.-m. Yao, C. Lengauer, M. Warmuth, W. R. Sellers, and M. Dorsch. Interfering with resistance to smoothened antagonists by inhibition of the PI3K pathway in medulloblastoma. *Science translational medicine*, 2(51):51ra70–51ra70, September 2010. 155, 156